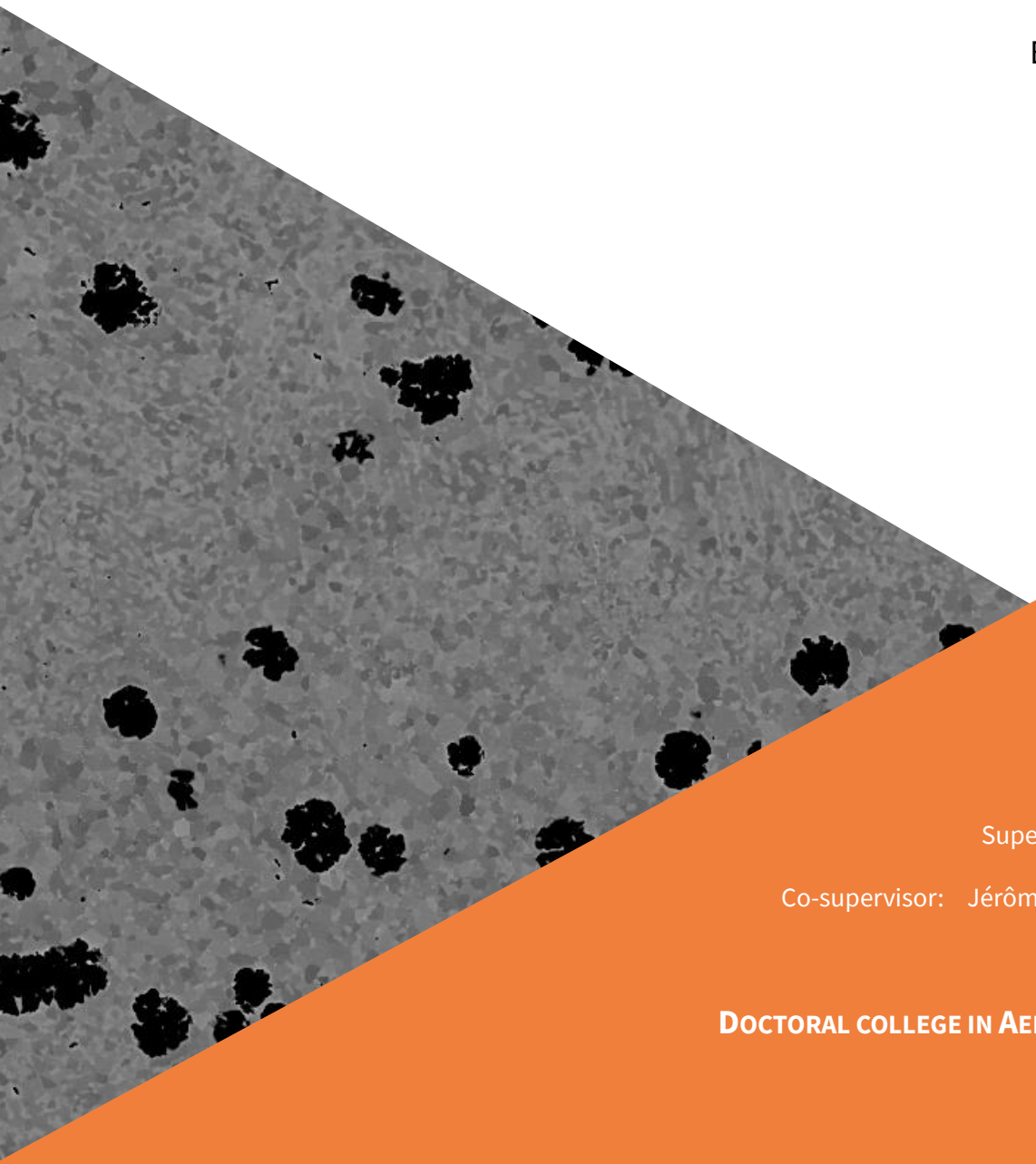
LIÈGE université
Sciences Appliquées

Development of graphitic tool steel for Laser Powder Bed Fusion with enhanced tribological properties

A thesis submitted in partial fulfilment of the requirements
for the degree of Doctor of Philosophy (PhD) in Engineering Science

by

Enrico SAGGIONETTO



Supervisor: Anne MERTENS

Co-supervisor: Jérôme Tchoufang TCHUINDJANG

DOCTORAL COLLEGE IN AEROSPACE AND MECHANICS

NOVEMBER 2026

Examination committee

Prof. **O. Bruls** (President)	*University of Liège, Belgium*
Prof. **A. Mertens** (Supervisor)	*University of Liège, Belgium*
Dr **J.T. Tchuindjang** (Co-Supervisor)	*University of Liège, Belgium*
Prof. **P. Duysinx**	*University of Liège, Belgium*
Dr **F. Boschini**	*University of Liège, Belgium*
Prof. **D. Brabazon**	*Dublin City University, Ireland*
Prof. **A. Molinari**	*Università di Trento, Italy*
Dr **M. Delmée**	*AM 4 AM, Luxembourg*

Gutta cavat lapidem

Abstract

The emergence of Additive Manufacturing (AM) has transformed the landscape of metal processing. This technology is proving particularly effective for developing novel metals with innovative microstructures, primarily due to the out-of-equilibrium conditions inherent to the process. However, AM is constrained by the limited availability or high cost of metal powders required as raw materials, and the difficult processability of some alloys.

This study presents the development of a novel iron-based alloy fabricated via AM, detailing the entire process from powder selection and preparation to processing through Laser Powder Bed Fusion (LPBF). It also examines the alloy's metallurgical characteristics, along with its mechanical and wear performance. The key innovation lies in the formation of a microstructure comprising graphite and carbides embedded within a hard matrix, resulting in enhanced wear resistance. While such microstructures, particularly those containing graphite, are well documented in conventional metallurgy, their successful realization using LPBF has not been previously reported.

The development of this alloy began with the selection of suitable raw materials for the LPBF process, commercially available at affordable prices. Two types of powders were selected: the first, which constitutes the majority of the mixture, is a low-alloy tool steel (AISI S2), and the second, added in varying proportions, is silicon carbide (SiC). SiC was chosen for its combined contribution of carbon and silicon. In fact, carbon can lead to both to the hardening of the matrix and to the formation of carbides; whereas silicon is known to be one of the elements that promotes graphite formation. Differential Thermal Analysis (DTA) under near-equilibrium conditions was carried out to assess the chemical compatibility between the two powders. This was followed by an experimental campaign aimed at optimizing the powder preparation method for the LPBF feedstock. Focus was placed on achieving an effective powder mixture with conventional devices such as ball milling and sieving station, with special attention given to powder rheology to ensure proper flowability and processability.

The processability of the different powder mixtures was then assessed through the development of a process map for the alloy, beginning with single-track prints (1D) and advancing to multi-track and cuboid (3D) samples. Process parameters were linked to the characteristics of the resulting melt pools, including their morphology and dimensions, as well as to the presence of process-induced defects. The role of SiC in influencing processability was also clarified.

The most promising 3D samples, those that were fully dense and defect-free, were selected for metallurgical characterization, both in the as-built state and after thermal post-processing. Microscopy and EBSD analysis combined with macro-hardness, nano-hardness and pin-on-disc test were used to elucidate the solidification sequence and to evaluate the mechanical and wear properties.

In conclusion, this work demonstrates the feasibility of achieving a tailored graphitic wear-resistant alloy for LPBF, needed for the next generation of materials FOR Additive Manufacturing.

Résumé

L'émergence de la Fabrication Additive (FA) a transformé le paysage de la mise en œuvre des métaux. Cette technologie s'avère particulièrement intéressante pour le développement de nouveaux métaux présentant des microstructures innovantes, principalement en raison des conditions hors équilibre inhérentes au procédé. Toutefois, il existe encore des restrictions à l'utilisation de la FA, notamment à cause de la disponibilité limitée ou le coût élevé des poudres métalliques nécessaires comme matières premières, ainsi que la difficulté de mise en œuvre de certains alliages.

Cette étude présente le développement d'un nouvel alliage à base de fer fabriqué par FA, en détaillant l'ensemble du processus, depuis la sélection et la préparation des poudres jusqu'à la mise en œuvre par fusion laser sur lit de poudre (Laser Powder Bed Fusion, LPBF). Elle examine également les caractéristiques métallurgiques de l'alliage, ainsi que ses performances mécaniques et tribologiques. L'innovation principale réside dans la formation d'une microstructure composée de graphite et de carbures incorporés dans une matrice dure, conduisant à une amélioration de la résistance à l'usure. Bien que de telles microstructures, en particulier celles contenant du graphite, soient bien documentées dans la métallurgie conventionnelle, leur mise en œuvre par LPBF n'a pas été rapportée auparavant.

Le développement de cet alliage a commencé par la sélection de matières premières appropriées pour le procédé LPBF, disponibles dans le commerce et à des prix abordables. Deux types de poudres ont été sélectionnés, à savoir le matériau principal représenté par un acier à outils faiblement allié (AISI S2), et le matériau secondaire composé par le carbure de silicium (SiC). Le choix de SiC a été fait notamment pour l'apport conjoint de carbone et de silicium. Concernant le carbone, il peut contribuer à la fois au durcissement de la matrice et à la formation de carbures. Et le silicium est connu comme un des éléments qui favorise la formation de graphite. L'analyse thermique différentielle (ATD) dans des conditions proches de l'équilibre a été réalisée afin d'évaluer la compatibilité chimique entre les deux poudres. Cette étape a été suivie d'une campagne expérimentale visant à optimiser la méthode de préparation des poudres destinées à l'alimentation du procédé LPBF. Une attention particulière a été accordée à l'obtention d'un mélange de poudres compatible avec la technique LPBF, du point de vue de la processabilité. Pour ce faire, des procédures ont été développées à l'aide d'équipements conventionnels tels qu'un broyeur à boulets et une station de tamisage, avec

une attention particulière portée à la rhéologie des poudres, afin de garantir une bonne aptitude à l'écoulement et à la mise en œuvre des poudres mélangées.

L'évaluation des différents mélanges de poudres a ensuite faite via l'élaboration de cartographies du procédé LPBF, en commençant par des impressions de mono-cordons (1D) pour arriver à des échantillons cuboïdes (3D), faits de multi-cordons et de multi-couches. Les paramètres du procédé ont été corrélés aux caractéristiques des bains de fusion, notamment leur morphologie et leurs dimensions, ainsi qu'à la présence de défauts induits par le procédé. Le rôle du SiC dans l'influence de la mise en œuvre a également été clarifié.

Les échantillons les plus prometteurs, ceux qui étaient entièrement denses et exempts de défauts, ont été sélectionnés pour une caractérisation métallurgique avancée, à la fois dans l'état brut de fabrication et après un post-traitement thermique. Pour ce faire, la microscopie et l'analyse EBSD, combinées à des mesures de macro- et de nano-dureté, ainsi qu'à un essai pion-disque, ont été utilisées respectivement pour élucider la séquence de solidification et évaluer les propriétés mécaniques et tribologiques.

En conclusion, ce travail démontre les conditions de faisabilité d'un alliage graphitique résistant à l'usure qui est adapté au procédé LPBF, ce type d'alliage préfigurant la prochaine génération de matériaux POUR la Fabrication Additive.

Contents

Acknowledgements 12
Chapter 1 – Introduction 15
1.1 Context 16
1.2 Purpose of the work 17
1.3 Thesis outline 18
Chapter 2 – State of the art 19
2.1 Introduction 20
2.2 Graphite in metallurgy 21
2.2.1 Graphitization in conventional Fe – C alloys and steels 21
2.2.2 Influence of alloying elements and inoculants 24
2.2.3 Effect of manufacturing conditions 26
2.2.3.1 Elemental segregation, metastability and supersaturation 26
2.2.3.2 Graphitization in close-to- and out-of-equilibrium conditions 28
2.3 Metal Additive Manufacturing 32
2.3.1 Current technologies and emerging trends 32
2.3.2 Powder feedstock for LPBF 34
2.3.3 Processability of conventional and modified tool steels by LPBF 37
2.3.3.1 Effect of carbon and alloying elements 37
2.3.3.2 Towards enhanced properties with additives enrichment 41
2.4 Redefining wear properties with materials for AM 43
2.4.1 Innovative wear mechanisms 43
2.4.2 New generation of self-lubricating tools 44
2.5 References 47
Chapter 3 – Powders for LPBF: selection, chemical affinity, preparation and characterization 57
3.1 Introduction 58
3.2 Selection of powder feedstock 59
3.3 Chemical affinity of raw materials 62
3.3.1 Dissolution of SiC during DTA heating stage 64
3.3.2 Graphite, carbides and matrix crystallization from liquid state 67
3.3.3 Solid-state transformations of the matrix phase 71
3.3.4 Main findings from DTA tests 73
3.4 Preparation of powder mixtures 75
3.5 Characterization of powder mixtures 80

3.5.1 Rheological properties 80
3.5.2 Absorbance 84
3.6 Conclusions 86
3.7 References 87
Chapter 4 – Processability by LPBF: from reference S2 alloy to modified S2 + SiC 89
4.1 Introduction 90
4.2 Reference material AISI S2 91
4.2.1 Single tracks 91
4.2.2 Multi-tracks and layers (cubes) 93
4.3 Powder mixtures S2 + SiC 101
4.3.1 S2 + 5, 10% SiC without preheating 101
4.3.2 Effect of preheating on S2 + 10% SiC 107
4.3.3 Difficult processability of S2 + 15% SiC 112
4.4 Effect of powder properties on processability 114
4.5 Conclusions 117
4.6 References 118
Chapter 5 – Macro- and microstructures in as-built conditions and after graphitization thermal treatment 121
5.1 Introduction 122
5.2 Metallurgical characterization in the as-built conditions 123
5.2.1 Macrostructures and solidification modes 123
5.2.1.1 Identification of solidification sub-structures within AISI S2 123
5.2.1.2 Effect of SiC and preheating on changes in macrostructures 125
5.2.2 Microstructures and in-situ thermal cycles 131
5.2.2.1 Solidification sequence of reference alloy AISI S2 131
5.2.2.2 Effect of SiC on martensitic transformation 138
5.2.2.3 Microstructural changes induced by preheating 141
5.2.2.3.1 Identification of phases within top layer 141
5.2.2.3.2 Heat Affected Zone 150
5.3 Graphitization mechanism during thermal treatment 152
5.4 Conclusions 159
5.5 References 160
Chapter 6 – Assessment of wear properties 163
6.1 Introduction 164
6.2 Approach for wear characterization 165
6.3 Wear sequence of reference material AISI S2 167
6.4 Wear properties of graphitic tool steels 174

6.4.1 Influence of hardness on the Coefficient of Friction 175
6.4.2 Effect of solidification carbides and graphite on wear resistance 181
6.5 Conclusions 185
6.6 References 186
Chapter 7 – General conclusions and perspectives 187
7.1 General conclusions 187
7.2 Perspectives 190
Appendix 193
A. Effect of laser defocus on processability of S2 + 15% SiC 194
B. Full DTA Heating stage of S2 + 10% SiC w/ and w/o preheating 197
C. Thermal treatments of S2 + 10% SiC w/o preheating 198
D. In-situ graphitization of S2 + 15% SiC 200
E. Worn volumes and track dimensions after high temperature pin-on-disc tests of LPBF as-built AISI S2 202
List of publications 203
Curriculum vitae 207

Acknowledgements

Here I am. I deliberately left this section to be the last one to be written, not because of its importance or difficulty to write, but to have the possibility to enjoy this moment and truly thank all the people who accompanied me during my PhD journey. These acknowledgements have an even deeper meaning for me because more than two years have passed since I officially left the M2AM team and Liège. Completing this section means that I am really at the official completion of my PhD.

First of all, my deepest thanks go to my colleagues of the M2AM team, starting with Prof. A. Mertens (Anne), who gave me the opportunity to come to Liège and pursue my doctoral studies. During the years, she guided and supported me, advising me on how to overcome all the challenges a PhD can bring. Thanks to Dr. Tchuindjang (Jérôme), whose extensive expertise in metallurgy somehow left me with even more questions than I had at the beginning of a discussion that started with a simple question from my side and turned into endless metallurgical discussions in his office. Thanks to Ir. Dedry (Olivier) for all the 'dirty jobs' done together to make the machines work. Thanks to the three Teaching Assistants of the team I met during the years, starting with Dr. Maurizi Enrici (Tommaso), who is guilty of having made me become a metallurgical and Additive Manufacturing 'nerd' from the first day of my Erasmus in Liège, when he was my supervisor. Thanks to Dr. Delahaye (Jocelyn) for supporting me since the beginning and hosting me in his apartment when I had just arrived in Liège. Thanks to Herrim Seidou, the current Teaching Assistant and the first student I supervised for his Master's thesis. To him and the other brilliant engineers I supervised (Elena Filippi, Gerard Roger Vila and Alessandra Segatto): thank you! Part of this manuscript has been realised thanks to your hard work. My goal during the time we spent together was to make you enjoy metallurgy and research. I hope you had a good and insightful time. Thanks to Sylvie Salieri and Antonio Martinez Aguilera, whom I asked to do a lot of 'cochonnerie' (as they were calling them). Their fabulous work in polishing, grinding, cutting, etc., and their extreme patience when handling my difficult-to-realise requests were important for the realisation of this project. Thanks to Rosine Pirson for all the administrative work, for all the biscuits and for her patience in understanding my French! Thanks to all the other members of my Thesis Committee (Prof. P. Duysinx, Dr. F. Boschini) for advising me during the annual meeting and to Granutools team for hosting me and make me use their equipment.

Thanks to all the friends I met in Liège, from my university mates to my roommates and other friends met during the years, from all the different countries: France, Belgium, Italy, Lebanon, Iran, Spain, Chile and many others. We shared many indelible moments that I will always carry in my memory.

A huge thanks to all the people I left behind in Italy, including my family and friends. You are too many to mention here. Thank you for your understanding of my choice to 'leave' you and for making me homesick every time I came back to Italy or when you came to visit me. It was meaningful for me.

My deepest thanks to my dear Leila. I can write many things here, but there is no need. We know. I will only say that the years in Liège were the start of our life adventure together.

Thanks to Liège and what it represented to me. A starting-from-zero experience with a lot of challenges and beautiful moments. I learned and grew as a human and an engineer every single day there. I wish for all young people to leave everything and live abroad for a period, meet different people and cultures, and embrace anything that at the beginning can seem 'different', but with time will not be different anymore. Your mind and you as a person will only be grateful.

Chapter 1

Introduction

Contents

1.1 Context 16
1.2 Purpose of the work 17
1.3 Thesis outline 18

1.1 Context

Additive Manufacturing (AM) is experiencing a rapid expansion, pushed by the interest of industries to adopt it for mass production and by industrial R&D and research institutions for the development of new materials. The two main advantages of AM widely accepted by the community are the possibility to obtain complex shape parts and the achievement of new materials with innovative properties. Regarding these aspects, it is worth mentioning the difference between materials by AM and materials for AM. The first group regards the classical metal alloys that showed easy processability, such as stainless steels and nickel-, titanium-, aluminium-based alloys. The second group regards a new class of alloys, with microstructures and properties only achievable with AM processes. The barrier between these groups is the lack of raw material, as the AM processes need specific feedstocks, still difficult to obtain. The AM community is now breaking this limitation. Thus, in the coming years, new alloys will be released specifically for AM. Sectors as aerospace, civil, defence, automotive, energy and medical will be positively affected by this trend.

The race towards the development of improved alloys by and for AM has started. The traditional metallurgical concepts accepted up to now are being redefined. Nevertheless, when considering the design of new alloys for AM, conventional metallurgy is still needed as tool for the developing. The Metallic Materials Science (MMS) team has acquired over the years wide experience in the solidification and properties of complex metal alloys. In the last decade, the MMS team also focused on metal AM, in particular Direct Energy Deposition (DED). The name of the team recently changed to ‘Metallic Materials for Additive Manufacturing’. One recent PhD projects of the team, finished in 2022, focused on the improvement by DED of stainless steel 316L with different types of ceramics. From those studies came the idea of developing a tailored alloy for AM, and so the current PhD project started. The acquisition by the laboratory of a Laser Powder Bed Fusion (LPBF) device allowed the in-house experiments, previously carried out in external facilities. Furthermore, around the LPBF device, equipment for handling powders is available (ball milling, sieving station). Classical metallographic devices for metal characterization are present (Optical and Scanning Electron Microscope equipped with Back-Scattered Electrons, Secondary Electron, Energy Dispersive X-ray Spectroscopy and Electron Backscatter Diffraction detectors. In complement, devices for thermophysical analyses (Differential Scanning Calorimetry, Differential Thermal Analysis, Quenching Dilatometer, Laser Flash Diffusivimeter, Pycnometer) and for characterizing mechanical properties (macro- and nano-indenter, high-temperature tribometer) are also

available. Specific tests are performed in other facilities. Physical properties of powders (Particle Size Distribution, X-Ray Diffraction and Spectrophotometer) are carried out at Greenmat facilities (University of Liège) and rheological properties of powders (flowability and packability) at Granutools (Liège).

1.2 Purpose of the work

The main aim of this PhD project is the achievement of an iron-based alloy with enhanced tribological properties which can be easily processed with LPBF. Specifically, the improved tribological behaviour is achieved thanks to the presence of graphite within the microstructure. This specific microstructure obtained via an AM process is innovative, as it is usually obtained through more conventional manufacturing methods. Several challenges needed to be faced for the achievement of this ambitious result.

The PhD project is based on an experimental approach. The successive steps of the work are as follows:

1. Design of alloy
2. Selection of commercial raw materials
3. Preparation of feedstock materials by mixing commercial powders
4. Processability with LPBF of the different mixtures
5. Selection of the best as-built alloy
6. Post-production thermal treatment
7. Assessment of wear properties

These points were carried out in chronological order. The first two steps were considered during the first semester of the project (August 2020 – January 2021). Then, during the following year (January 2021 – February 2022), the studies focused on the tribological properties of a material previously developed within the MMS laboratory. That work, even though it is not directly part of the thesis project, proved useful to deeply understand wear properties of complex alloys and to later serve as a basis for investigating the wear behaviour of the alloys developed in this project. It resulted in the publication of a paper in the journal 'Tribology International' (not included in this work). The reason for the deviation from the original plan was the unavailability of the LPBF device in the MMS laboratory at the time. The following steps, from the preparation of the feedstock material to the post-production thermal treatments, were carried out from February 2022 until summer 2023. From these investigations, different alloys

were developed, starting from the commercial reference alloy to the modified steel grades. Finally, the more suitable alloy for the aim of the project was selected and its wear properties were assessed. The promising results achieved allowed to deposit a patent application (Europe: application ref. n° EP24167458 (28/03/24); International: application ref. n° PCT/EP2025/058128 (25/03/25), published under WO/2025/202196).

During these years, the PhD project served as a base for four Master Thesis, whose results are included in this work. Furthermore, collaborations were built with external universities (Università di Padova, Italy and Universidad de La Frontera, Chile), which led to the publication of joint works (not included in this manuscript).

1.3 Thesis outline

After the ongoing introduction (chapter 1) and an initial review of the state of the art of the relevant topics (chapter 2), the manuscript is divided in four main chapters (from chapter 3 to 6), based on the steps mentioned previously. Specifically, the main chapters consist of:

- **Chapter 3, Powders:** the selection, chemical affinity, preparation and characterization of the different powder mixtures are explained (Master Thesis[1,2]).
- **Chapter 4, Processability:** the powder mixtures previously developed are processed by LPBF. The process maps are discussed, and the best samples are selected (Master Thesis[2,3]).
- **Chapter 5, As-built microstructures and graphitization:** defect-free samples are considered for metallurgical characterization, from the as-built reference (Master Thesis[3] and conference paper[4]) to the modified (Master Thesis[2] and conference paper[5]) alloys. The graphitization mechanism during the post-process thermal treatment is discussed.
- **Chapter 6, Wear properties:** the wear sequence of the as-built reference material at room temperature is elucidated (Master Thesis[6]). General assessments of the tribological properties of the new graphitic steels are given.

[1] Herrim Seidou, 2022, Development and evaluation of the powders mix low alloyed steel + SiC for Selective Laser Melting
[2] Gerard Roger Vila, 2023, Fabrication and characterization of AISI S2 Tool Steel + SiC by Laser Powder Bed Fusion
[3] Elena Filippi, 2022, Fabrication and characterization of low alloyed tool steel obtained by Selective Laser Melting
[4] Saggionetto et al., Esaform 2023, Development and processability of AISI S2 Tool Steel by Laser Powder Bed Fusion
[5] Saggionetto et al., Esaform 2024, Effect of SiC addition on processability of AISI S2 tool steel for Laser Powder Bed Fusion
[6] Alessandra Segatto, 2024, Thermal stability and wear behaviour of AISI S2 Tool Steel processed by Laser Powder Bed Fusion

Chapter 2

State of the art

Contents

2.1 Introduction 20
2.2 Graphite in metallurgy 21
2.2.1 Graphitization in conventional Fe – C alloys and steels 21
2.2.2 Influence of alloying elements and inoculants 24
2.2.3 Effect of manufacturing conditions 26
2.2.3.1 Elemental segregation, metastability and supersaturation 26
2.2.3.2 Graphitization in close-to- and out-of-equilibrium conditions 28
2.3 Metal Additive Manufacturing 32
2.3.1 Current technologies and emerging trends 32
2.3.2 Powder feedstock for LPBF 34
2.3.3 Processability of conventional and modified tool steels by LPBF 37
2.3.3.1 Effect of carbon and alloying elements 37
2.3.3.2 Towards enhanced properties with additives enrichment 41
2.4 Redefining wear properties with materials for AM 43
2.4.1 Innovative wear mechanisms 43
2.4.2 New generation of self-lubricating tools 44
2.5 References 47

2.1 Introduction

This chapter includes the state of the art relevant to the main topics studied on this work. First, graphite aspects in metallurgy are described, giving examples of different ways to achieve graphitization within metal alloys. Then, Additive Manufacturing (AM) with a particular focus on Laser Powder Bed Fusion (LPBF), is reviewed from the preparation and properties of the powder feedstock to the processability and microstructure of new high carbon tool steels. Finally, wear properties are discussed, focusing on the raise of new wear mechanisms and self-lubricating alloys for AM.

2.2 Graphite in metallurgy

This section wants to provide information on the metallurgical aspects of graphite, starting from its type and characteristics, then moving on the effect of chemical composition and process conditions to achieve graphitization within a metal.

2.2.1 Graphitization in conventional Fe – C alloys and steels

Graphite as phase in metals is well known. It is typically associated as a main constituent of Cast Iron (CI), which is one of the most important and conventional Fe – C alloys. Its first appearance is dated back to 500 BC. From that moment, humans continuously developed the casting of iron, starting from the use in art, evolving into a technology and finally emerging as the complex and interdisciplinary science that it has become nowadays (*Stefanescu, 2018*). CI production still constitutes the majority of today's metal casting, about 70 % (*Tewary, 2022*). Its importance relies on the intrinsic advantages of this alloy thanks to the presence of graphite, making it an important material for many applications.

The main elements of CIs are iron and carbon. The solidification of such alloys follows the Fe – C diagram. Carbon is available in form of free graphite in the stable Fe – C diagram, whereas the metastable diagram implies the presence of the intermetallic Fe – C compound known as cementite Fe_3C. The Fe – Graphite phase diagram refers to the solidification of Grey Cast Iron (GCI), whereas the Fe – Fe_3C phase diagram refers to the solidification of White Cast Iron (WCI) (*Pero-Sanz Elorz, 2018*). In casting processes, the solidification following the stability or metastability depends on chemical compositions, cooling rates, dimensions of the part and superheating/cooling phenomena. Achieving graphite within the microstructure of GCIs is usually a result of a transformation occurring from liquid to solid, referred as primary graphitization. Indeed, depending on the carbon content, graphite can be either the first phase to crystallize from the liquid, or nucleate and grow together with the parent matrix, or else be the last solid to form as in eutectic reactions. Different morphologies are achieved depending on those reactions. Typical morphologies are flakes, vermicular or spheroidal (*Fig. 2.1*a). Graphite types are standardized according to EN ISO 945-1 and ASTM A247-16a (*Fig. 2.1*b,c) (*Friess, 2020*). Graphite is also classified based on its distribution from type A to type D (*Fig. 2.1*d). Each type of graphite promotes specific macro- and micro-properties in the alloy. Flake-like graphite is desired in applications such as brake discs for road vehicles, in view of sufficient strength properties, good thermal conductivity and vibration absorbing capacity (*Luo, 2024*). Vermicular graphite in Compacted Graphite Iron (CGI) is preferred for diesel

engines because of its better thermal fatigue resistance and strength than traditional flake morphology (*X. song Wang, 2017*). Spheroidal graphite present within Nodular Cast Iron (NCI) has been proved to be more advantageous in application were ductility and fracture toughness are required (*Theuwissen, 2016*).

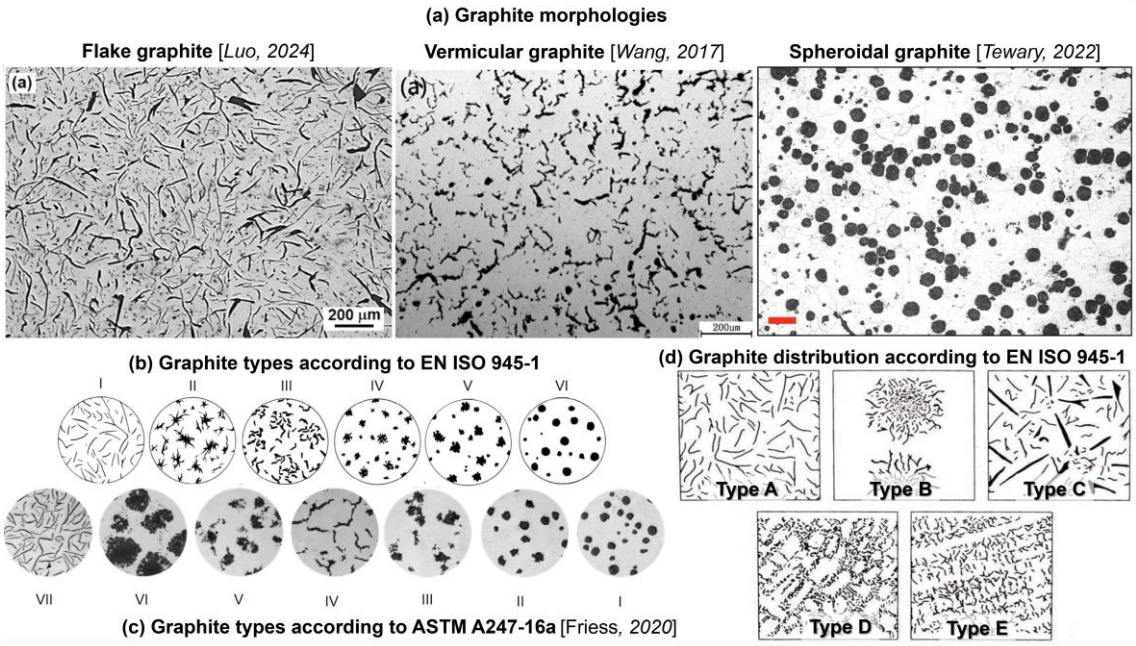


Fig. 2.1: (a) Graphite morphologies, graphite types according to (b) EN ISO 945-1 and (c) ASTM A247-16a and (d) and graphite distribution.

Primary graphite can also be found within High Speed Steels (HSS), usually obtained through centrifugal casting (*Aigner, 2023*; *Maurizi Enrici, 2020*; *Villanueva Bravo, 2012*; *Yamamoto, 1998*). In those cases, the high content of alloying elements leads to complex microstructures, with graphite and different type of carbides (*Fig. 2.2*). These characteristics are desired for abrasive wear resistant applications such as roll mills.

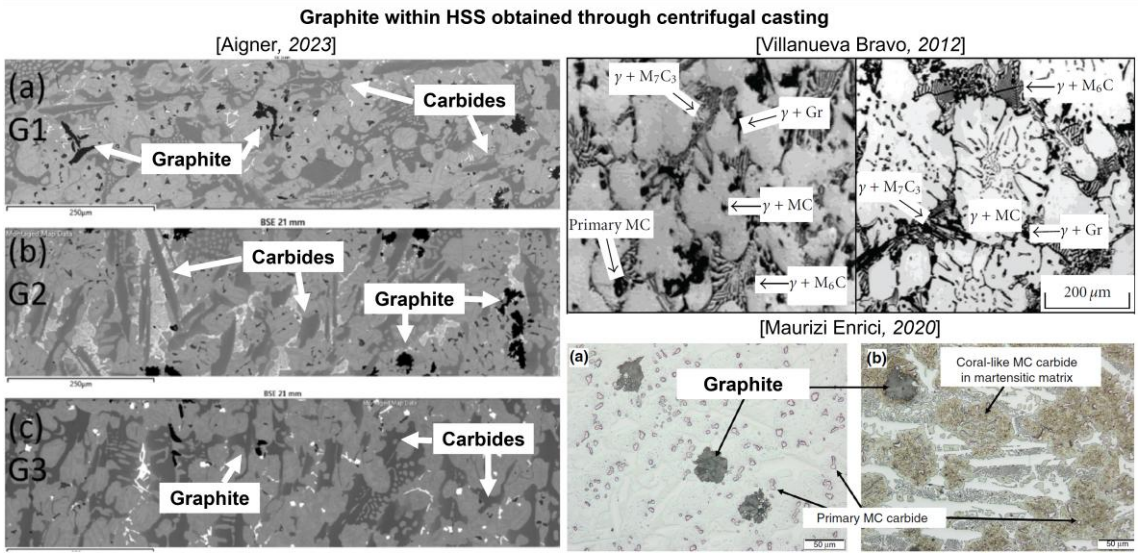


Fig. 2.2: Primary graphite obtained with centrifugal casting.

Other types of graphite can be obtained during solid-state transformations known as secondary graphitization, either in CIs and steels. This transformation consists in the nucleation of a large number of small graphite nodules and ferritic grains in the solid state, usually during tempering or annealing thermal treatments. Rate of graphitization depends on the type of matrix, such as martensite, bainite or pearlite (*Fig. 2.3*a). Both temperature and time affect the dimensions and count of graphite particles within the microstructure (*Fig. 2.3*b,c) (*Gao, 2016*; *Inam, 2015*; *Kim, 2021*; *Ogata, 2022*; *Rounaghi, 2011*). Secondary graphitization can also occur by decomposing iron carbides into graphite (*Kante, 2019*). This transformation usually occurs when thermal treating WCIs, forming an alloy known as Malleable Cast Iron (MCI) which contain irregular-shaped graphite nodules. The advantage of MCIs is the higher ductility and toughness compared to the parent WCI.

More recently, in a work of the MMS team about graphitic HSS produced with centrifugal casting (*Maurizi Enrici, 2020*), free lamellar secondary graphite was obtained through decomposition of a metastable carbon supersaturated carbide (*Fig. 2.3*d), something which has not been mentioned elsewhere.

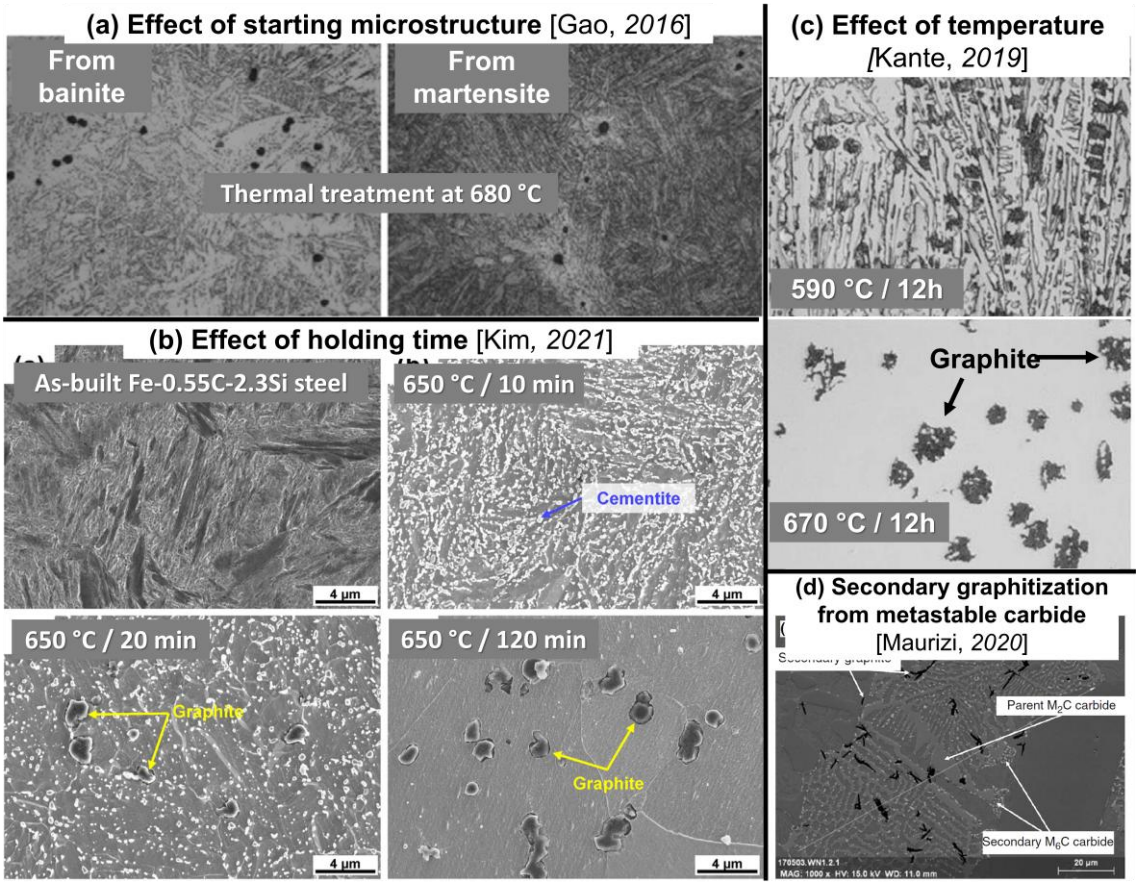


Fig. 2.3: Secondary graphitization depending on the (a) starting microstructure, (b) holding time and (c) temperature of the thermal treatment. (d) Secondary graphite from a metastable carbide.

2.2.2 Influence of alloying elements and inoculants

Either from liquid state or during solid-state transformations, the nucleation and growth of graphite is affected by the chemical composition of the alloy. When elements such as Ti, V, Cr, Nb, Mo, Ta or W are present together with C, solidification of hard carbides is promoted at the expense of graphite, in view of the low enthalpy of formation necessary to form such phases. Carbides are usually referred as intermetallic compounds M_xC_y, where M stands for one of the elements mentioned above. Similar to the cases of graphite mentioned earlier, carbides can solidify as primary (PC), pseudo-primary (PPC), eutectic (EC) and secondary (SC) (*Tchuindjang, 2011*). Different types of carbides exist depending on the stoichiometry and the elements (*Fig. 2.4*). MC type is promoted by the addition of V, Ti, Ta, Nb, Hf and Zr and it can be in different morphologies such as divorced or irregular (*Boccalini, 2001*; *Lecomte-Beckers, 2009*). Mo and W promote the solidification of M_2C and M_6C, whereas Cr and Fe usually favoured the appearance of M_7C_3, M_3C and $M_{23}C_6$ (*Boccalini, 2001*; *S. Liu, 2016*; *Tchuindjang, 2011*).

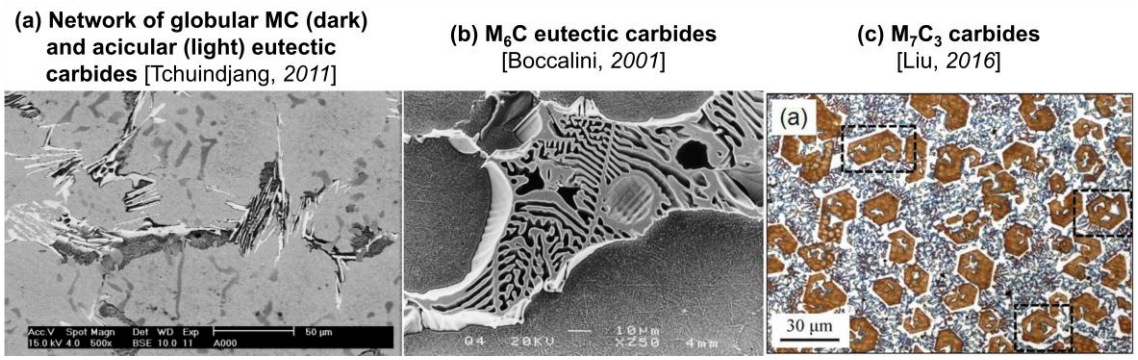


Fig. 2.4: (a) MC, (b) M_6C and (c) M_7C_3 carbides.

Contrary to the effect of carbides forming elements, Si, Mn, Al, P and S promote graphite crystallization. Among those elements, Si is one of the most important. It is usually added in CIs for this reason. Indeed, the solidification of GCIs following the Fe – Graphite phase diagram is valid only with a content of silicon above 1 wt. %. For this reason, CIs are usually referred as Fe – C – Si alloys (*Stefanescu, 2016*). The role of silicon is to inhibit the formation of cementite, or more generally iron carbides, thus promoting graphite crystallization. The elements cited above are added within the molten metal as inoculants during casting processes, with techniques such as 'in-mould process' (*Fesenko, 2020*). Inoculative additives such as ferrosilicon (FeSi) promote the appearance of lamellar graphite, whereas FeSiMg, NiMg, MgCaS, MgSi inoculants have the effect of spheroidizing the graphite (*Fesenko, 2020*; *Khuntrakool, 2024*; *Skaland, 1993*). Rare earth elements such as La and Ce are also known to increase the number and uniformity of graphite nodules (*Ng, 2018*; *Zhang, 2024*). Many other types of commercial inoculants exist. One important type of additive is Silicon Carbide (SiC), as it can act as direct source of carbon and silicon, promoting either the appearance of graphite type A or the increase in nodule count (*Fig. 2.5*a,b) (*Edalati, 2005*; *Popescu, 2009*). The mechanism established by (*Xue, 2016*) proposes that an initial reaction between iron oxides of the molten slag and SiC leads to the formation of SiO_2 on the surface of SiC. Then, SiC slowly diffused into the molten iron, inducing the precipitation of a large amount of free carbon in the molten iron which served as a substrate for the subsequent precipitation of a large amount of graphite (*Fig. 2.5*c).

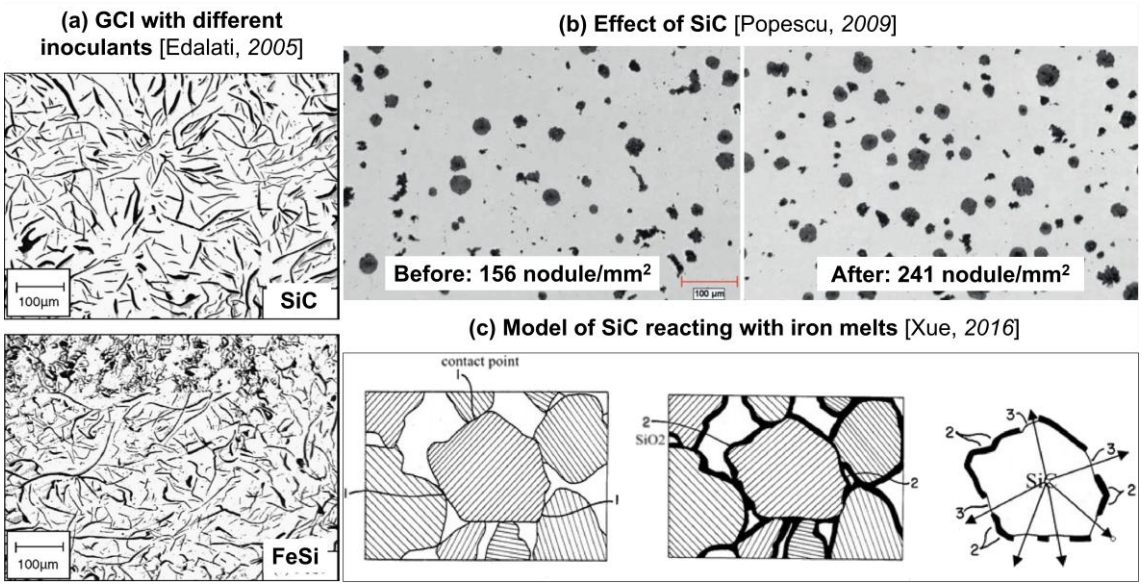


Fig. 2.5: (a) Effect of SiC and FeSi on graphite morphology, (b) effect of SiC on graphite nodules count and (c) model of SiC reacting with iron melts.

2.2.3 Effect of manufacturing conditions

Phases obtained according to the stable Fe – C diagram are the result of a solidification under equilibrium conditions, where atoms can ideally diffuse in their thermodynamic most stable positions. Usually, one way to study the equilibrium solidification is with ThermoCalc®. Conventional casting processes, Differential Thermal Analysis (DTA) and Powder Metallurgy (PM) techniques such as press and sintering and powder injection moulding are in close-to-equilibrium solidification conditions, with cooling rates of about 1 °C/s. Centrifugal casting has slightly higher cooling rates (5 °C/s). Cooling rates further increase (10^3 – 10^4 °C/s) with welding and Additive Manufacturing (AM) techniques such as Direct Energy Deposition (DED), Laser Powder Bed Fusion (LPBF), Plasma Metal Injection (PMI), Gas Tungsten Arc Welding (GTAW), and Laser Surface Alloying (LSA). The highest cooling rates are achieved with atomization processes and drop-tube techniques (10^4 – 10^6 °C/s). The processes in out-of-equilibrium conditions lead to the achievement of complex microstructures, with supersaturation and metastability conditions.

2.2.3.1 Elemental segregation, metastability and supersaturation

The solidification of PCs, ECs and graphite in CIs and steels is the result of elemental segregation. Especially for carbides, nucleation and growth is preceded by elemental segregation of the carbide forming elements in the residual liquid within intercellular/dendritic or intergranular spaces (*X. Liu, 2023*). When the relation between M and C is satisfied, a certain

carbide precipitate. Similarly, primary graphite crystallization is the result of a preliminary segregation of carbon atoms. Elemental segregation is enhanced with low cooling rates, thus in processes in equilibrium or close-to-equilibrium conditions such as in conventional casting, PM and DTA techniques. When increasing the cooling rates (*Fig. 2.6*), the out-of-equilibrium conditions do not favour the diffusion of atoms in their thermodynamic most stable position, thus limiting the segregation behaviour of elements and promoting metastability and supersaturation phenomena.

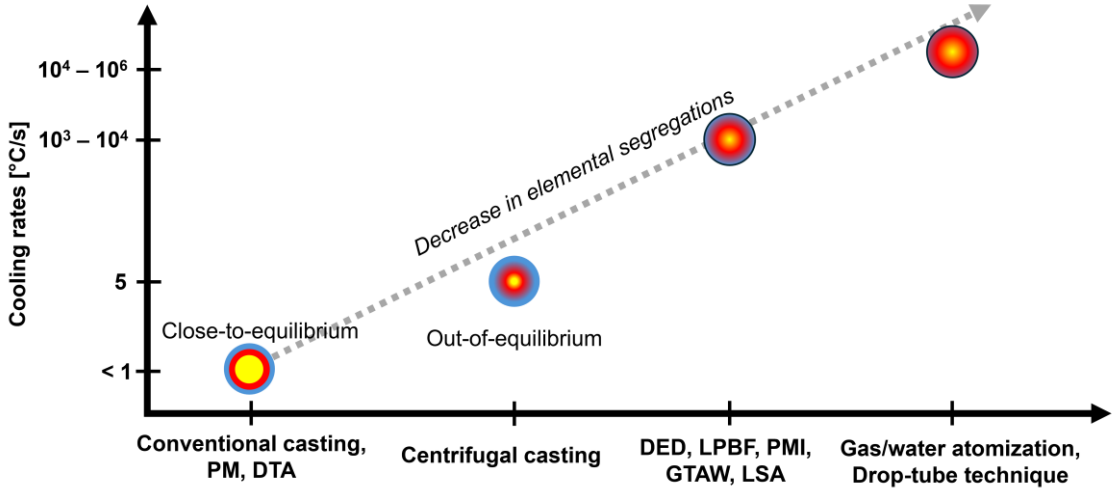


Fig. 2.6: Representation of the variation of the segregations and cooling rates occurring in the different manufacturing processes, adapted from (*Maurizi Enrici, 2022*).

The work of (*Tchuindjang, 2011*) explained the metastability condition of a Mo-rich M_2C carbide present within the microstructure of a HSS for Hot Strip Mill (HSM), obtained through centrifugal casting. During a subsequent thermal treatment, such carbide undergoes an in-situ transformation, driven by the preferential migration of some atoms that escape from the parent M_2C carbide. As a result, new phases are formed. The decomposition of such carbide highlighted the effect of out-of-equilibrium conditions on the nature of the as-solidified carbide, which promote the entrapment of some atoms within the lattice structure of the parent phase. Another example of metastability was given in a previous section (2.2.1), with the precipitation of graphite from a metastable M_2C carbide (*Maurizi Enrici, 2020*). Metastability imply a supersaturation of the parent phase in certain elements. Besides carbides, primary matrix phases with BCC or FCC crystal lattices can also be subjected to supersaturation when the cooling rates are high. Carbon capability to supersaturate a BCC lattice structure is well known. Typical phases formed with such condition are martensite and bainite, where the

distortion played by carbon atoms leads to a BCT lattice structure. The typical FCC austenite can also be supersaturated in carbon, which allow for its retention at room temperature.

All these phenomena are favoured in out-of-equilibrium conditions, where the high cooling rates do not promote the formation of stable phases. Thus, in view of the necessity of equilibrium conditions for the formation of graphite, the appearance of this phase can be inhibited during some manufacturing processes. In order to enhance the graphitization behaviour, SiC as additive has been proved beneficial not only in conventional casting processes (section 2.2.2), but also in out-of-equilibrium processes. The next section will show some examples, referring to the processes and corresponding cooling rates in *Fig. 2.6*.

2.2.3.2 Graphitization in close-to- and out-of-equilibrium conditions

Table 2.1 lists the processes for which the obtention of primary or secondary graphite has been reported up to now. Other examples of graphite obtained during conventional and centrifugal casting processes were given in section 2.2.

Publications	Process	Conditions	Graphite type
(*Binder, 2016*; *Campos, 2015*; *de Mello, 2011*, *2013*, *2017*; *Hammes, 2014*; *Salvaro, 2023*),	Powder Metallurgy	Close-to-equilibrium	Primary nodules and flakes
(*Guo, 2008*)	Plasma Metal Injection	Out-of-equilibrium	Primary (or secondary?) vermicular graphite
(*Thawari, 2003*)	Laser Surface Alloying		Primary (or secondary?) irregular nodules
(*Buytoz, 2006*; *Lin, 2013*)	Gas Tungsten Arc Welding		Primary (or secondary?) vermicular graphite
(*Riquelme, 2022*)	Direct Energy Deposition		Primary nodules and flakes
-	Laser Powder Bed Fusion		-
(*Oloyede, 2016*; *Ozdemir, 2006*; *M. Yang, 2010*)	Drop-tube, Atomization		None or secondary through annealing

Table 2.1: Publications regarding the formation of graphite with different manufacturing processes.

Examples of in-situ graphitization in close-to-equilibrium conditions regard PM techniques. These processes involve the preliminary forming of a sample usually through pressing or injecting powders into a mould. Subsequently, this sample is sintered through heating up to a certain temperature below its melting point, followed by an isothermal holding and a final cooling. According to (*Campos, 2015*; *de Mello, 2011*, *2013*, *2017*; *Hammes, 2014*; *Salvaro, 2023*), graphite can be obtained by adding SiC particles within the powder mixture (*Fig. 2.7*a,b). A model of the formation of graphite during sintering was proposed in the work

of (*Binder, 2016*). Silicon and carbon diffuse from the SiC particles to the γ-Fe matrix and liquid. Silicon further stabilizes a solid α-Fe matrix in the vicinity of the SiC particle, whereas carbon diffuse in the γ-Fe matrix and remaining liquid. When the two fronts (α-Fe and γ-Fe) approach, the carbon in solution in the γ-Fe austenite phase precipitates, forming graphite flakes and leading to elongated graphite structures (*Fig. 2.7*c). All the examples in PM mentioned above highlight the importance of adding a SiC precursor to enhance the graphitization.

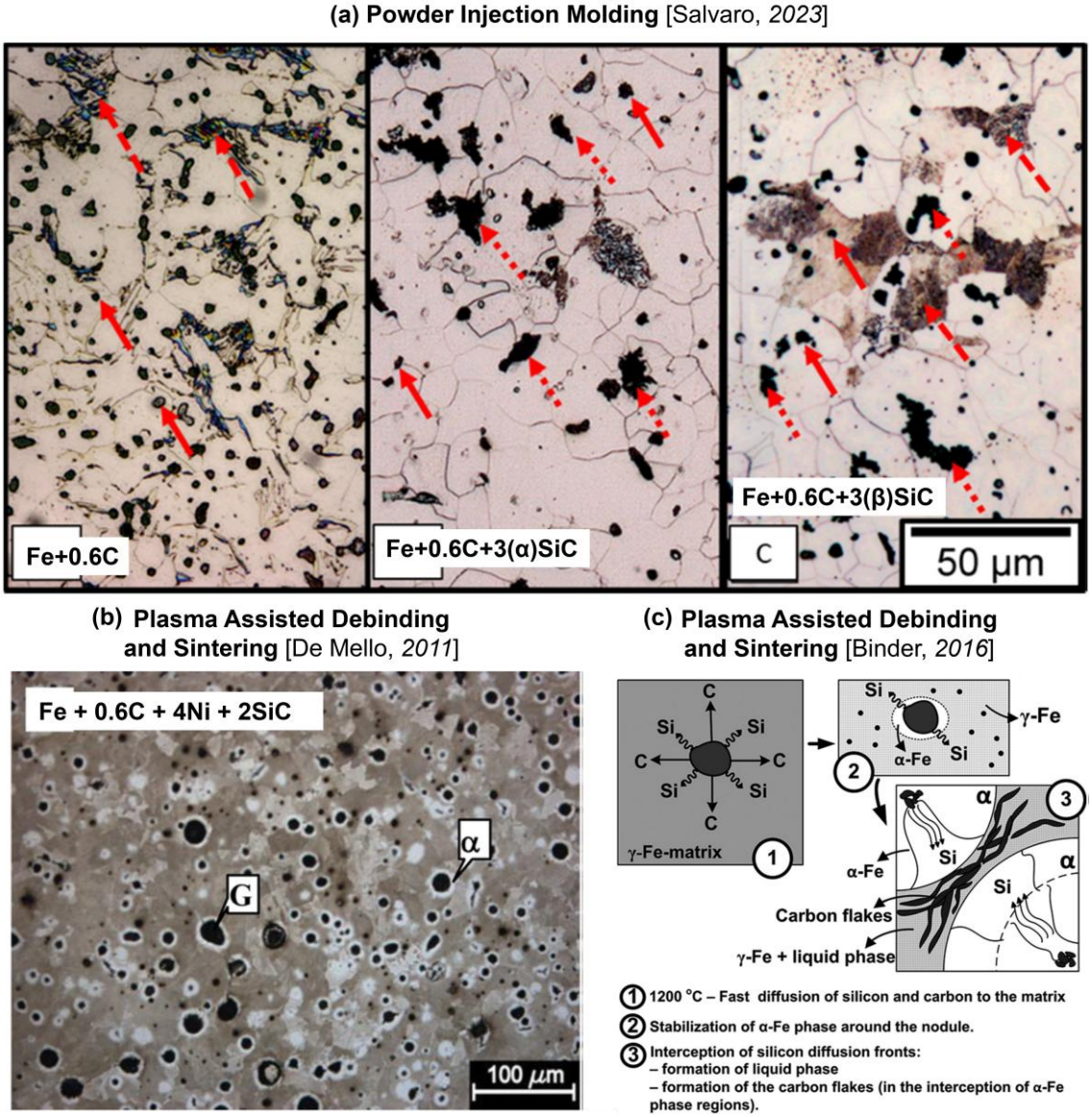


Fig. 2.7: Graphite in different PM techniques in close-to-equilibrium conditions, (a) Powder Injection Molding with different SiC (α-SiC or β-SiC), (b) Plasma Assisted Debinding and Sintering with SiC and (c) model of graphite formation from SiC dissolution.

Similarly, the formation of graphite in out-of-equilibrium conditions is promoted by the addition of SiC. In processes with high cooling rates such as PMI, LSA, GTAW and DED the

mechanism for graphite precipitation relies on dissolution reactions between SiC particles and the iron rich melt. The work of (*Guo, 2008*) explained the graphite formation during a PMI of SiC particles into a low carbon steel sheet. During the operation, most SiC particles dissolve into the liquid metal. After the plasma torch leaves, the liquid metal begins to solidify to form austenite. When the carbon and silicon contents in the liquid metal are high enough, graphite forms (*Fig. 2.8*a). Graphite was also found incidentally after the LSA of a medium carbon steel with SiC particles using a high-power CO_2 laser (*Fig. 2.8*b) (*Thawari, 2003*). Also in this case, graphite precipitation is attributable to the carbon enrichment of the melt resulting from the dissolution of SiC particles, with silicon enrichment also contributing. Meanwhile, in the work of (*Lin, 2013*), graphite was formed in-situ during the cladding of SiC powders on a die steel substrate using GTAW. Two solidification systems were identified, being the stable system and the metastable system. In the regions of the stable system, the nucleation of graphite precipitates was promoted by the high silicon and carbon content in the melt pool. Another possible reaction is that the metastable Fe_3C phase could be gradually converted into the stable graphite phase. However, the main solidification system was the metastable system, where a primary Fe_8Si_2C phase, either in a coarse or in a fine lamellar structure, was formed (*Fig. 2.8*c). Another work where SiC particles were cladded on a steel substrate with GTAW (*Buytoz, 2006*), reported the formation of M_7C_3 primary carbides, Fe_3Si, SiC, and graphite. Graphite was also formed in-situ during DED of a mixture of 316L and SiC powders (*Fig. 2.8*d) (*Riquelme, 2022*). SiC particles dissolved into the 316L matrix, modifying the chemical composition. Silicon reacted with iron, whereas part of the carbon reacted with chromium, forming chromium carbides. Also, graphite flakes and nodules were formed in the matrix when the percentage of SiC particles was higher than 20 wt. % and their size increased forming graphite needles, as the percentage of SiC raised. The incorporation of a higher concentration of SiC particles caused saturation of the matrix and reduced their dissolution.

In contrast, to the best of the author knowledge, no works were found regarding primary or secondary precipitation of graphite during LPBF processes, in view of the low processability of high carbon steels with this technique. Further explanations and examples are given in the next section (2.3.3.2). The present work will fill that gap.

Meanwhile, in the work of (*Oloyede, 2016*), GCI was used as feedstock material to produce powders using the drop-tube technique. The microstructure of the rapidly cooled droplets did not reveal the presence of graphite, in view of the high cooling rates of this process (*Fig. 2.6*). Similarly, in the works of (*Ozdemir, 2006*; *M. Yang, 2010*) where gas and water atomization

was used to produce powders starting from CI bars, no graphite was obtained in the as-atomized powders. However, (*Ozdemir, 2006*) reported that the CI powder achieved full graphitization with an annealing thermal treatment at 900 °C for less than 120 s.

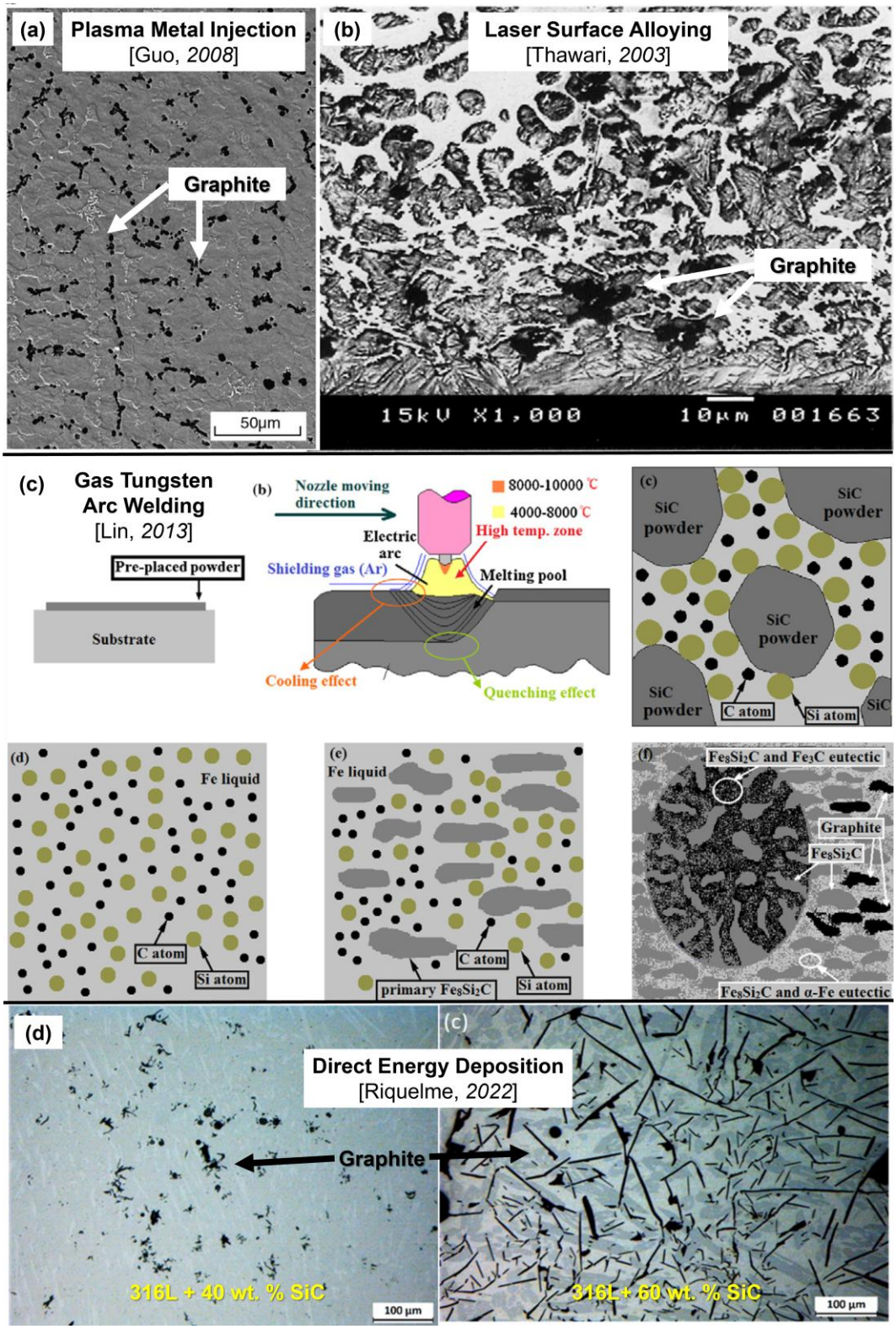


Fig. 2.8: Graphite within the microstructure of alloys processed in out-of-equilibrium conditions with (a) PMI, (b) LSA, (c) GTAW and (d) DED.

2.3 Metal Additive Manufacturing

Additive Manufacturing (AM), also commonly known as 3D Printing, is a manufacturing technique which has raised in the past 30 years. The name 'additive' stands for the manufacturing of a part by adding material layer by layer. In contrast, in conventional manufacturing techniques such as near-net-shape processes (i.e. forging, casting etc.) and subtractive processes (i.e. CNC machining, electrical discharge machining EDM), material is removed from an initial blank to obtain the final part. The main advantage of AM techniques is the possibility of achieving complex shape parts with low waste of material. On the other hand, the main limitation is the lower competitiveness of serial production compared to conventional methods.

2.3.1 Current technologies and emerging trends

The first commercial AM devices date back to the 1980s (*Abdulhameed, 2019*), with the release of Selective Laser Sintering (SLS) and Stereolithography (SLA) to process polymers-based parts. SLS for metals was commercialized by EOS® in 1994, which evolved into Selective Laser Melting (SLM) in 1999 with the commercialization of a device developed by Fockele and Schwarze (*Velu, 2021*). Recently, SLM has been renamed as Laser Powder Bed Fusion (LPBF), according to the standard ISO/ASTM 52911-1:2019. The rise of this technology was possible thanks to the development of high energy fiber lasers capable to directly melt metal alloys. LPBF is part of Powder Bed Fusion (PBF) techniques. Another PBF technology is Electron Beam Melting (EBM). LPBF and EBM involve the interaction of a powder bed with the laser or electron beam that selectively scans the layer of powder. Subsequently, the powder bed is lowered by the defined layer thickness and a new layer of powder is added. The process repeats until the part is completely built. The laser scanning path in each layer is defined by the part geometry at the corresponding z location and the selected scanning strategy (*Sun, 2017*). Different ways of adding a new layer of powder are possible, either by letting fall powder from a tank placed above the working platform (Nikon SLM Solutions®, EOS®) or through a recoater which spread the powder from the feedstock cylinder to the working platform (Aconity3D®). Furthermore, the company Aerosint® recently developed a system that allows the LPBF processing of multi-material parts.

Another type of AM technology is Direct Energy Deposition (DED), which can work either with powder or with wire (Wire Arc Additive Manufacturing WAAM) as feedstock materials. DED with powder, also known as Laser Cladding (LC), is a useful technique either to repair

damaged parts or to deposit a coating on a substrate, in order to improve properties such as wear resistance (*Maurizi Enrici, 2022*). Meanwhile, the use of WAAM is dated back to 1920 and, after a period during which it was almost forgotten, it is nowadays re-emerging in view of its benefits as lower machine capital costs and increased material flexibility compared to laser-based AM processes (*Meena, 2024*). An example of the increasing attention from the industry is the commercialization in 2023 of Aconity *WIRE* by Aconity3D®.

Another emerging AM technology is Binder Jetting (BJG), with which a binder is selectively printed on the powder bed to join the powders layer-by-layer and form a porous green part. After curing and de-powdering, the green body undergoes a de-binding process to pyrolyze the binder and initiate solid-state bonding between particles, resulting in a brown body which is further consolidated through sintering or by infiltrating the porous structure with a lower melting point metal (*Huang, 2023*). BJG processes include seven steps: printing, curing, de-powdering, sintering, infiltration, annealing, and finishing (*Mirzababaei, 2019*).

The combination of two or more manufacturing processes in a technique known as hybrid AM has also emerged in recent years. Initially, the term was coined referring to the combination of additive and subtracting manufacturing techniques with the aim to overcome the main limitations of AM, such as inadequate accuracy and surface roughness (*Torres, 2023*). However, more recently, hybrid AM has also been referred to the combination of laser and arc heat sources, giving the name Laser-Arc Hybrid Additive Manufacturing (LHAM) for ease of description, despite the various types of laser and arc sources that are involved. LHAM exhibits enormous potential in improving efficiency and accuracy, optimizing microstructure, and enhancing mechanical properties (*Gong, 2024*).

The last decade saw a rush from the major actors in AM industry to manufacture more efficient AM devices, not only to increase the competitiveness in mass production, but also to enable the manufacturing of large parts. Nikon SLM Solutions® has recently commercialized a new system capable of printing large parts up to 3.0 x 1.2 x 1.2 metres. However, the race for larger and more robust devices is now being equalled by more subtle aspects of the AM process chain. Indeed, R&D industrial departments and academic institutes are now giving attention on the quality of the feedstock material, on the improvement of existing printable alloys and on the development of new ones. Furthermore, despite being only at its dawn, Artificial Intelligence (AI) is starting to be implemented in AM processes, as is the scope of the company

'Ai Build ®'. The future will reserve even more surprises, with the raise of new technologies and new materials.

2.3.2 Powder feedstock for LPBF

After having provided an overview of the commercial AM systems, this and the next section will focus on the LPBF technique, which is the technology used in this work. As mentioned in the previous section, during LPBF operations powders are spread cyclically from the feedstock cylinder to the working platform. Therefore, powders must exhibit proper and stable rheological properties. Indeed, the homogeneity and density of each spread layer of powders is essential to grant a good interaction between powders and laser, in order to have a proper melting and overlapping between each track and layer and obtaining a defect-free final solid part. While defects such as lack of fusion, key-holes, balling, spattering are mainly processing-induced defects, their appearance is also affected by the powders properties (*Gokcekaya, 2021*; *Riener, 2020*; *Ziri, 2022*). Therefore, a good homogeneity of the powder layer is one of the first thing to ensure.

Powders properties that directly affect the homogeneity of the spread layers are many, such as Particle Size Distribution (PSD), morphology, surface roughness, flowability, spreadability, and Packing Density (PD). Usually, powders for LPBF are in spherical morphology, in the range 25 – 45 μm (*Vock, 2019*). These characteristics are desired to ensure good rheological properties. Spreadability, flowability and packing density properties are a consequence of attractive forces (i.e. Van Der Waals) that can increase the cohesion between each powder particle. Usually, high cohesive forces result in particles adhesion promoting a cohesive flow behaviour and worsening the spreadability (*Gärtner, 2023*). Previous works reported the possibility to study powders properties with rheological devices and correlate them to in-process performances (*Fig. 2.9*) (*Baesso, 2021*; *Capozzi, 2022*; *Neveu, 2022*). An example is given by Granutools®, a company with which the author has collaborated during the past years, resulting in the preparation of a common paper (*Saggionetto, Bio Seidou, n.d.*). This company has developed some devices such as Granudrum and Granupack, which allow to analyse the spreadability and packability properties of powders. However, the overall understanding of the powder characteristics is challenging, and some properties of powders can have contrary and unexpected effect during the LPBF process (*Vock, 2019*). Furthermore, substrate preheating (up to 800 °C) is being used to process crack-susceptible materials, to decrease residual stresses and to improve mechanical properties (*Ali, 2017*; *Casati, 2018*; *Malý, 2022*; *Mertens, 2018*).

Different works showed the beneficial effect of preheating to process high alloyed tool steels (*Boes, 2020*; *Qin, 2023*; *Saewe, 2021*; *Saewe, Wilms, 2019*; *Zumofen, 2018*), high entropy alloys (*Hecht, 2023*; *Vogiatzief, 2020*), titanium, nickel, aluminium-based alloys (*Caprio, 2020*; *Chen, 2023*; *Ghasemi, 2022*; *Tan, 2023*; *Tian, 2020*). So far, works have been limited to discuss the effect of the preheating on the quality and mechanical properties of the final part, but no mention is done on the modification of the powder properties modification brought about by pre-heating, due to the lack of in-situ and ex-situ devices for these studies.

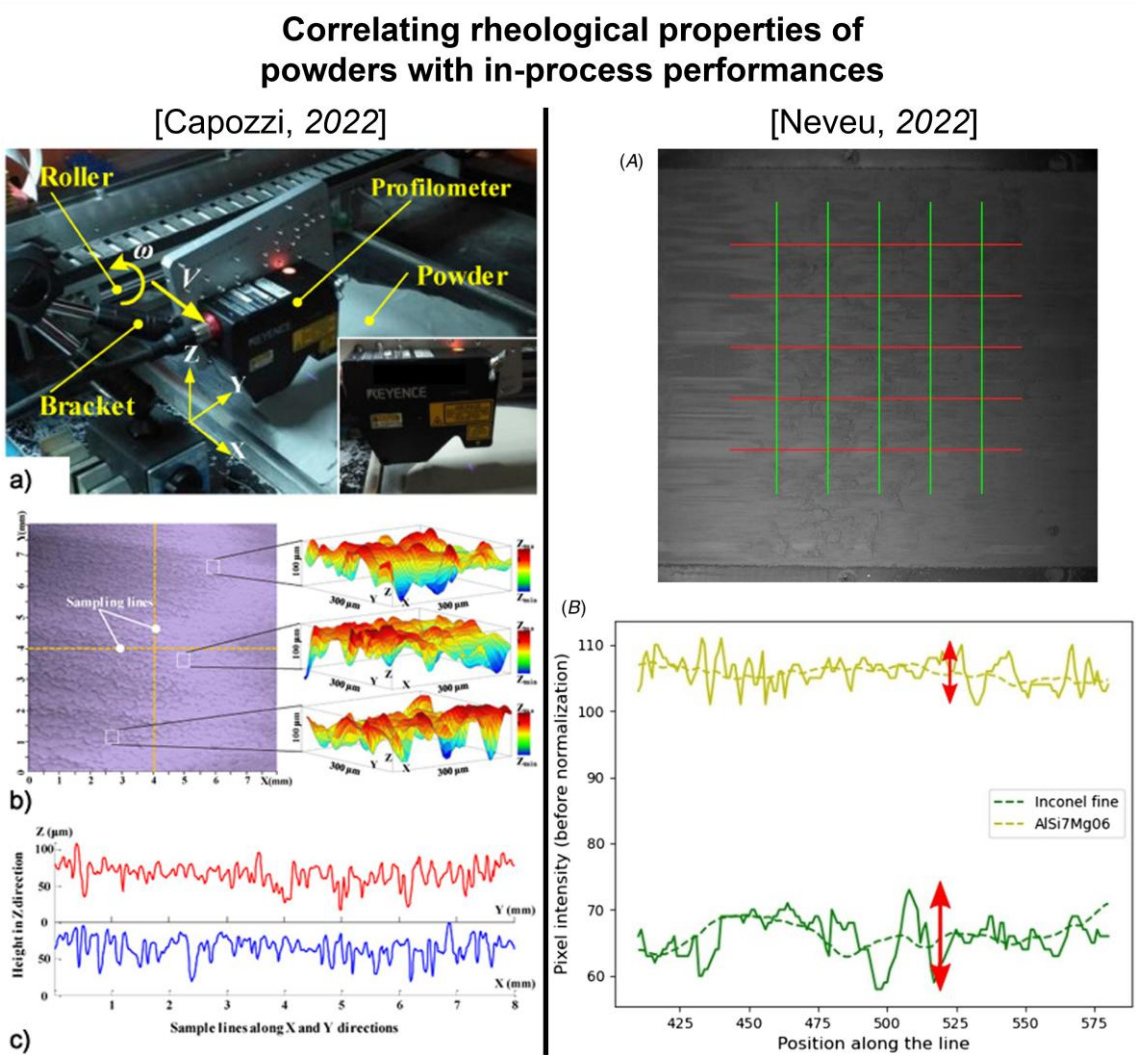


Fig. 2.9: Hardware and software to monitor in-situ the rheological properties of the powders.

Among all the metallic alloys that exists, few are available in form of powders suitable for the LPBF process. Usually, powders for LPBF are obtained by gas atomization, a process that allows the production of spherical powders (*Kassym, 2019*). However, the industrial scale of atomizers does not encourage the search for new fine-tuned alloys, due to the high cost and troublesome chemical composition of some metals (*Dawes, 2015*; *Rodowski, 2021*). A recent

method to obtain small (hundreds of grams) and customized batches of powder for LPBF is through ultrasonic atomisation technology, as developed by 'Amazemet' and '3DLAB'. A more conventional and cost-effective way is the simple mixing of different powders easily available in the market. Different mixing methods are used, such as dry mixing, ball milling and others non-mechanical routes (*Lüddecke, 2021*). The complexity of the phenomena affecting the rheological properties of the powder feedstock increases when two or more different types of powders are mixed. However, recent works reported that the addition of nanoparticles offers a variety of useful features, such as enhance flowability and powder layer density as well as mitigating key-hole pore formation (*Fig. 2.10*) (*Gärtner, 2021*, *2023*; *Lüddecke, 2021*; *Mussatto, 2019*).

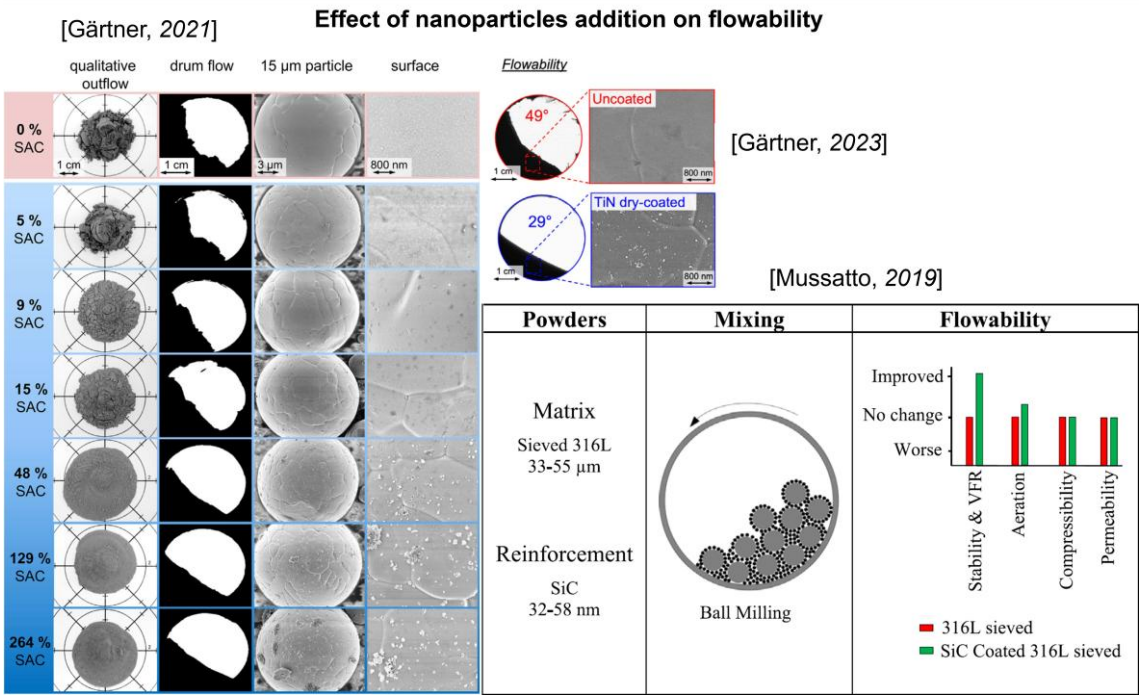


Fig. 2.10: Effect of nanoaparticles addition on the improvement of flowability properties of powder mixtures for LPBF.

The development of new alloys starting from powder mixtures requires some preliminary investigations, as the direct investigation with LPBF or, more generally, with powder-based AM technologies can be costly and time consuming. ThermoCalc® is being used by many materials research facilities as preliminary tool to develop new printable alloys. Recently, this tool was used in the work of (*Galbusera, 2022*) to investigate the hot cracking susceptibility of a high-alloyed tool steel during LPBF, as well as in (*Tobah, 2024*) to verify the reheating cycles effect. Complementarily, Differential Thermal Analysis (DTA) is also useful to test the chemical affinity of different powders in close-to-equilibrium conditions. This approach has

been developed and validated by the MMS group, first introduced with the work of (*Maurizi Enrici, 2022*), then validated with the present work and, more recently, used by (*Bio Seidou, 2024*) to assist the design of a novel corrosion-resistant high entropy alloy.

2.3.3 Processability of conventional and modified tool steels by LPBF

2.3.3.1 Effect of carbon and alloying elements

This section provides an extensive literature review about tool steels processed with LPBF in the last decade (*Table 2.2*).

Publications	Alloy	Carbon content (wt. %)	Processability (w/ preheating)	Microstructure
(*Huber, 2019*; *Raffeis, 2022*)	H11	0.3-0.4	up to 500 °C	Bainite, martensite, retained austenite and carbides
(*Fonseca, 2020*)	H13	0.3-0.4	without preheating	Martensite, retained austenite and carbides
(*Kempen, 2014*; *Z. H. Liu, 2013*)	M2	0.9	up to 200 °C	Martensite, ferrite, austenite
(*Qin, 2023*; *Saewe, Gayer, 2019*)	M50	0.8-0.9	up to 650 °C	Martensite/bainite and retained austenite
(*Galbusera, 2022*; *Saewe, 2021*; *Saewe, Gayer, 2019*)	HS6-5-8-3	1.2	350 °C	Martensite, retained austenite and carbides
(*Dilip, 2017*)	HY1000	0.18	without preheating	Untempered and tempered martensite
(*Abdelwahed, 2021*; *Damon, 2019*; *Hearn, 2023*; *Jelis, 2018*; *Ryder, 2021*; *W. Wang, 2016*)	4130, 4140, 4340, 8620	0.2-0.4	up to 200 °C	Untempered and tempered martensite, retained austenite and carbides
(*Boes, 2018*, *2020*)	X65MoCrWV3-2	0.6	300 °C	Untempered and tempered martensite
(*Krell, 2018*)	X40CrMoV5-1	0.4	up to 300 °C	Ferrite and austenite
(*Kosiba, 2023*)	FeCr4Mo1V1W8C1	1	without preheating	Martensite, retained austenite and carbides
(*Taha, 2012*)	High Carbon Steel	2.1	without preheating	Martensite, bainite and austenite

Table 2.2: Publications on tool steels processed with LPBF.

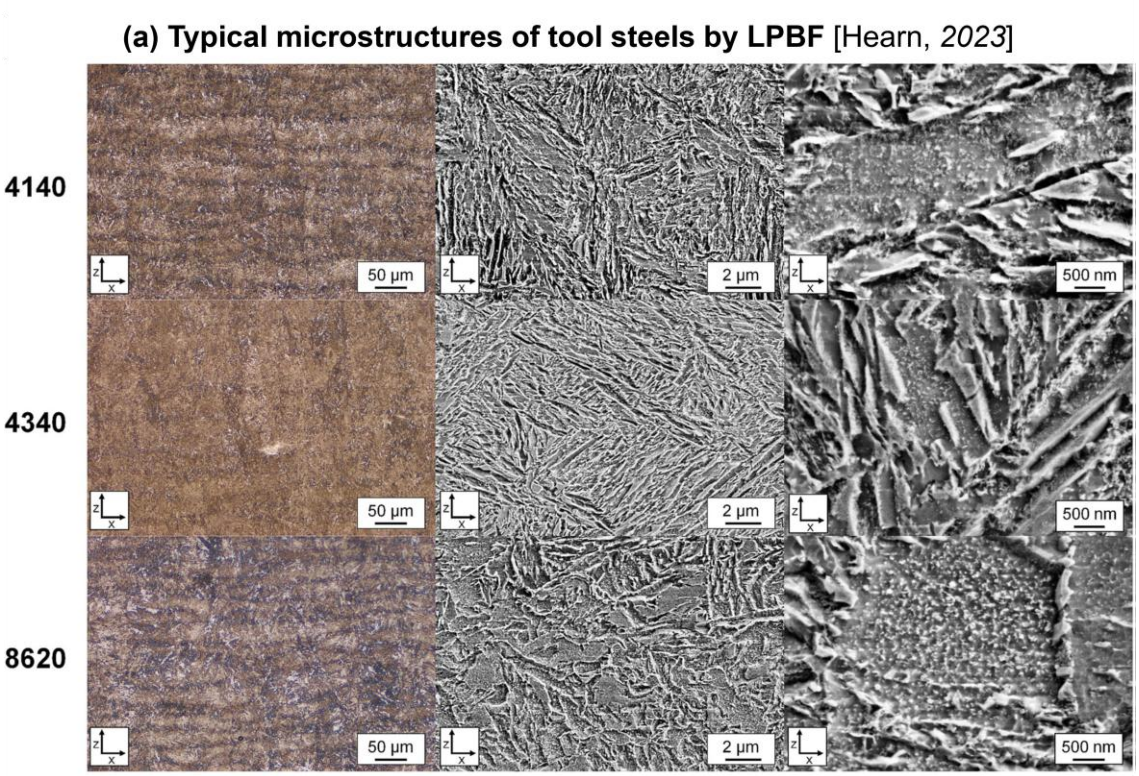
Processability of tool steels is affected either by the generation of process-induced defects such as lack of fusion, key-hole and spattering and by hot and cold cracking phenomena. Process-induced defects are correlated to the combination of the process parameters (power, hatch distance, layer thickness, scan speed), which affects the overall volumetric energy density ($E_{d,v}$). Process maps are usually developed to investigate the effect of the process parameters and to select those that allow the achievement of sound parts. In contrast, hot and cold cracks are correlated to the type of microstructure and the in-situ thermal cycles occurring during the process. Most of the as-built microstructure of tool steels consists of martensite/bainite and residual austenite (*Fig. 2.11*a) (*Table 2.2*). The formation of these phases causes a large amount of residual stresses, which lead to the nucleation and propagation of cold cracks and the subsequent delamination of the part from the substrate. Carbon plays an important role both in the appearance of process-induced defects and in cold-cracking phenomena. The work of (*Hearn, 2022*) reported that increasing the carbon content limited the formation of lack of fusion porosity at low $E_{d,v}$, while also increasing the susceptibility to form key-hole porosity. In parallel, high carbon content increased the crack susceptibility. Indeed, increase of the carbon content leads to the increase in martensite hardness which, combined with the residual stresses, leads to the formation of cracking defects. Even at high carbon content, reducing the susceptibility to cold cracking was possible with increasing $E_{d,v}$, due to the enhancement of the intrinsic heat treatment during the process, which lowered the hardness of the as-built specimens. Although the authors did not discuss this observation, lowering the hardness could be correlated to an in-situ tempering of the martensite, thus promoting secondary carbides precipitation and decreasing residual stresses.

The role of carbon in crack susceptibility was also explained in the work of (*Saewe, 2021*), where carbon was directly added within the powder mixture. The authors reported that increasing the carbon content allows the stabilization of the retained austenite, in view of the lowering of martensite starting temperature, which can be favourable for the decrease in residual stresses. However, since the increased carbon content led to more carbide precipitation within the interdendritic regions, these carbides favoured crack nucleation because of an increase in the stress concentration.

Carbides forming elements are also responsible for the appearance of hot cracking during solidification. Indeed, as explained in the work of (*Qin, 2023*), a high content of alloying elements enhance the segregation behaviour, favouring hot cracking. Hot cracks can also be promoted by preheating the substrate. However, up to now, preheating is the main tool that

allows to achieve fully dense and defect-free parts (*Fig. 2.11*b). Preheating allows to decrease residual stresses and to avoid cracks formation, in view of changes of the solidification sequence. Depending on the chemical composition of the alloy, the right combination of process parameters and temperature of preheating allows to achieve good processability. Only few works reported the achievement of crack-free parts without preheating (*Table 2.2*). In general, the higher the content of carbon and alloying elements, the higher is the preheating temperature necessary, as is the case of M50, H11, X65MoCrWV3-2, X40CrMoV5-1. In contrast, lower preheating temperatures are enough to process low alloyed steels such as AISI 4130, 4140, 4340, 8620. The achievement of defect-free high alloyed tool steels without preheating is a current hot topic, and specific alloys are being developed for this reason, as reported in (*Kosiba, 2023*) (*Fig. 2.11*c). This is an example of the current focus on developing and improving metals for additive manufacturing with LPBF.

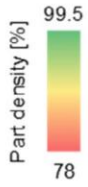
To the best of the author's knowledge, only one example of a ultra-high carbon tool steel with 2 wt. % of carbon is reported in (*Taha, 2012*). In this case, even the best sample exhibited spherical pores with an average diameter ranging from 10 to 80 μm, with an overall relatively low density (92 %). In view of the high carbon content, this can still be considered a good achievement. Although the author of that work did not discuss this issue, the fair processability can be associated to the fact that no carbide forming elements were present within the chemical composition, whereas the main alloying elements, were silicon and copper.



(b) Effect of preheating [Qin, *2023*]

	RT					200 °C					350 °C				
E_V [J/mm³]	25	50	80	100	125	25	50	80	100	125	25	50	80	100	125
130 W	78.84	97.11	99.80	99.96	99.91	81.73	98.87	99.95	99.95	99.85	85.14	98.21	99.78	99.94	99.85
200 W	86.97	99.34	99.99	99.98	99.96	92.00	99.67	99.98	99.97	99.96	94.14	99.84	99.98	99.95	99.90
260 W	93.21	99.91	99.99	99.91	99.91	97.50	99.96	99.98	99.97	99.96	99.92	99.93	99.97	98.21	99.93

	500 °C					650 °C				
E_V [J/mm³]	25	50	80	100	125	25	50	80	100	125
130 W	83.50	97.30	99.90	99.94	99.78	93.63	99.69	99.92	99.89	98.10
200 W	96.42	99.80	99.97	99.98	99.98	87.00	99.95	99.99	100.00	99.96
260 W	96.79	99.99	99.99	97.30	99.96	99.95	99.97	99.99	99.97	99.99



(c) Microstructure of LPBF-tailored high-alloyed tool steel without preheating

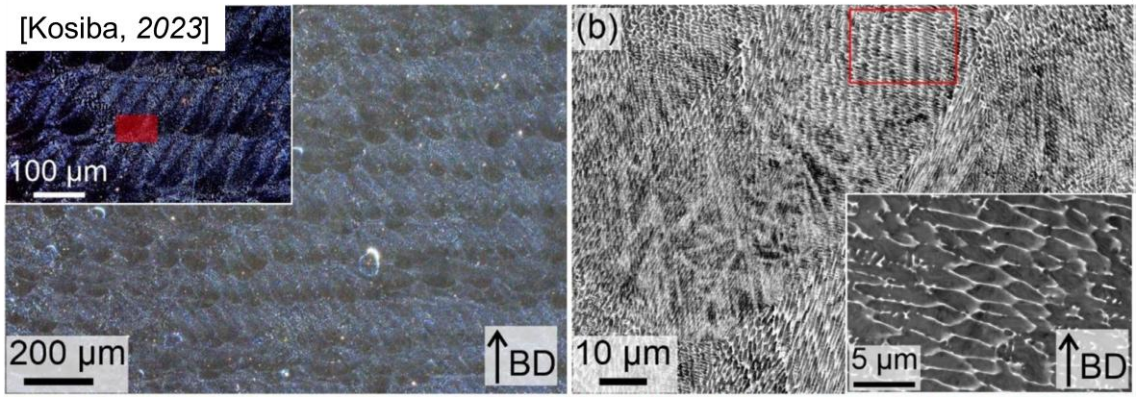


Fig. 2.11: (a) Typical microstructures of tool steels processed by LPBF, (b) effect of preheating on processability and (c) LPBF-tailored tool steel processable without preheating.

2.3.3.2 Towards enhanced properties with additives enrichment

Modified alloys are being investigated by processing a mixture of powders, resulting from the mixing of classical steels together with other powders, such as carbides (TiC, SiC, WC, VC, Cr_2C_3 etc.). This is done not only to achieve a specific chemical composition, as explained in the previous section (2.3.2), but also to increase the properties of existing metals. Among those types of additives, SiC particles are being widely used as reinforcements, especially to improve the wear resistance. SiC has a low density, high hardness, good wettability with iron and higher laser absorption than steels, thus theoretically promoting a good processability of the alloy. Furthermore, SiC has the potential to modify the microstructure of steels due to the dissolution of carbon and silicon in the matrix, thus enhancing the properties of the microstructure. To the best of the author's knowledge regarding Fe-based alloys for LPBF, so far SiC has been added to 316L, C300 and X3NiCoMoTi18-9-5 maraging tool steels, and to pure iron (*Table 2.3*).

Publications	Matrix	SiC particles size	SiC dissolution	Microstructure
(*D. Wang, 2022*; *Zou, 2021*)	316L	29 µm	Partial	Austenite
(*Pannitz, 2021*; *Tan, 2022*, *2023*)	Maraging tool steels	6 µm, 100 nm	Partial/Complete	Martensite and retained austenite
(*Song, 2013*)	Fe	0.7 µm	Partial	Martensite and pearlite
(*Strauch, 2021*)	Fe	37 µm	Complete	Martensite, bainite and retained austenite

Table 2.3: Publications on Fe-based alloys with SiC addition, processed with LPBF.

Different solidification phenomena occur depending on the main powder used. With 316L, the matrix of the solidified microstructure was austenite, corresponding to the parent matrix of 316L (*D. Wang, 2022*; *Zou, 2021*). SiC addition did not change the matrix type (*Fig. 2.12*b). Meanwhile, in these cases, increasing the addition in SiC led to a shift from equiaxed to dendrites morphology of the microstructure (*Fig. 2.12*a). Similarly, this phenomenon was also observed in the work of (*Tan, 2022*), where a maraging tool steel was used as main powder (*Fig. 2.12*b). However, in contrast to the austenitic 316L matrix, martensite and retained austenite are found within the microstructure due to the higher carbon content of the starting maraging steel powder. Furthermore, the authors reported that increasing the content of SiC allows to retain more austenite at room temperature, as also stated in (*Pannitz, 2021*; *Strauch, 2021*).

The appearance of martensite and austenite is linked to the dissolution of SiC particles within the parent matrix. Despite the good affinity between Fe and SiC, particles can also be only

partially dissolved, as shown in some works cited above. The rate of dissolution of the SiC particles depends on two main factors, which are the initial size of the particle and the chemical composition of the main alloying powder. Beside the $E_{d,v}$ used in the process and other intrinsic features of the LPBF device, such as its laser type, can also have an influence. When the main powder was 316L, maraging steels or pure iron and the average size of SiC particles was ranging from 0.7 to 29 µm, partially dissolved and homogeneously distributed particles were found within the final microstructure (*Fig. 2.12*c). In contrast, SiC with a smaller size (100 nm) were completely dissolved even with maraging steel as main powder (*Pannitz, 2021*). Complete dissolution also occurred with SiC particles with a d50 of 37 µm. In this case, the mixture was composed only by pure iron and SiC (*Strauch, 2021*). Therefore, SiC can either be completely or partially dissolved, and the choice of its size depends on the desired final microstructure. Indeed, SiC can be added to promote ex-situ strengthening of the microstructure, to favour in-situ reactions that allow the solidification of new phases or a compromise between the two. These aspects are part of the expertise of the MMS team. For instance, SiC properties in AM were investigated during the PhD project of (*Maurizi Enrici, 2022*), former member of the MMS team. The current PhD project relies on the basis of the observations reported in one of his works (*Maurizi Enrici, n.d.*).

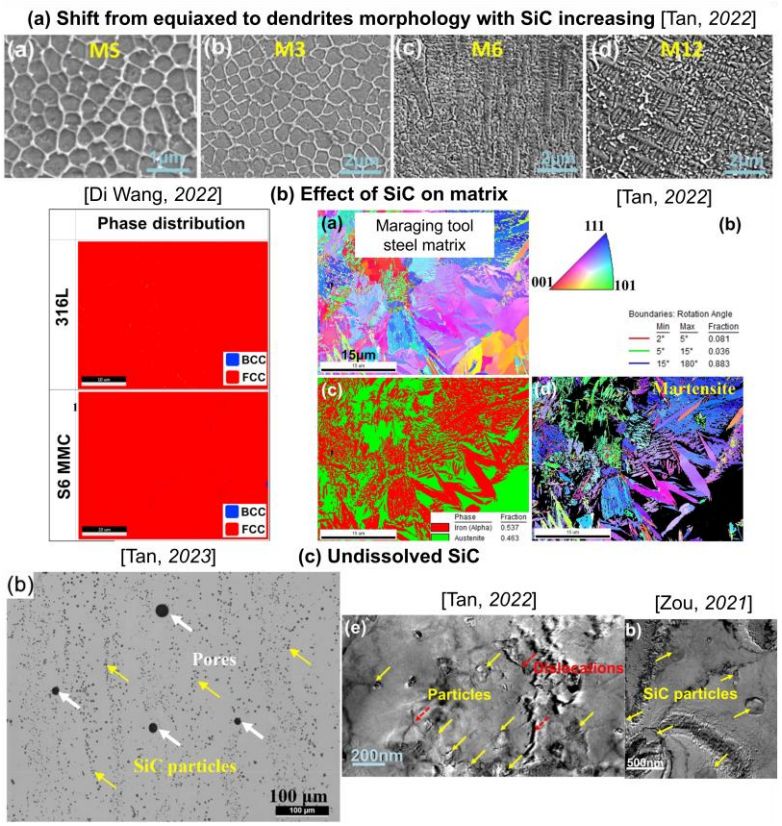


Fig. 2.12: Effect of SiC addition on (a) the shift from equiaxed to dendrites morphologies, (b) the type of matrix and (c) undissolved SiC particles within the solidified microstructure.

2.4 Redefining wear properties with materials for AM

This section aims to provide a modern review on the development of new metal alloys for AM.

2.4.1 Innovative wear mechanisms

Over the recent years, there has been increasing interest in the development of innovative wear-resistant materials. This can help to reduce energy losses resulting from friction and wear by ~ 40% over the next decade (*Zhai, 2021*). This trend is even growing with the raise of AM technologies. The rapid heating and cooling cycles in the out-of-equilibrium conditions allow to form innovative microstructures, with metastable and supersaturated phases, and with small-sized carbides. These characteristics allow to achieve better wear resistance compared to conventional materials, and some industrial applications already exist. For example, the Swedish company VBN has successfully created a new generation of high-strength, carbide-rich tool materials processed with EBM (Vibenite®). These unique, patented alloys are transforming tool and wear component performance across a range of applications, from gear cutting hobs to food processing and mining sector (*"Metal AM magazine," 2019*).

Most of the classical wear phenomena and studies on tribology were discussed during the last century. Nowadays, the conventional wear mechanisms such as abrasion, adhesion, fatigue, oxidation, tribo-chemical reactions etc. still lie the basis for understanding wear properties, but their classical occurrence is altered by the innovative microstructures. For example, different microstructure configuration can be induced within the same material by changing the AM process parameters. The work of (*Y. Yang, 2019*), reported that a LPBF 316L exhibited a certain anisotropy of wear due to the presence of cells with different orientations, each of which result in different wear behaviour. By adjusting the scan strategy of the process, it is possible to tailor the primary cells/dendrites orientation, with the aim of enhancing a specific wear behaviour. Furthermore, even with the presence of LPBF process-induced defects, the microstructure can have knock-on effects capable of alleviating the wear rate (*Bahshwan, 2020*).

Another example of redefined wear properties is carried by the capability of AM processes to tailor the microstructure, achieving complex hierarchical structures. Thus, each scale of the microstructure (macro, meso, micro, nano) can contribute with specific phenomena to the overall wear behaviour. The design of heterogeneous hierarchical structures makes it possible to achieve specific tribological properties within the surface and/or in the core of the material, which can help in improving the wear based on the scale of interaction during the application.

This aspect was discussed in the publication of the author of this work (*Saggionetto, Maurizi Enrici, 2025.*).

Therefore, AM must be seen as a way to engineer and improve metals, in order to achieve tailored microstructures with specific wear properties, as in the case of this work.

2.4.2 New generation of self-lubricating tools

In industry, the manufacturing of parts (metal, ceramic, plastic, wood) through operations such as cutting, forming, stamping, shearing, punching, drawing and others involves the use of a tool as working part. During the manufacturing operation, the continuous interaction between tool and workpiece and friction lead to the wear of the tool. The result might be the breakage of the tool and its substitution, negatively affecting the economic aspect as well as the energy consumption of the manufacturing operation. To reduce and minimize both friction and tool wear, in order to increase the tool life, the use of an external lubricant is needed. Different lubricants are available, being natural or synthetic oils, water, grease or in solid-state such as MoS_2, WS_2, $MoSe_2$, NbS_2, $TaSe_2$, $MoTe_2$, TiB_2, h-BN, low melting metals like Ag, Sn and Pb, graphite and polytetrafluoroethylene (*Hammes, 2014*). The selection of the best lubricant is often a challenge for the industry, as it depends on the material properties of both tool and workpiece on one hand, and on the operating conditions on the other hand. The use of external lubricants represents a problem for human health and the environment due to the presence of contaminants. Therefore, there is a need for self-lubricating materials. One advantage of solid-lubricating compounds within self-lubricating metals is that they can be gradually released during service to minimize friction and wear over a wide range of temperatures. Over the recent years, efforts are being made to combine the advantages of AM implementing traditional lubricant compounds, in order to develop a new class of self-lubricating cutting tools for the new era of green machining.

One class of material often used in tool production is High Speed Steel (HSS), thanks to its high hardness and intrinsic wear resistance. Self-lubricating properties of HSS are usually obtained through deposition by laser cladding of a coating that protect the material underneath from wear. Several academic works and patents reported the benefits of self-lubricating tools. For example, the work of (*Xing, 2023*), explained the development of a Self-Lubricating Coated (SLC) cutting tool. In that work, a Ni-based powder was mixed with MoS_2 and Al_2O_3, and then coated on a AISI 1045 tool substrate (*Fig. 2.13*a). The SLC cutting tools exhibited excellent friction and cutting properties. Both the friction coefficient and surface wear were

reduced in sliding friction tests, along with significantly reduced cutting forces, tool-chip friction, cutting power and tool wear compared to conventional HSS cutting tools. The improved friction and wear resistance of SLC cutting tools were attributed to the increased surface hardness reinforced by Al_2O_3 phases and the lubricating effect of MoS_2 phases. During the cutting process, MoS_2 lubricants were released and smeared at the tool-chip interfaces forming a lubricating film.

The patent of Wang Cheng et al. (CN114774912A, 2022-07-22) describes a laser cladding process wherein the starting powders (stainless steel, pure titanium, graphite, h-BN) react to form a wear resistant coating on a forging mold H13 steel. This is due to the fact that h-BN partially decomposes into B and N during the laser cladding process, in which N reacts with Ti to form TiN, C reacts with Cr in the stainless steel powder to form Cr_3C_2, and C combines with Ti to form TiC. Such phases, together with the residues of graphite and h-BN, play the role of self-lubricant in laser cladding coatings, decreasing the Coefficient of Friction (*Fig. 2.13*b).

The work of (*Torres, 2023*) has presented a combination of laser cladding and LPBF for the development of maraging steel tools for high temperature forming of aluminium alloys. The as-printed maraging tools were successfully functionalized by cladding self-lubricating Ni-based and Fe-based coatings. The maraging tools with self-lubricating Ni-base coating showed more stable frictional conditions against the AA6082 workpiece in ring compression tests performed at 300 °C (*Fig. 2.13*b).

Laser cladding is limited only to improve the properties of a starting material with simple geometries. In contrast, LPBF allows to produce a whole complex shape part with tailored properties. Not many examples of self-lubricating tools processed by LPBF are available. The patent of Xiaoliang et al. (CN106801194B, 2019-06-25) shows the methodology to achieve a Ti_3SiC_2-containing M50 spherical powder by atomization, with properties suitable for use in LPBF. Afterwards, the patent describes the processability of such composite powders by LPBF. The final material obtained exhibits self-lubricating wear properties due to the presence of Ti_3SiC_2 as the lubricating phase, showing low wear rates and coefficient of friction.

Therefore, the development of a self-lubricating tool with LPBF is a cutting-edge topic for materials innovation and can contribute not only to expand the academic knowledge, but also find application in real industry.

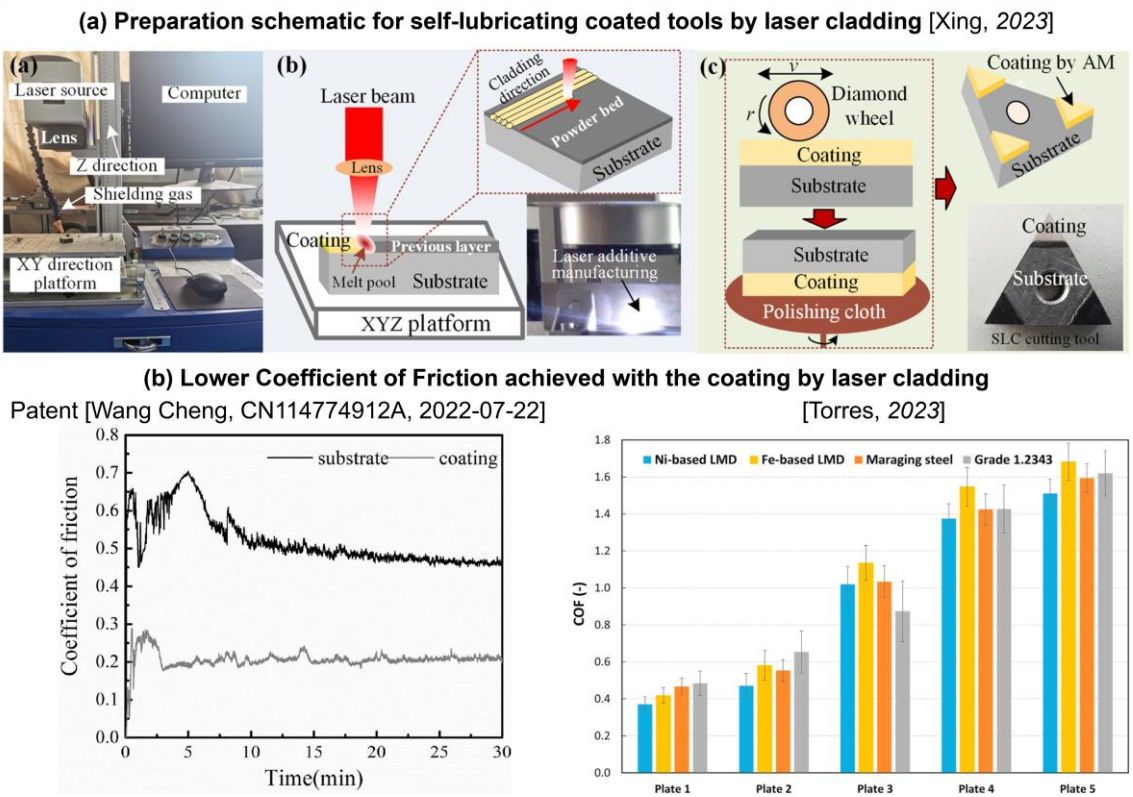


Fig. 2.13: (a) Self-lubricating coating on cutting tools by laser cladding and (b) its effect on the Coefficient of Friction.

2.5 References

Abdelwahed, M., Bengtsson, S., Casati, R., Larsson, A., Petrella, S., & Vedani, M. (2021). "Effect of water atomization on properties of type 4130 steel processed by L-PBF." Materials and Design, 210, 110085. https://doi.org/10.1016/j.matdes.2021.110085

Abdulhameed, O., Al-Ahmari, A., Ameen, W., & Mian, S. H. (2019). "Additive manufacturing: Challenges, trends, and applications." Advances in Mechanical Engineering, 11(2), 1–27. https://doi.org/10.1177/1687814018822880

Aigner, M., Pellizzari, M., Domitner, J., Elizondo, L., Fischbacher, M., Laubichler, I., … Sommitsch, C. (2023). "Influence of microstructure on degradation of cast graphitic high-speed steel." Wear, 522(September 2022), 204702. https://doi.org/10.1016/j.wear.2023.204702

Ali, H., Ma, L., Ghadbeigi, H., & Mumtaz, K. (2017). "In-situ residual stress reduction, martensitic decomposition and mechanical properties enhancement through high temperature powder bed pre-heating of Selective Laser Melted Ti6Al4V." Materials Science and Engineering: A, 695(April), 211–220. https://doi.org/10.1016/j.msea.2017.04.033

Baesso, I., Karl, D., Spitzer, A., Gurlo, A., Günster, J., & Zocca, A. (2021). "Characterization of powder flow behavior for additive manufacturing." Additive Manufacturing, 47(June), 102250. https://doi.org/10.1016/j.addma.2021.102250

Bahshwan, M., Myant, C. W., Reddyhoff, T., & Pham, M. S. (2020). "The role of microstructure on wear mechanisms and anisotropy of additively manufactured 316L stainless steel in dry sliding." Materials and Design, 196, 109076. https://doi.org/10.1016/j.matdes.2020.109076

Binder, C., Bendo, T., Pereira, R. V., Hammes, G., de Mello, J. D. B., & Klein, A. N. (2016). "Influence of the SiC content and sintering temperature on the microstructure, mechanical properties and friction behaviour of sintered self-lubricating composites." Powder Metallurgy, 59(5), 384–393. https://doi.org/10.1080/00325899.2016.1250036

Bio Seidou, A. H., Blondiau, C., & Dedry, O.. (2024). "Differential thermal analysis to assist the design of corrosion-resistant high entropy alloys for laser powder bed fusion," 41, 353–362.

Boccalini, M., & Goldenstein, H. (2001). "Solidification of high speed steels." International Materials Reviews, 46(2), 92–115. https://doi.org/10.1179/095066001101528411

Boes, J., Röttger, A., Mutke, C., Escher, C., & Theisen, W. (2018). "Microstructure and mechanical properties of X65MoCrWV3-2 cold-work tool steel produced by selective laser melting." Additive Manufacturing, 23(August), 170–180. https://doi.org/10.1016/j.addma.2018.08.005

Boes, J., Röttger, A., & Theisen, W. (2020). "Processing of X65MoCrWV3-2 Cold Work Tool Steel by Laser Powder Bed Fusion." Steel Research International, 91(5). https://doi.org/10.1002/srin.201900445

Buytoz, S. (2006). "Microstructural properties of SiC based hardfacing on low alloy steel." Surface and Coatings Technology, 200(12–13), 3734–3742. https://doi.org/10.1016/j.surfcoat.2005.01.106

Campos, K. R., Kapsa, P., Binder, C., Klein, A. N., & de Mello, J. D. B. (2015). "Tribological evaluation of self-lubricating sintered steels." Wear, 332–333, 932–940. https://doi.org/10.1016/j.wear.2015.01.056

Capozzi, L. C., Sivo, A., & Bassini, E. (2022). "Powder spreading and spreadability in the additive manufacturing of metallic materials: A critical review." Journal of Materials Processing Technology, 308(July), 117706. https://doi.org/10.1016/j.jmatprotec.2022.117706

Caprio, L., Demir, A. G., Chiari, G., & Previtali, B. (2020). "Defect-free laser powder bed fusion of Ti – 48Al – 2Cr – 2Nb with a high temperature inductive preheating system Defect-free laser powder bed fusion of Ti – 48Al – 2Cr – 2Nb with a high temperature inductive preheating system." JPhis Photonics.

Casati, R., Nasab, M. H., Coduri, M., Tirelli, V., & Vedani, M. (2018). "Effects of platform pre-heating and thermal-treatment strategies on properties of alsi10mg alloy processed by selective laser melting." Metals, 8(11), 954. https://doi.org/10.3390/met8110954

Chen, X., Xie, X., Wu, H., Ji, X., Shen, H., Xue, M., … Liu, Q. (2023). "In-situ control of residual stress and its distribution in a titanium alloy additively manufactured by laser powder bed fusion," 201(February), 23–25. https://doi.org/10.1016/j.matchar.2023.112953

Damon, J., Koch, R., Kaiser, D., Graf, G., Dietrich, S., & Schulze, V. (2019). "Process development and impact of intrinsic heat treatment on the mechanical performance of selective laser melted AISI 4140." Additive Manufacturing, 28(November 2018), 275–284. https://doi.org/10.1016/j.addma.2019.05.012

Dawes, J., Bowerman, R., & Trepleton, R. (2015). "Introduction to the additive manufacturing powder metallurgy supply chain." Johnson Matthey Technology Review, 59(3), 243–256. https://doi.org/10.1595/205651315X688686

de Mello, J. D. B., Binder, C., Binder, R., & Klein, A. N. (2011). "Effect of precursor content and sintering temperature on the scuffing resistance of sintered self lubricating steel." Wear, 271(9–10), 1862–1867. https://doi.org/10.1016/j.wear.2010.11.038

de Mello, J. D. B., Binder, C., Hammes, G., Binder, R., & Klein, A. N. (2017). "Tribological behaviour of sintered iron based self-lubricating composites." Friction, 5(3), 285–307. https://doi.org/10.1007/s40544-017-0186-2

de Mello, J. D. B., Binder, C., Hammes, G., & Klein, A. N. (2013). "Effect of the metallic matrix on the sliding wear of plasma assisted debinded and sintered MIM self-lubricating steel." Wear, 301(1–2), 648–655. https://doi.org/10.1016/j.wear.2013.01.011

Dilip, J. J. S., Ram, G. D. J., Starr, T. L., & Stucker, B. (2017). "Selective laser melting of HY100 steel: Process parameters, microstructure and mechanical properties." Additive Manufacturing, 13, 49–60. https://doi.org/10.1016/j.addma.2016.11.003

Edalati, K., Akhlaghi, F., & Nili-Ahmadabadi, M. (2005). "Influence of SiC and FeSi addition on the characteristics of gray cast iron melts poured at different temperatures." Journal of Materials Processing Technology, 160(2), 183–187. https://doi.org/10.1016/j.jmatprotec.2004.06.007

Fesenko, M. A., & Fesenko, A. M. (2020). "In-mould graphitizing, spheroidizing, and carbide stabilizing inoculation of cast iron melt." Progress in Physics of Metals, 21(1), 83–101. https://doi.org/10.15407/ufm.21.01.083

Fonseca, E. B., Gabriel, A. H. G., Araújo, L. C., Santos, P. L. L., Campo, K. N., & Lopes, E. S. N. (2020). "Assessment of laser power and scan speed influence on microstructural features and consolidation of AISI H13 tool steel processed by additive manufacturing." Additive Manufacturing, 34(August 2019), 101250. https://doi.org/10.1016/j.addma.2020.101250

Friess, J., Sonntag, U., Steller, I., & Bührig-Polaczek, A. (2020). "From Individual Graphite Assignment to an Improved Digital Image Analysis of Ductile Iron." International Journal of Metalcasting, 14(4), 1090–1104. https://doi.org/10.1007/s40962-020-00416-3

Galbusera, F., Demir, A. G., Platl, J., Turk, C., Schnitzer, R., & Previtali, B. (2022). "Processability and cracking behaviour of novel high-alloyed tool steels processed by Laser Powder Bed Fusion." Journal of Materials Processing Technology, 302(November 2021). https://doi.org/10.1016/j.jmatprotec.2021.117435

Gao, J. X., Wei, B. Q., Li, D. D., & He, K. (2016). "Nucleation and growth characteristics of graphite spheroids in bainite during graphitization annealing of a medium carbon steel." Materials Characterization, 118, 1–8. https://doi.org/10.1016/j.matchar.2016.05.003

Gärtner, E., Jung, H. Y., Peter, N. J., Dehm, G., Jägle, E. A., Uhlenwinkel, V., & Mädler, L. (2021). "Reducing cohesion of metal powders for additive manufacturing by nanoparticle dry-coating." Powder Technology, 379, 585–595. https://doi.org/10.1016/j.powtec.2020.10.065

Gärtner, E., Witte, A., Peter, N. J., Devulapalli, V., Ellendt, N., Dehm, G., … Mädler, L. (2023). "Melt pool signatures of TiN nanoparticle dry-coated Co25Cr25Fe25Ni25 metal powder in laser-powder-bed-fusion." Materials and Design, 226. https://doi.org/10.1016/j.matdes.2023.111626

Ghasemi, A., Fereiduni, E., Balbaa, M., Elbestawi, M., & Habibi, S. (2022). "Unraveling the low thermal conductivity of the LPBF fabricated pure Al, AlSi12, and AlSi10Mg alloys through substrate preheating." Additive Manufacturing, 59(PA), 103148. https://doi.org/10.1016/j.addma.2022.103148

Gokcekaya, O., Ishimoto, T., Todo, T., Wang, P., & Nakano, T. (2021). "Influence of powder characteristics on densification via crystallographic texture formation: Pure tungsten prepared by laser powder bed fusion." Additive Manufacturing Letters, 1(October), 100016. https://doi.org/10.1016/j.addlet.2021.100016

Gong, M., Zhang, S., Lu, Y., Jiang, L., Liao, W., & Gao, M. (2024). "Achieving impressive strength and mitigated anisotropy in high-power laser-arc hybrid additive manufacturing of stainless steel through tailored microstructures composition." Materials Science and Engineering: A, 894(September 2023), 146204. https://doi.org/10.1016/j.msea.2024.146204

Guo, M., Liu, A., Zhao, M., Hu, H., & Wang, Z. (2008). "Microstructure and wear resistance of low carbon steel surface strengthened by plasma melt injection of SiC particles." Surface and Coatings Technology, 202(16), 4041–4046. https://doi.org/10.1016/j.surfcoat.2008.02.019

Hammes, G., Schroeder, R., Binder, C., Klein, A. N., & De Mello, J. D. B. (2014). "Effect of double pressing/double sintering on the sliding wear of self-lubricating sintered composites." Tribology International, 70, 119–127. https://doi.org/10.1016/j.triboint.2013.09.016

Hearn, W., Harlin, P., & Hryha, E. (2023). "Development of powder bed fusion–laser beam process for AISI 4140, 4340 and 8620 low-alloy steel." Powder Metallurgy, 66(2), 94–106. https://doi.org/10.1080/00325899.2022.2134083

Hearn, W., & Hryha, E. (2022). "Effect of Carbon Content on the Processability of Fe-C Alloys Produced by Laser Based Powder Bed Fusion." Frontiers in Materials, 8(January), 1–10. https://doi.org/10.3389/fmats.2021.800021

Hecht, U., Vayyala, A., Barriobero-Vila, P., Navaeilavasani, N., Gein, S., Cazic, I., & Mayer, J. (2023). "Microstructure evolution in the hypo-eutectic alloy Al0.75CrFeNi2.1 manufactured by laser powder bed fusion and subsequent annealing." Materials Science and Engineering: A, 862(September 2022), 144315. https://doi.org/10.1016/j.msea.2022.144315

Huang, N., Cook, O. J., Argüelles, A. P., & Beese, A. M. (2023). "Review of Process–Structure–Property Relationships in Metals Fabricated Using Binder Jet Additive Manufacturing." Metallography, Microstructure, and Analysis, 12(6), 883–905. https://doi.org/10.1007/s13632-023-00998-4

Huber, F., Bischof, C., Hentschel, O., Heberle, J., Zettl, J., Nagulin, K. Y., & Schmidt, M. (2019). "Laser beam melting and heat-treatment of 1.2343 (AISI H11) tool steel – microstructure and mechanical properties." Materials Science and Engineering: A, 742(November 2018), 109–115. https://doi.org/10.1016/j.msea.2018.11.001

Inam, A., Brydson, R., & Edmonds, D. V. (2015). "Effect of starting microstructure upon the nucleation sites and distribution of graphite particles during a graphitising anneal of an experimental medium-carbon machining steel." Materials Characterization, 106, 86–92. https://doi.org/10.1016/j.matchar.2015.05.014

Jelis, E., Hespos, M. R., & Ravindra, N. M. (2018). "Process Evaluation of AISI 4340 Steel Manufactured by Laser Powder Bed Fusion." Journal of Materials Engineering and Performance, 27(1), 63–71. https://doi.org/10.1007/s11665-017-2989-8

Kante, S., Leineweber, A., Holst, A., & Buchwalder, A. (2019). "Low-temperature annealing and graphitizing of white-solidified low-alloy cast irons." Materialwissenschaft Und Werkstofftechnik, 50(6), 682–695. https://doi.org/10.1002/mawe.201800169

Kassym, K., & Perveen, A. (2019). "Atomization processes of metal powders for 3D printing." Materials Today: Proceedings, 26, 1727–1733. https://doi.org/10.1016/j.matpr.2020.02.364

Kempen, K., Vrancken, B., Buls, S., Thijs, L., Van Humbeeck, J., & Kruth, J. P. (2014). "Selective Laser Melting of Crack-Free High Density M2 High Speed Steel Parts by Baseplate Preheating." Journal of Manufacturing Science and Engineering, Transactions of the ASME, 136(6). https://doi.org/10.1115/1.4028513

Khuntrakool, C., Janudom, S., Muangjunburee, P., Yodjan, A., Mahathaninwong, N., & Chucheep, T. (2024). "Control of Graphite Structure in High Phosphorus Grey Cast Iron Brake Shoes through Ferro-Silicon Inoculant." International Journal of Metalcasting, (October 2023). https://doi.org/10.1007/s40962-024-01302-y

Kim, Y. J., & Park, S. H. (2021). "Effect of initial microstructure on graphitization behavior of Fe–0.55C–2.3Si steel." Journal of Materials Research and Technology, 15, 4529–4540. https://doi.org/10.1016/j.jmrt.2021.10.071

Kosiba, K., Wolf, D., Bönisch, M., Neufeld, K., Hühne, R., Gustmann, T., … Hufenbach, J. K. (2023). "Achieving exceptional wear resistance in a crack-free high-carbon tool steel fabricated by laser powder bed fusion without pre-heating." Journal of Materials Science and Technology, 156, 1–19. https://doi.org/10.1016/j.jmst.2023.02.012

Krell, J., Röttger, A., Geenen, K., & Theisen, W. (2018). "General investigations on processing tool steel X40CrMoV5-1 with selective laser melting." Journal of Materials Processing Technology, 255(January), 679–688. https://doi.org/10.1016/j.jmatprotec.2018.01.012

Lecomte-Beckers, J., & Tchuindjang, J. T. (2009). "Structural investigations of solidification and heat treatments influence on high alloyed cast irons grades with Nb-V-Ti additions." Defect and Diffusion Forum, 289–292, 77–86. https://doi.org/10.4028/www.scientific.net/DDF.289-292.77

Lin, Y. C., Chen, H. M., & Chen, Y. C. (2013). "Analysis of microstructure and wear performance of SiC clad layer on SKD61 die steel after gas tungsten arc welding." Materials and Design, 47, 828–835. https://doi.org/10.1016/j.matdes.2013.01.007

Liu, S., Zhou, Y., Xing, X., Wang, J., Ren, X., & Yang, Q. (2016). "Growth characteristics of primary M7C3 carbide in hypereutectic Fe-Cr-C alloy." Scientific Reports, 6(May), 1–8. https://doi.org/10.1038/srep32941

Liu, X., Zhou, G., Shen, Y. Y., Yan, W., & Li, J. (2023). "Evolution of primary carbides during accelerated solidification process of high-carbon martensitic stainless steels." Journal of Materials Research and Technology, 27(November), 5935–5944. https://doi.org/10.1016/j.jmrt.2023.11.068

Liu, Z. H., Zhang, D. Q., Chua, C. K., & Leong, K. F. (2013). "Crystal structure analysis of M2 high speed steel parts produced by selective laser melting." Materials Characterization, 84, 72–80. https://doi.org/10.1016/j.matchar.2013.07.010

Lüddecke, A., Pannitz, O., Zetzener, H., Sehrt, J. T., & Kwade, A. (2021). "Powder properties and flowability measurements of tailored nanocomposites for powder bed fusion applications." Materials and Design, 202. https://doi.org/10.1016/j.matdes.2021.109536

Luo, Q., Shen, J., Wang, X., Farmilo, N., & Guo, X. (2024). "Microstructure evolution and tribo-oxidation induced by friction and wear of cast iron brake discs." Surface Science and Technology, 2(1), 1–11. https://doi.org/10.1007/s44251-023-00031-4

Malý, M., Nopová, K., Klakurková, L., Adam, O., Pantělejev, L., & Koutný, D. (2022). "Effect of Preheating on the Residual Stress and Material Properties of Inconel 939 Processed by Laser Powder Bed Fusion." Materials, 15(18), 1–16. https://doi.org/10.3390/ma15186360

Maurizi Enrici, T. (2022). Development, metallurgical and tribological characterization of complex alloys and metal matrix composites obtained from manufacturing processes under non-equilibrium conditions. University of Liège.

Maurizi Enrici, T., Mertens, A., Sinnaeve, M., & Tchuindjang, J. T. (2020). "Elucidation of the solidification sequence of a complex graphitic HSS alloy under a combined approach of DTA and EBSD analyses." Journal of Thermal Analysis and Calorimetry, 141(3), 1075–1089. https://doi.org/10.1007/s10973-019-09093-9

Maurizi Enrici, T., Saggionetto, E., Dedry, O., Ertugrul, O., Boschini, F., Tchuindjang, J. T., & Mertens, A. (n.d.). "Fabrication and metallurgy of high-silicon austenitic stainless steel produced by Laser Cladding."

Meena, R. P., N, Y., & Vipin. (2024). "A review on wire arc additive manufacturing based on cold metal transfer." Materials and Manufacturing Processes, 00(00), 1–27. https://doi.org/10.1080/10426914.2024.2323441

Mertens, R., Dadbakhsh, S., Van Humbeeck, J., & Kruth, J. P. (2018). "Application of base plate preheating during selective laser melting." Procedia CIRP, 74(March), 5–11. https://doi.org/10.1016/j.procir.2018.08.002

"Metal AM magazine." (2019). Vol. 5 No. 2, 143–149. Retrieved from www.metal-am.com

Mirzababaei, S., & Pasebani, S. (2019). "A review on binder jet additive manufacturing of 316L stainless steel." Journal of Manufacturing and Materials Processing, 3(3), 8–12. https://doi.org/10.3390/jmmp3030082

Mussatto, A., Groarke, R., A-Hameed, A., Ahad, I. U. I., Vijayaraghavan, R. K., O'Neill, A., … Brabazon, D. (2019). "Evaluation via powder metallurgy of nano-reinforced iron powders developed for selective laser melting applications." Materials and Design, 182, 108046. https://doi.org/10.1016/j.matdes.2019.108046

Neveu, A., Francqui, F., & Lumay, G. (2022). "How to Relate the Spreadability of Powder to the Layer Homogeneity in Powder Bed Fusion Additive Manufacturing: A Correlation between Cohesion Assessments and In Situ Printer Measurements." Progress in Additive Manufacturing 2020, 40–50. https://doi.org/10.1520/stp163720200118

Ng, K. L., Sasaki, H., Kimura, H., Yoshikawa, T., & Maeda, M. (2018). "Heterogeneous nucleation of graphite on rare earth compounds during solidification of cast iron." ISIJ International, 58(1), 123–131. https://doi.org/10.2355/isijinternational.ISIJINT-2017-398

Ogata, P. H., Guesser, W. L., & Goldenstein, H. (2022). "Secondary graphitization kinetics in a gray cast iron." Tecnologia Em Metalurgia, Materiais e Mineração, 19, e2643. https://doi.org/10.4322/2176-1523.20222643

Oloyede, O., Bigg, T. D., Cochrane, R. F., & Mullis, A. M. (2016). "Microstructure evolution and mechanical properties of drop-tube processed, rapidly solidified grey cast iron." Materials Science and Engineering: A, 654, 143–150. https://doi.org/10.1016/j.msea.2015.12.020

Ozdemir, I., Tsunekawa, Y., Okumiya, M., & Ueno, T. (2006). "Graphitization potential of cast iron powder in atmospheric plasma spray conditions." Materials Transactions, 47(7), 1710–1716. https://doi.org/10.2320/matertrans.47.1710

Pannitz, O., Großwendt, F., Lüddecke, A., Kwade, A., Röttger, A., & Sehrt, J. T. (2021). "Improved process efficiency in laser-based powder bed fusion of nanoparticle coated maraging tool steel powder." Materials, 14(13), 1–22. https://doi.org/10.3390/ma14133465

Pero-Sanz Elorz, J. A., González, D. F., & Verdeja, L. F. (2018). Physical Metallurgy of Cast Irons. Physical Metallurgy of Cast Irons. https://doi.org/10.1007/978-3-319-97313-5

Popescu, M., Zavadil, R., & Sahoo, M. (2009). "SiC - The most efficient addition to increase the nodule count in ductile iron." International Journal of Metalcasting, 3(1), 53–63. https://doi.org/10.1007/BF03355441

Qin, S., Saewe, J., Kunz, J., Herzog, S., Kaletsch, A., Schleifenbaum, J. H., & Broeckmann, C. (2023). "Influence of Preheating Temperature on Microstructure Evolution and Hardness of High-Speed Steel AISI M50 Processed by Laser Powder Bed Fusion." Steel Research International, 94(6). https://doi.org/10.1002/srin.202200784

Raffeis, I., Adjei-Kyeremeh, F., Ewald, S., Schleifenbaum, J. H., & Bührig-Polaczek, A. (2022). "A Combination of Alloy Modification and Heat Treatment Strategies toward Enhancing the Properties of LPBF Processed Hot Working Tool Steels (HWTS)." Journal of Manufacturing and Materials Processing, 6(3). https://doi.org/10.3390/jmmp6030063

Riener, K., Albrecht, N., Ziegelmeier, S., Ramakrishnan, R., Haferkamp, L., Spierings, A. B., & Leichtfried, G. J. (2020). "Influence of particle size distribution and morphology on the properties of the powder feedstock as well as of AlSi10Mg parts produced by laser powder bed fusion (LPBF)." Additive Manufacturing, 34(May), 101286. https://doi.org/10.1016/j.addma.2020.101286

Riquelme, A., Sánchez de Rojas Candela, C., Rodrigo, P., & Rams, J. (2022). "Influence of process parameters in additive manufacturing of highly reinforced 316L / SiCp composites." Journal of Materials Processing Technology, 299(July 2021). https://doi.org/10.1016/j.jmatprotec.2021.117325

Rodowski, Ł., Wr, R., Choma, T., Moro, B., Łacisz, W., Błyskun, P., & Wr, J. S. (2021). "Novel Cold Crucible Ultrasonic Atomization Powder Production Method for 3D Printing." Materials, 1–11.

Rounaghi, S. A., & Kiani-Rashid, A. R. (2011). "A study on graphitisation acceleration during annealing of martensitic hypereutectoid steel." Phase Transitions, 84(11–12), 981–991. https://doi.org/10.1080/01411594.2011.563153

Ryder, M. A., Montgomery, C. J., Brand, M. J., Carpenter, J. S., Jones, P. E., Spangenberger, A. G., & Lados, D. A. (2021). "Melt Pool and Heat Treatment Optimization for the Fabrication of High-Strength and High-Toughness Additively Manufactured 4340 Steel." Journal of Materials Engineering and Performance, 30(7), 5426–5440. https://doi.org/10.1007/s11665-021-05836-8

Saewe, J., Carstensen, N., Kürnsteiner, P., Jägle, E. A., & Schleifenbaum, J. H. (2021). "Influence of increased carbon content on the processability of high-speed steel HS6-5-3-8 by laser powder bed fusion." Additive Manufacturing, 46(May). https://doi.org/10.1016/j.addma.2021.102125

Saewe, J., Gayer, C., Vogelpoth, A., & Schleifenbaum, J. H. (2019). "Feasability Investigation for Laser Powder Bed Fusion of High-Speed Steel AISI M50 with Base Preheating System." BHM Berg- Und Hüttenmännische Monatshefte, 164(3), 101–107. https://doi.org/10.1007/s00501-019-0828-y

Saewe, J., Wilms, M. B., Jauer, L., & Schleifenbaum, J. H. (2019). "Influence of Preheating Temperature on Hardness and Microstructure of High-Speed Steel Hs6-5-3-8." Metal Additive Manufacturing Conference (MAMC), (November), 11–19.

Saggionetto, E., Bio Seidou, A. H., Caubergh, S., Boschini, F., Dedry, O., Tchuindjang, J. T., & Mertens, A. (n.d.). "Preparation of powder feedstock and processability of a low alloy tool steel modified by SiC for Laser Powder Bed Fusion."

Saggionetto, E., Maurizi Enrici, T., Dedry, O., Boschini, F., Tchuindjang, J. T., & Mertens, A. (2025). "On the role of the hierarchical structures in the friction- induced phenomena of directed energy deposited 316L+WC sliding against different counter-bodies.", Tribology International, 10.1016/j.triboint.2025.110973

Salvaro, D., Neves, G. O., Binder, C., Klein, A. N., & Biasoli de Mello, J. D. (2023). "Influence of SiC polytypes on the mixed lubrication regime of self-lubricating composites containing in situ generated 2D turbostratic graphite." Tribology International, 184(January). https://doi.org/10.1016/j.triboint.2023.108446

Skaland, T., Grong, O., & Grong, T. (1993). "A Model for the Graphite Formation in Ductile Cast Iron : Part I . Inoculation Mechanisms." Metallurgical Transactions A, 24A(OCTOBER), 2321–2345.

Song, B., Dong, S., Coddet, P., Zhou, G., Ouyang, S., Liao, H., & Coddet, C. (2013). "Microstructure and tensile behavior of hybrid nano-micro SiC reinforced iron matrix composites produced by selective laser melting." Journal of Alloys and Compounds, 579, 415–421. https://doi.org/10.1016/j.jallcom.2013.06.087

Stefanescu, D. M. (2018). "A History of Cast Iron." Cast Iron Science and Technology, (October), 3–11. https://doi.org/10.31399/asm.hb.v01a.a0006320

Stefanescu, D. M., Alonso, G., Larrañaga, P., & Suarez, R. (2016). "On the stable eutectic solidification of iron-carbon-silicon alloys." Acta Materialia, 103, 103–114. https://doi.org/10.1016/j.actamat.2015.09.043

Strauch, A. L., Uhlenwinkel, V., Steinbacher, M., Großwendt, F., Röttger, A., Chehreh, A. B., … Fechte-Heinen, R. (2021). "Comparison of the processability and influence on the microstructure of different starting powder blends for laser powder bed fusion of a fe3.5 si1.5 c alloy." Metals, 11(7). https://doi.org/10.3390/met11071107

Sun, S., Brandt, M., & Easton, M. (2017). Powder bed fusion processes: An overview. Laser Additive Manufacturing: Materials, Design, Technologies, and Applications. Elsevier Ltd. https://doi.org/10.1016/B978-0-08-100433-3.00002-6

Taha, M. A., Yousef, A. F., Gany, K. A., & Sabour, H. A. (2012). "On selective laser melting of ultra high carbon steel: Effect of scan speed and post heat treatment." Materialwissenschaft Und Werkstofftechnik, 43(11), 913–923. https://doi.org/10.1002/mawe.201200030

Tan, C., Ma, W., Deng, C., Zhang, D., & Zhou, K. (2023). "Additive manufacturing SiC-reinforced maraging steel: Parameter optimisation, microstructure and properties." Advanced Powder Materials, 2(1), 100076. https://doi.org/10.1016/j.apmate.2022.100076

Tan, C., Zou, J., Wang, D., Ma, W., & Zhou, K. (2022). "Duplex strengthening via SiC addition and in-situ precipitation in additively manufactured composite materials." Composites Part B: Engineering, 236(February), 109820. https://doi.org/10.1016/j.compositesb.2022.109820

Tchuindjang, J. T., Sinnaeve, M., & Lecomte-Beckers, J. (2011). "Influence of High Temperature Heat Treatment on in situ Transformation of Mo-rich Eutectic Carbides in HSS and Semi-HSS Grades." Abrasion 2011, (August 2011), 61–75.

Tewary, U., Paul, D., Mehtani, H. K., Bhagavath, S., Alankar, A., Mohapatra, G., … Samajdar, I. (2022). "The origin of graphite morphology in cast iron." Acta Materialia, 226, 117660.

https://doi.org/10.1016/j.actamat.2022.117660

Thawari, G., Sundararajan, G., & Joshi, S. V. (2003). "Laser surface alloying of medium carbon steel with SiC(P)." Thin Solid Films, 423(1), 41–53. https://doi.org/10.1016/S0040-6090(02)00974-4

Theuwissen, K., Lacaze, J., & Laffont, L. (2016). "Structure of graphite precipitates in cast iron." Carbon, 96, 1120–1128. https://doi.org/10.1016/j.carbon.2015.10.066

Tian, Z., Zhang, C., Wang, D., Liu, W., & Fang, X. (2020). "A Review on Laser Powder Bed Fusion of Inconel 625." Applied Scien.

Tobah, M., Zhang, Z., Andani, M. T., Sundararaghavan, V., & Misra, A. (2024). "Processing-microstructure relationships in ferrous alloys via mixed powder laser powder bed fusion." Journal of Materials Research and Technology. https://doi.org/10.1016/j.jmrt.2024.04.115

Torres, H., Panaitescu, I., Gangl, R., Hubmann, R., Scheerer, M., & Rodríguez Ripoll, M. (2023). "Laser metal deposition of self-lubricating alloys on selective laser melting maraging tools for the high temperature forming of aluminium." Wear, 524–525(March), 204883. https://doi.org/10.1016/j.wear.2023.204883

Velu, R., Kumar, A. V., Balan, A. S. S., & Mazumder, J. (2021). Laser aided metal additive manufacturing and postprocessing: A comprehensive review. Additive Manufacturing. Elsevier Inc. https://doi.org/10.1016/B978-0-12-818411-0.00023-9

Villanueva Bravo, S., Yamamoto, K., Miyahara, H., & Ogi, K. (2012). "Control of Carbides and Graphite in Cast Irons Type Alloy's Microstructures for Hot Strip Mills." Journal of Metallurgy, 2012(March 2012), 1–6. https://doi.org/10.1155/2012/438659

Vock, S., Klöden, B., Kirchner, A., Weißgärber, T., & Kieback, B. (2019). "Powders for powder bed fusion: a review." Progress in Additive Manufacturing, 4(4), 383–397. https://doi.org/10.1007/s40964-019-00078-6

Vogiatzief, D., Evirgen, A., Gein, S., Molina, V. R., Weisheit, A., & Pedersen, M. (2020). "Laser Powder Bed Fusion and Heat Treatment of an AlCrFe2Ni2 High Entropy Alloy." Frontiers in Materials, 7(July), 1–12. https://doi.org/10.3389/fmats.2020.00248

Wang, D., Huang, J., Tan, C., Ma, W., Zou, Y., & Yang, Y. (2022). "Mechanical and corrosion properties of additively manufactured SiC-reinforced stainless steel." Materials Science and Engineering: A, 841(January), 143018. https://doi.org/10.1016/j.msea.2022.143018

Wang, W., & Kelly, S. (2016). "A Metallurgical Evaluation of the Powder-Bed Laser Additive Manufactured 4140 Steel Material." Jom, 68(3), 869–875. https://doi.org/10.1007/s11837-015-1804-y

Wang, X. song, & Zhang, W. zheng. (2017). "Oxidation and Thermal Cracking Behavior of Compacted Graphite Iron under High Temperature and Thermal Shock." Oxidation of Metals, 87(1–2), 179–188. https://doi.org/10.1007/s11085-016-9664-6

Xing, Y., Luo, C., Zhu, M., Zhao, Y., Ehmann, K., Wu, Z., & Liu, L. (2023). "Assessment of self-lubricating coated cutting tools fabricated by laser additive manufacturing technology for friction-reduction." Journal of Materials Processing Technology, 318(April). https://doi.org/10.1016/j.jmatprotec.2023.118010

Xue, W., & Li, Y. (2016). "Pretreatments of gray cast iron with different inoculants." Journal of Alloys and Compounds, 689, 408–415. https://doi.org/10.1016/j.jallcom.2016.07.052

Yamamoto, K., Kubota, T., Murai, N., & Ogi, N. (1998). "Solidification Process and Crystallization of Graphite in High Carbon High Speed Steel Type Alloy." Journal of Japan Foundry Engineering Society, 70(11), 786–792. https://doi.org/10.11279/jfes.70.786

Yang, M., Dai, Y., Song, C., & Zhai, Q. (2010). "Microstructure evolution of grey cast iron powder by high pressure gas atomization." Journal of Materials Processing Technology, 210(2), 351–355. https://doi.org/10.1016/j.jmatprotec.2009.09.023

Yang, Y., Zhu, Y., Khonsari, M. M., & Yang, H. (2019). "Wear anisotropy of selective laser melted 316L stainless steel." Wear, 428–429(March), 376–386. https://doi.org/10.1016/j.wear.2019.04.001

Zhai, W., Bai, L., Zhou, R., Fan, X., Kang, G., Liu, Y., & Zhou, K. (2021). "Recent Progress on Wear-Resistant Materials: Designs, Properties, and Applications." Advanced Science, 8(11), 1–29. https://doi.org/10.1002/advs.202003739

Zhang, Y., Chen, R., Wang, Q., Chen, C., Li, Z., & Song, Q. (2024). "Examining the role of rare earth elements on grey iron's microstructural and mechanical properties." International Journal of Cast Metals Research, 37(2), 117–124. https://doi.org/10.1080/13640461.2024.2313409

Ziri, S., Hor, A., & Mabru, C. (2022). "Combined effect of powder properties and process parameters on the density of 316L stainless steel obtained by laser powder bed fusion." International Journal of Advanced Manufacturing Technology, 120(9–10), 6187–6204. https://doi.org/10.1007/s00170-022-09160-w

Zou, Y., Tan, C., Qiu, Z., Ma, W., Kuang, M., & Zeng, D. (2021). "Additively manufactured SiC-reinforced stainless steel with excellent strength and wear resistance." Additive Manufacturing, 41(November 2020), 101971. https://doi.org/10.1016/j.addma.2021.101971

Zumofen, L., Beck, C., & Kirchheim, A. (2018). "Quality Related Effects of the Preheating Temperature on Laser Melted High Carbon Content Steels." Industrializing Additive Manufacturing - Proceedings of Additive Manufacturing in Products and Applications - AMPA2017. https://doi.org/10.1007/978-3-319-66866-6

Chapter 3

Powders for LPBF: selection, chemical affinity, preparation and characterization

Contents

3.1 Introduction 58
3.2 Selection of powder feedstock 59
3.3 Chemical affinity of raw materials 62
3.3.1 Dissolution of SiC during DTA heating stage 64
3.3.2 Graphite, carbides and matrix crystallization from liquid state 67
3.3.3 Solid-state transformations of the matrix phase 71
3.3.4 Main findings from DTA tests 73
3.4 Preparation of powder mixtures 75
3.5 Characterization of powder mixtures 80
3.5.1 Rheological properties 80
3.5.2 Absorbance 84
3.6 Conclusions 86
3.7 References 87

3.1 Introduction

This chapter aims to discuss the criteria for the powder selection, introducing a method to test the chemical affinity between different powders under close-to-equilibrium conditions. Indeed, in order to avoid energy and material consuming tests directly performed with a LPBF device, chemical affinity of powders can be tested through a common DTA device, as explained in section 2.3.2. Finally, different mixing methods are discussed, and the best one is selected, leading to mixtures with properties suitable for the LPBF process. Rheological properties such as spreadability and packability are analysed. Powders absorptivity properties are also reported here and later used in chapter 4 to discuss their impact on the processability by LPBF. Therefore, this chapter highlights the importance of understanding powder properties for LPBF, and the need to include it as part of the development of new alloys.

3.2 Selection of powder feedstock

The main criteria considered for the selection of the powder feedstock were the chemical composition and the commercial availability of powders suitable for LPBF. As mentioned earlier, the approach for the development of the alloy considered in this work aimed to avoid the high cost and long delivery time for customized gas atomized powders. Therefore, two commercially available powders were selected to achieve the desired chemical composition, by mixing them together with simple laboratory devices, thus decreasing costs and waiting times.

The chemical composition was designed with the aim of obtaining graphite within the final microstructure. As reported in section 2.2, graphitization is possible under certain conditions, regarding both the influence of the alloying elements and the cooling rates of the process. Carbon and silicon are known as graphitizing elements under an environment free of carbide-forming elements, such as vanadium, titanium, chromium, molybdenum, tungsten etc. Therefore, the latter elements were discarded, whereas carbon and silicon were given high importance. Among the existing classes of metal alloys, the tool steel class was selected in view of the presence of carbon among the alloying elements and of their intrinsic high mechanical and wear resistance properties.

AISI S2 tool steel was selected as main powder, in view of its medium content of carbon, its high content of silicon, the presence of only molybdenum as carbide-forming element (*Fig. 3.1*a) and overall, as the only commercially available[7] powder for LPBF with a desired composition. The powder was purchased from Sandvik Osprey. *Fig. 3.1*b,c,d shows a SEM micrograph of the powders and their Particle Size Distribution (PSD). Such spherical morphology and PSD are optimal for the processability by LPBF.

[7] Research and purchase of powders in November 2020.

(a)

wt %

Fe	C	Si	Mo	Mn
Bal.	0.49	1.2	0.6	0.6

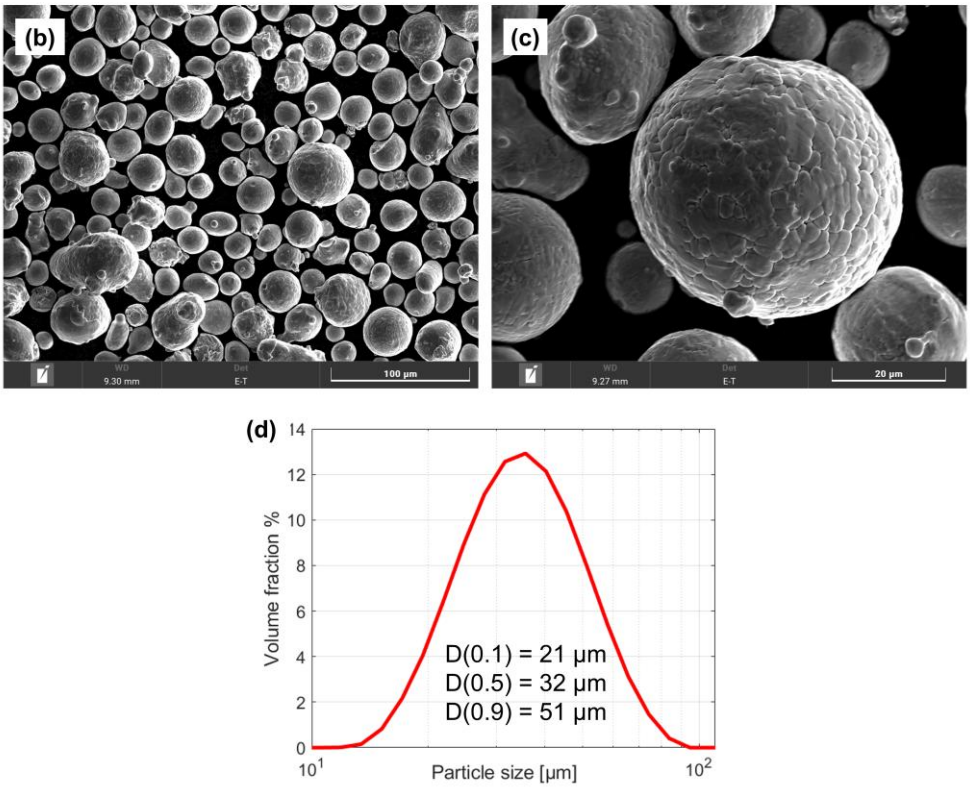


Fig. 3.1: (a) Chemical composition, (b,c) morphology and (d) Particle Size Distribution of as-received AISI S2 powder.

In order to enhance the graphitization behaviour of the alloy, silicon carbide (α-SiC) was selected as the second powder as source of carbon and silicon. As explained further in section 3.5 and as already mentioned in section 2.3.2, powders for LPBF requires certain rheological properties to ensure correct processability. Furthermore, complete dissolution of SiC is desired during the LPBF process. Therefore, SiC nanoparticles were chosen and purchased from Kyocera Fineceramics Precisions GmbH (StarCeram® S grade UF-15). *Fig. 3.2* shows the as-received SiC powders and their physical properties. In the as-received state, such nanoparticles (*Fig. 3.2*d) were agglomerated in form of granules by spray drying, giving a final spherical shape (*Fig. 3.2*b,c). Indeed, granulometry analysis revealed the presence of two main populations of particles within the PSD (*Fig. 3.2*e). The first one with D'(0.5) of 180 nm corresponds to the nanoparticles, whereas the second population with D''(0.5) of 45 µm corresponds to the granules. These characteristics allow to have a morphology suitable for the rheological properties required for the LPBF process. Moreover, such granules are a source of

nanoparticles which are easier to dissolve compared to bigger particles, and an improvement of the flowability of the powder mixtures is expected.

(a)

wt %

Si	C	O	Fe	Al	Ca
Bal.	29.2	0.8	0.02	0.01	0.004

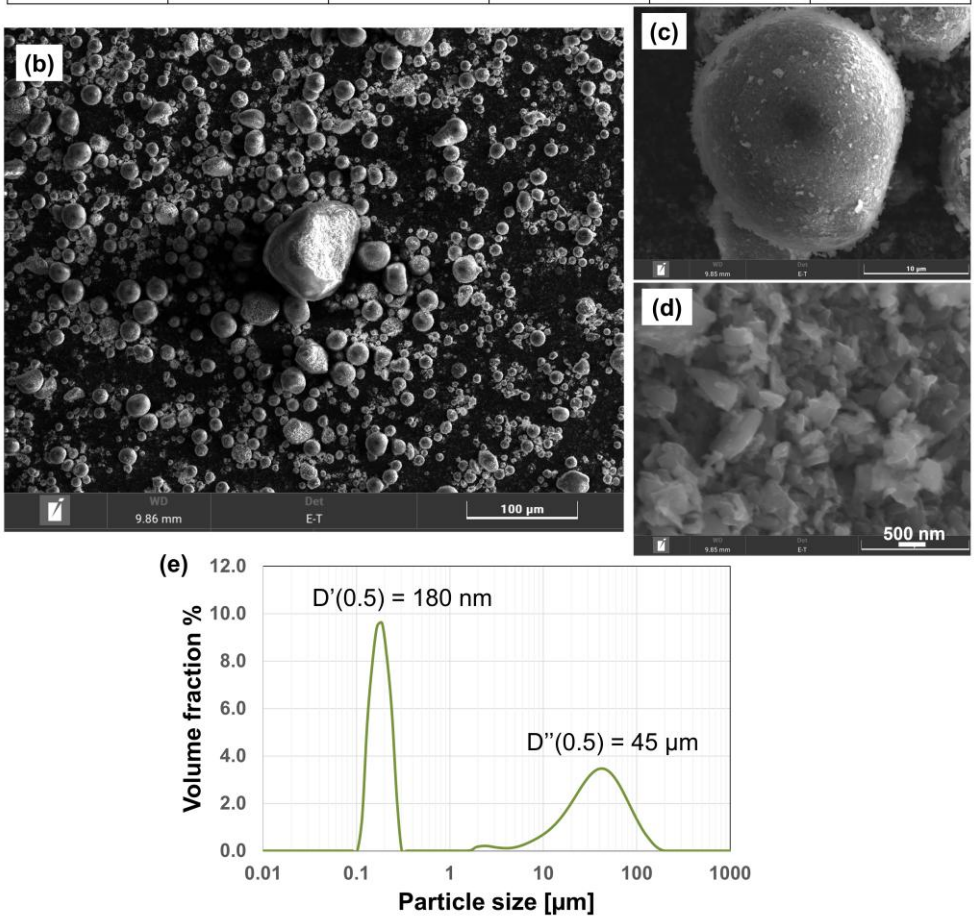


Fig. 3.2: (a) Chemical composition, (b,c) overview of SiC powder at the granule scale, (d) SiC powder at the nanoparticle scale and (e) PSD of as-received SiC powder.

3.3 Chemical affinity of raw materials

Prior to the mixing preparation and the processability by LPBF, the chemical affinity between AISI S2 and SiC powders was investigated through DTA. First, this section will discuss the results obtained with DTA heating stage, focusing on the dissolution of SiC. Subsequently, the crystallization of the microstructure obtained under cooling will be discussed, correlating the phases observed and the peaks present within the DTA curve.

Reference DTA tests were performed on the powder mixtures S2, S2 + 5, 10, 15, 20% (in volume) SiC, obtained by simply mixing the two powders to achieve a total mass of 850 mg in order to fill the Al_2O_3 crucible of the DTA device. The final chemical composition of each mixture is displayed in *Table 3.1*. For all DTA tests, a heating rate of 5 °C/min (0.08 °C/s) up to 1550 °C was used. The subsequent cooling was performed with two cooling rates of 5 and 20 °C/min (0.08 and 0.3 °C/s). In this section, only results obtained at 5 °C/min will be shown, as minor differences between the two cooling rates only concerned the quantity and size of the phases within the final microstructures (*Bio Seidou, 2022*). Two additional DTA tests were performed on S2 up to 1200 °C and on S2 + 20% SiC up to 1120 °C. *Table 3.2* lists all the DTA tests that were performed. A general overview of the reference DTA heating and cooling curves is visible in *Fig. 3.3*. As explained in more details in section 3.3.1, DTA heating curves were useful to investigate the dissolution of SiC during heating. Therefore, all the transformations that occurred and the corresponding peaks will not be reported here. Additionally, a comprehensive discussion is available in (*Bio Seidou, 2022*). Each peak of the DTA cooling curves will be discussed in section 3.3.2 and 3.3.3, as they are useful to characterize the microstructures obtained at the end of the DTA tests.

	wt. %				
	Fe	**C**	**Si**	**Mo**	**Mn**
S2	97.11	0.49	1.20	0.60	0.60
S2 + 5% SiC	96.16	1.08	1.58	0.59	0.59
S2 + 10% SiC	92.89	1.77	4.19	0.57	0.58
S2 + 15% SiC	90.69	2.44	5.75	0.56	0.56
S2 + 20% SiC	88.26	3.17	7.47	0.55	0.55

Table 3.1: Theoretical chemical composition of the different powder mixtures.

Powders	Heating rate [°C/min]	Target Temperature [°C]	Cooling rate [°C/min]
S2, S2 + 5, 10, 15, 20% SiC	5	1550	5
S2	5	1200	5
S2 + 20% SiC	5	1120	5

Table 3.2: Parameters of the DTA tests performed.

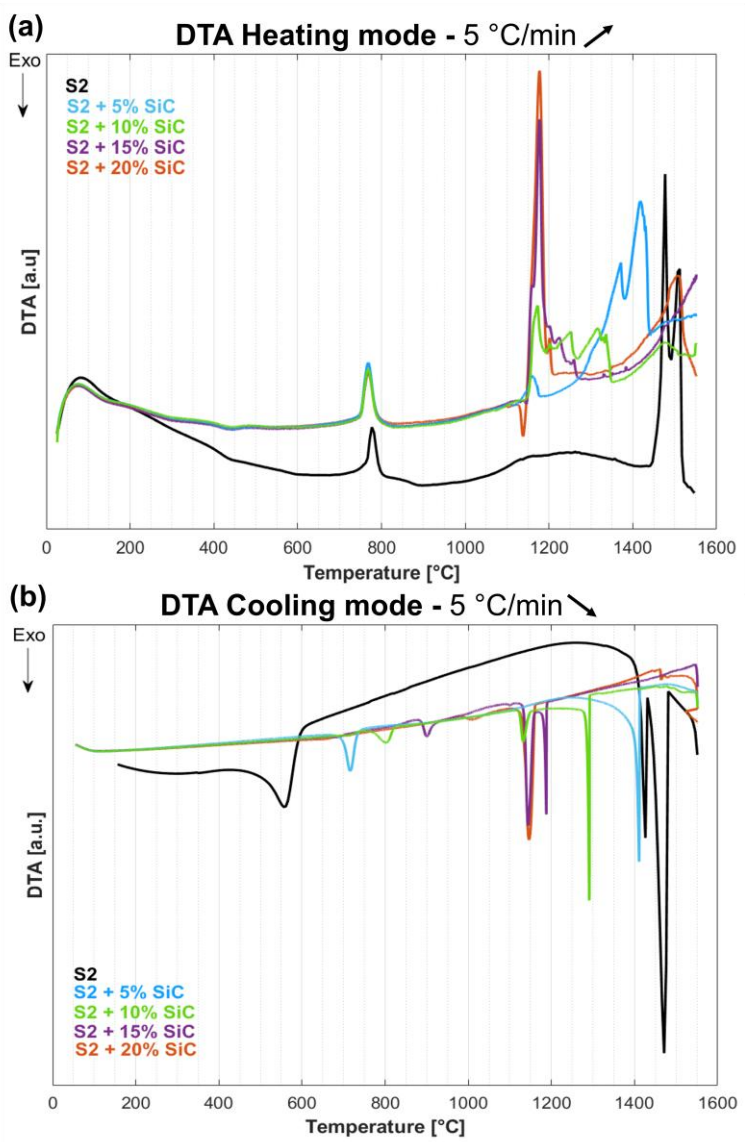


Fig. 3.3: (a) DTA Heating and (b) Cooling curves of each powder mixtures.

3.3.1 Dissolution of SiC during DTA heating stage

SiC has a melting point of 2700°C, much higher than the temperature reached during the DTA test (1550 °C). Therefore, one might expect to find un-melted SiC after the DTA test. However, in this work, SiC powder was selected to provide a source of silicon and carbon from the dissolution of the powder elements during the LPBF process, with the purpose of achieving an iron-based melt pool from the melting of S2 powders enriched with carbon and silicon. In equilibrium conditions, strong reactivity has already been proved between Fe and SiC and no wetting problem arises in the Fe – SiC system. Indeed, SiC has a high solubility in Fe rich melts (*Kalogeropoulou, 1995*). However, the heating rates reached during the LPBF, in the order of 10^3-10^4 °C/s, result in out-of-equilibrium conditions leading to the possibility of not melting SiC powders or of dissolving them only partially. Therefore, as preliminary investigations prior to the real LPBF process, close-to-equilibrium conditions reached through a DTA device were chosen to test the chemical affinity and the dissolution of SiC.

As explained in the next sections, no undissolved SiC particles were found within the solidified microstructure after DTA for all mixtures, as desired. Therefore, the solidification started from a liquid enriched by all the elements of the two powders. Before arriving to the liquid state, interfacial reactions between S2 and SiC powders occurred during heating, allowing the complete dissolution of SiC. A specific DTA was carried out to investigate such dissolution reactions. Specifically, the mixture S2 + 20% SiC was considered for this investigation and a DTA test was performed until a temperature of 1120 °C (marked with 'X' on the red curve in *Fig. 3.4*). This temperature was set based on the curves of the reference DTA on S2 + 20% SiC up to 1550 °C. Moreover, within the range 1000 – 1400 °C of the DTA heating curve of S2 powders (*Fig. 3.3*a and *Fig. 3.4*) a sintering occurs. Such sintering was investigated through another specific DTA performed on S2 up to 1200 °C (marked with 'X' on the black curve in *Fig. 3.4*). The result was the formation of necks between S2 particles (*Fig. 3.5*a). With the addition of SiC, the sintering was affected by the presence of SiC particles, as visible within the DTA heating curve of S2 + 20% SiC (*Fig. 3.4*) where complex peaks occurred from 1150 °C. It can be assumed that these peaks are due to interfacial reactions between S2 and SiC. Such peaks are present within all curves of the different powder mixtures (S2 + 5, 10, 15, 20% SiC).

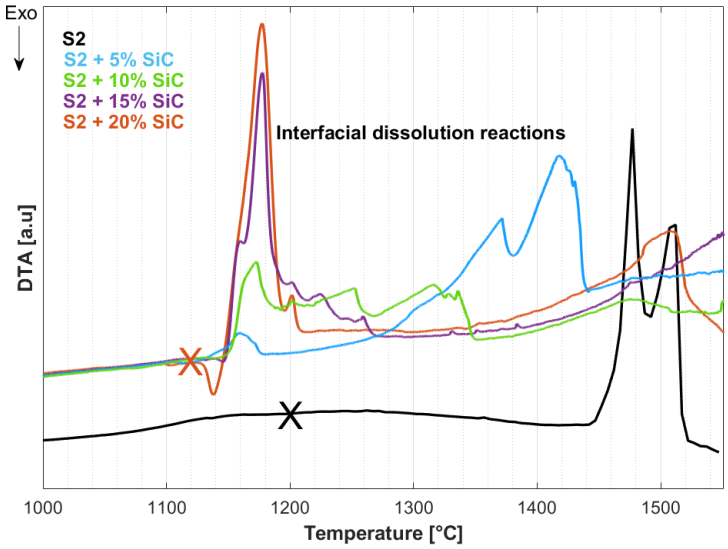


Fig. 3.4: DTA Heating curves within the range 1000 – 1550 °C of each powder mixture. The mark 'X' highlights the temperature of the specific DTA test performed on S2 (1200 °C) and S2 + 20% SiC (1120 °C) powders.

Based on micrographs of the microstructure obtained after the DTA on S2 + 20% SiC up to 1120 °C (Fig. 3.5b,c), the outer part of S2 particles is the first area to be affected by the dissolution reaction of SiC. It can be assumed that at 1120 °C, partial sintering occurred together with partial dissolution of SiC. One mechanism responsible for sintering phenomena is diffusion, which is responsible for the movement of atoms (*Kang, 2005*). Thus, the dissolution of SiC leads to the diffusion of silicon and carbon atoms from SiC, modifying the chemical composition of the outer part of S2 particles in proximity. In particular, the enrichment in silicon stabilizes the solidification of α-Fe with BCC crystal lattice during the subsequent DTA cooling step, as revealed by the phase map obtained through EBSD analysis (*Fig. 3.5*d). Thus, carbon cannot dissolve into the parent ferritic matrix, due to the very low solubility of carbon within the α-Fe (< 0.02 wt.%). Therefore, the crystallization of graphite occurs (*Araya, 2020*). Indeed, *Fig. 3.5* shows graphite lamellae that grow starting from SiC particles through S2. Despite α-Fe and graphite are formed during the DTA cooling step from 1120 °C, their appearance is due to preliminary interface dissolution reactions between S2 and SiC during the DTA heating mode, highlighting the chemical affinity between the two powders. Assuming the continuation of the in-situ reaction between S2 and SiC, it can be stated that at 1550°C (end of the DTA heating step) all SiC particles are dissolved, and a liquid enriched in silicon and carbon is formed.

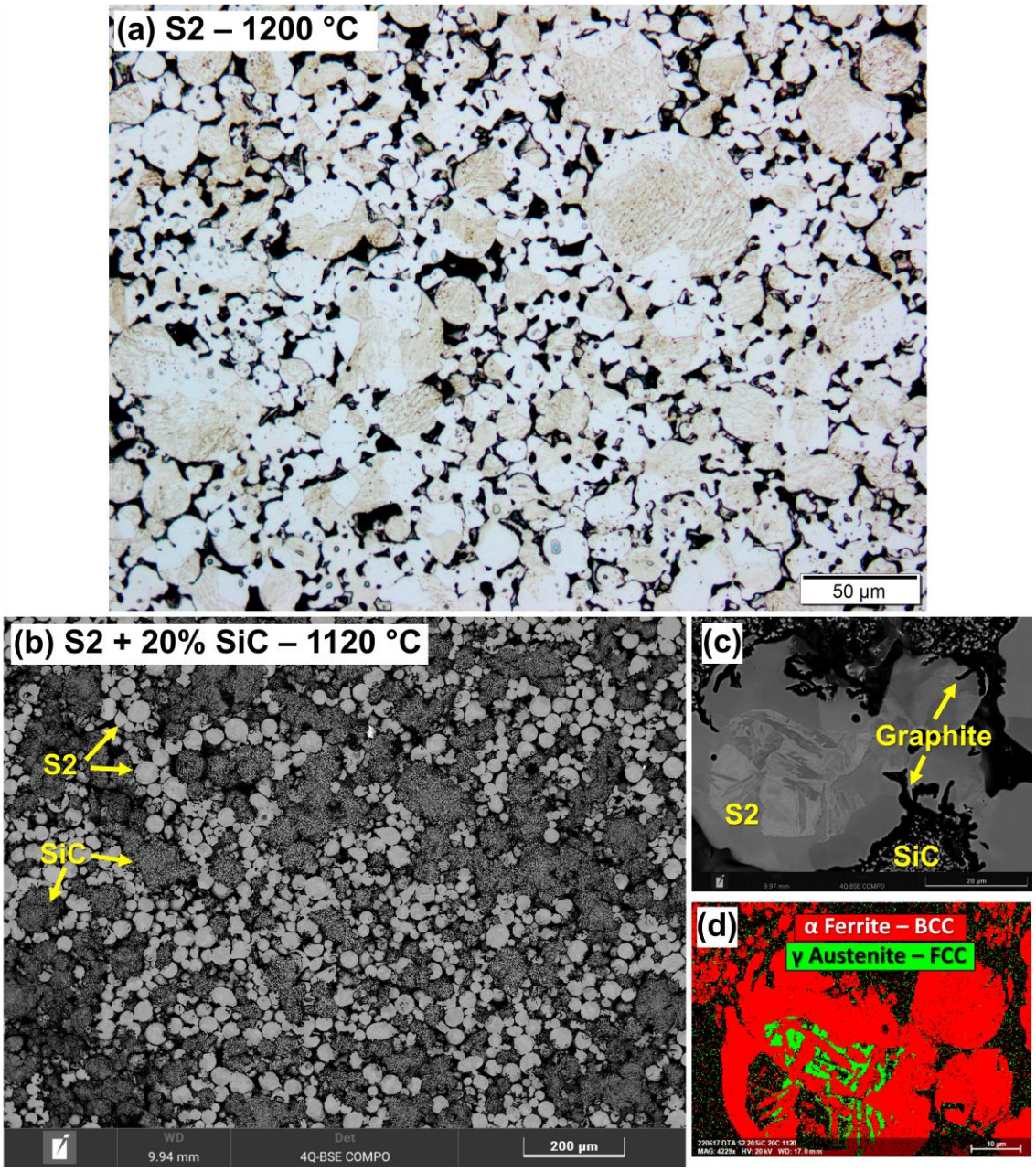


Fig. 3.5: (a) SEM micrographs of S2 powders after DTA performed up to 1200 °C, (b) S2 + 20% SiC after DTA performed up to 1120 °C. (c) Magnification on the interface between S2 and SiC and (d) correspondent phase map obtained through EBSD analysis after DTA performed up to 1120 °C on S2 + 20% SiC.

3.3.2 Graphite, carbides and matrix crystallization from liquid state

When the melting of S2 and the complete dissolution of SiC is reached at the end of the DTA heating at 1550°C, the cooling down to room temperature begins. The low cooling rates of DTA (5 °C/min) allow the time necessary for the primary phases to nucleate and grow from the liquid state in a close-to-equilibrium state. Changing the starting amount of SiC, the primary phase to nucleate from the liquid is different, as well as the liquidus temperature. For all compositions, the first phase to form is γ-Fe with an FCC crystal lattice (Austenite) (peaks 5.1, 10.1 and 15.1 in figure 3.7 and table 3.3), except for S2 + 20% SiC where α-Fe with a BCC crystal lattice (Ferrite) is formed (peak 20.1 in *Fig. 3.7* and *Table 3.3*). Indeed, according to Thermocalc calculation (*Fig. 3.6*) and as shown in (*Lacaze, 1991*), when the amount of silicon is above 6.5 wt.% (7.47 wt.% for the mixture S2 + 20% SiC, *Table 3.1*) the first phase is α-Ferrite, in view of the ferrite-stabilizing effect of Si. For S2 + 15% SiC, α Ferrite also forms (peak 15.2) together with the formation of γ-Austenite (peak 15.1), as also shown by Thermocalc (*Fig. 3.6*).

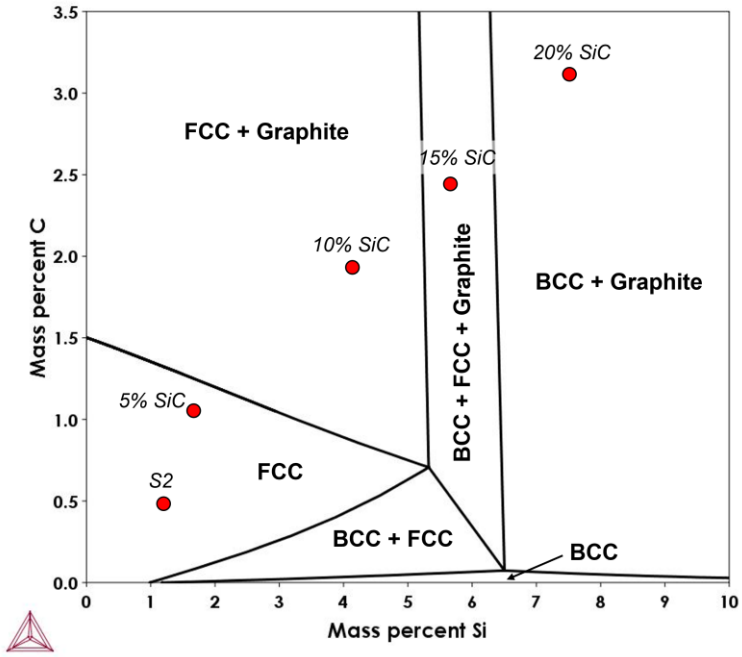


Fig. 3.6: Isothermal section at 1000 °C of the stable Fe-C-Si system obtained with Thermocalc®.

Together with iron FCC or BCC, graphite is found as primary phase to form from the liquid for the mixtures S2 + 10, 15, 20% SiC (peaks 10.1, 15.1 and 20.1 in figure 3.7 and table 3.3). The designation of graphite related to its morphology according to ISO 945-1 is shown in *Fig. 3.8*, with variations based on the amount of SiC. The different types of graphite are the result of the

different solidification phenomena that occurred depending on the initial composition of the mixture (*Table 3.1*). For S2 + 20% SiC, the high silicon content leads to the nucleation of primary α-Fe dendrites as matrix phase that lowers the solubility of carbon in the matrix, thus making it available in high amount as free carbon and promoting the appearance of long flakes of graphite type C (*Fig. 3.8*d). On the contrary, the lower amount of silicon promotes the nucleation of γ-Fe dendrites as matrix phase for the mixture S2 + 10% and S2 + 15% SiC allowing a higher solubility of carbon in the matrix. The remaining carbon available forms eutectic graphite cells that grow together with the primary austenitic dendrites, forming graphite type D for S2 + 15% SiC (*Fig. 3.8*c). Meanwhile, with S2 + 10% SiC, the graphite type E is limited to the interdendritic regions (*Fig. 3.8*b), as lower carbon content is available. The cooperative nucleation and growth of the primary iron (FCC or BCC) and graphite (*Rivera, 2004*) is detected within the DTA cooling curves as the first unique exothermic peak (*Fig. 3.7*). There is no evidence of two distinct peaks referred to matrix and graphite, possibly due to the low exothermicity of the crystallization of graphite. The occurrence of this first peak, which can be referred as the liquidus point of the system, is shifted towards lower temperatures upon increasing the amount of SiC, as also shown in (*Janerka, 2020*). The microstructure obtained after DTA on S2 + 5% SiC does not reveal the presence of graphite. In this case, the DTA cooling curve reveals the presence of one exothermic peak at 1410 °C (peak 5.1), as result of the nucleation of primary austenitic dendrites. The lower carbon available (1.08 wt. %, Table 3.1) is limited to saturate the iron FCC matrix, thus avoiding the crystallization of graphite.

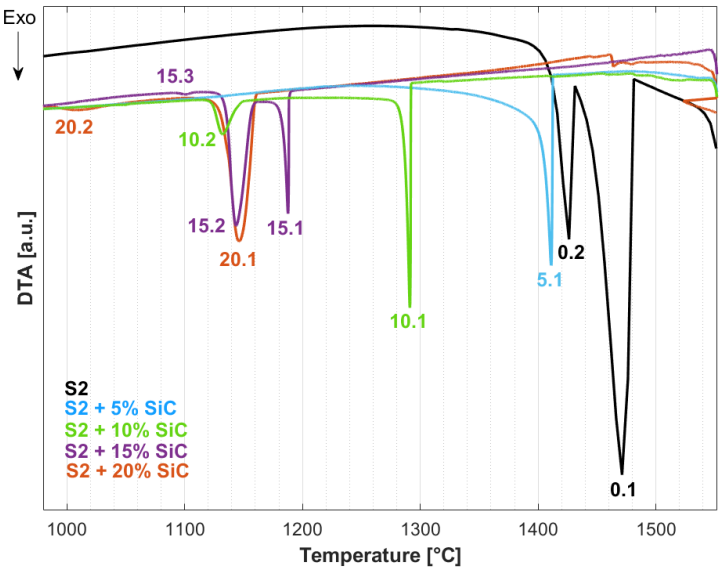


Fig. 3.7: DTA Cooling curve of each powder mixture within the range 1000 - 1550 °C.

Peak	Temperature [°C]	Reaction
0.1	1470	L⟶δ Ferrite (Liquidus)
0.2	1425	L+δ⟶γ Austenite (Solidus)
5.1	1410	L⟶γ Austenite
10.1	1290	L⟶γ_1 Austenite + Graphite (Liquidus)
10.2	1135	L⟶γ_2 Austenite + Mo-rich carbides (Solidus)
15.1	1190	L⟶γ_1 Austenite + Graphite (Liquidus)
15.2	1145	L⟶α Ferrite + Graphite
15.3	1100	L⟶γ_2 Austenite + Mo-rich carbides (Solidus)
20.1	1145	L⟶α_1 Ferrite + Graphite (Liquidus)
20.2	1010	L⟶α_2 Ferrite + Mo-rich carbides (Solidus)

Table 3.3: Relevant peaks temperatures and reactions detected on DTA cooling curves of each powder mixture within the temperature range 1000 – 1550 °C.

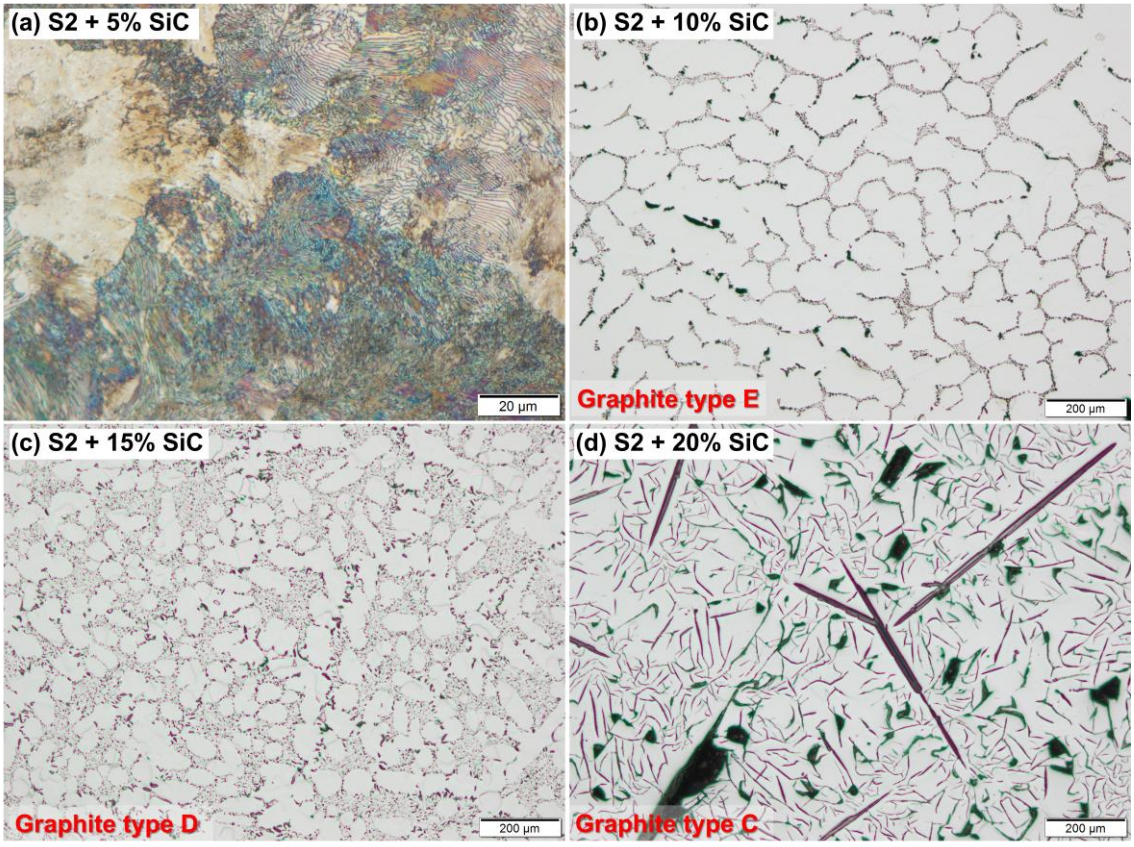
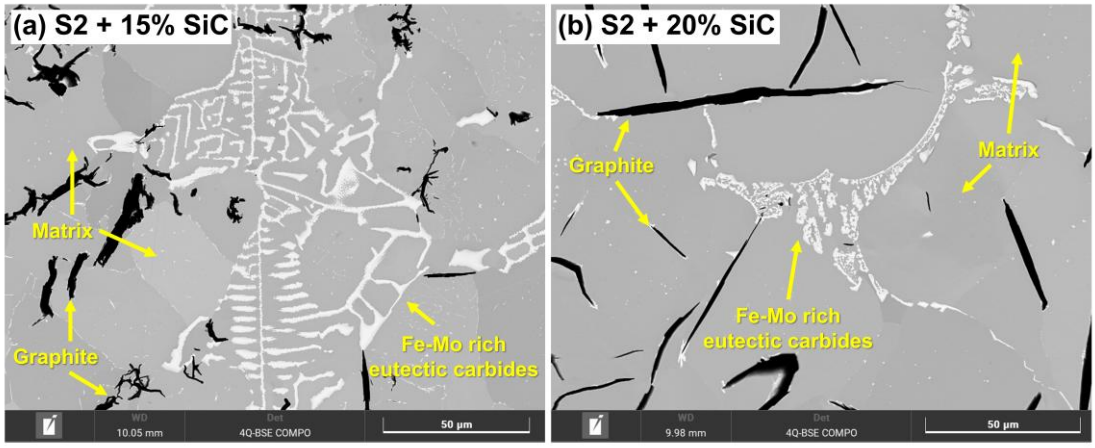


Fig. 3.8. Overview of the microstructure obtained after DTA cooling mode performed on each powder mixture (a) S2+5%SiC, (b) S2+10%SiC, (c) S2+15%SiC, (d) S2+20%SiC.

The second distinct peak within the DTA cooling curve of S2 + 10%, S2 + 15%, and S2 + 20% SiC is associated to a eutectic reaction which leads to the formation of Fe-Mo rich carbides (30 and 20 at.% of Fe and Mo respectively), based on their morphology, on the EDS analysis of *Fig. 3.9*c and in view of the carbide-forming properties of Fe and Mo (*Boccalini, 2001*). These carbides are formed with the remaining carbon available, while the greatest part of the carbon is crystallized in form of graphite and/or in solid solution in the austenitic or ferritic matrix, as shown by the high content of carbon (around 20 at.%) within the matrix (*Fig. 3.9*c). The morphology and fraction of the carbides is similar in all compositions (*Fig. 3.9*). Such eutectic reactions set the solidus point of each system, that is shifted towards lower temperatures with increasing SiC content, passing from 1135 °C for S2 + 10% SiC (peak 10.2) to 1010 °C for S2 + 20% SiC (peak 20.2).



(c) *Atomic %*

	Carbon	*Iron*	*Molybdenum*	*Silicon*	*Manganese*
Fe-Mo rich eutectic carbides *(S2+15%SiC)*	40 ± 2	31 ± 3	20 ± 1	8.9 ± 0.6	0.54 ± 0.1
Fe-Mo rich eutectic carbides *(S2+20%SiC)*	43 ± 2	28 ± 3	20 ± 2	8.8 ± 0.4	0.51 ± 0.1
Matrix *(S2+15%SiC)*	19 ± 2	72 ± 2	0.15 ± 0.1	8.3 ± 0.3	0.34 ± 0.1
Matrix *(S2+20%SiC)*	22 ± 1	67 ± 1	0.14 ± 0.1	11 ± 0.6	0.38 ± 0.1

Fig. 3.9: Fe-Mo rich eutectic carbides solidified after DTA cooling mode with (a) S2 + 15% SiC and (b) S2 + 20% SiC and (c) corresponding compositions of matrix and carbides.

Without SiC, the liquid formed from the melting of S2 powder experienced a different solidification sequence. Starting from high temperature, in the range 1500-1400 °C, the first reaction that occurs is the formation of δ ferrite (peak 0.1), followed by the peritectic reaction (peak 0.2), which leads to the formation of austenite (*Fig. 3.7*). Eutectic reaction does not occur, as a third peak is not present.

3.3.3 Solid-state transformations of the matrix phase

As the solid state was reached, the cooling went on and solid-state transformations occurred within the temperature range 500 – 900 °C (*Fig. 3.10* and *Table 3.4*). A eutectoid reaction occurred in S2 + 5% SiC at 715 °C (peak 5.2). Due to the carbon saturation of the austenitic matrix, the transformation into pearlite occurred, with the formation of lamellae of cementite (Fe_3C) and α-Fe (Ferrite BCC), as highlighted by chemical etching with Nital 3% (*Fig. 3.11*b). For the compositions S2 + 10% and S2 + 15% SiC the transformation from γ-Fe with FCC crystal lattice to α-Fe with BCC crystal lattice occurred, detected as an exothermic peak within the DTA cooling curves (peaks 10.3 and 15.4). For S2 + 10% SiC a subsequent peak is present (peak 10.4), enhanced within the derivative curve of the DTA (*Fig. 3.11*a). Such peak is associated to the formation of troostite in the vicinity of Fe-Mo rich carbides (*Fig. 3.11*c,d), as these areas may have been richer in carbon compared to the rest of the matrix. The troostite has been revealed and differentiated from pearlite by the different degree of density of the structure and by the carbon content that is higher in troostite compared to pearlite (*Bio Seidou, 2022*; *Howell, 1998*; *Tchuindjang, 2011*). The peaks of these solid-state transformations are shifted towards lower temperatures when decreasing the amount of SiC (Fig. 3.10). On the contrary, no solid-state transformations occurred for the matrix of S2 + 20% SiC, in view of the presence of α-Ferrite since the beginning of the solidification (*González-Martínez, 2018*). For S2 alone, the exothermic peak at 560 °C corresponds to the formation of a ferritic microstructure (peak 0.3).

For the compositions with 10, 15 and 20% SiC where a matrix of α-Fe with a BCC crystal lattice was achieved earlier, the shallow peaks at 715, 690, 660 °C respectively (peaks 10.5, 15.5, 20.3) correspond to the magnetic Curie transformation of α-Fe Ferrite from para- to ferro-magnetic, at a temperature that decreases with increasing SiC content (*González-Martínez, 2018*).

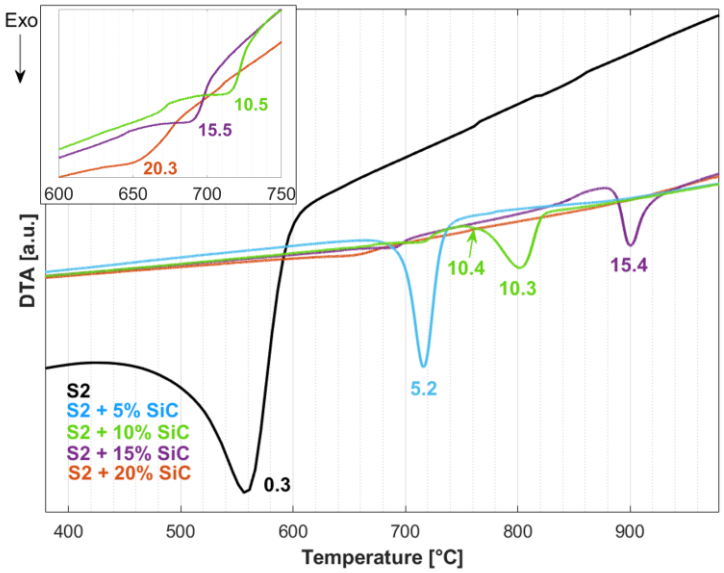


Fig. 3.10: DTA Cooling curve of each powder mixture within the range 400 - 1000 °C.

Peak	Temperature [°C]	Solid-State Transformation
0.3	555	γ Austenite → α Ferrite
5.2	715	γ Austenite → α Ferrite + Fe_3C Cementite (Pearlite)
10.3	800	γ_1 Austenite → α Ferrite
10.4	760	γ_2 Austenite → Troostite
10.5	715	Curie transformation
15.4	900	$\gamma_{1,2}$ Austenite → α Ferrite
15.5	690	Curie transformation
20.3	660	Curie transformation

Table 3.4: Relevant peaks temperatures and reactions detected on DTA cooling curves of each powder mixture within the temperature range 400 – 1000 °C.

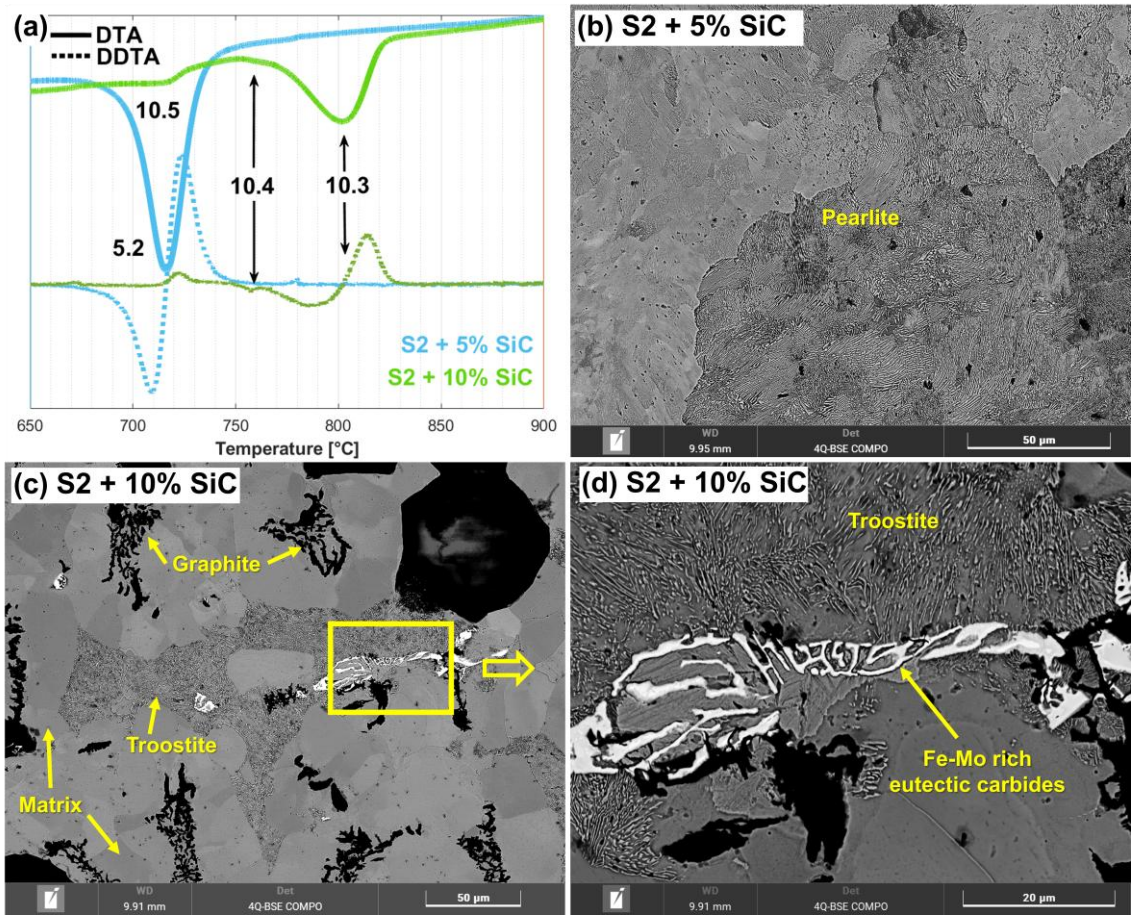


Fig. 3.11: Focus on the solid-state transformations that occur within the systems S2 + 5 and 10% SiC. (a) DTA cooling curves, (b,c,d) overviews of the microstructures.

3.3.4 Main findings from DTA tests

- DTA was selected as a method to test the chemical affinity of powders prior to the LPBF process. Despite the fact that the conditions during DTA tests and LPBF process are not comparable in view of the different heating and cooling rates, DTA proved a useful tool to investigate the dissolution behaviour of SiC and the microstructures obtained in close-to-equilibrium conditions. Such considerations are needed as complementary insights to understand the microstructure evolution that occurs in the out-of-equilibrium conditions of the LPBF process, reported in chapter 5.
- After a reference DTA test up to 1550 °C performed on all powder mixtures, specific DTA tests were performed to investigate the dissolution behaviour of SiC in contact with S2 powders. No undissolved SiC particles were found within the final solidified microstructure after DTA, confirming that interface reaction between S2 and SiC started from 1100 °C during heating, leading to the complete dissolution of SiC and to

the formation of a Fe-based liquid enriched in carbon and silicon at the end of the DTA heating stage (1550 °C).

- The solidification sequence during cooling was highlighted combining the peaks of the DTA cooling curves with the phases detected in the final microstructures. Changing the initial amount of SiC (0, 5 ,10, 15 or 20% in vol.) affects the solidification. Primary phases are γ-Austenite for S2 + 5%, S2 + 10% and S2 + 15% and α-Ferrite for S2 + 20% SiC, as well as different types of Graphite (type C for S2 + 20% SiC, type D for S2 + 15% SiC and type E for S2 + 10% SiC). Liquidus and solidus temperatures were shifted towards lower temperatures when increasing the SiC content.
- The presence of graphite within the final microstructures after DTA on S2 + 10%, S2 + 15% and S2 + 20% SiC is a positive signal that highlights the chemical affinity between S2 and SiC and supports the selection of such compositions for further experiments with LPBF.
- Solid-state transformations and magnetic Curie transformations that occurred within the range 500 – 900 °C during cooling were analysed. They are important for understanding the microstructures obtained in close-to-equilibrium conditions, and they will be used as comparison with the dissimilar microstructures obtained in the out-of-equilibrium conditions of the LPBF process.

3.4 Preparation of powder mixtures

After discussing the selection of the powders for use as feedstock in LPBF, the subsequent step was the preparation of the powder mixtures. In recent years, the MMS laboratory has acquired expertise in powders handling and preparation, as demonstrated in two works to which the author contributed (*Ertugrul, 2020*; *Maurizi Enrici, n.d.*).

The mixtures investigated were the same as listed in *Table 3.1*, with SiC added in 5, 10 and 15% (in volume) in S2 powders. In what follows, experimental methods for the preparation are discussed. Detailed explanations can be found in a paper (in preparation) (*Saggionetto, n.d.*). The devices used for the preparation methods were a planetary ball mill Pulverisette 6 (Fritsch) equipped with WC balls and vials. Sieving was carried out with Haver EML 200 Premium (Haver and Bocker) using test sieves with 63 and 50 µm of mesh size.

A first experiment was made by mixing manually S2 with 5% SiC, both powders in the as-received state. After LPBF processing, microstructural characterization of the printed samples revealed the presence of undissolved (or partially dissolved) SiC granules randomly located within the sample, with dimensions of a few tens of microns (*Fig. 3.12*). In view of the desired complete dissolution of SiC, this outcome should be avoided. Therefore, other mixing techniques were triedwith the additional purpose of achieving homogeneous powder mixtures with rheological properties suitable for the LPBF process, as explained in section 2.3.2. Simple manual mixing is not sufficient to obtain homogenous powder mixtures, as segregation phenomena may occur.

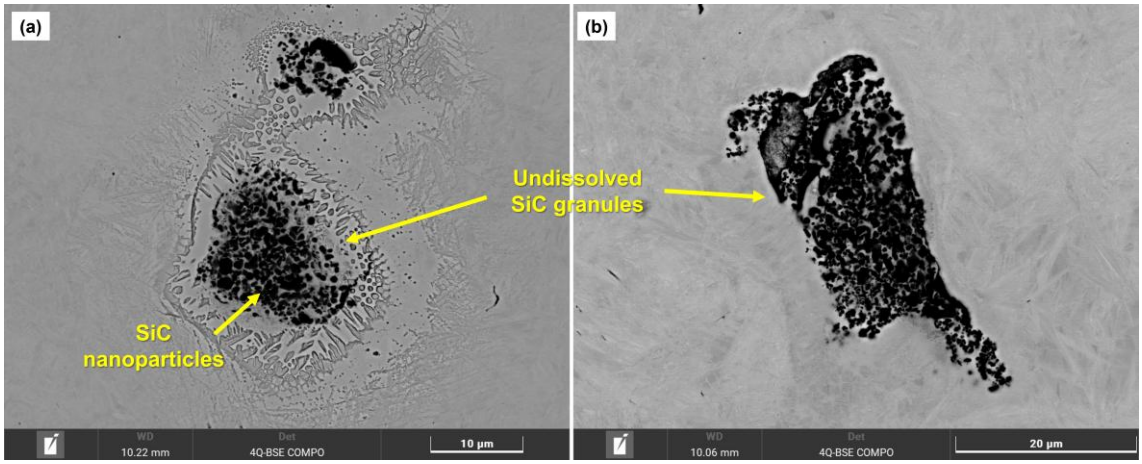


Fig. 3.12: (a,b) Residual of SiC granules within the microstructure of the LPBF processed S2 + 5% SiC, due to partial dissolution.

Original S2 powders were purchased with characteristics appropriate for the LPBF process, as mentioned in section 3.2. In contrast, the purchased SiC granules were not customized for LPBF, as shown by their PSD, which revealed granules with dimensions higher than 100 µm (*Fig. 3.2*). These big granules were only partially dissolved within the melt pool as shown earlier (*Fig. 3.12*). Furthermore, when handling the SiC powder, a bad flowability was observed, compared to that of S2. Considering the lower density of SiC (3.2 g/cm^3) compared to that of S2 powder (7.8 g/cm^3), a high amount of SiC was added to reach the desired concentration within the mixtures. Therefore, SiC had an important effect on the final properties of the mixture. For these reasons, preliminary investigations were performed on the mixture with the highest content of SiC (S2 + 15%) and on pure SiC. In particular, ball milling was performed on SiC with a Ball to Powder Ratio (BPR) of 1:3 at 100 and 200 RPM as rotational speed for various milling times up to 90 min. Similarly, S2 + 15% SiC was ball milled with a BPR of 1:5, a rotational speed of 180 RPM and different milling times (30, 60, 120, 240, 360 min).

After 90 minutes of milling of pure SiC, some zones on the top layer of powders within the bowl exhibited different coloration, corresponding to compacted SiC particles (*Fig. 3.13*a). Using 200 RPM as rotational speed led to extreme compaction after 30 minutes. SiC were compacted along the surface of the bowl due to centrifugal forces and the WC balls were visible on the bottom of the bowl (*Fig. 3.13*b). When milling the mixture S2 + 15% SiC, strong segregation of SiC occurred as early as 30 minutes, as visible in the top layer of powders within the bowl (*Fig. 3.13*c). Furthermore, broken SiC granules were detected, which allowed for the generation of free nanoparticles that adhered over the surface of S2 powders (*Fig. 3.13*d). This phenomenon increased with the increase of the milling time. After high milling times, S2 particles are completely embedded within agglomerated SiC nanoparticles (*Fig. 3.13*d).

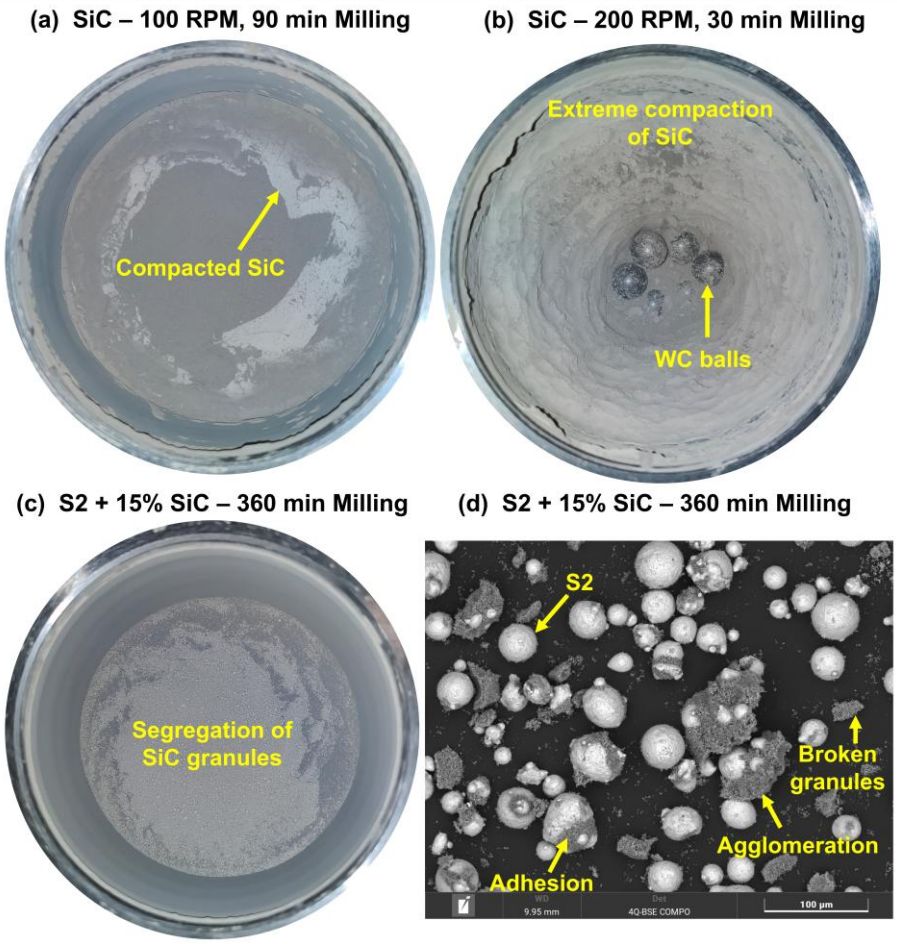


Fig. 3.13: Preliminary investigations through ball milling with pure SiC (a,b) and (c,d) S2 + 15% SiC.

All the above-mentioned phenomena highlight the sensitive nature of the purchased SiC powder, in particular a high cohesiveness. Considering the delicacy of the LPBF process, especially the effect of the quality of the spread layer on the processability, the preparation of the powder mixtures needed to be optimized. The results explained above were important for understanding how to achieve a proper mixture. Thus, a specific preparation sequence was designed and experimented on all the mixtures (*Fig. 3.14*a). The first step was a sieving of the as-received SiC with a test sieve of 50 µm, in order to exclude big granules difficult to dissolve during LPBF processing (*Fig. 3.12*). The second step was a careful manual dry mixing of the mixture, in order to avoid segregation during the subsequent ball milling. For the latter, a BPR of 1:4 and a low rotational speed of 100 RPM were used for all mixtures. A low rotational speed (the minimum for the device used) and few balls were used in order to not affect the quality of the original S2 powders. The milling time was 90, 45 and 20 minutes for the mixture with 5, 10 and 15% SiC respectively. The different milling time, in particular a lower time when

increasing SiC content, was necessary to avoid the formation of agglomerates, like those shown in *Fig. 3.13*d. The aim of the ball milling was to break the SiC granules, thus releasing SiC nanoparticles which can adhere to the larger surface of S2 powders, as shown in *Fig. 3.13*d. This mechanism has been proved beneficial for flowability properties, as mentioned in section 2.3.2. The last step was a sieving using a test sieve of 63 µm, in order to exclude any agglomerates that may have formed. Powders prepared following this method exhibit good homogeneity and an apparent good flowability (*Fig. 3.14*b).

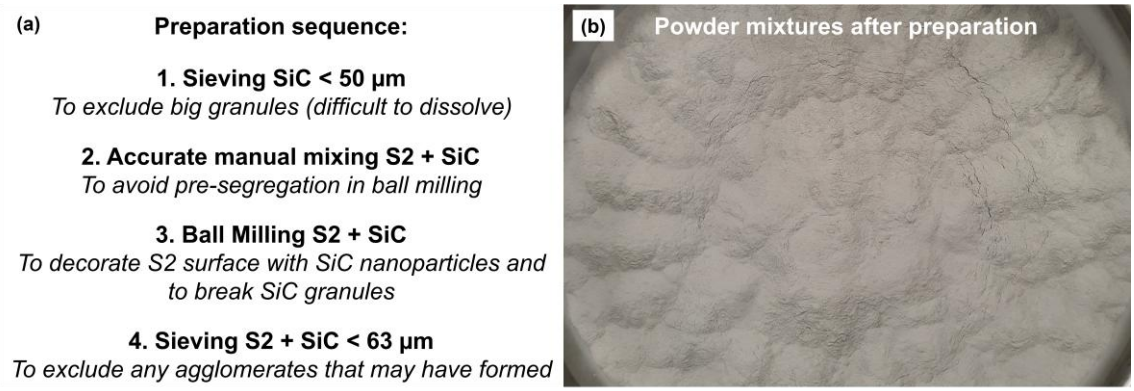


Fig. 3.14: (a) Optimal preparation sequence and (b) homogeneous powder mixture obtained.

Under SEM, the three mixtures reveal a good homogeneity between S2 and SiC powders (*Fig. 3.15*a,c,e). Some SiC granules are broken and SiC nanoparticles partially cover the surface of S2, accommodating preferentially on cavities, thus modifying the roughness of the surface (visible with SE detector, *Fig. 3.15*b,d,f). S2 morphology remains spherical as the original, and no visible deformations are observed. Analysis of PSD were performed in water (*Fig. 3.15*g). The sieving of the as-received SiC granules with 50 µm of test sieve proved successful, as the overall particle size is less than 50 µm. Two population exist, one with dimensions less than 1 µm, corresponding to the nanoparticles, and the other with dimensions of tens of µm, corresponding to the intact granules. The trend of the curve generated by these two populations is combined with the gaussian trend of the original S2 powder when considering the three mixtures. The latter have particles of similar size, but in different volume fractions. Increasing SiC, there is an increase in the population at the nano- and micro-scale, whereas there is a decrease in the population of big particles.

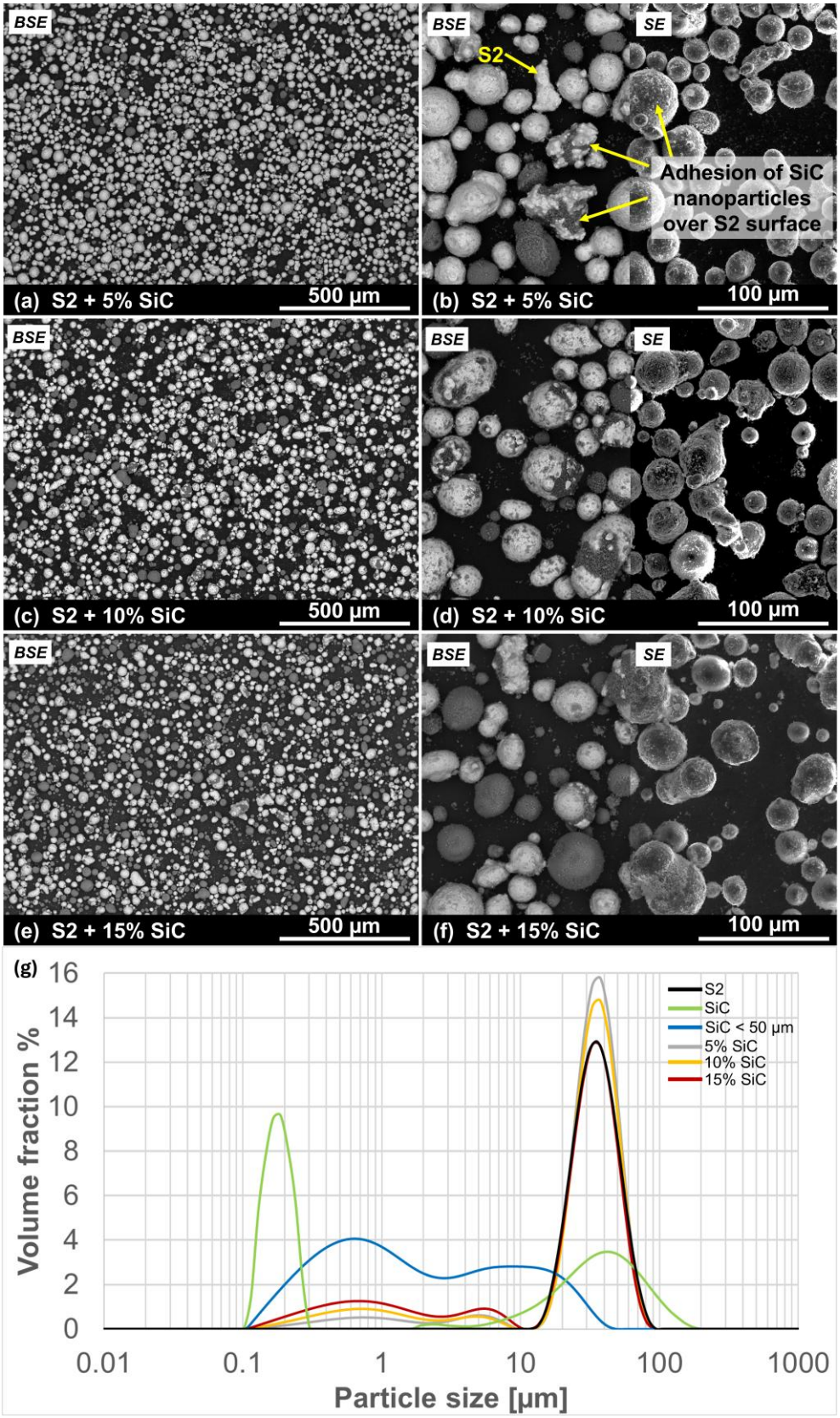


Fig. 3.15: Powder mixtures S2 + (a,b) 5, (c,d) 10, (e,f) 15 % SiC after the optimized preparation. (a,c,e) Good homogeneity is visible in the overviews, and (b,d,f) adhesion of SiC nanoparticles over S2 surface is visible at higher magnification. (g) PSD of the different powders.

3.5 Characterization of powder mixtures

3.5.1 Rheological properties

Rheological properties of the optimized powder mixtures were investigated using the Granudrum and Granupack equipment from Granutools. Measurements were repeated three times for each mixture. Flowability analyses were performed with Granudrum, based on a rotating drum device composed of a horizontal cylinder with transparent sidewalls, half-filled with powders (50 ml). The drum rotated with an angular velocity ranging from 2 to 60 RPM (increasing and decreasing) and at each velocity 40 snapshots separated by 1 s were taken by a charge-coupled device camera. The air/powder interface and the fluctuations around its average position were computed with a custom edge detection algorithm. The dynamic angle of repose and the cohesive index were computed from the average interface position of each rotating speed. Packability properties of powder mixtures were analysed with Granupack. This automated device is designed to characterize powder packing and densification behaviour. It is essentially an advanced, highly repeatable version of the conventional tapped-density ("tap-tap") test. A cell was filled with powder and tapped 1000 times with 1mm free fall. After each tap, the height of the samples was automatically measured with an inductive sensor. Volume and density were calculated from the measured height and the software plotted in real-time the packing dynamic of the powder. From the measurements, the free settled bulk density (ρ[0], initial density before tapping) and the tapped bulk density (ρ[1000], final density after 1000 taps) were used to compute the Hausner ratio (Hr), according to the following equation:

$$Hr = \frac{\rho[1000]}{\rho[0]} \tag{3.1}$$

*Fig. 3.16*a,b shows the measurements of the cohesive index and dynamic angle of repose for the three mixtures. For a better understanding, S2 curve is also displayed. Generally, the difference between increasing and decreasing velocity is referred as hysteresis effect, which was not detected for the tested materials. Indeed, the ‘increasing’ and ‘decreasing’ curves exhibit the same trend, confirming that no segregation or agglomeration occurred during the test (*Lüddecke, 2021*). S2 powders exhibit a shear thickening behaviour, due to the increase of the cohesive index with the increase of the speed (*Fig. 3.16*a), indicating a decrease in flowability for increased applied stress (*Baesso, 2021*). For the three different mixtures, the trend of the curves is similar, showing a slight decrease of the cohesive index at high speed, as a result of a shear thinning phenomena at high applied stress. In general, the addition of SiC

leads to a decrease of the cohesive index (*Fig. 3.16*a). In contrast, the addition of SiC increases the dynamic angle of repose at low speed, passing from 33° for S2 alone to 40° - 44° with SiC (*Fig. 3.16*b). For more clarity, only the curves obtained when increasing the rotational speed are displayed in *Fig. 3.16*b. *Fig. 3.16*d shows the snapshots taken by Granudrum at 12 RPM. At this speed, the dynamic angle of repose increases with increasing content of SiC, and the same trend is observed for the irregularity of the fluctuations of the interface air/powders. Granupack analysis reveals a decrease of both the freely settled bulk density (ρ[0]) and the tapped bulk density (ρ[1000]) of the mixtures when increasing SiC content (*Fig. 3.16*c and *Table 3.5*).

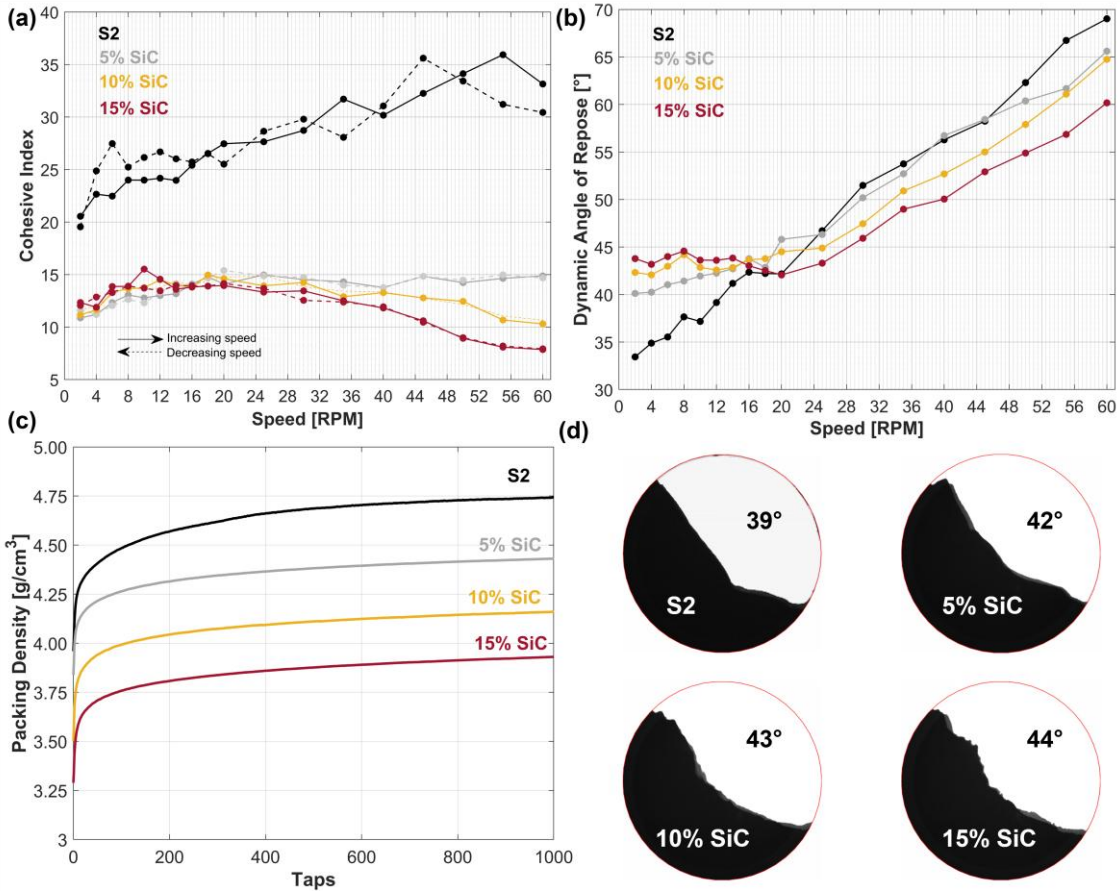


Fig. 3.16: (a) Measurements of cohesive index, (b) dynamic angle of repose and (c) packing density for the different powders. (d) Snapshots taken with Granudrum at 12 RPM.

The combination of the results obtained with Granudrum and Granupack provides an understanding of the flowability properties of the powders. This gives the possibility to correlate the powder flowability with the quality of the spread layers during the LPBF process, as it is crucial for the processability (section 2.3.2). However, the correlation between flowability and in-process performances is a debated topic and researchers are trying to define

some guidelines (*Baesso, 2021*). Furthermore, the complexity of the phenomena increases when powder mixtures are handled. In this case, as shown in *Fig. 3.15*, the mixtures are composed of S2 powders partially decorated with SiC nanoparticles, free SiC nanoparticles and SiC granules intact or broken. Therefore, several phenomena occur at different scales.

Testing the powders with the Granudrum device can provide an important information on the recoater speed to be set for the spreading of a layer of powders. Indeed, based on the trend of the curve of the dynamic angle of repose (*Fig. 3.16*b), the selection of an optimal value (or range) can provide the corresponding rotational speed, which can be transformed in turn into a linear speed. The calculated linear speed thus corresponds to the speed to set for the recoater. Therefore, evaluating the curve of the dynamic angle of repose is crucial. In the present case, there is an increase of the angle of repose when increasing the speed (*Fig. 3.16*b). According to the classification proposed by Carr, the flow behaviour of powders is cohesive when the angle of repose is higher than 45°. At higher angles, the flow behaviour becomes worst. Very cohesive powders negatively affect the spreadability, thus leading to a poorly homogeneous layer of powder during the LPBF process. In the work of (*Gärtner, 2021*), a limiting dynamic angle of repose of 50° was defined to achieve homogenous powder layers. In this work, such value was obtained at around 30 RPM of rotational speed. However, in the range 20 – 30 RPM, the slope of all the curves started to increase, whereas for speed lower than 20 RPM the trend was almost linear and more stable. For this reason, the speed selected was 12 RPM, corresponding to 50 mm/s of linear speed. This speed was also set as the recoater speed for the LPBF process of all mixtures. At this speed, the dynamic angle of repose of the different powders corresponds to a fair to passable flow behaviour (*Fig. 3.16*d), according to Carr's classification (*Table 3.5*). Lower values of the dynamic angle of repose were achieved at lower rotational speeds. In particular, S2 powder exhibits a free-flowing behaviour at speeds lower than 12 RPM (34 – 38°). In contrast, the minimum value of the angle of repose for the three mixtures is 40°. Therefore, the chosen value of 12 RPM (50 mm/s) is a compromise between all the powders. With this speed, no problems arose during the spreading steps of the LPBF process without preheating. Further details will be provided in section 4.4.

The other classification of the powder flowability proposed by Hausner considers the ratio Hr between ρ[1000] and ρ[0] (*Eq. 3.1*), which were obtained with Granupack. Based on the value of Hr, S2 powders revealed a fair flow behaviour. For the mixtures, increasing the content of SiC leads to increase Hr, thus suggesting a decrease in flowability (*Table 3.5*).

Based on the above explanations, thus considering the dynamic angle of repose and Hr as indicators of the flowability, adding SiC leads to a decrease of the flowability. An opposite result emerges from the evaluation of the cohesive index. Indeed, all the three mixtures reveal lower cohesive index than that of pure S2, i.e. the cohesive index for the mixtures is even less than half that of S2 alone (*Fig. 3.16*a), thus suggesting an improvement in the flowability. The reduced cohesiveness is also visible in *Fig. 3.16*d, where the fluctuations of the interface air/powders increase with increasing the content of SiC. However, this is not realistic, as noticed during the handling and preparation of powders. Therefore, this result might have a deeper significance, which was not further investigated here.

Powder	***Hausner***				***Carr***	
	ρ[0] [g/cm^3]	**ρ[1000] [g/cm^3]**	**Hr**	**Flow characteristics**	**Angle of repose**	**Flow characteristics**
S2	3.96	4.74	1.2	Fair	39°	Fair to passable
5% SiC	3.84	4.44	1.16	Good	42°	
10% SiC	3.50	4.16	1.19	Fair	43°	
15% SiC	3.29	3.93	1.2	Fair	44°	

Table 3.5: Classifications of flowability according to Hausner and Carr.

Fig. 3.17 shows the combination of the flowability classification methods based on Hr and on the dynamic angle of repose. The values of the dynamic angle of repose are those obtained at 12 RPM. For the three mixtures, increasing the content of SiC worsened the flowability properties, as both Hr and the angle of repose increase. Correlation between the measured properties of flowability and visual observations during the LPBF process will be given in section 4.4. All these results are valid at room temperature, thus when substrate preheating is not applied.

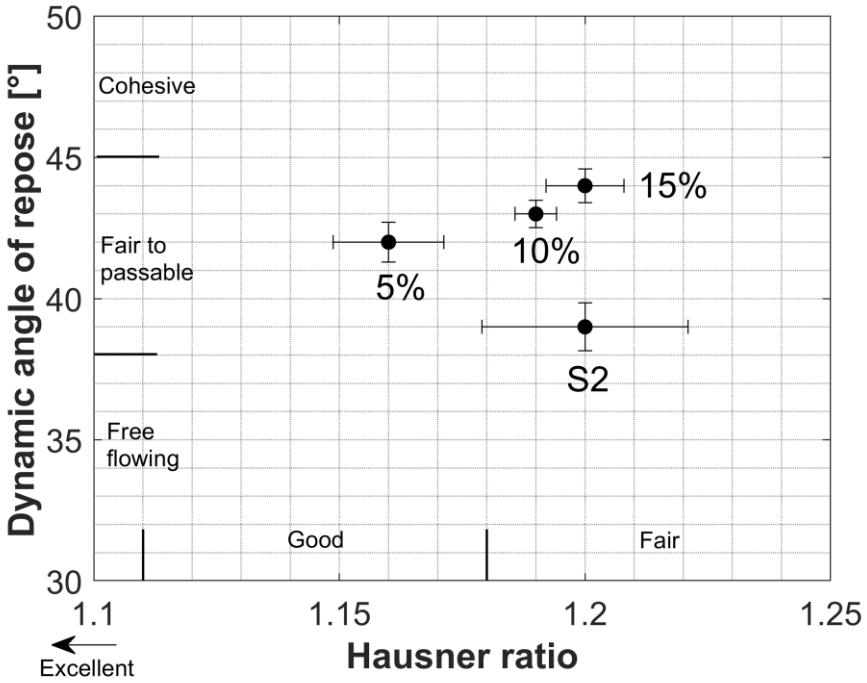


Fig. 3.17: Comparison between Hausner ratio and dynamic angle of repose for all powders.

3.5.2 Absorbance

During the selective scanning of the powder bed by the laser, the laser beam interacts with each powder particle due to the multiple reflections between powders. With each reflection, the beam also penetrates the material where it can be absorbed or transmitted. Thus, in laser-based AM processes, the interaction between laser and powders leads to three mechanisms, being Reflection (R), Absorption (A) and Transmission (T). These three variables are influenced by the wavelength of the source. The relation between them is as follows:

$$R + A + T = 1 \tag{3.2}$$

The LPBF device used in this work, as most of the commercial ones, is equipped with a Yb-fiber laser with a wavelength of 1070 nm. At this wavelength, metals exhibit a very low radiation penetration depth in the nm range, and for this reason transmission mechanisms can be neglected (*Brandau, 2022*; *Zhang, 2019*). Thus, the efficiency and process stability of laser-based AM processes are largely dependent on absorbance and reflectance (*Brandau, 2022*). In general, multiple reflections have the greatest impact on the absorbance. Absorbance causes heating of each particle, resulting in their melting and in the formation of the melt pool. Therefore, the value of absorbance is a significant factor that drive the temperature and depth of the melt pool (*Khorasani, 2022*).

From *Eq. 3.2*, considering T = 0, absorbance can be easily calculated knowing the reflectance of the powder. This property can be measured with spectrometer devices. In this work, a Shimadzu UV-3600 Plus UVVIS-NIR spectrophotometer was used to analyse the reflectance properties of the three powder mixtures (S2 + 5, 10, 15% SiC) and of the pure S2 and SiC powders, in the wavelength range 350 – 1400 nm. After measuring the reflectance, the absorbance was computed as follows:

$$A = 1 - R \tag{3.3}$$

Original S2 powder exhibited the highest value at 1070 nm (68 %), whereas pure SiC has a lower absorbance by10% (58.5%) (*Fig. 3.18*). The general trend of these two curves is different. When considering the three powder mixtures, there is a clear tendency to approach the curve of pure SiC when increasing the content of SiC of the mixture. At 1070 nm, the absorbance values are intermediate between those of the two original powders, with the value decreasing as the SiC in the mixture increases. Therefore, it can be stated that the presence of SiC decreases the laser absorbance of the powders. This phenomenon affects the melt pool generated during the process and the consequent LPBF processability of the powder mixture. Further explanations will be given in section 4.4.

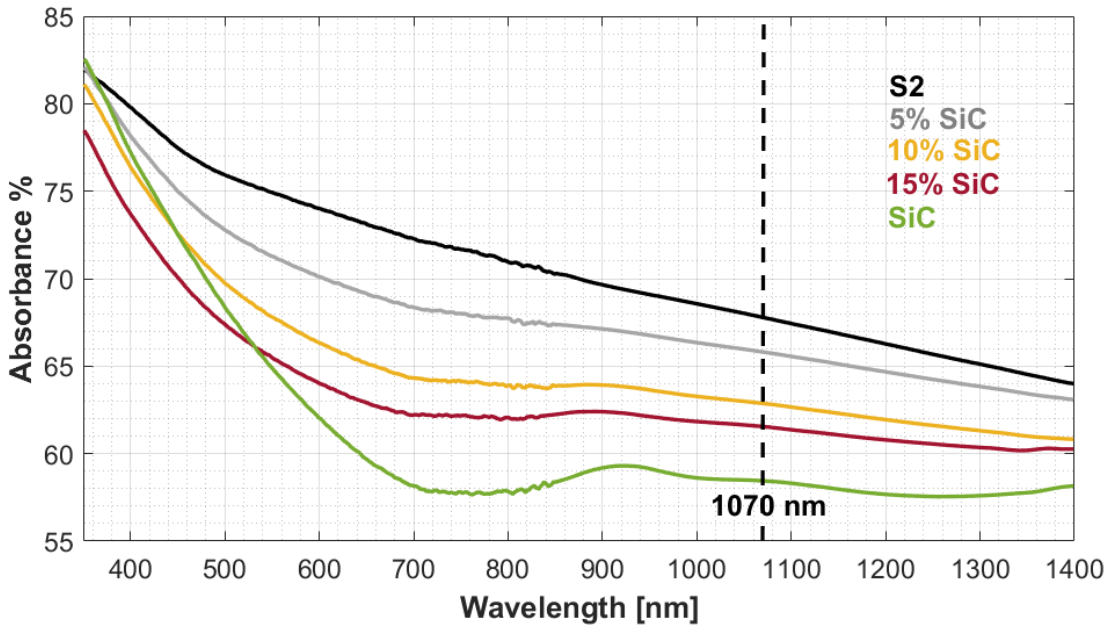


Fig. 3.18: Absorbance of the different powders.

3.6 Conclusions

- The chemical composition was designed to promote graphitization. Two different commercial powders were selected. AISI S2 tool steel was selected as main powder, with characteristics suitable for LPBF. SiC granules were selected as a source of silicon and carbon.
- The chemical affinity between those two powders was investigated through DTA in close-to-equilibrium conditions. Results proved the dissolution reactions between S2 and SiC occurring during heating, and the crystallization of different types of graphite occurring during cooling, based on the content of SiC.
- LPBF experiments require appropriate rheological properties of the powder. The preparation methodology of the mixtures S2 + 5, 10, 15% (in volume) SiC was optimized using a combination of different mixing techniques. Homogeneous mixtures were obtained, suitable for use in LPBF.
- Rheological properties of the different powders were investigated with the Granudrum and Granupack devices, to analyse the flowability and packability behaviour. Adding SiC leads to a decrease of flowability and packability. The evaluation of the dynamic angle of repose served to select the value of the speed for the recoating step of the LPBF process.
- Absorbance properties of the two original S2 and SiC powders and of the three mixtures were analysed. Adding SiC leads to a decrease in absorbance.

3.7 References

Araya, N., Neves, G. O., Ramos Filho, A. I., Aguilar, C., Biasoli de Mello, J. D., Binder, C., Hammes, G. (2020). "Study of silicon carbide dissociation into Fe and Fe C matrixes produced by die pressing and sintering." Materials Chemistry and Physics, 253(April). https://doi.org/10.1016/j.matchemphys.2020.123442

Baesso, I., Karl, D., Spitzer, A., Gurlo, A., Günster, J., & Zocca, A. (2021). "Characterization of powder flow behavior for additive manufacturing." Additive Manufacturing, 47(June), 102250. https://doi.org/10.1016/j.addma.2021.102250

Bio Seidou, A. H. (2022). "Development and evaluation of the powders mix low alloyed steel + SiC Selective Laser Melting." Master Thesis, University of Liège.

Boccalini, M., & Goldenstein, H. (2001). "Solidification of high speed steels." International Materials Reviews, 46(2), 92–115. https://doi.org/10.1179/095066001101528411

Brandau, B., Da Silva, A., Wilsnack, C., Brueckner, F., & Kaplan, A. F. H. (2022). "Absorbance study of powder conditions for laser additive manufacturing." Materials and Design, 216, 110591. https://doi.org/10.1016/j.matdes.2022.110591

Ertugrul, O., Maurizi Enrici, T., Paydas, H., Saggionetto, E., Boschini, F., & Mertens, A. (2020). "Laser cladding of TiC reinforced 316L stainless steel composites: Feedstock powder preparation and microstructural evaluation." Powder Technology, 375, 384–396. https://doi.org/10.1016/j.powtec.2020.07.100

Gärtner, E., Jung, H. Y., Peter, N. J., Dehm, G., Jägle, E. A., Uhlenwinkel, V., & Mädler, L. (2021). "Reducing cohesion of metal powders for additive manufacturing by nanoparticle dry-coating." Powder Technology, 379, 585–595. https://doi.org/10.1016/j.powtec.2020.10.065

González-Martínez, R., de la Torre, U., Lacaze, J., & Sertucha, J. (2018). "Effects of high silicon contents on graphite morphology and room temperature mechanical properties of as-cast ferritic ductile cast irons. Part I – Microstructure." Materials Science and Engineering: A, 712(November 2017), 794–802. https://doi.org/10.1016/j.msea.2017.11.050

Howell, P. R. (1998). "The pearlite reaction in steels: Mechanisms and crystallography." Materials Characterization, 40(4–5), 227–260. https://doi.org/10.1016/s1044-5803(98)00024-2

Janerka, K., Kostrzewski, Ł., Stawarz, M., & Jezierski, J. (2020). "The importance of SiC in the process of melting ductile iron with a variable content of charge materials." Materials, 13(5), 1–10. https://doi.org/10.3390/ma13051231

Kalogeropoulou, S., Baud, L., & Eustathopoulos, N. (1995). "Relationship between wettability and reactivity in Fe/SiC system." Acta Metallurgica Et Materialia, 43(3), 907–912. https://doi.org/10.1016/0956-7151(94)00336-G

Kang, S. J. (2005). "Initial Stage Sintering." Sintering, 39–55. https://doi.org/10.1016/B978-0-7506-6385-4.X5000-6

Khorasani, M., Ghasemi, A. H., Leary, M., Sharabian, E., Cordova, L., Gibson, I., … Rolfe, B. (2022). "The effect of absorption ratio on meltpool features in laser-based powder bed fusion of IN718." Optics and Laser Technology, 153(January), 108263. https://doi.org/10.1016/j.optlastec.2022.108263

Lacaze, J., & Sundman, B. (1991). "An assessment of the Fe-C-Si system." Metallurgical Transactions A, 22(10), 2211–2223. https://doi.org/10.1007/BF02664987

Lüddecke, A., Pannitz, O., Zetzener, H., Sehrt, J. T., & Kwade, A. (2021). "Powder properties and flowability measurements of tailored nanocomposites for powder bed fusion applications." Materials and Design, 202. https://doi.org/10.1016/j.matdes.2021.109536

Maurizi Enrici, T., Saggionetto, E., Dedry, O., Ertugrul, O., Boschini, F., Tchuindjang, J. T., & Mertens, A. (n.d.). "Fabrication and metallurgy of high-silicon austenitic stainless steel produced by Laser Cladding."

Rivera, G. L., Boeri, R. E., & Sikora, J. A. (2004). "Solidification of gray cast iron." Scripta Materialia, 50(3), 331–335. https://doi.org/10.1016/j.scriptamat.2003.10.019

Saggionetto, E., Bio Seidou, A. H., Caubergh, S., Boschini, F., Dedry, O., Tchuindjang, J. T., & Mertens, A. (n.d.). "Preparation of powder feedstock and processability of a low alloy tool steel modified by SiC for Laser Powder Bed Fusion."

Tchuindjang, J. T., & Lecomte-Beckers, J. (2011). "Study of the origin of the unexpected pearlite during the cooling stage of two cast high-speed steels." Solid State Phenomena, 172–174, 803–808. https://doi.org/10.4028/www.scientific.net/SSP.172-174.803

Zhang, J., Gu, D., Yang, Y., Zhang, H., Chen, H., Dai, D., & Lin, K. (2019). "Influence of Particle Size on Laser Absorption and Scanning Track Formation Mechanisms of Pure Tungsten Powder During Selective Laser Melting." Engineering, 5(4), 736–745. https://doi.org/10.1016/j.eng.2019.07.003

Chapter 4

Processability by LPBF: from reference S2 alloy to modified S2 + SiC

Contents

4.1 Introduction 90
4.2 Reference material AISI S2 91
4.2.1 Single tracks 91
4.2.2 Multi-tracks and layers (cubes) 93
4.3 Powder mixtures S2 + SiC 101
4.3.1 S2 + 5 or 10% SiC without preheating 101
4.3.2 Effect of preheating on S2 + 10% SiC 107
4.3.3 Difficult processability of S2 + 15% SiC 112
4.4 Effect of powder properties on processability 114
4.5 Conclusions 117
4.6 References 118

4.1 Introduction

After considering the role of powder properties in the LPBF process in chapter 3, the subsequent step for the development of the new alloy is the selection of the optimal process parameters to achieve a fully dense, defect-free part. This involves an understanding of the effect of SiC on the appearance of process-induced defects such as lack of fusion, key-hole porosities, balling and spattering. The development of the process maps started by investigating the processability of the reference material AISI S2. For this purpose, 53 single scan tracks were printed out of AISI S2 powder. Then, the best 20 parameters were selected to print cubes (multi- tracks and layers). This preliminary work was conducted at Aconity3D facilities[8]. Then, the processability of the S2 alloy modified by SiC addition (5 and 10 % in volume) will be discussed focusing on the nature of the melt pool. Afterwards, the effect of preheating during processing of S2 + 10% SiC will be elucidated. Finally, the difficult processing of S2 + 15% SiC will be explained. The processability of the different powders will be correlated with the properties of the powders, previously discussed in section 3.5.

[8] Processing of S2 powder was conducted in January 2022 at Aconity3D facilities. The Aconity Mini LPBF device was installed at the MMS laboratory in September 2022.

4.2 Reference material AISI S2

4.2.1 Single tracks

The single scan track approach allows to print many tracks in a single job with a wide range of parameters, in view of the simple geometry of the scan track. The parameters involved in this preliminary study were only the laser power (P) and the scan velocity (v_s). Hatch distance (h) and layer thickness (t) were not to be set, as no multiple tracks and layer were created. Combinations of 53 parameters were selected, with power varying between 50 – 250 W and scan velocity between 200 – 2000 mm/s (*Table 4.1*). The linear energy density ($E_{d,l}$) is considered as follows:

$$E_{d,l} = \frac{P}{v_s} \tag{4.1}$$

Single Track	P [W]	v_s [mm/s]	$E_{d,l}$ [J/mm]
1	50	200	0.250
2	50	400	0.125
3	50	600	0.0833
4	50	800	0.0625
5	50	1000	0.0500
6	50	1200	0.0417
7	75	200	0.375
8	75	400	0.188
9	75	600	0.125
10	75	800	0.0938
11	75	1000	0.0750
12	75	1200	0.0625
13	75	1400	0.0536
14	75	1600	0.0469
15	75	1800	0.0417
16	75	2000	0.0375
17	100	200	0.500
18	100	400	0.250
19	100	600	0.167
20	100	800	0.125
21	100	1000	0.100
22	100	1200	0.0833
23	100	1400	0.0714
24	100	1600	0.0625
25	100	1800	0.0556
26	100	2000	0.0500
27	150	400	0.375
28	150	600	0.25
29	150	800	0.188
30	150	1000	0.150
31	150	1200	0.125
32	150	1400	0.107
33	150	1600	0.0938
34	150	1800	0.0833
35	150	2000	0.0750
36	200	400	0.500
37	200	600	0.333
38	200	800	0.250
39	200	1000	0.200
40	200	1200	0.167
41	200	1400	0.143
42	200	1600	0.125
43	200	1800	0.111
44	200	2000	0.100
45	250	400	0.625
46	250	600	0.417
47	250	800	0.313
48	250	1000	0.250
49	250	1200	0.208
50	250	1400	0.179
51	250	1600	0.156
52	250	1800	0.139
53	250	2000	0.125

Table 4.1: Process parameters of the single tracks.

A typical set-up of the machine platform with the single tracks is visible in *Fig. 4.1*a. After printing, the dimensions and quality of each single track were evaluated. Some tracks appear narrow and irregular, as result of a power below 100 W, a scan velocity higher than 1000 mm/s and in general a linear energy density below 0.1 J/mm. Such tracks were not considered for width measurements. Best tracks appeared homogenous and regular, with a width close to 100 µm. When the linear energy density exceeded 0.3 J/mm, wide tracks were generated with a width up to 210 µm. Among the 53 combinations of parameters, 20 were selected for further development of multi tracks and layers, as explained in the next section.

Evaluations of single tracks are also needed to set the hatch distance value for the processing of multi-tracks. Best tracks width varied between 60 – 185 µm (*Fig. 4.1*b), with an average of 100 µm. The hatch distance for multi-tracks printing was set as 0.7 – 0.9 times the width of the best single tracks, in order to ensure a proper overlapping. Thus, hatch distance was decided to be 80 µm.

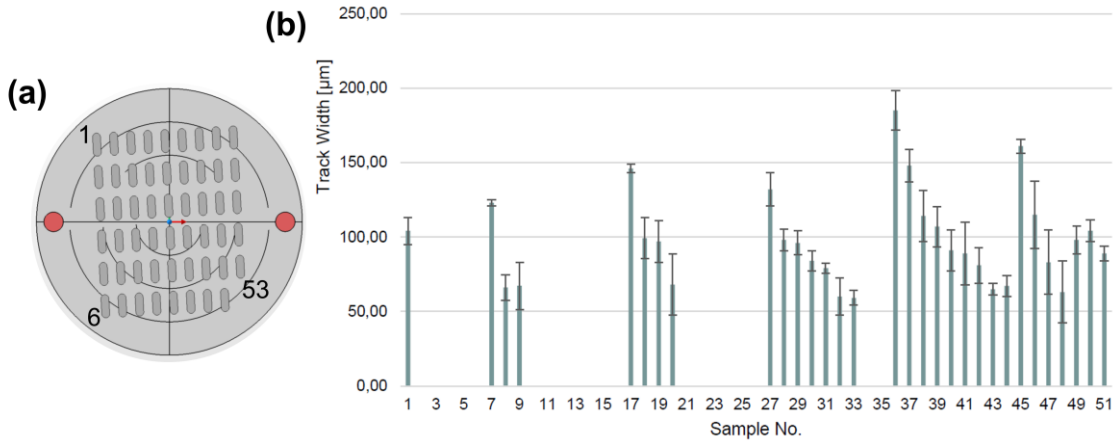


Fig. 4.1: (a) Configuration of the platform with the 53 single tracks and (b) measurements of the track width of each single track.

4.2.2 Multi-tracks and layers (cubes)

20 cubes of 10x10x10 mm^3 were processed from AISI S2 powder, choosing different combinations of power and scan velocity from the single tracks evaluation (section 4.2.1). P is considered as low (100 W), moderate (150 W), medium (200 W) and high (250 W). v_s is considered as low (400 – 800 mm/s), medium (800 – 1250 mm/s) and high (1250 – 2000 mm/s). Hatch distance was set at 80 µm. The layer thickness was set at 30 µm, in view of the D50 of the particle size distribution of the powders being 31 µm (section 3.2). A laser spot size of 80 µm with a gaussian distribution was used for all samples. The scanning strategy implied a rotation of 90° for each layer, with no contouring. No substrate preheating was applied. Fully printed samples showed good dimensional tolerances (*Fig. 4.2*a), according to the desired initial geometrical features. Samples 1-2-3-6-11 were stopped during manufacturing due to evident surface defects that affect the quality of the subsequent layers (*Fig. 4.2*b,c,d). These samples were not considered for subsequent analysis.

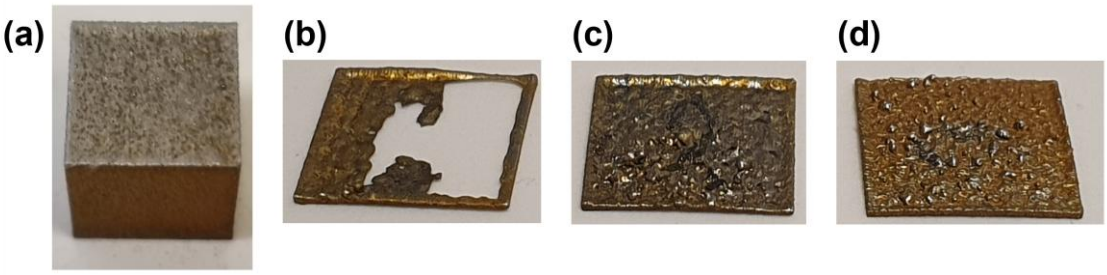


Fig. 4.2: (a) Examples of a fully printed and (b,c,d) interrupted samples.

The volumetric energy density ($E_{d,v}$) was used to correlate the results observed with the processing parameters (*Eq. 4.2*). This equation is similar to the linear energy density $E_{d,l}$ previously mentioned (*Eq. 4.1*), but it also considers volumetric features such as hatch distance (h) and layer thickness (t).

$$E_{d,v} = \frac{P}{t*h*v_s} \tag{4.2}$$

Sample	P [W]	v_s [mm/s]	$E_{d,v}$ [J/mm^3]
1	100	400	104
2	100	600	69
3	100	800	52
4	100	1000	42
5	100	1200	35
6	150	500	125
7	150	750	83
8	150	1000	63
9	150	1250	50
10	150	1500	42
11	200	500	167
12	200	750	111
13	200	1000	83
14	200	1500	56
15	200	2000	42
16	250	500	208
17	250	750	139
18	250	1000	104
19	250	1500	69
20	250	2000	52

Table 4.2: Processing parameters and volumetric energy density for each sample.

After production, the density of each sample (ρ) was measured through a gas pycnometer and the relative density was calculated using the bulk density of powders, according to *Eq. 4.3*.

$$\%\, Density = \frac{\rho}{\rho_{bulk}} * 100\% \tag{4.3}$$

The surface of the as-built samples was checked using an Alicona Infinite Focus G5 optical profilometer for roughness analysis. All the as-built samples were cut by Electro Discharge Machining perpendicularly to the laser scan direction of the last layer to obtain the cross section. After cutting, samples were hot mounted with an electrically conductive bakelite, then ground and polished down to 1 µm. Defects within the cross sections were analysed through an optical microscope Olympus BX60 and quantified through Olympus Stream Analysis Software. Nital 3% was used to etch the cross sections.

According to *Eq. 4.3*, all samples show a density above 96.5 %. A good correlation is observed between the density value and the fraction of internal porosity obtained by image analysis (*Fig. 4.3*a). In image analysis, all kinds of defects are considered. Small gas porosities are detected in all samples. Key-hole porosities at the bottom of melt pools are observed in samples

produced with high $E_{d,v}$ (*Fig. 4.3*b). Large spatters containing a porosity are detected in samples with low v_s (*Fig. 4.3*c). Cracks perpendicular to the building direction, and initiated from the edge are detected in a few samples, without any specific correlation with processing parameters (Fig. 4.3d). Lack of fusion defects are visible in samples with low $E_{d,v}$ (*Fig. 4.3*e).

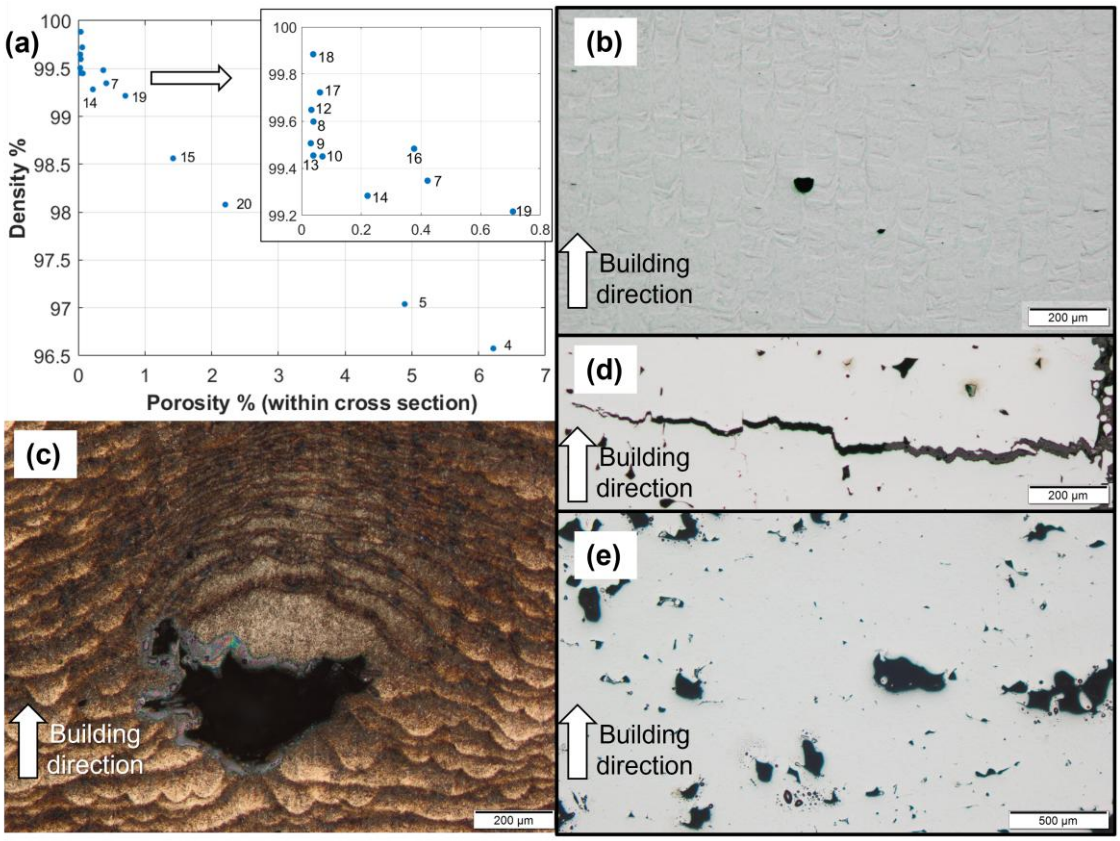


Fig. 4.3: (a) Correlation between density and porosity, (b) key-hole porosity, (c) entrapped porosity within large spatter, (d) crack perpendicular to the building direction initiated from sample edge and (e) lack of fusion defects.

Fig. 4.4 shows the most representative overviews of the samples' cross sections together with the corresponding zoom on the top area. Nital etching allows to observe the features of the tracks within the sample and to distinguish the brighter top layer. The melt pool morphology is clearly visible. Increasing $E_{d,v}$ (from top to bottom in *Fig. 4.4*) leads to a change in the type of defects due to a different melt pool morphology.

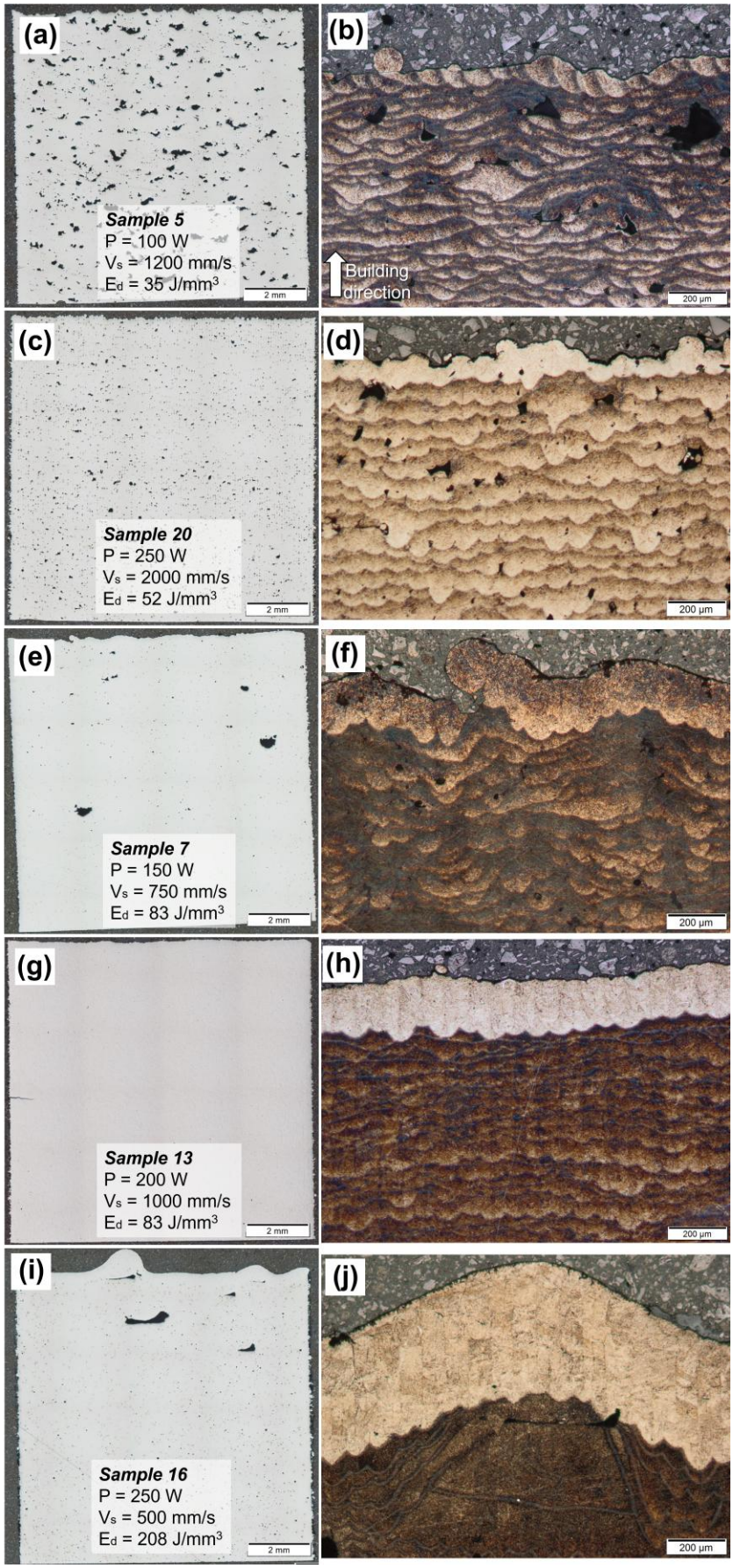


Fig. 4.4: (a,c,e,g,i) Cross section overviews and zoom on tracks and (b,d,f,h,j) top layer after etching with Nital.

Profilometer observations reveal different features of the surface roughness. The surface aspect depends on the quality of the tracks generated by the laser passage. The tracks generated with low $E_{d,v}$ as result of low P (*Fig. 4.5*a) are more irregular than those obtained with high P (*Fig. 4.5*b). With intermediate value of $E_{d,v}$, P and v_s, the surface appears more regular, with only small spatters (*Fig. 4.5*c). On the contrary, high $E_{d,v}$ and P and low v_s lead to an irregular surface despite the good overlapping of the scan tracks (*Fig. 4.5*e). In general, low v_s results in an irregular surface (*Fig. 4.5*d).

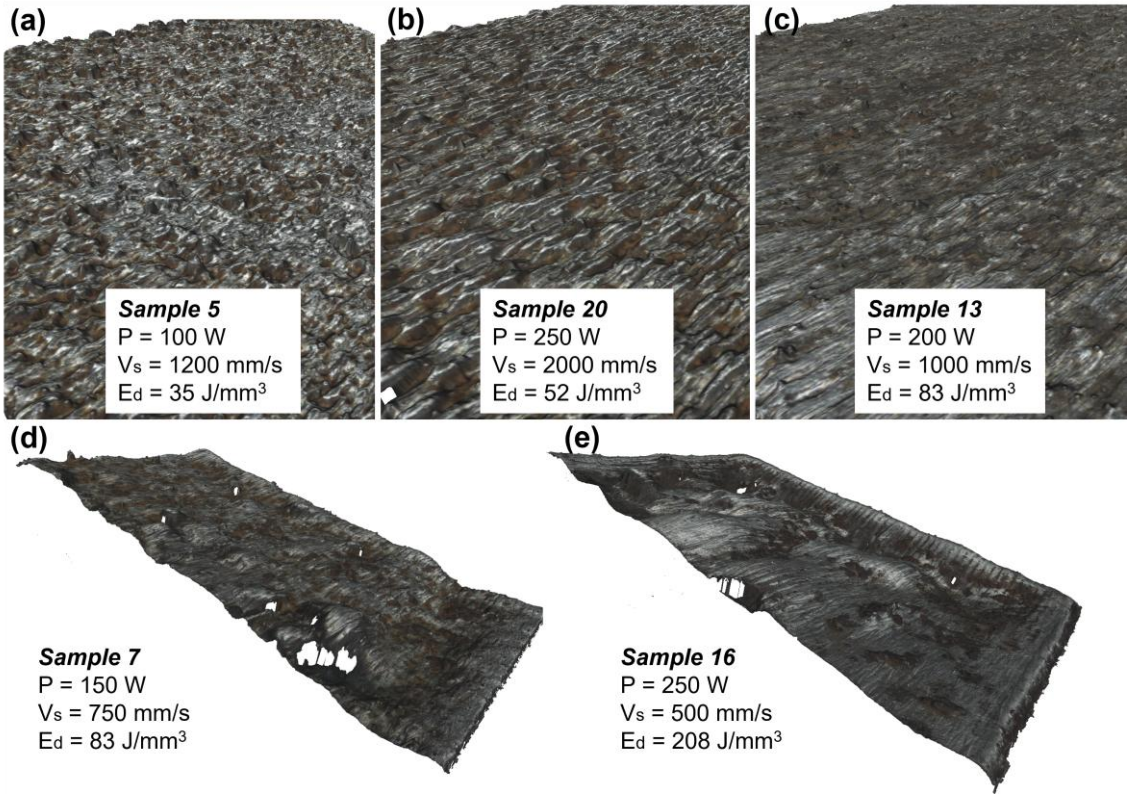


Fig. 4.5: Profilometer observations of the top surface after printing.

The first approach in the LPBF of a new alloy consists in searching the best parameters to achieve fully dense and defect-free samples. Process maps are commonly used for this purpose. Although the primary aim is to obtain the best parts, investigations of defects generated using different parameters can provide good insights of both the alloy studied and the functioning of the LPBF process.

In this work, the effects of the two variable parameters (P and v_s) are investigated together with the variation in $E_{d,v}$ (*Eq. 2*). All samples are compared in terms of density, amount and type of defects, tracks overlapping, melt pool morphology and surface quality. Particular attention is given to the quality of the top surface and the morphology of the melt pool within the top layer.

Indeed, they can provide useful indications on the defects that may form in a hypothetical subsequent layer and thus understand the phenomena that have occurred in the layers below.

The use of low/moderate P (100 – 150 W) and low v_s (400 – 800 mm/s) (samples 1, 2, 3, 6 and 7) does not allow for fully printed samples. The printing was stopped, excepted for sample 7. Despite the wide range of $E_{d,v}$ (52 – 125 J/mm^3), the low P could not generate sufficient liquid phase for the powders to bond together, resulting in poor densification (*Chowdhury, 2022*). The metallurgical bond between layers is also compromised, leading to material tear out (*Fig. 4.2*b), as also occurred in the top layer of sample 7 (*Fig. 4.4*f). Moreover, the low v_s causes an unstable melt pool generating big spatters (*Fig. 4.2*c,d) (*Zheng, 2018*) that are not re-melted by the subsequent passage of the laser. If spatters are larger than the layer thickness, the spreadability of a new layer of powders is impeded, causing gaps and compromising the metallurgical layers bond (*Wang, 2017*). Large pores (~ 400 µm) are found for instance in sample 7, that are located inside a big spatter (*Fig. 4.3*c). As the process advances, the presence of poorly printed layers leads to an irregular surface (*Fig. 4.5*d), affecting the printing of the subsequent layers.

With similar P (100 – 150 W) but higher v_s (1000 – 1250 mm/s) (sample 4 and 5), low $E_{d,v}$ values (~ 40 J/mm^3) generate a shallow melt pool (*Fig. 4.4*b) (*Ryder, 2021*). As consequence, the metallurgical bond between two subsequent layers is compromised, causing the presence of lack of fusion areas (*Fig. 4.4*a,b) (*Platl, 2021*) that leads to low density (*Fig. 4.3*a). In this case, the poor metallurgical bond is caused by balling phenomena (*Chowdhury, 2022*), visible in the top surface (*Fig. 4.5*a) where the tracks are clearly discontinuous. The increase in v_s is thus seen to avoid the generation of large spatters. This is easily understood since the higher v_s allows a faster cooling of the melt pool, and decreases the possibility of melted droplets being splashed out of the melt pool (*Zheng, 2018*).

Low $E_{d,v}$ values (~ 54 J/mm^3) resulting from higher P (200 – 250 W) and high v_s (1500 – 2000 mm/s) (samples 14, 15, 19, 20), leads to similar observations. Indeed, balling phenomena also occur, bringing about a low density (*Fig. 4.3*a) due to lack of fusion areas (*Fig. 4.4*c,d). However, this effect is more restrained than observed at lower P. Indeed, the parts density is higher and the internal porosity is lower (*Fig. 4.3*a). In the present case, the higher P allows a better melting of the powders, leading to a better overlapping of the tracks as visible in the top layer (*Fig. 4.5*b). Furthermore, the melt pool height increases (*Fig. 4.4*d), allowing a better metallurgical bond with the previous layer. Therefore, the little increase of $E_{d,v}$ (from 40

to 54 J/mm^3) results in a better processability, but the level of defects remains still high (*Fig. 4.3*a and *Fig. 4.4*c).

The combination of a moderate/medium P (150 – 200 W) and a medium v_s (750 – 1200 mm/s) (Ed = 50 – 111 J/mm^3) allows to achieve fully dense and defect-free parts (sample 8, 9, 10, 12 and 13). Indeed, this combination of parameters generate an ideal melt pool (*Fig. 4.4*h), regular and homogeneous within the cross section. The tracks have a proper overlap, which affects positively the density of the samples (*Fig. 4.3*a) and the spreadablilty of the subsequent powder layer. Indeed, no defects are found (*Fig. 4.4*g). Only small gas porosities are observed, which does not adversely affect the quality of the final part. Small spatters are visible in the top surface (*Fig. 4.5*c), but these can be easily re-melted by the subsequent laser passage. This range of parameters and especially the combination 200 W / 750-1000 mm/s ($E_{d,v}$ ~ 97 J/mm^3) is thus considered as optimum for the realization of AISI S2 steel parts manufactured by LPBF.

Finally, high P (250 W) and low v_s (500 – 1000 mm/s) lead to a high $E_{d,v}$ (104 – 208 J/mm^3) (sample 11, 16, 17 and 18). The deep melt pool (*Fig. 4.4*j) allows a good overlap of the tracks (*Fig. 4.5*e), resulting in high density above 99,5% (*Fig. 4.3*a). Despite this, the high $E_{d,v}$ causes an instability of the melt pool, which is clearly irregular within the cross section (*Fig. 4.4*j). Indeed, increasing the melt pool depth also increases the possibility of gas entrapment, resulting in higher porosity. The large porosity detected (*Fig. 4.4*i) may be formed due to denudation process of powders around the melt pool due to the high $E_{d,v}$ (*Zhang, 2017*). Key-hole defects (*Fig. 4.3*b) are also observed, formed due to the high $E_{d,v}$ that causes metal evaporation and generate a recoil pressure towards the melt pool bottom (*Huang, 2022*). Furthermore, the combination of low v_s and high $E_{d,v}$ increases spattering (*Wang, 2017*), in terms of number and size of spatters. As a result, the spreadability of the subsequent layer of powders is compromised. The final part exhibits many surface irregularities, as shown by profilometer observations (*Fig. 4.5*e) and in the top layer of the cross section (*Fig. 4.4*i).

Based on the above explanations, it can be assumed that the "not processed" window (*Fig. 4.6*) results in an insufficient $E_{d,v}$ to generate an adequate melt pool. Extensive balling and lack of fusion areas are expected due to the low P (100 – 150 W) and the high v_s (1500 – 2000 mm/s).

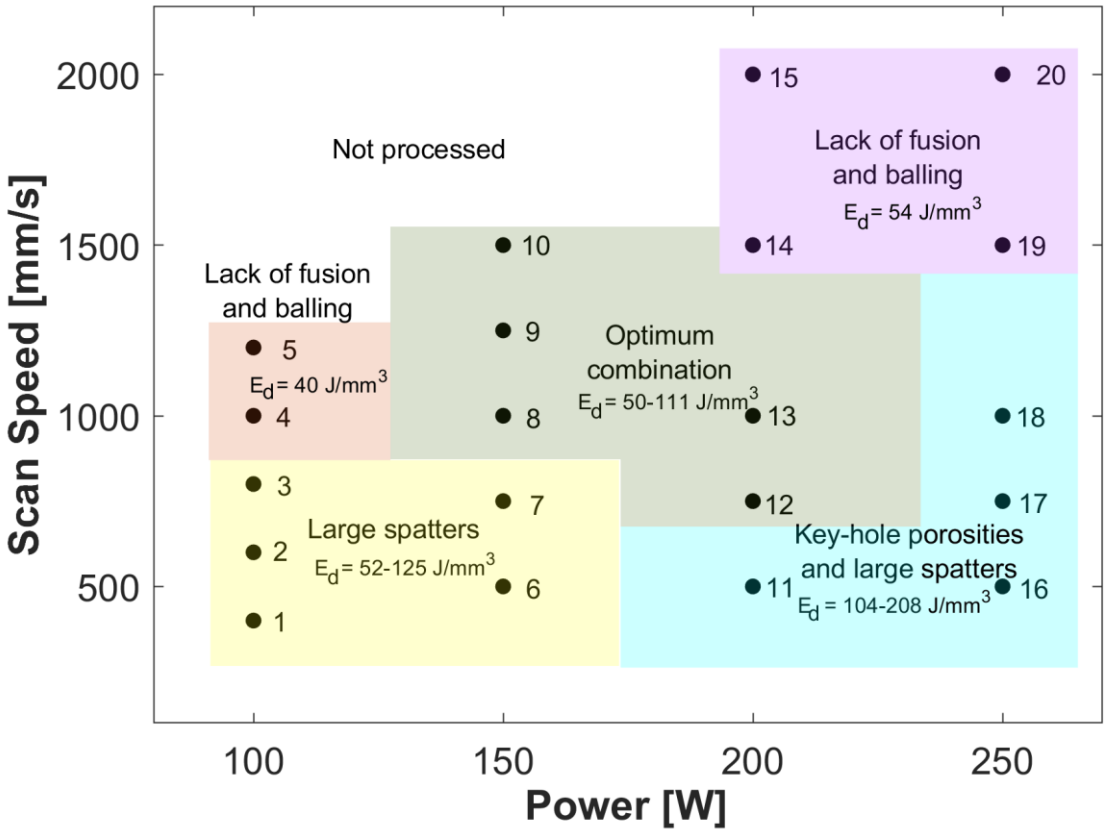


Fig. 4.6: Process map for AISI S2 tool steel by Laser Powder Bed Fusion.

4.3 Powder mixtures S2 + SiC

After the development of the process maps for multi tracks and layers of AISI S2, mixtures with the addition of SiC (5, 10 or 15 in volume %) were processed. The preparation of the powder mixtures was explained in section 3.4. Within the optimum combination of parameters of S2 (*Fig. 4.6*), sample 0.13 exhibited the best characteristics, with the power being 200 W. Such value of power set the limit for the device present in the MMS laboratory. Lower values of power were also used for the processing of the different mixtures, but the best results were obtained at 200 W. Therefore, the current section will discuss the effect on the processability of SiC addition on S2, limiting such discussion to a use of 200 W of power and only varying the scan velocity.

Moreover, to discuss the processability of the different powder mixtures a different approach compared to that used in section 4.2.2 for S2 will be used. In particular, the process maps of each powder mixture will not be shown as the one developed for S2 (*Fig. 4.6*). Different combinations of process parameters were tried to push the limit of the processable amount of SiC within the mixture. As will be shown, a restriction of the process window occurs when increasing SiC. Thus, not all the combinations of parameters used for S2 were used for the powder mixtures, but only a limited process window was investigated. Consequently, the discussion will not focus on the macro effects of many combinations of parameters on the process-induced defects but instead, particular attention will be given to specific factors. First, the effect of variations in melt pools morphology and dimensions in the processability of mixtures with 5 and 10% SiC either with or without preheating will be explained. Secondly, the difficulties in processing S2 + 15% SiC will be shown. Such approach was called ‘dynamic refinement’ of parameters, since starting from S2 and arriving to S2 + 15% SiC the parameters were refined for each powder mixture.

4.3.1 S2 + 5 or 10% SiC without preheating

In this section, results from the processability of multi tracks and layers of S2 shown in the previous section will also be included. *Table 4.3* lists the samples studied in this work, together with their processing parameters. The codification of each sample considers the powder mixture used (0, 5, 10 for the mixture S2, S2 + 5% SiC, S2 + 10% SiC respectively) followed by the level of $E_{d,v}$ (1, 2, 3, 4). $E_{d,v}$ is classified based on the intensity from low to high, with numbers from 1 to 4 corresponding to an approximative value of $E_{d,v}$ of 40, 80, 115, 170 J/mm^3 respectively. Sample 10.1 was not fully processed, as the printing was stopped after few layers

due to the appearance of an irregular surface. Therefore, sample 10.1 was not considered for further analysis. Moreover, all samples processed with S2 + 10% SiC exhibited cracks nucleated from the bottom during the printing process (*Fig. 4.7*). Such cracks nucleation and propagation are due to residual stresses and phase transformation within the microstructure, which will be discussed in chapter 5.

Powder mixture	**Sample**	**P [W]**	**v_s [mm/s]**	**$E_{d,v}$ [J/mm^3]**
S2	0.1	200	2000	42
	0.2	200	1000	83
	0.3	200	750	111
	0.4	200	500	167
S2 + 5% SiC	5.1	200	2000	42
	5.2	200	1000	83
	5.3	200	750	111
	5.4	200	500	167
S2 + 10% SiC	10.1	200	2000	42
	10.2	200	1000	83
	10.3	200	700	119
	10.4	200	500	167

Table 4.3: Process parameters and volumetric energy density ($E_{d,v}$) for each sample.

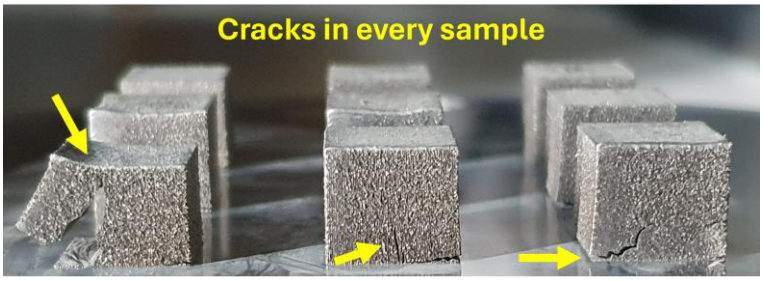


Fig. 4.7: Cracks appearance within samples processed with S2 + 10% SiC.

Fig. 4.8 shows an overview of the cross section of each sample, where the main defects present are highlighted and quantified through the percentage of porosity ε. Samples obtained with S2 powder exhibits lack of fusion defects for low $E_{d,v}$ (sample 0.1) and key-hole porosities for high $E_{d,v}$ (sample 0.4). At the intermediate values of $E_{d,v}$ of 80 and 115 J/mm^3 (sample 0.2, 0.3) only small gas porosities are spotted. With the addition of SiC, the amount of lack of fusion defects significantly increases for low $E_{d,v}$ of 40 J/mm^3, passing from being 1.4% in sample 0.1 to 19% in sample 5.1. Similarly, for $E_{d,v}$ of 80 J/mm^3, sample 0.2 has 0.04% porosity, being mainly small gas porosities, whereas sample 5.2 has 0.2% porosity, associated to lack of fusion defects which increase up to 1% in sample 10.2. For $E_{d,v}$ of 115 J/mm^3 only small gas porosities

are spotted in all samples. At the highest value of $E_{d,v}$, key-hole porosities are visible in all samples (0.4, 5.4, 10.4), with an amount remaining within the same order of magnitude between 0.4 – 0.7%.

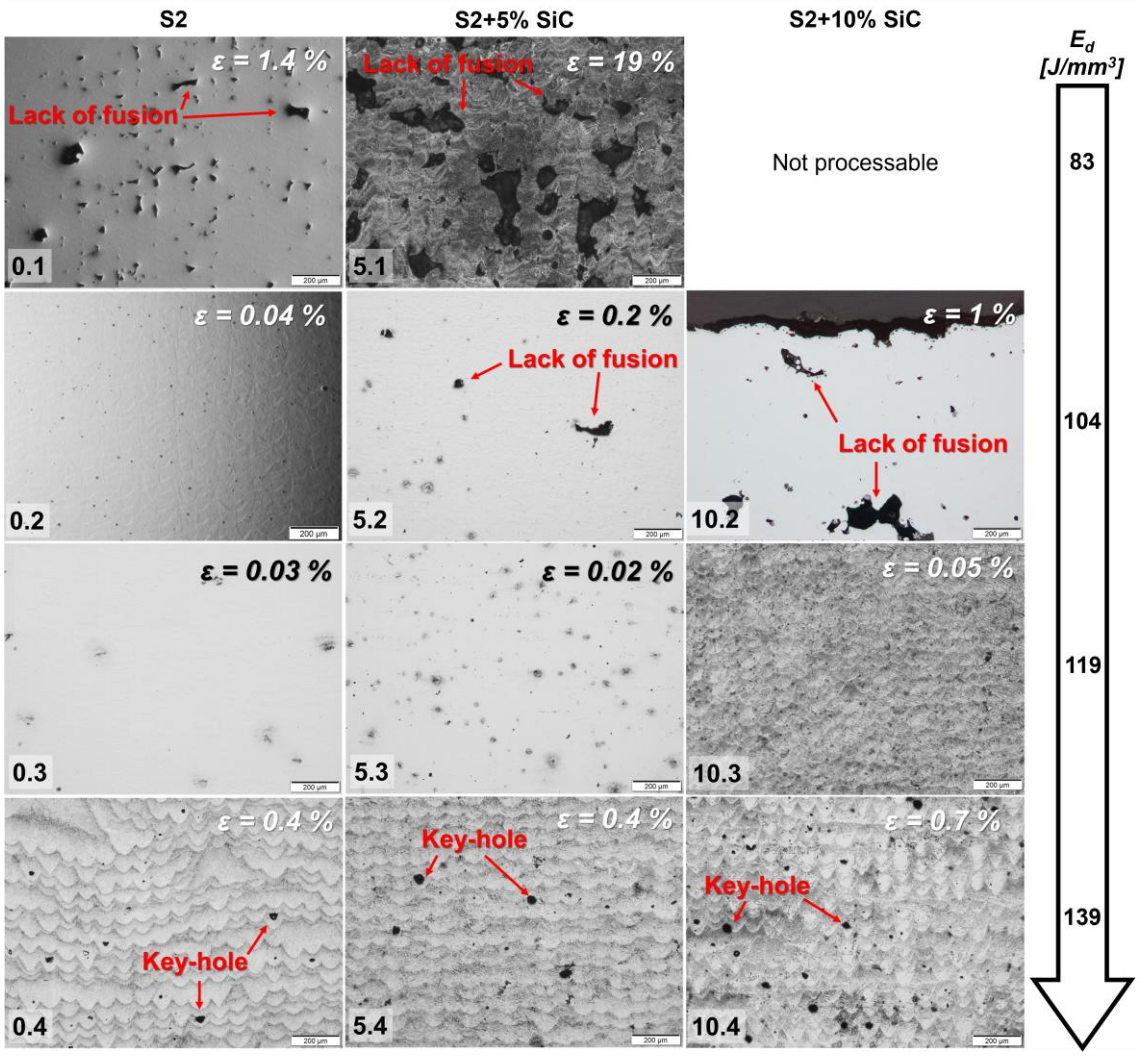


Fig. 4.8: Cross section overviews of each sample, varying the amount of SiC and E_d. Defects are highlighted in terms of type (lack of fusion or key-hole) and amount (percentage of porosity ε). Samples 0.3, 5.2 and 5.3 exhibits imperfections due to the polishing conditions.

Fig. 4.9 shows an overview of the top layer of each sample, where melt pools are highlighted. Shallow melt pools are visible at the lowest value of $E_{d,v}$, with a semi-circular shape and poor overlapping between each track. The irregularity of each track and layer increases passing from sample 0.1 to 5.1. Increasing $E_{d,v}$, in the range 80 – 170 J/mm^3 the melt pool morphology changes to key-hole like, except for sample 10.2 where the melt pool morphology is still semi-circular. Key-hole defects are visible at the bottom of the melt pool of samples 0.4, 5.4, 10.4 generated at the highest $E_{d,v}$ of 170 J/mm^3.

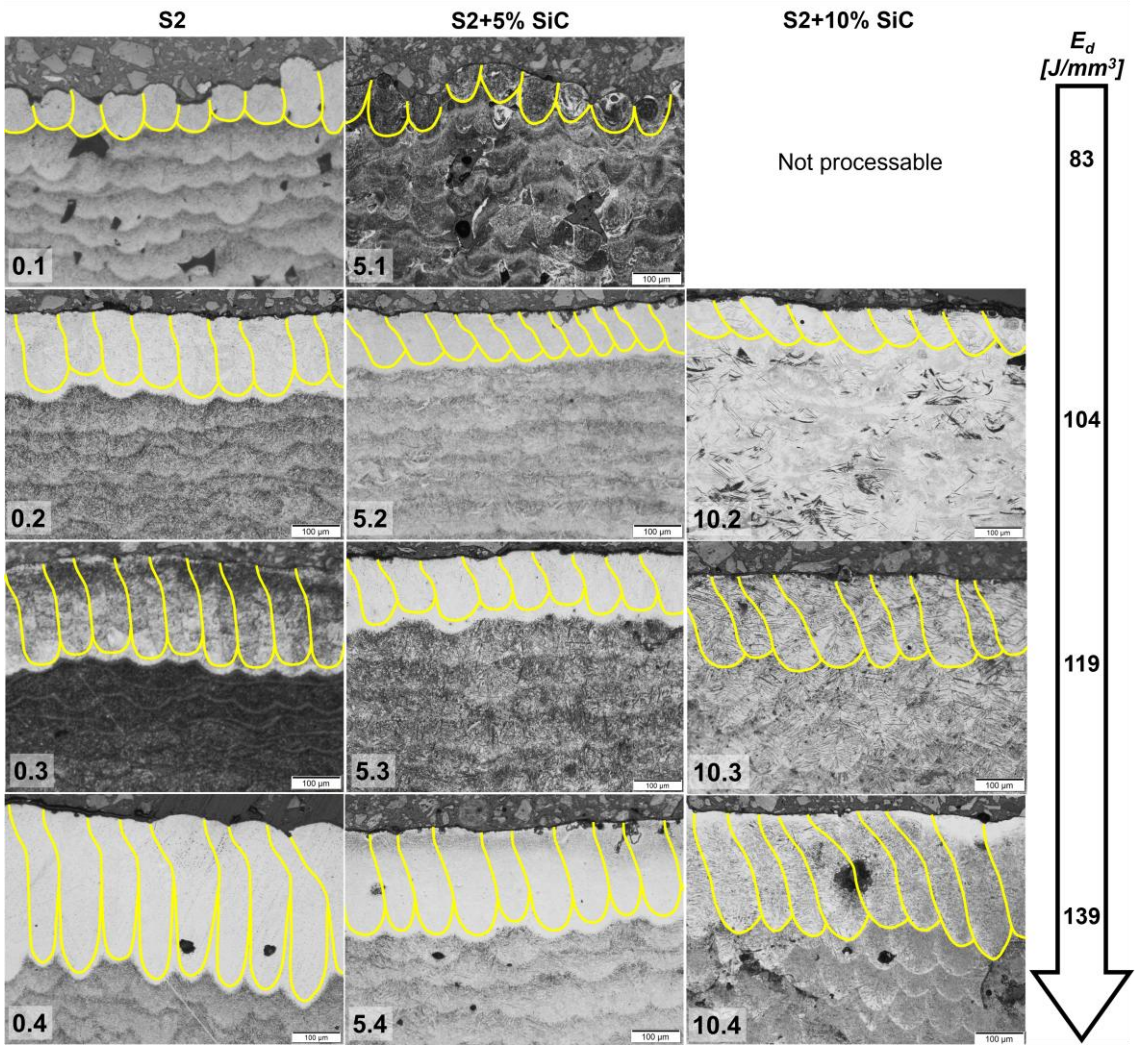


Fig. 4.9: Top layer overviews of each sample, varying the amount of SiC and $E_{d,v}$. Melt pools morphologies are highlighted.

Fig. 4.10 shows the melt pool depth of each sample. In general, the depth clearly increases as $E_{d,v}$ increases. Furthermore, the addition of SiC leads to a decrease in melt pool depth for all $E_{d,v}$. For $E_{d,v}$ of 40 J/mm^3, the depth is similar for S2 and S2 + 5% SiC, being around 100 µm. Similarly, for $E_{d,v}$ of 80 J/mm^3 the depth is between 90 – 120 µm with 5 and 10% SiC, increasing up to 190 µm for S2. For $E_{d,v}$ of 115 J/mm^3, the melt pool depth is within the range 150 – 250 µm. Finally, for $E_{d,v}$ of 170 J/mm^3, all the melt pool depths are higher than 250 µm, with S2 reaching a value close to 350 µm.

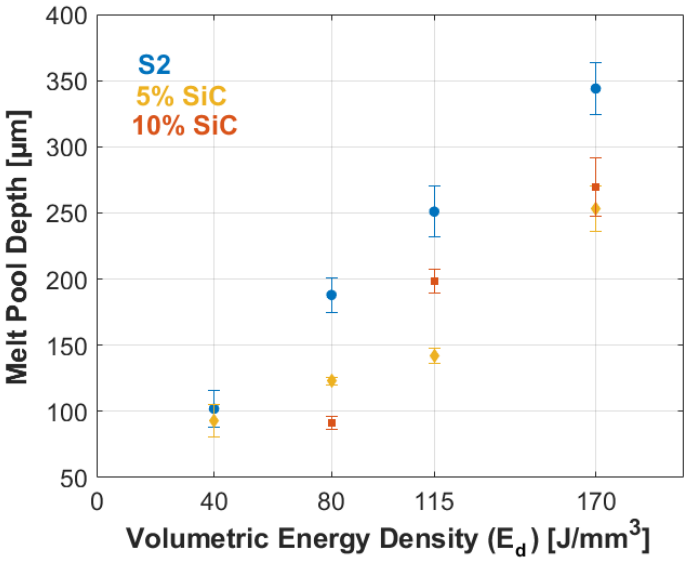


Fig. 4.10: Melt pool depths changes varying the amount of SiC and $E_{d,v}$.

The nature of the melt pools generated during the LPBF process is responsible for the achievement of a sound part, fully dense and defect-free or, on the contrary, for the appearance of defects such as lack of fusion or key-hole porosities. According to *Eq. 4.2*, $E_{d,v}$ depends on four different parameters: laser power, laser scan velocity, layer thickness and hatch distance. The type of melt pool generated depends on the final value of $E_{d,v}$ as well as on the individual value of each single parameter. To consider this aspect, in this work, different values of $E_{d,v}$ are investigated, as a result of the change of the laser scan velocity as the only parameter that is varied. Laser power, layer thickness and hatch distance are fixed. Furthermore, samples obtained by processing the mixture of S2 + 10% (in vol.) SiC exhibited cracks at all $E_{d,v}$. Nevertheless, these samples are still considered in this work for a more comprehensive investigation on the effect of SiC addition on the processability of S2 tool steel powder.

Fig. 4.9 shows the melt pool formed depending on the initial amount of SiC and on the applied $E_{d,v}$. A semi-circular shape with a depth close to 100 µm (*Fig. 4.10*) is observed for low $E_{d,v}$ of 40 J/mm^3. Such morphology is associated with a conductive melt pool type, which leads to the appearance of lack of fusion defects. Indeed, the melt pool generated is not sufficient to melt a significant amount of powders. Only a limited re-melting of the underneath material occurs, thus creating poor overlapping between each track and layer. Despite the similar depth of melt pools of samples 0.1 and 5.1 (*Fig. 4.10*), the addition of 5% SiC leads to the generation of more irregular melt pools in sample 5.1 compared to sample 0.1 (*Fig. 4.9*), worsening the overlapping and the quality of each track and layer with the advancement of the process. Thus, there is a significant increase in the amount of porosity ε from 1.4 up to 19% when passing

from 0 to 5% SiC (*Fig. 4.8*). With 10% SiC, the printing of sample 10.1 was interrupted due to the appearance of an irregular surface. It can be assumed that, in this case, the melt pool formed is shallow and conductive, leading to bad overlapping between each track causing irregular layers that finally affect the surface quality.

Increasing $E_{d,v}$ up to 80 J/mm^3 leads to the appearance of a stable key-hole melt pool for samples 0.2 and 5.2. However, sample 0.2 alone does not exhibit any defect (*Fig. 4.8*). With the addition of 5% SiC, few lack of fusion defects are still present in sample 5.2 (*Fig. 4.8*), due to the generation of a shallow melt pool that leads to poor overlapping (*Fig. 4.9*). Indeed, despite a stable key-hole morphology, the depth of the melt pool is around 120 µm (*Fig. 4.10*), which remains close to the melt pool depth at 40 J/mm^3 (100 µm). In contrast, sample 0.2 exhibits a deeper melt pool around 200 µm, which allows for good overlapping between each track and layer. With 10% SiC (sample 10.2), the melt pool has still a conductive morphology (*Fig. 4.9*) with a depth of 90 µm (*Fig. 4.10*). Thus, as in the case of an $E_{d,v}$ of 40 J/mm^3, lack of fusion defects are present.

At 115 J/mm^3, for all compositions a stable key-hole melt pool is generated, avoiding the presence of defects. Only few little gas porosities are spotted. The depth of the melt pool is between 150 and 250 µm.

Finally, for the highest $E_{d,v}$ of 170 J/mm^3, an unstable key-hole melt pool is visible for all compositions, leading to presence of key-hole defects at the bottom of the melt pool (*Fig. 4.8* and *Fig. 4.9*). Such defects are present in similar amount for all compositions, i.e. less than 1%.

For all the processed powder mixtures, a sound part free of process-induced defects is obtained when the melt pool exhibits a stable key-hole like morphology with a depth between 150 and 250 µm. The threshold for the change from conductive to stable key-hole melt pool is observed to be of $E_{d,v}$ of 80 J/mm^3 for the powder mixtures S2 and S2 + 5% SiC. However, with the addition of 5% SiC, a proper stable key-hole melt pool with sufficient depth is only generated at 115 J/mm^3, which remains appropriate for S2 powder alone. With 10% SiC, the threshold for the change from conductive to stable key-hole melt pool is shifted to $E_{d,v}$ of 115 J/mm^3. When further increasing $E_{d,v}$ up to 170 J/mm^3, an unstable key-hole melt pool is generated for all compositions. Therefore, the addition of SiC restrict the optimal process window to obtain a sound part. Such restriction of the optimal process window may be ascribed to powder properties such as particle size distribution, laser energy absorptivity and reflection as well as packing density and conductivity of both the powders and solidified material. *Fig. 4.11* shows

a schematic representation of the melt pool types and corresponding defects with varying $E_{d,v}$ and SiC addition.

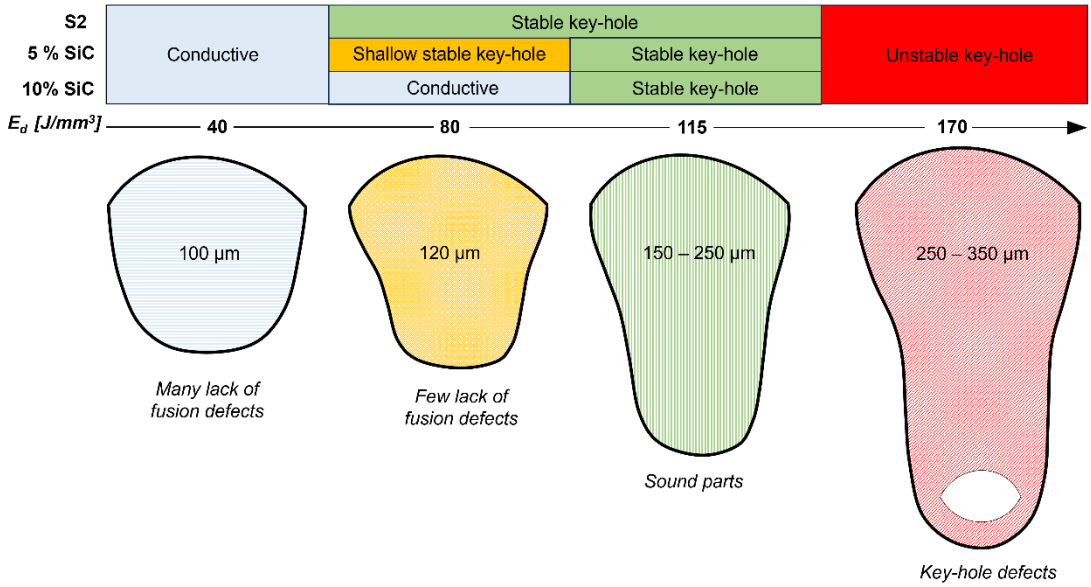


Fig. 4.11: Schematic representation of the types of melt pool generated during the LPBF process with varying E_d and SiC addition. A stable key-hole like melt pool with a depth between 150 and 250 µm is desired to obtain a sound part. For S2 parts, such melt pool is obtained for E_d between 80 and 115 J/mm^3, being limited to 115 J/mm^3 when 5 and 10% SiC is added.

4.3.2 Effect of preheating on S2 + 10% SiC

The main objective is to obtain a sound part. In view of cracks appearance during the processing of S2 + 10% SiC (*Fig. 4.7*), a preheating of the platform was implemented, as this has been proved beneficial to avoid cracks (section 2.3). The temperature for the preheating was set at 500 °C, i.e. the maximum achievable for our Aconity Mini printer. Furthermore, such high temperature was also chosen to try and promote in-situ graphitization during the LPBF process, which will be further discussed in chapter 5. Other preheating temperatures may have been correct for the achievement of a sound part (e.g. 200, 300, 400°C), but this was not investigated in the current work. The current section will discuss the effect of the preheating on the processability of S2 + 10% SiC, referring to results obtained without preheating. Considering the objective to obtain a sound part, only a restricted combinations of parameters were chosen starting from the results explained in the previous chapters, according to the 'dynamic refinements of parameters' approach. The combinations of parameters used and corresponding samples' denomination are listed in *Table 4.4*. The characterization of sample 10.25 was

difficult due to the presence of a big vertical crack (first sample from the left in *Fig. 4.7*) and thus, some data are missing.

	Sample	**P [W]**	**v_s [mm/s]**	**$E_{d,v}$ [J/mm^3]**
Without preheating	10.2	200	1000	83
	10.25	200	800	104
	10.3	200	700	119
	10.35	200	600	139
With preheating 500 °C	10.2P	200	1000	83
	10.25P	200	800	104
	10.3P	200	700	119
	10.35P	200	600	139

Table 4.4: Process parameters of samples processed from S2 + 10% SiC with and without preheating the substrate at 500 °C.

Fig. 4.12 shows a cross section overview of each sample. At low $E_{d,v}$ (83 J/mm^3) lack of fusion are present in both cases with and without preheating. Key-hole porosities are found at high $E_{d,v}$ (139 J/mm^3). Samples with intermediate $E_{d,v}$ exhibited only a few small gas porosities. In general, the percentage of porosity ε remains similar with or without preheating. As shown in *Fig. 4.7*, cracks appeared in every sample without preheating. On the contrary, with the same parameters no cracks were present when preheating was applied.

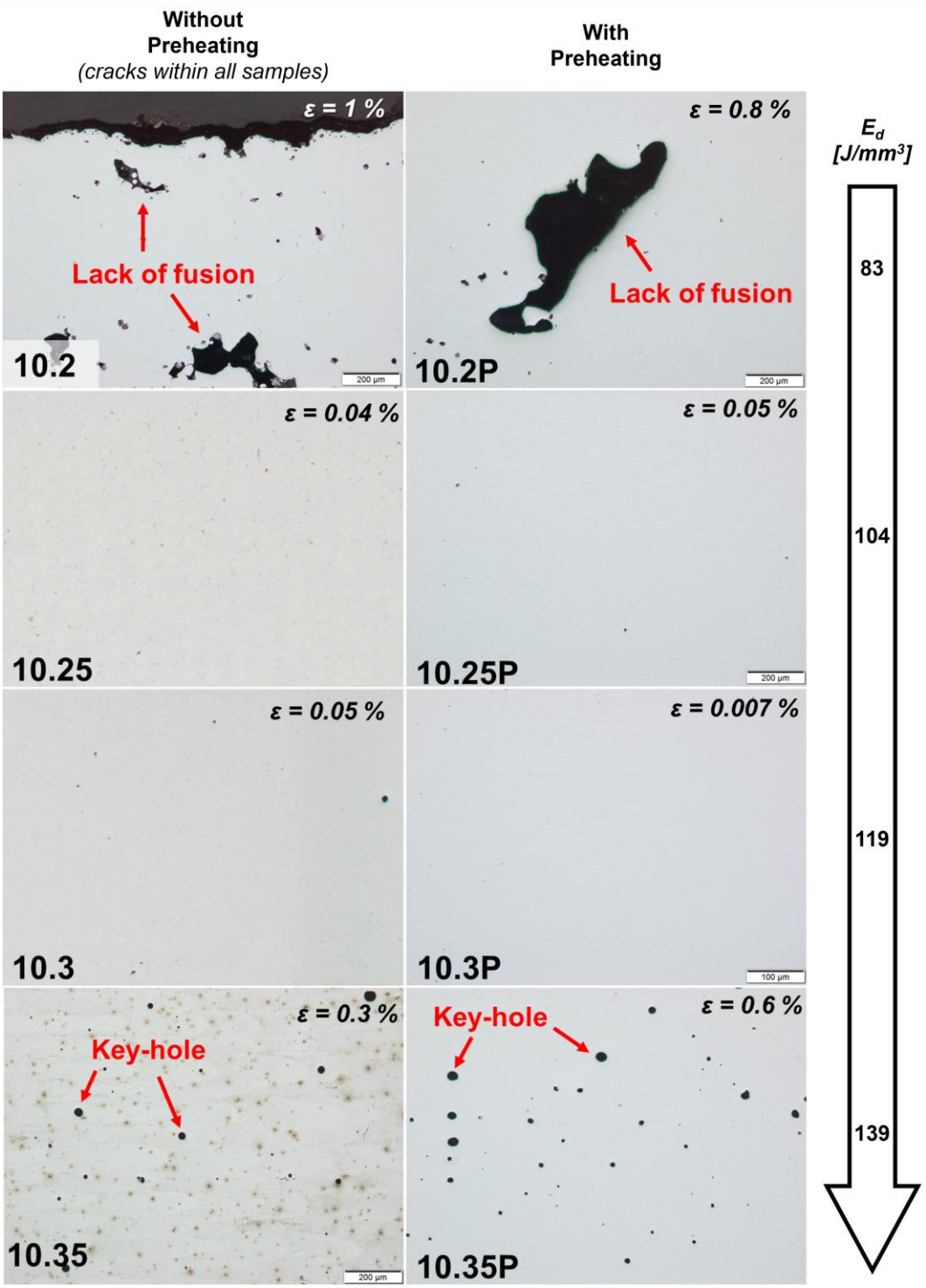


Fig. 4.12: Cross section overviews of each sample made of S2 + 10% SiC with and without preheating the substrate at 500 °C, varying the amount of $E_{d,v}$. Defects are highlighted in terms of type (lack of fusion or key-hole) and amount (percentage of porosity ε).

Fig. 4.13 shows the top layer of each sample. Despite some issues in revealing the morphology for sample 10.25, 10.25P, 10.3P, in general the morphology is similar at the same $E_{d,v}$ with and without preheating. The explanation of the defects generated based on the type of melt pool is the same to that reported in section 4.3.1. The novelty here is that applying the preheating lead to a small increase in melt pool depth (~ 20 µm) at all $E_{d,v}$.

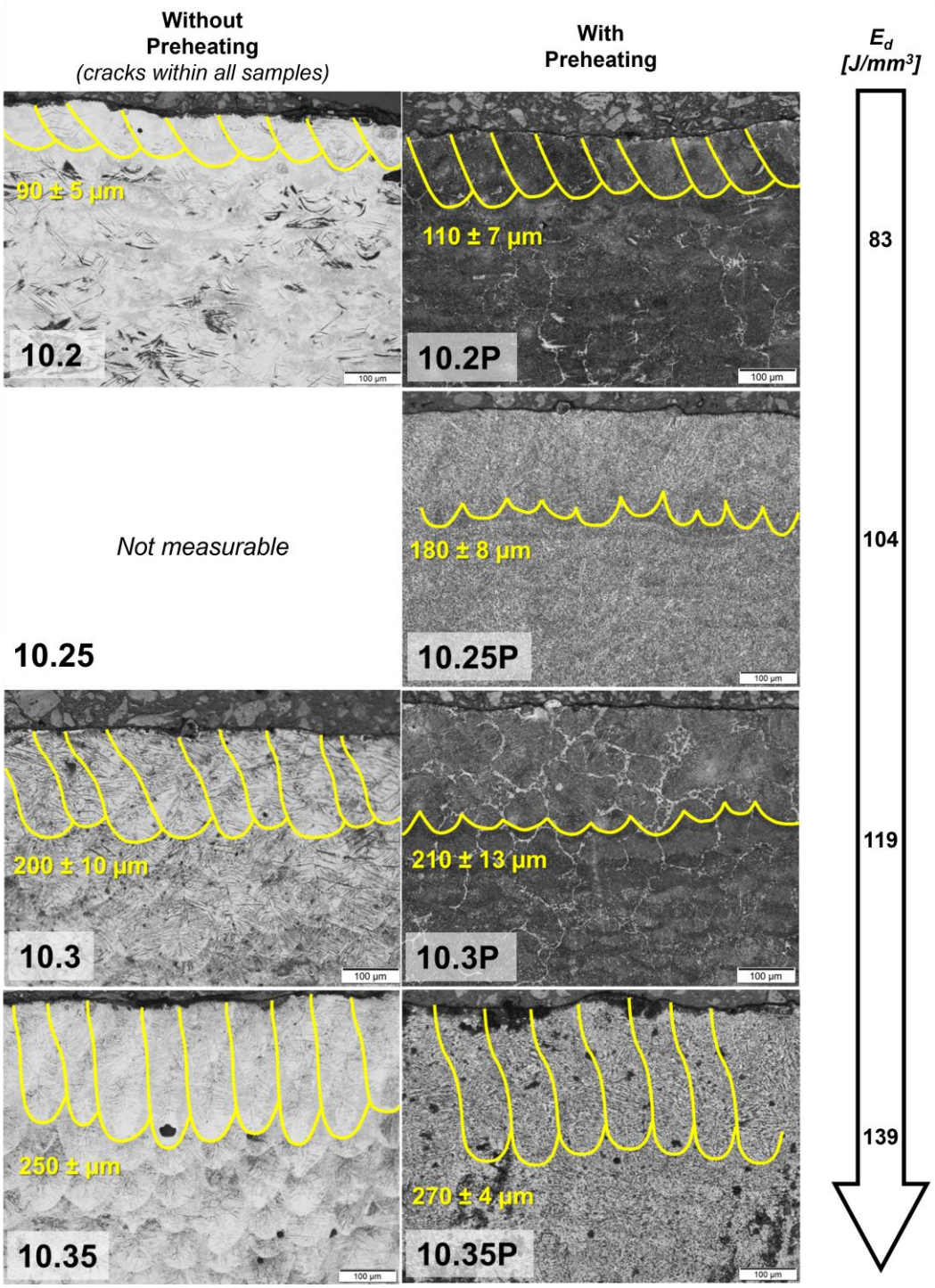


Fig. 4.13: Top layer overviews of each sample, with and without preheating the substrate at 500 °C, varying the amount of $E_{d,v}$. Melt pools morphologies and depth are highlighted.

Applying the preheating proved to be advantageous for the achievement of sound parts, as no cracks were observed in any of the samples. Indeed, maintaining the preheating of the substrate for all the duration of the process served as a source of heat which is conducted from the substrate through the above solidified material and powder bed, where a certain temperature is reached. Such temperature can change when increasing the distance from the substrate (*Pannitz, 2021*). In such case, depending on the distance from the substrate, the material can experience a different solidification history, leading to an inhomogeneous microstructure. As will be explained in chapter 5, the microstructure was found homogeneous in the whole cross section, thus assuming that the temperature reached in the solidified material during the process was the same at all heights. This is due to the low height of the printed samples (10 mm) as well as to the efficient preheating system of the LPBF device. However, the set preheating temperature is the one achieved from the heating unit, which is placed below the substrate. The substrate is reheated through heat conduction from the resistive heating unit. Therefore, a lower temperature than the one set might be reached in the substrate, which might be also decreased when increasing distance from the substrate, due to heat dissipation. For a more precise and comprehensive work, infrared cameras or other systems which can detect temperatures and heat should be installed in the machine, which is not currently the case. Therefore, in this work it is assumed that the preheating value set (500 °C) corresponds to the temperature reached on the substrate as well as on the solidified material until a height of 10 mm.

In view of the above considerations, when the laser scans a new layer of powder and a melt pool is created, this melt pool is at a certain temperature which can be up to 4000 K (*Hooper, 2018*). Underneath the melt pool, the solidified material is at a temperature somewhat higher than room temperature. Therefore, there is a certain thermal gradient between melt pool and underneath solidified material, which is higher in the absence of preheating. Such thermal gradient affects the solidification sequence of the melt pool from liquid to solid state, as well as the solid-state transformations that occur within the Heat Affected Zone (HAZ). As chapter 5 will better explain, the microstructures obtained with and without preheating are different, with the one without preheating being more prone to cracks nucleation and propagation due to higher thermal gradients.

Moreover, from the results showed above, it can be deducted that applying the preheating did not affect much the process-induced defects. Indeed, lack of fusions are still present at low $E_{d,v}$, as well as key-hole porosities at high $E_{d,v}$. In the case of intermediate values, all samples exhibited few gas porosities and a quite low porosity ε. The appearance of similar defects with

and without preheating is due to the formation of similar melt pools, as visible in *Fig. 4.13*. Indeed, a shallow stable key-hole melt pool is present at 83 J/mm^3, whereas an unstable key-hole like melt pool is present at high $E_{d,v}$ (139 J/mm^3). At intermediate values, a stable key-hole melt pool is formed. The only difference is the increase in melt pool depth when preheating was applied, which is observed to be around 20 µm in all cases. This phenomenon can be linked to the fact that with preheating additional energy comes from the substrate to the powder bed, increasing the energy within the laser-powder interaction (*Qin, 2023*). Such increase in energy leads to the formation of a deeper melt pool in both conductive and key-hole mode regime, due to an increase of heat conduction, evaporation, recoil pressure and energy absorption due to laser ray reflections, as shown in a recent work where experimental and modelling data where compared (*Chen, 2021*).

Therefore, in terms of process-induced defects, applying the preheating did not shift the process map and thus, the best sound sample remains the one achieved with the parameters set at 200 W of power, 700 mm/s of scan velocity and 119 J/mm^3 of $E_{d,v}$. Such sample (10.3P and 10.3 with and without preheating respectively) will be considered for the metallurgical characterization in chapter 5.

4.3.3 Difficult processability of S2 + 15% SiC

After demonstrating the beneficial effect of the preheating for the processability of S2 + 10% SiC, the powder mixture S2 + 15% SiC was processed directly with preheating at 500°C, without passing through a trial without preheating. Up to now, the addition of SiC required higher $E_{d,v}$ for the achievement of sound parts. Therefore, for S2 + 15% SiC, high $E_{d,v}$ up to 278 J/mm^3 were tested by varying v_s while keeping a fixed P of 200 W. *Table 4.5* shows the parameters used.

Sample	P [W]	v_s [mm/s]	$E_{d,v}$ [J/mm^3]
15.1	200	300	278
15.2	200	400	208
15.3	200	500	167
15.4	200	600	139
15.5	200	700	119
15.6	200	800	104
15.7	200	900	93
15.8	200	1000	83
15.9	200	1200	69

Table 4.5: Processing parameters used for S2 + 15% SiC.

Fig. 4.14 shows a cross section overview of each sample. All samples exhibit defects, varying from key-hole for high $E_{d,v}$ of 208 and 278 J/mm^3 (sample 15.1, 15.2) to lack of fusion for lower $E_{d,v}$ from 104 to 69 J/mm^3 (sample 15.6, 15.7, 15.8, 15.9). At intermediate $E_{d,v}$ from 119 to 167 J/mm^3 (sample 15.3, 15.4, 15.5) a combination of lack of fusion and key-hole defects occurred. Such outcomes showed the difficult processability of the powder mixture S2 + 15% SiC. There are several reasons for such failure, from the high content of carbon within the final chemical composition (up to 2.46 wt.%) to the physical and rheological properties of the powder mixture. Further explanations will be given in section 4.4 and chapter 5.

In order to improve the processability of the powder mixture S2 + 15% SiC, another approach was tested, i.e. changing the laser beam diameter. Such method is described in Appendix A. However, it was not possible to achieve sound samples. Some possible solutions are described and discussed in chapter 7 as perspectives of the work.

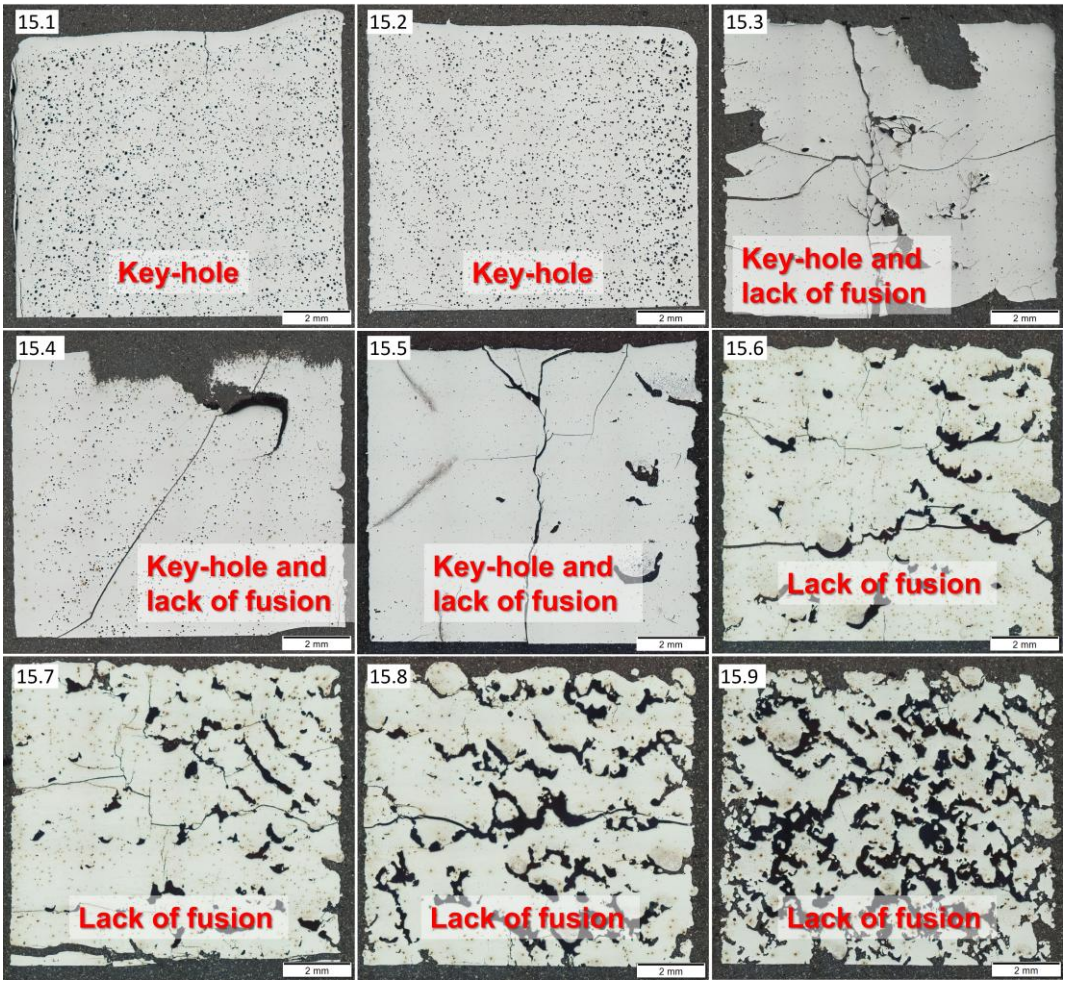


Fig. 4.14: Cross section overviews of each sample made of S2 + 15% SiC with preheating the substrate at 500 °C. Defects are highlighted in terms of type (lack of fusion or key-hole).

4.4 Effect of powder properties on processability

The processability of the different powder mixtures was deeply dependent on both rheological and physical properties of powders such as the Particle Size Distribution (PSD), flowability, packability and laser absorptivity. Such properties were discussed in a previous section (3.5) and are used here to explain their impact on the processability.

The dimensions and morphology (conductive or key-hole) of the melt pool generated during the process was discussed in the previous sections (4.3.1 and 4.3.2). The characteristics of the melt pool were correlated with $E_{d,v}$ and the content of SiC. In general, at a fixed $E_{d,v}$, the melt pool depth decreases when increasing SiC content, notwithstanding whether preheating was applied or not. The processability of pure S2 powders was easy in view of the intrinsic properties of this powder, appositely produced for LPBF. In contrast, SiC powder was not customized for the LPBF process and, already during the preparation of the mixtures, it revealed a problematic handling with the necessity of optimizing the preparation methodology (section 3.4).

As mentioned in section 3.5.2, absorption and reflection mechanisms induced by the interaction between laser and powders are responsible for the formation of the melt pool. In particular, laser transformation has two steps (*Khorasani, 2022*). In the first step, photons of the laser are absorbed by the electron of the powder atoms. This leads to an increase in the internal energy and energy transfer occurs by surface vibration. When the induced energy exceeds a certain amount, the energy transfer occurs through intermolecular vibration which can break chemical bonding, and melting takes place. Thus, the melt pool is formed. In general, higher melt pool depths and volumes are promoted by a high absorption ratio. Thus, low melt pool depths are achieved when increasing the content of SiC, in view of its lower absorbance (section 3.5.2). To enhance the processability for high SiC content, an increase in $E_{d,v}$ was necessary (section 4.3). Indeed, higher $E_{d,v}$ allows to achieve higher temperatures thus promoting higher absorptivity and, as a consequence, higher melt pool volumes, favouring the appearance of a stable key-hole morphology (*Khorasani, 2021*, *2022*).

In addition, adding SiC affects the PSD, with a consequent influence on the packability behaviour of the mixtures. In particular, increasing the content of SiC leads to an increase in the volume fraction of the population of small SiC particles at the micro- (< 10 μm) and at the nano-scale (< 1 μm), according to the PSD shown in section 3.4. In contrast, the volume fraction of the population of bigger particles (D50 = 32 μm) decreases as the content of SiC

increases. This bigger population is composed by both S2 powders and intact SiC granules. As a result of these phenomena, the packability properties of the mixtures are affected. In particular, both the bulk and tapped density of the mixtures decrease with the increase in SiC content. Low packing density are characterized by large open spaces between particles, allowing a high penetration depth of the laser. This can lead to a rapid build-up of heat during the action, which in turn causes an explosion due to a sudden expansion of the gas trapped in the interparticle spaces (*Pal, 2021*). This phenomenon leads to massive material spattering, through which the melt pool loses a lot of material. Furthermore, low packing density means less material within the same volume, reducing the melt pool depth caused by the absence of particles ahead of the wetting front of the melt pool (*Gärtner, 2023*).

As a consequence of lower absorbance and packing density with the increase in SiC in the mixture, lower depths of the melt pool are achieved, thus negatively affecting the processability as explained in section 4.3. A schematic representation of these phenomena is shown in *Fig. 4.15*.

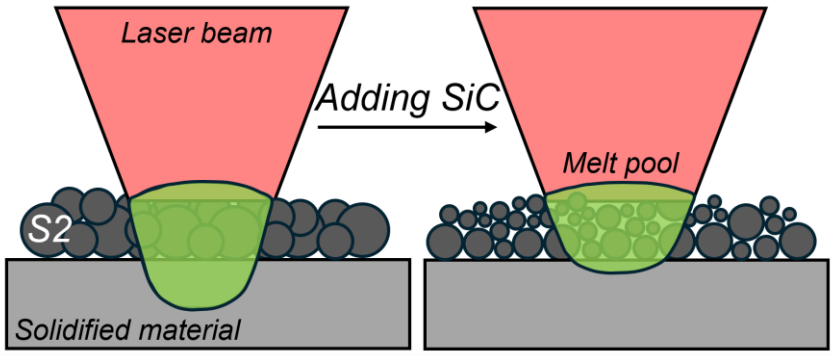


Fig. 4.15: Schematic representation of the effect of SiC addition on the melt pool depth.

Increasing $E_{d,v}$ to promote a stable processability is valid only for a content of SiC up to 10%. The mixture S2 + 15% SiC showed difficult processability, with defects present at all the investigated $E_{d,v}$ (section 4.3.3). All the phenomena explained earlier are accentuated during the processing of this mixture, such as lower absorptivity, lower packing density and higher spattering which was observed during the LPBF experiment. Furthermore, applying the preheating on the substrate (500°C) visually worsened the quality of the powder bed (*Fig. 4.16*). This phenomenon further increased the difficulties to achieve a stable melt pool, in view of the inhomogeneous distribution and of the lack of powders in some areas.

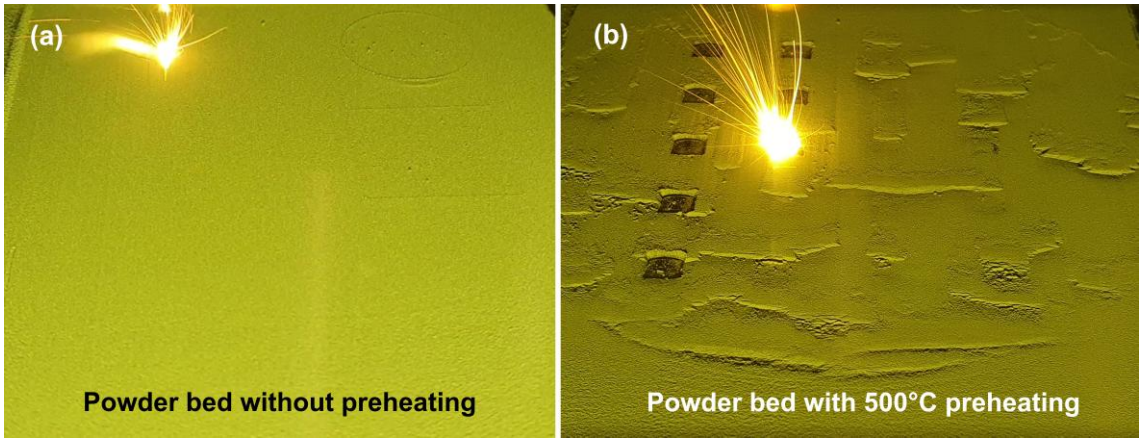


Fig. 4.16: Effect of substrate preheating on the quality of the powder bed during LPBF process.

As mentioned in section 2.3.2, no work in the literature has discussed the effect of preheating on the rheological properties of powders and the quality of the powder bed. This lack is due to the absence of in-situ or ex-situ devices capable of analysing the effect of temperature on the rheological behaviour of powders. For instance, Granudrum only allows to perform tests up to a temperature of 200°C, far from the preheating temperatures that can be set in the LPBF printer (500°C with our Aconity Mini device, or even higher with other commercial devices). The quality of the powder bed is affected by the spreadability of powders (section 2.3.2). This rheological property depends on the speed of the recoater, which was set at 50 mm/s based on the results obtained with Granudrum at room temperature (section 3.5.1). This speed was maintained for all experiments with LPBF, whether preheating was applied or not. To optimize the spreadability with high preheating temperatures, further investigations should be carried out in the future by changing the speed of the recoater. However, despite the bad quality of the powder bed, the mixture S2 + 10% SiC was successfully processed even with a preheating at 500°C. Therefore, in this work, the poor quality of the powder bed is not the main responsible for the poor processability of S2 + 15% SiC. With this mixture, the problem more likely lies with the nature of the purchased SiC powder. Thus, this mixture might be processable with different types of SiC. Further investigations should be carried out in the future.

4.5 Conclusions

- The processability of the reference material AISI S2 tool steel has been investigated starting from single tracks experiments with 53 combinations of parameters, subsequently refined to 20 sets of parameters to produce multi-tracks and layers (cubes). The process map has been built considering surface morphology, density measurements, defects characterization and quantification, tracks overlapping and melt pool morphology.
- Compared to the process map of AISI S2, a restriction of the optimal process window was observed when adding SiC, due to a change in melt pool morphology and dimensions. A stable key-hole melt pool was necessary to achieve samples free of process-induced defects (lack of fusion and key-hole). Such melt pool morphology has a depth between 150 and 250 μm and was found for $E_{d,v}$ ranging from 80 J/mm^3 to 115 J/mm^3 for S2, limited to 115 J/mm^3 when SiC is added in proportion of 5 or 10% in volume.
- Although being free of process-induced defects, even the sample S2 + 10% SiC processed with optimal parameters exhibited cracks. Applying a preheating on the substrate (500°C) was necessary to achieve crack-free samples. Applying the preheating only allows to avoid cracks, since no shift of the process map was observed, although there is a little increase in melt pool depth (20 μm).
- The powder mixture S2 + 15% SiC exhibited difficult processability, since no sound samples were achieved. Defects are present for all the $E_{d,v}$ investigated.
- Rheological and physical properties of powders had an important impact on the processability. The addition of SiC led to a decrease in absorbance and packing density, thus decreasing the dimensions of the melt pool.

4.6 References

Chen, Q., Zhao, Y., Strayer, S., Zhao, Y., Aoyagi, K., Koizumi, Y., … To, A. C. (2021). "Elucidating the effect of preheating temperature on melt pool morphology variation in Inconel 718 laser powder bed fusion via simulation and experiment." Additive Manufacturing, 37(September 2020), 101642. https://doi.org/10.1016/j.addma.2020.101642

Chowdhury, S., Yadaiah, N., Prakash, C., Ramakrishna, S., Dixit, S., Gupta, L. R., & Buddhi, D. (2022). "Laser powder bed fusion: a state-of-the-art review of the technology, materials, properties & defects, and numerical modelling." Journal of Materials Research and Technology, 20, 2109–2172. https://doi.org/10.1016/j.jmrt.2022.07.121

Gärtner, E., Witte, A., Peter, N. J., Devulapalli, V., Ellendt, N., Dehm, G., … Mädler, L. (2023). "Melt pool signatures of TiN nanoparticle dry-coated Co25Cr25Fe25Ni25 metal powder in laser-powder-bed-fusion." Materials and Design, 226. https://doi.org/10.1016/j.matdes.2023.111626

Hooper, P. A. (2018). "Melt pool temperature and cooling rates in laser powder bed fusion." Additive Manufacturing, 22(May), 548–559. https://doi.org/10.1016/j.addma.2018.05.032

Huang, Y., Fleming, T. G., Clark, S. J., Marussi, S., Fezzaa, K., Thiyagalingam, J., … Lee, P. D. (2022). "Keyhole fluctuation and pore formation mechanisms during laser powder bed fusion additive manufacturing." Nature Communications, 13(1), 1–11. https://doi.org/10.1038/s41467-022-28694-x

Khorasani, M., Ghasemi, A. H., Leary, M., O'Neil, W., Gibson, I., Cordova, L., & Rolfe, B. (2021). "Numerical and analytical investigation on meltpool temperature of laser-based powder bed fusion of IN718." International Journal of Heat and Mass Transfer, 177, 121477. https://doi.org/10.1016/j.ijheatmasstransfer.2021.121477

Khorasani, M., Ghasemi, A. H., Leary, M., Sharabian, E., Cordova, L., Gibson, I., … Rolfe, B. (2022). "The effect of absorption ratio on meltpool features in laser-based powder bed fusion of IN718." Optics and Laser Technology, 153(January), 108263. https://doi.org/10.1016/j.optlastec.2022.108263

Pal, S., Gubeljak, N., Bončina, T., Hudák, R., Toth, T., Zivcak, J., … Drstvenšek, I. (2021). "The effects of locations on the build tray on the quality of specimens in powder bed additive manufacturing." International Journal of Advanced Manufacturing Technology, 112(3–4), 1159–1170. https://doi.org/10.1007/s00170-020-06563-5

Pannitz, O., Lüddecke, A., Kwade, A., & Sehrt, J. T. (2021). "Investigation of the in situ thermal conductivity and absorption behavior of nanocomposite powder materials in laser powder bed fusion processes." Materials and Design, 201. https://doi.org/10.1016/j.matdes.2021.109530

Platl, J., Leitner, H., Turk, C., Demir, A. G., Previtali, B., & Schnitzer, R. (2021). "Defects in a Laser Powder Bed Fused Tool Steel." Advanced Engineering Materials, 23(12), 1–11. https://doi.org/10.1002/adem.202000833

Qin, S., Saewe, J., Kunz, J., Herzog, S., Kaletsch, A., Schleifenbaum, J. H., & Broeckmann, C. (2023). "Influence of Preheating Temperature on Microstructure Evolution and Hardness of High-Speed Steel AISI M50 Processed by Laser Powder Bed Fusion." Steel Research International, 94(6). https://doi.org/10.1002/srin.202200784

Ryder, M. A., Montgomery, C. J., Brand, M. J., Carpenter, J. S., Jones, P. E., Spangenberger, A. G., & Lados, D. A. (2021). "Melt Pool and Heat Treatment Optimization for the Fabrication of High-Strength and High-Toughness Additively Manufactured 4340 Steel." Journal of Materials Engineering and Performance, 30(7), 5426–5440. https://doi.org/10.1007/s11665-021-05836-8

Wang, D., Wu, S., Fu, F., Mai, S., Yang, Y., Liu, Y., & Song, C. (2017). "Mechanisms and characteristics of spatter generation in SLM processing and its effect on the properties." Materials and Design, 117, 121–130. https://doi.org/10.1016/j.matdes.2016.12.060

Zhang, B., Li, Y., & Bai, Q. (2017). "Defect Formation Mechanisms in Selective Laser Melting: A Review." Chinese Journal of Mechanical Engineering (English Edition), 30(3), 515–527. https://doi.org/10.1007/s10033-017-0121-5

Zheng, H., Li, H., Lang, L., Gong, S., & Ge, Y. (2018). "Effects of scan speed on vapor plume behavior and spatter generation in laser powder bed fusion additive manufacturing." Journal of Manufacturing Processes, 36, 60–67. https://doi.org/10.1016/j.jmapro.2018.09.011

Chapter 5

Macro- and microstructures in as-built conditions and after graphitization thermal treatment

Contents

5.1 Introduction 122
5.2 Metallurgical characterization in the as-built conditions 123
5.2.1 Macrostructures and solidification modes 123
5.2.1.1 Identification of solidification sub-structures within AISI S2 123
5.2.1.2 Effect of SiC and preheating on changes in macrostructures 125
5.2.2 Microstructures and in-situ thermal cycles 131
5.2.2.1 Solidification sequence of reference alloy AISI S2 131
5.2.2.2 Effect of SiC on martensitic transformation 138
5.2.2.3 Microstructural changes induced by preheating 141
5.2.2.3.1 Identification of phases within top layer 141
5.2.2.3.2 Heat Affected Zone 150
5.3 Graphitization mechanism during thermal treatment 152
5.4 Conclusions 159
5.5 References 160

5.1 Introduction

The development of the process maps discussed in chapter 4 allowed to select the best process parameters to achieve sound samples. The latter will be considered in this chapter for their macro- and micro-structural characterization in the as-built conditions. The mechanism for graphitization will also be discussed considering the sample obtained from S2 + 10% SiC powder mixture processed with preheating. The innovative microstructure achieved with enhanced wear properties (see further in chapter 6) gave the possibility to deposit a patent[9].

[9] Saggionetto, E., Tchuindjang, J. T., Mertens, A. "GRAPHITE-BASED STEEL ALLOY AND METHOD FOR PRODUCING IT USING LASER POWDER BED FUSION". Europe: application ref. n° EP24167458 (28/03/24); International: application ref. n° PCT/EP2025/058128 (25/03/25), published under WO/2025/202196

5.2 Metallurgical characterization in the as-built conditions

Metals microstructures often reveal a complex hierarchical organization. Macrostructure stands for what is inherited from the solidification process, such as grain types which can be more or less linked to the solidification mode (cellular, dendritic, etc.). These structures will be discussed in section 5.2.1. Meanwhile, the microstructure, explained in section 5.2.2, is given by the phases that are present at room temperature and in this case, after solid-state transformations. Features of macro- and micro-structures usually intersects each other. Thus, it is not possible to explain their characteristics in a distinct way. For instance, in what follows, characteristics of the microstructure will be used to explain the macrostructure and vice versa.

5.2.1 Macrostructures and solidification modes

The macrostructure involves features that remind of what happened during the solidification, and which is not evident to distinguish because of the subsequent solid-state transformations. However, the assumption here it that the reminiscence of the solidification structures is given by segregation features that account for cells or dendrites boundaries, named as solidification sub-structures. Cells or dendrites boundaries represent micro-segregations occurring during solidification, and the thickness of such boundaries is very small (< 1 μm). Nevertheless, they can be clearly determined under SEM. The identification of primary solidification macrostructures was assessed within the top layer, thus considering the original structure which was not heat affected due to the deposition of a subsequent layer.

5.2.1.1 Identification of solidification sub-structures within AISI S2

As will be better explained in a later section (5.2.2.1), the main constituents of the microstructure within the top layer of AISI S2 are the martensitic laths, formed after a solid-state transformation of the parent original austenite. According to (*Kitahara, 2006*), lath martensite has a three-level hierarchy in its morphology, i.e. laths, blocks, and packets. The martensite lath is a single crystal of martensite with a high density of lattice defects. The block is aggregations of the laths with the same crystallographic orientation (variant). The packet is aggregations of the blocks with the same $\{1\ 1\ 1\}_\gamma$ plane in austenite. Several packets can appear within a single prior austenite grain. Each packet includes several blocks that are composed of the martensite laths with different variants, but the same $\{1\ 1\ 1\}_\gamma$ planes. Similar outcomes were achieved in the work of (*Morito, 2006*), while using Transmission Electron Microscope (TEM) analysis together with EBSD analysis. Therefore, when considering each martensitic lath as a variant, there are typical orientation relationships between group of variants and the

parent austenitic grain that can help rebuild the original grain. This is explained in the work of (*Cayron, 2006*), who started to do that on a theoretical basis before developing his own software for the Automatic Reconstruction of Parent Grains (ARPGE) (*Cayron, 2007*). Typical studies based on the use of ARPGE can be found in (*Cayron, 2014*, *2018*; *Suikkanen, 2013*).

In this work, such advanced way to investigate the original grains was not used. Meanwhile, the grains were identified based on SEM observations, in particular on visual orientations of both martensitic laths and of the thin and parallel segregation sub-structures. Therefore, the following results need further validations that can be carried out in future works.

The parallel segregations sub-structures are associated to a cellular solidification mode within each grain. The orientation of each grain is dictated by thermal gradients and by the scan strategy used during the LPBF process. The thermal gradient within the melt pool is driven by the gaussian distribution of the laser power. Indeed, such power distribution leads to achieve certain temperatures within the melt pool, being higher in the centre (from bottom to top) and lower on the sides. Therefore, the thermal gradient in the centre of the melt pool is vertical, whereas on the sides it gradually changes direction when approaching the centre (*Pham, 2020*). As a consequence, grains growth follows the direction of such thermal gradients, leading to the appearance of a central vertical grain surrounded by lateral grains orientated towards the centre (*Fig. 5.1*a). When a new layer of powder is scanned by the laser, the new melt pool interacts with the solidified material underneath. Because the thermal gradient is vertical at the centre of the melt pool, the vertical grain of the previous solidified melt pool can grow in a columnar mode within the new melt pool, leading to the typical epitaxial grain growth (*Fig. 5.1*c). In this mode, vertical grains grow epitaxially from the bottom to the top of the sample. Epitaxial growth also occurs between grains of adjacent melt pools (*Fig. 5.1*a,b). The epitaxial grains growth between two adjacent melt pool affects the cellular sub-structure with a side branching effect, where intercellular segregations form an angle of 90° between each other (*Fig. 5.1*d,e). These phenomena are linked to the scan strategy used in this work, consisting of a rotation of 90° between each new layer of powder. Therefore, the vertical thermal gradient is in the same direction as the building direction, thus favouring the epitaxial grain growth (*Pham, 2020*).

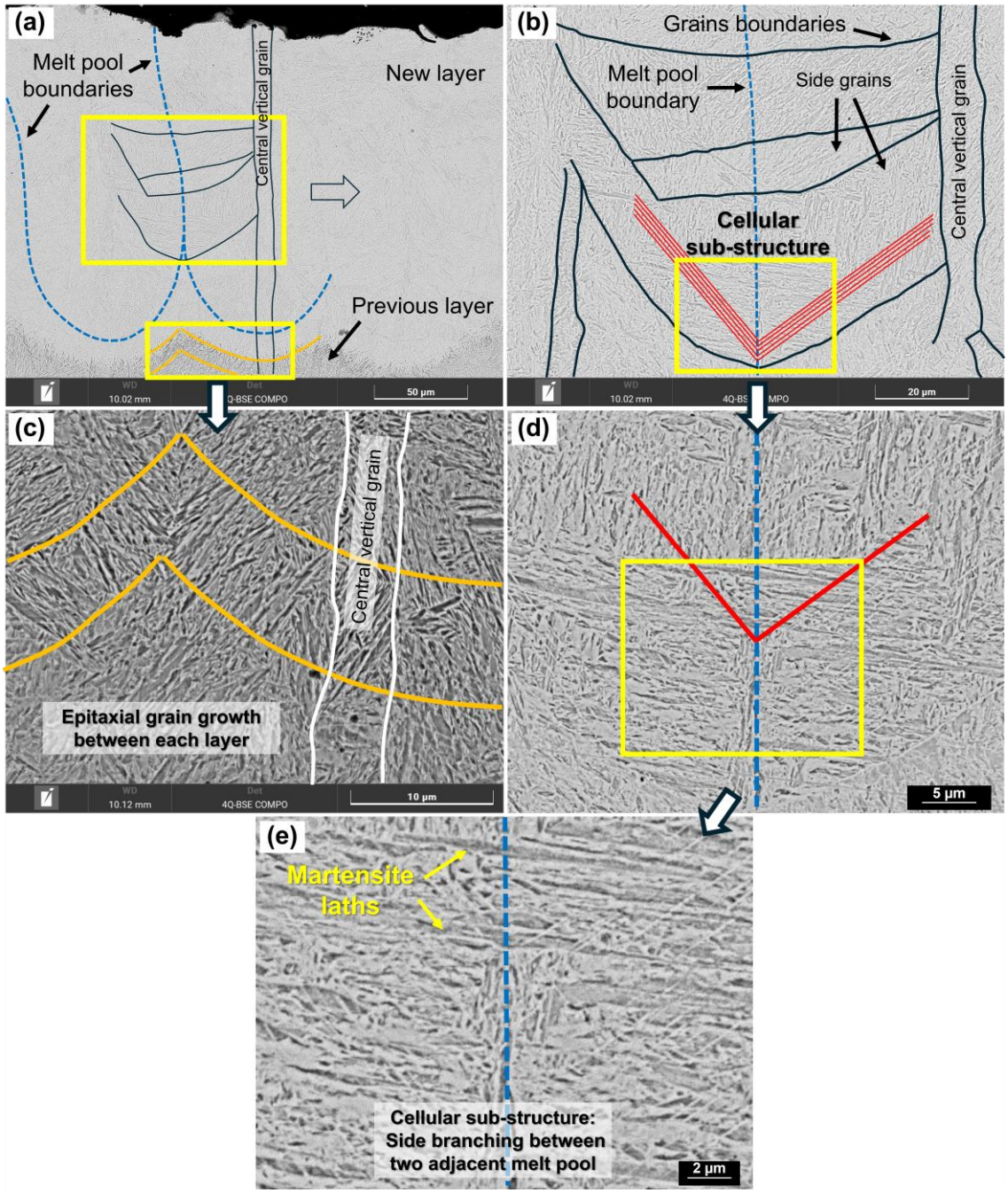


Fig. 5.1: As-built reference material AISI S2: (a) top layer overview, (b, c) epitaxial grains growth between melt pools and layers, (d, e) side branching of cellular sub-structure. The matrix consists of martensitic laths.

5.2.1.2 Effect of SiC additions and of preheating on changes in macrostructures

In the case of S2, cellular sub-structures are observed (*Fig. 5.2*b), as explained in the previous section. On the contrary, the macrostructure of S2 + 10% SiC without preheating reveals cellular dendrites (*Fig. 5.2*c). Additionally, the macrostructure of S2 + 10% SiC with preheating reveals a columnar-dendritic sub-structure (*Fig. 5.2*d). The appearance of such sub-structures is linked with the thermal gradient (G) and solidification rates (R) achieved within a melt pool

during solidification. According to the G-R diagram, in general the solidification sub-structures obtained with AM processes are shifted towards finer structures in view of the high G and R (high G*R). Meanwhile, G/R value control the morphology of the sub-structures. In particular, when G/R decreases, the solidification mode is shifted from cellular to dendritic (*Fig. 5.2*a). Such consideration implies that G decrease and/or R increase, in a separate or synergic way. The solidification following a certain mode is the result of the constitutional supercooling at the solidification front, affected by G/R. Understanding the intensity of G and R can be done through numerical modelling or through in-situ monitoring of the process. In this work, those tools were not used. Thus, in what follows, explanations about the different solidification modes are done using conventional metallurgical characterization, which can be extended in the future with more in-depth tools of analysis.

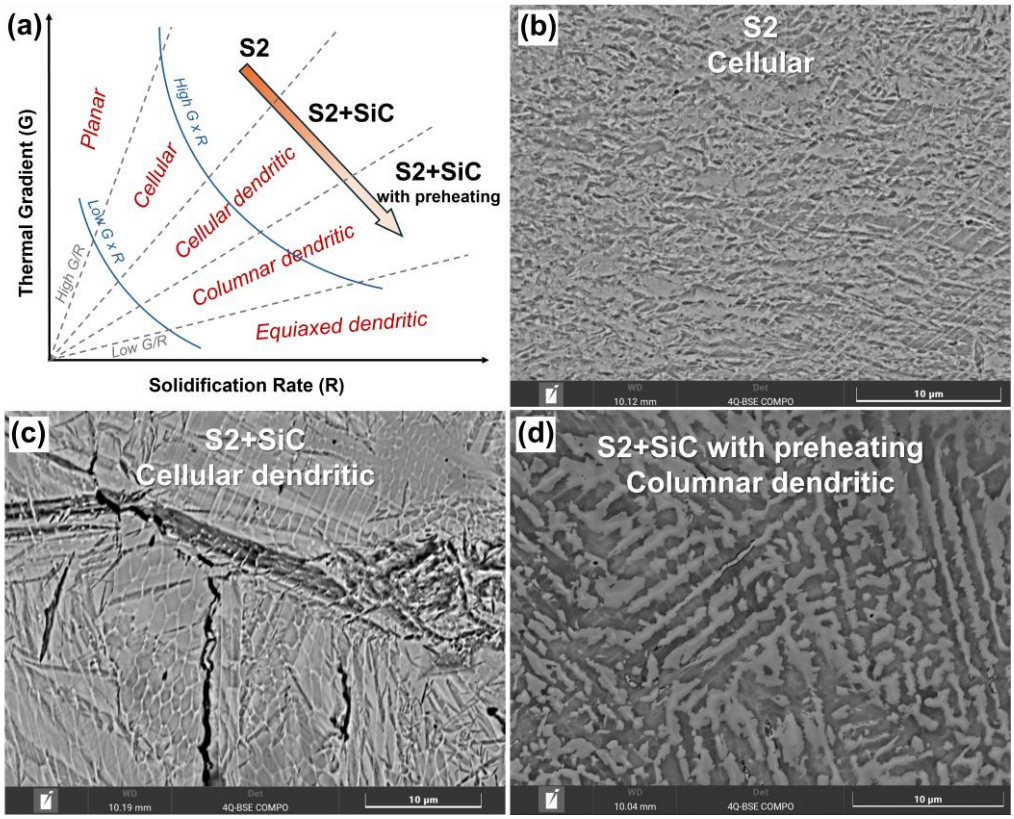


Fig. 5.2: (a) Thermal Gradient G - Solidification Rate R diagram, adapted from (*Lee, 2014*)*, (b) cellular, (c) cellular dendritic and (d) columnar dendritic sub-structures within S2, S2 + 10% SiC without and with preheating respectively.*

A similar approach to that used in section 5.2.1.1 will be used here for the assessment of the solidification mode and grain morphology. The microstructure of S2 + 10% SiC consists of lenticular martensite and retained austenite, as will be better explained in a later section (5.2.2.2). As in the case of martensitic laths, lenticular martensite can also have variants with

several orientations (*Shinohara, 2021*), which can help for the reconstruction of the prior austenite grain. As in the previous case, advanced approaches for the reconstruction of prior austenitic grains from EBSD data were not used in this work. Assessments were done through SEM observations of orientations of sub-structures and lenticular-shaped martensite.

The grains highlighted in *Fig. 5.3*c might only be considered as sub-grains, as they can be part of a bigger parent grain. Such sub-grains converge towards the centre of the melt pool (*Fig. 5.3*). The distinct vertical grain in the centre of the melt pool, present within S2, is not visible in this case (*Fig. 5.*3b,c). Furthermore, there is no evidence that the sub-grains grow epitaxially from nearby existing grains (*Fig. 5.3*c) Thus, the effect of SiC is to hinder the epitaxial grain growth.

Another metallurgical aspect can be mentioned here and further investigated. Considering SiC granules as inoculant agents within the melt pool, their effect is to promote grain refinement, according to the interdependence theory (*Stjohn, 2011*). In support of this, recent works of (*Fang, 2023*; *Zhai, 2022*) stated that it is possible to promote grain refinement within LPBF microstructures by adding nanoparticles, as in this case.

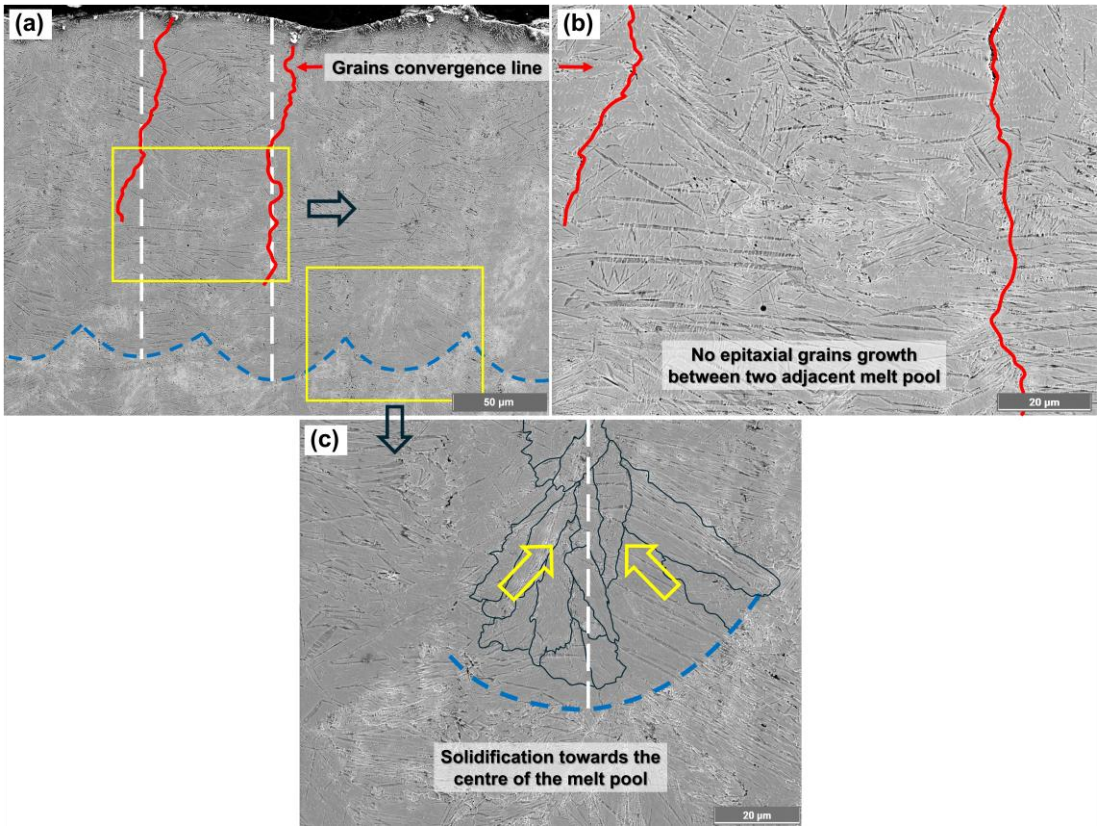


Fig. 5.3: S2 + 10% SiC without preheating: (a) Top layer overview, highlighting the central line where grains converge, (b) no epitaxial growth between adjacent melt pool and (c) grains orientation towards the centre.

Further shifting towards lower G/R occurred when preheating was applied. Indeed, a columnar-dendritic sub-structure is observed (*Fig. 5.2*d) within the macrostructure of S2 + 10% SiC with preheating, due to a decrease of G. As in the previous cases, the general assessment of grains morphology was only based on SEM observations. However, in this case the microstructure is not composed by martensite, as section 5.2.2.3 will show, making the identification easier. Furthermore, etching with Alkaline Sodium Picrate (ASP) at 90°C (2 g of picric acid, 25 g of NaOH and 100 ml of distilled water) allowed to highlight features of the prior grain boundaries formed at the beginning of the solidification (*Fig. 5.4*a).

A columnar grain growth is observed at the bottom of the melt pool, as in the case without preheating, where columnar grains converge to the centre (*Fig. 5.4*b,d). Meanwhile, many equiaxed grains are also visible when moving to the top of the melt pool (*Fig. 5.4*c). Therefore, it seems that a columnar-to-equiaxed (CET) grain growth transition occurred during solidification. The CET occurs due to heterogeneous nucleation in the liquid ahead the columnar grains, preventing their growth (*Narayana Samy, 2023*). Heterogenous nucleation is activated by SiC granules, which act as nuclei for the solidification of grains, and it is promoted by the lower G induced by preheating.

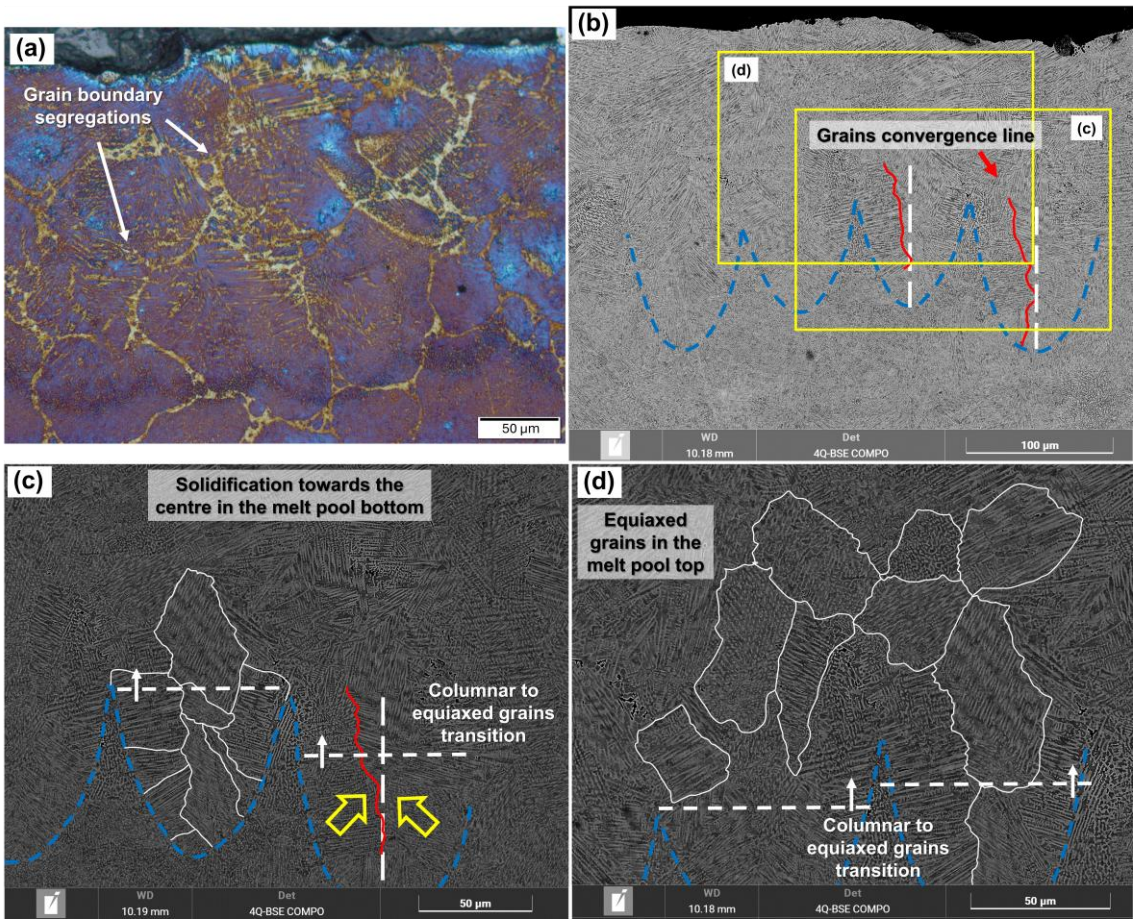


Fig. 5.4: S2 + 10% SiC with preheating 500°C: (a) OM overview after etching with ASP, where grain boundary segregations are highlighted, (b) SEM overview of the top layer, highlighting the central line where grains converge at the bottom of the melt pools, (c, d) columnar to equiaxed grains transition.

Other complex phenomena may have been involved in the change of grain morphology, such as Marangoni effect or buoyancy flow (*Li, 2024*). However, no signs of such phenomena were spotted. A schematic representation of all the phenomena explained above is visible in *Fig. 5.5*. These solidification models have two main limitations. The first issue refers to the fact that the melt pools considered here are formed under different $E_{d,v}$, in order to achieve optimal processability. Thus, G and R could also be affected by the different $E_{d,v}$. However, section 4.3 showed that the optimum processability was achievable when a stable key-hole melt pool was formed for all the different compositions (S2, S2 + SiC). Thus, G and R might only be affected by the addition of SiC and the application of the preheating. The second limitation is linked with the characterization techniques used. For a deeper discussion, EBSD analysis together with the use of the ARPGE software should be considered. This was not considered here because of the relatively low quality of the EBSD analysis that were carried out. In view of the supersaturation and distortion phenomena within the crystal lattice of the different phases, the

indexation rate remained relatively low, thus limiting the possibility for post-processing analysis.

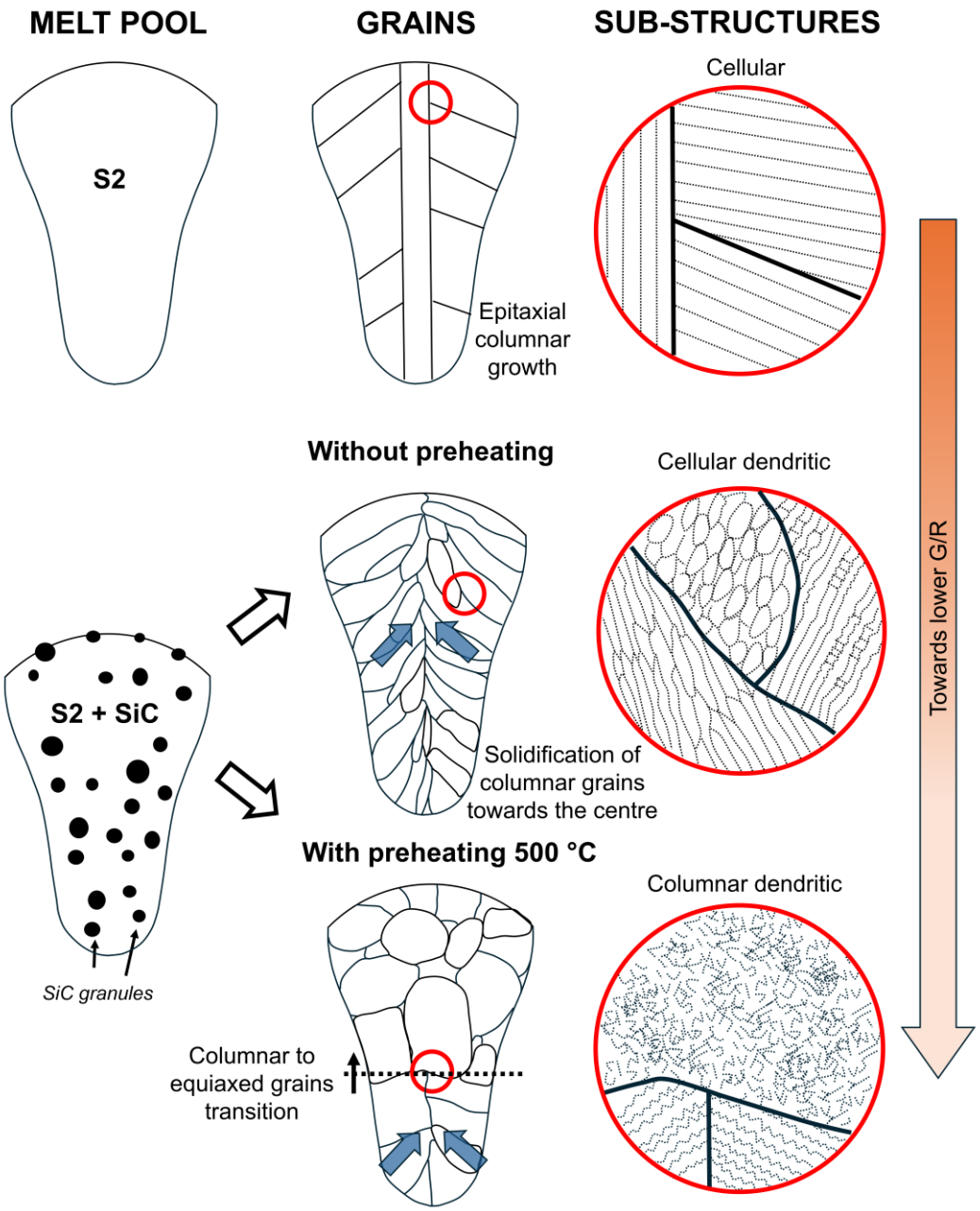


Fig. 5.5: Schematic representation of the effect of G/R on grains growth and sub-structures induced by the addition of SiC and the application of preheating during the LPBF process.

5.2.2 Microstructures and in-situ thermal cycles

The microstructures will be elucidated considering both top layer and underneath solidified material. The overall understanding of the solidification sequence can be achieved based on what occurs in a single melt pool upon cooling. Even if the melt pool can reach temperatures as high as 4000 K (*Hooper, 2018*) which allows boiling and evaporating, the assumption in what follows will be to neglect such phenomena while considering only a temperature higher than liquidus (melting point) of AISI S2 at the beginning of the solidification.

5.2.2.1 Solidification sequence of reference alloy AISI S2

To establish the solidification sequence of the as-built sample, a typical DTA-SEM reverse analysis approach is used based on the work of (*Maurizi Enrici, 2020*). This approach consists of a backwards interpretation of phase transformation peaks occurring during reheating up to complete remelting within a DTA test. Even if the scanning is performed at relatively low heating rate (5 °C/min), the ranges for the reverse transformation temperatures can be considered consistent with the actual temperature achieved during LPBF. In addition, the assumption will be made to approximate what is happening to the DTA bulk sample to what is also occurring within the melt pool.

Fig. 5.6 shows the DTA heating curve of the as-built S2 sample. The main peaks are highlighted and listed in *Table 5.1* with the corresponding phase transformation reaction and designation. The corresponding temperature was set based on the maximum (or minimum) of the peak.

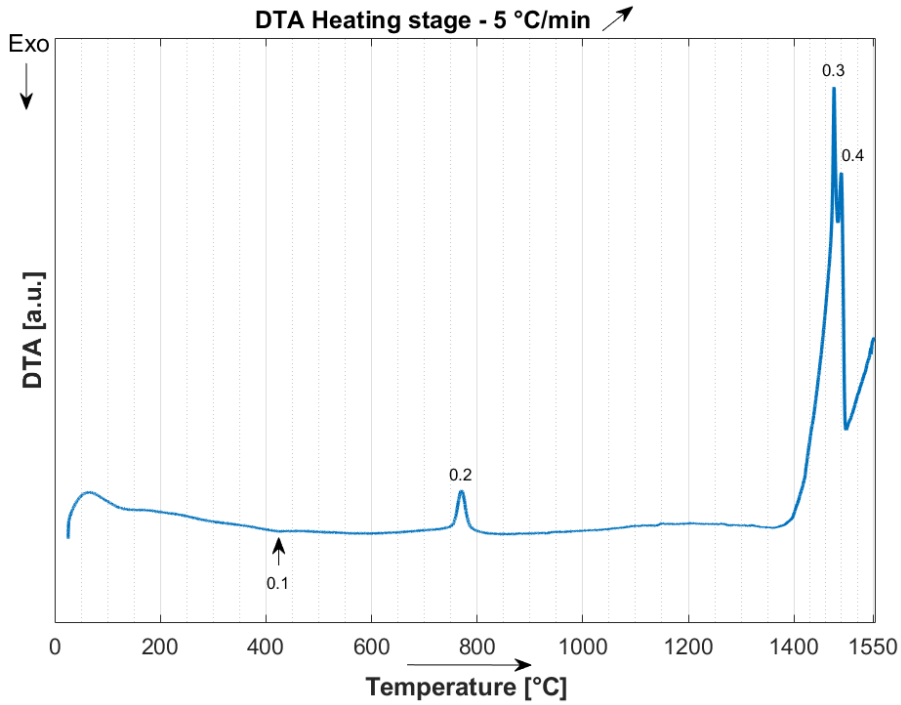


Fig. 5.6: DTA heating stage of as-built reference material AISI S2.

Peak	Temperature [°C]	Phase transformation reactions	Phase transformation designations
0.1	425	α' ⟶ α'' + carbides	Decomposition of martensite and fine carbides precipitation
0.2	774	α'' ⟶ γ	Reverse eutectoid
0.3	1476	γ ⟶ δ + L	Reverse peritectic
0.4	1490	δ ⟶ L	Complete melting (Liquidus)

Table 5.1: Relevant peaks temperature and transformation detected within DTA heating curve of sample 0.13.

According to the DTA reverse analysis, a peritectic transformation occurred in the range 1400 – 1500 °C (*Fig. 5.6*). Thus, the solidification from liquid state began with the formation of δ ferrite (peak 0.4) within the melt pool, which continues until the peritectic temperature is attained (peak 0.3). At such temperature, liquid and δ ferrite react to form austenite until the solid state is reached. Similar observations were done by (*Dilip, 2017*).

Upon further cooling, austenite transforms into martensite in view of the high cooling rates achieved during the LPBF process. According to Andrew equation (*Andrews, 1965*), martensitic start temperature (M_s) for S2 steel is 296 °C. Such temperature is well above the temperature reached at the end of the solidification of the melt pool, assumed to be slightly higher than room temperature in the absence of substrate preheating (as explained in section 4.3.2). Therefore, reaching such temperature during the solidification and the carbon content

(0.49 wt. %) of S2 steel ensure for a complete transformation of austenite into lath martensite (*Fig. 5.7*a) (*Dilip, 2017*; *Krauss, 1971*). This lath martensite is identified as a BCC phase after EBSD analysis (*Fig. 5.7*b). However, it is more correct to refer to a BCT crystal lattice, typical of martensitic phases. The BCT lattice is the result of carbon atoms entrapped within a BCC lattice, bringing a supersaturated condition. Such condition was also detected under DTA analysis. Indeed, peak 0.1 of the curves corresponds to the decomposition of martensite and the precipitation of fine carbides. Furthermore, the combination of supersaturation and high cooling rates leads to distortion within the crystal lattice. Indeed, the identification of phases within the top layer through EBSD analysis was difficult in the as-built conditions. Thus, the EBSD was conducted on a heat-treated sample at 300 °C for 1 hour. The aim of this heat treatment was to better index the BCC lattice. However, a relatively low indexation rate (i.e. high proportion of zero solution) of the EBSD patterns was still achieved (*Fig. 5.7*c).

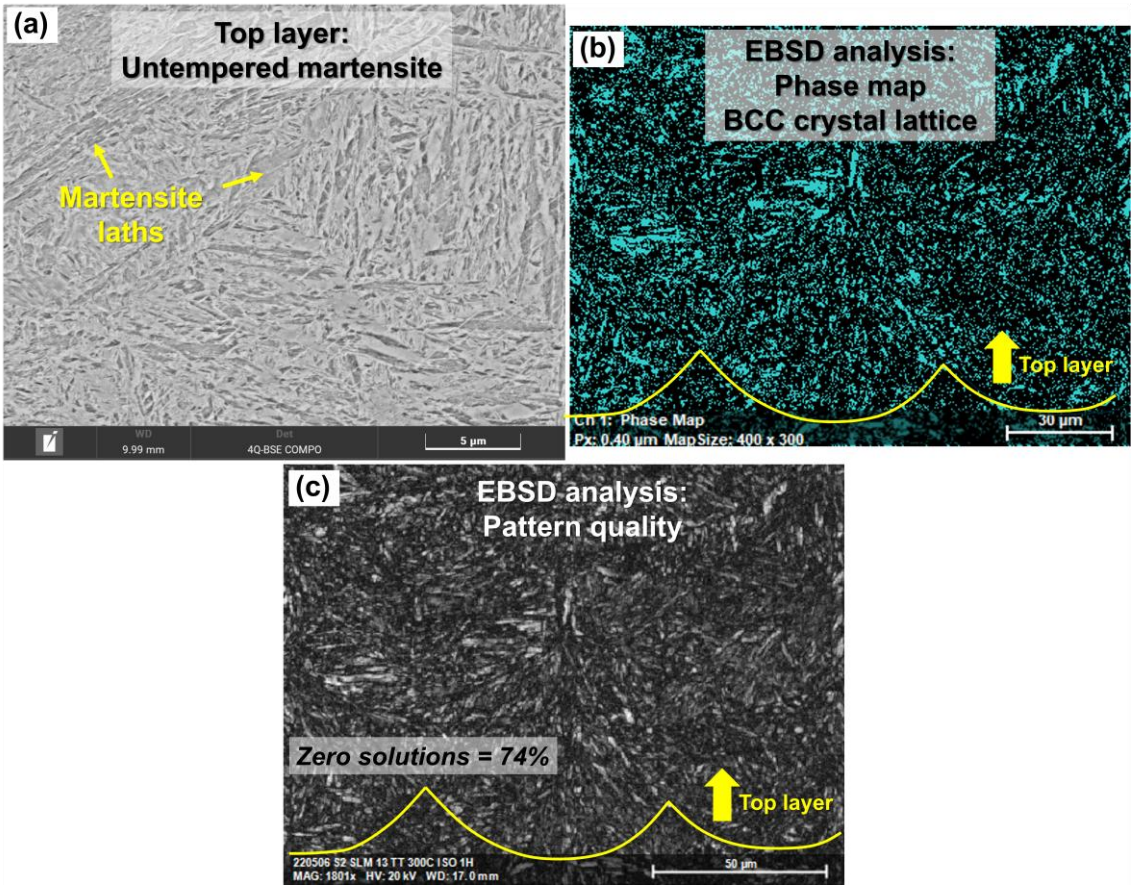


Fig. 5.7: Reference material AISI S2: (a) Untempered lath martensite within top layer, EBSD analysis performed on a thermal treated sample at 300 °C for 1 hour, (b) phase map and (c) pattern quality.

The original martensitic microstructure present within the top layer is named as untempered martensite (U-martensite). In the layers underneath, such untempered microstructure is affected

by in-situ thermal cycles due to the laser scanning a new layer of powder above the solidified material. Indeed, macro-hardness measurements on the cross section revealed different values between the top layer and the rest of the sample, with average values of 667 ± 27 and 557 ± 15 HV5 respectively. When a new melt pool is formed, melting of the freshly deposited powder layer occurs together with partial melting of the solidified material underneath. As stated earlier, temperatures achieved within a melt pool are well above the melting point of steel. Therefore, there is a certain thermal gradient between the new melt pool and the previously solidified material, which promotes different in-situ thermal treatments at the solid state, based on the distance from the melt pool. Etching with Nital allowed to highlight the Heat Affected Zones (HAZs) (*Fig. 5.8*a), as this etching is sensible to the carbon concentration within the microstructure. Dark brown coloration corresponds to carbon depleted areas.

Close to the melt pool boundaries, U-martensite is still present, similar to that of the top layer, as revealed by OM and SEM observations (*Fig. 5.8*a). The temperature reached in this region is well above the temperature for austenization. Thus, when the existent U-martensite is reheated up to a temperature above the austenization temperature, it transforms to austenite, which reverts into U-martensite during subsequent cooling due to the high thermal gradient and cooling rates achieved in proximity of the melt pool. Such area is called Upper HAZ (UHAZ) and has a thickness of about 15 µm. It was also named as austenization zone in the work of (*Hearn, 2022*). Nano-hardness measurements revealed values of about 8.5 GPa, i.e. 1 GPa less than the values achieved in the U-martensite of the top layer. Scanning the surface with the tip of the nano-indenter revealed a different surface roughness, helping on the identification of this zone (*Fig. 5.8*g). Below such region, the zone with a dark brown coloration is named Central HAZ (CHAZ). SEM observations revealed a microstructure similar to upper bainite composed of partially segmented films of martensite or austenite (bright areas in *Fig. 5.8*h) between lath of bainitic ferrite (black areas in *Fig. 5.8*h), according to (*Bartels, 2022*; *Ryder, 2021*). Nano-hardness analysis revealed values of about 6.8 GPa, the lowest within the HAZ. Finally, the Lower HAZ (LHAZ) is also present. This zone consists of tempered martensite (T-martensite), where carbides precipitated within the martensitic laths. The identification of such carbides was difficult, due to their size at the nanoscale. As a tempering effect, the nano-hardness decreased compared to that of the original U-martensite. A lower loss in nano-hardness is observed when increasing the distance, since at the bottom of the melt pool nano-hardness values are similar to those of the U-martensite (*Fig. 5.8*b,c).

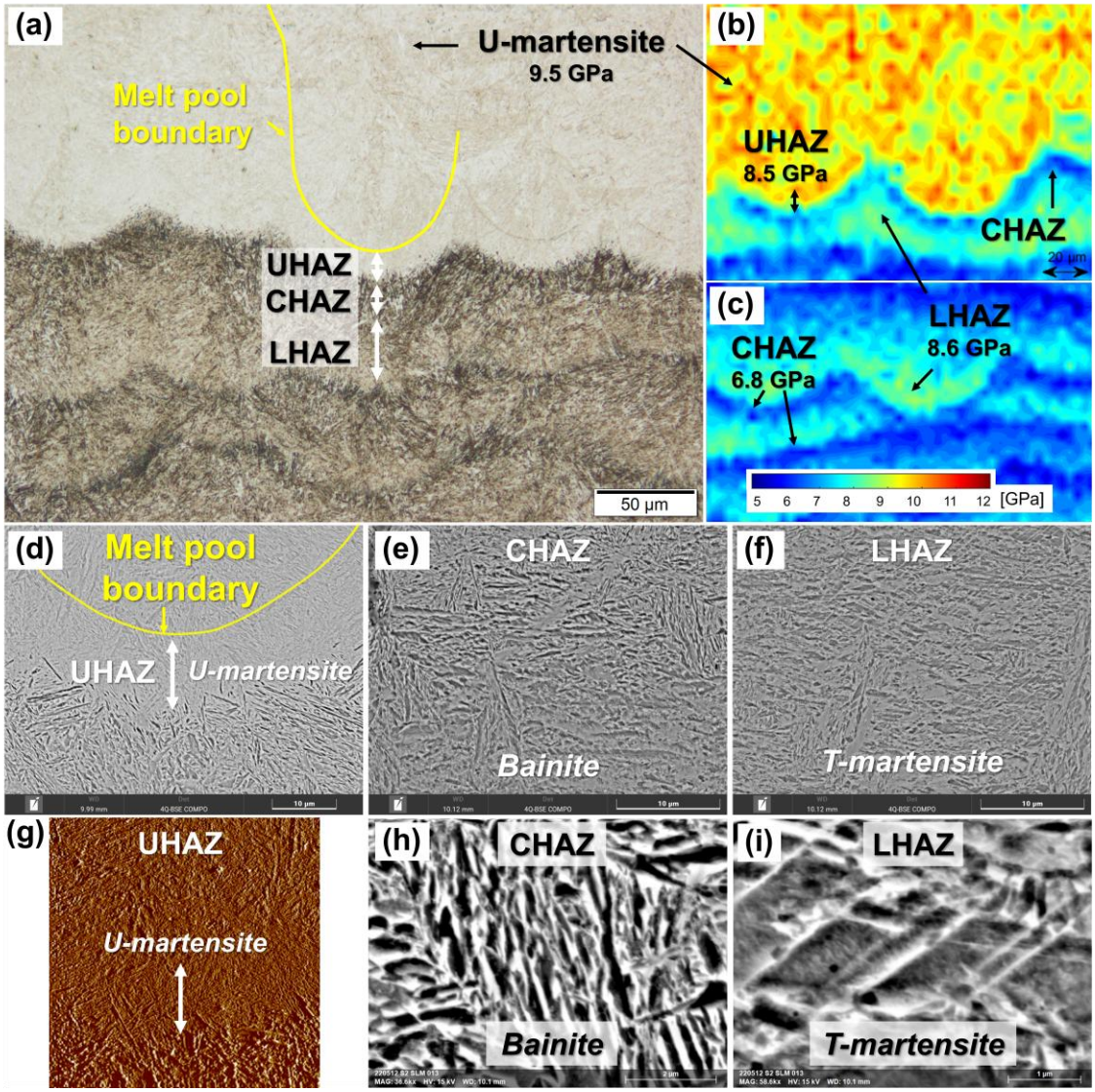


Fig. 5.8: Reference material AISI S2: (a) Heat affected zones and (b, c) their nano-hardness. Higher magnification of the (d) austenization zone, (e, h) bainite and (f, i) tempered martensite. (g) Smooth zone that corresponds to the Upper HAZ as observed under topography mode with the nanoindentation device.

EBSD helped on the identification of the different HAZs. Both pattern quality and phase map reveal the melt pool morphology, since in these areas a low indexation occurred (*Fig. 5.9*a,b). The phase map only allowed to identify the BCC crystal lattice of all the phases, but without differentiating them. The dark areas within the pattern quality correspond to the bottom of the melt pool (LHAZ), where incomplete tempering occurred, also according with the results obtained with nano-hardness measurements. The low indexation within this zone is due to the supersaturation of the U-martensite. Indeed, depending on the size, the type and the location of a given atom in the supersaturated lattice, more or less distortion can arise, thus influencing the pattern quality for subsequent EBSD investigation (*Maurizi Enrici, 2020*).

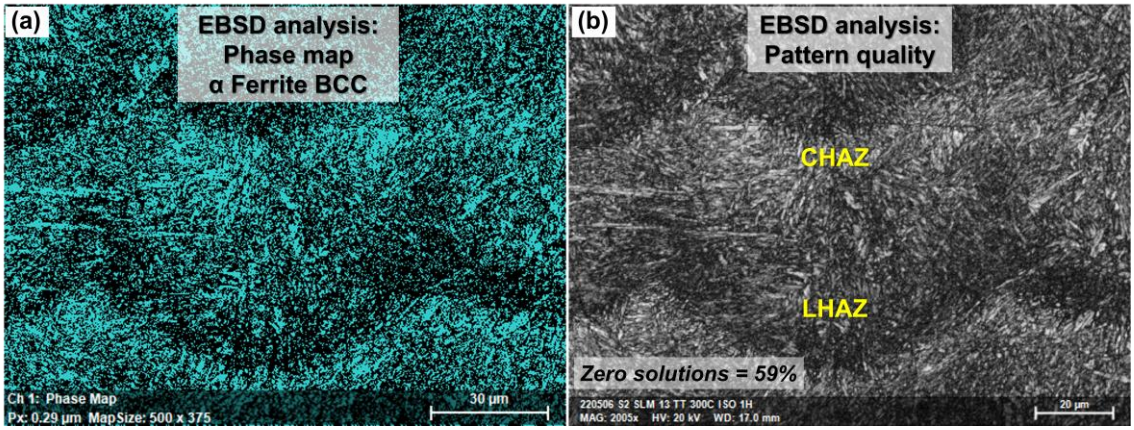


Fig. 5.9: Reference material AISI S2: (a) Phase map and (b) pattern quality obtained with EBSD analysis carried out at the centre of the sample.

Fig. 5.10 shows a sketch of the microstructure evolution during the LPBF process of S2 steel. The different HAZs are the result of transformations at the solid-state starting from the original laths of the U-martensite. The techniques used in this work allowed to identify the phases within UHAZ (U-martensite) and LHAZ (T-martensite). In contrast, bainite within the CHAZ was assumed based on literature sources. Further testing needs to be carried out to validate those assumptions, such as dilatometry and TEM analysis.

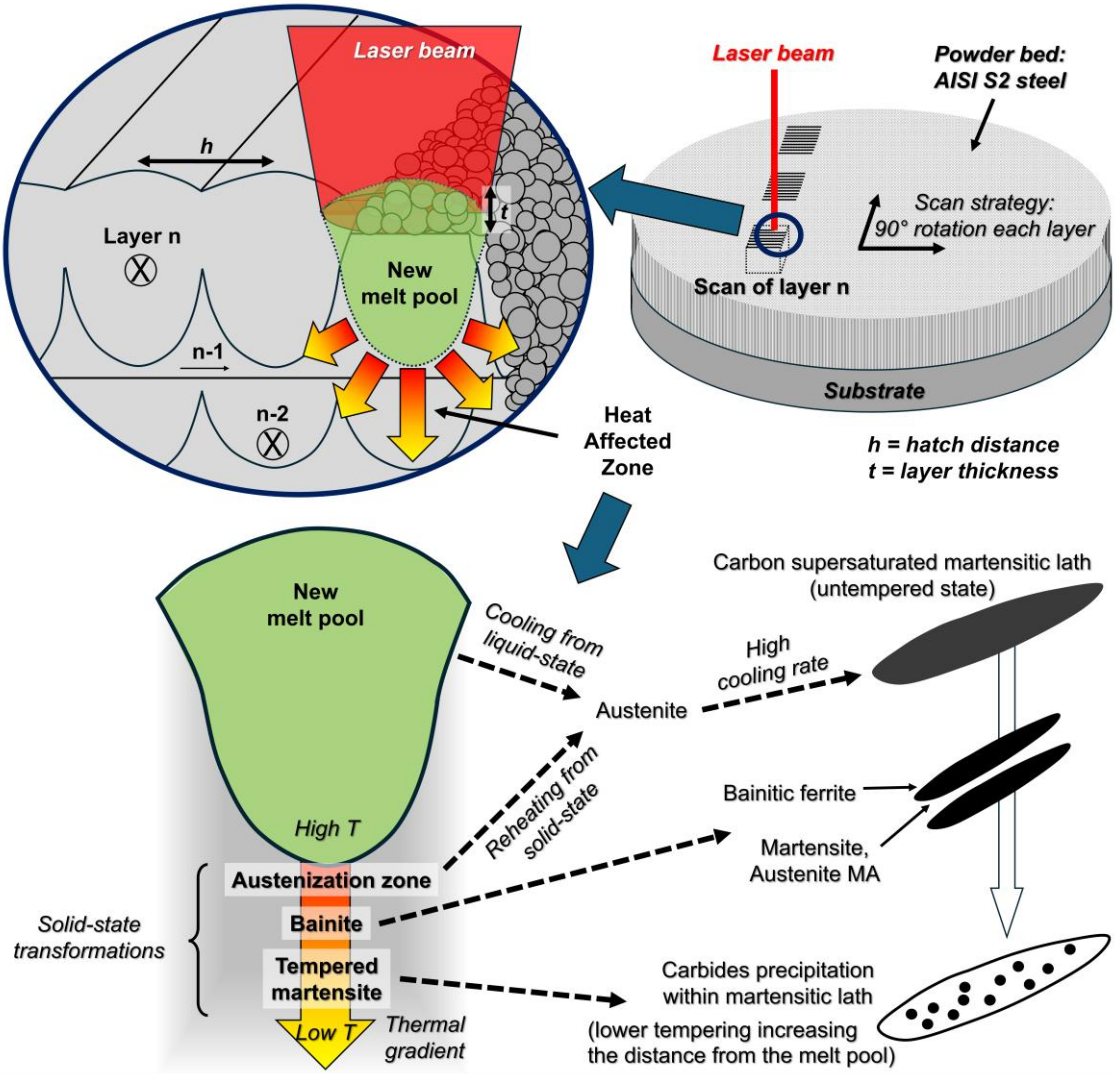


Fig. 5.10: Reference material AISI S2: sketch of the microstructure evolution during the LPBF process.

5.2.2.2 Effect of SiC on martensitic transformation

The addition of SiC also affected the solid-state transformations. The microstructure S2 + 10% SiC exhibit a high-volume fraction of residual austenite, as highlighted within the EBSD phase map (showing about 90 % of FCC phase) and from the unetched areas within OM micrographs (*Fig. 5.11*c,d). The EBSD pattern quality reveals well indexed bright areas corresponding to the residual austenite, whereas low indexed dark areas correspond to martensite, detected as a BCC phase within the phase map (*Fig. 5.11*a,b). The poor indexation of this BCC phase is due to the distortion of its crystal lattice, as discussed previously (5.2.2.1). In this case, the morphology of the martensite is lenticular (*Fig. 5.11*d,f), with the classical 'zig-zag' pattern and the midrib in the centre of plates (*Fig. 5.11*e). Its appearance is due to the increase in carbon content (1.76 wt. %), according to the classification established by (*Maki, 2012*).

The different types of microstructures within S2 and S2 + 10% SiC affect the macro-hardness. Indeed, the untempered martensite of S2 exhibits values of about 667 HV5. In contrast, S2 + 10% SiC exhibits macro-hardness values of about 623 HV5. The slight decrease in hardness might be associated to the different type of martensite and the higher content of residual austenite. The latter phase is retained at room temperature at the end of the solidification process. Indeed, the high carbon content has the effect to stabilize austenite since it decreases the M_s temperature, down to -273 °C according to (*Andrews, 1965*). Despite the fact that M_s is well below room temperature, martensite appears within the final microstructure. This demonstrates that commonly used M_s temperature equations may not be directly applicable to LPBF, also according to (*Galbusera, 2022*).

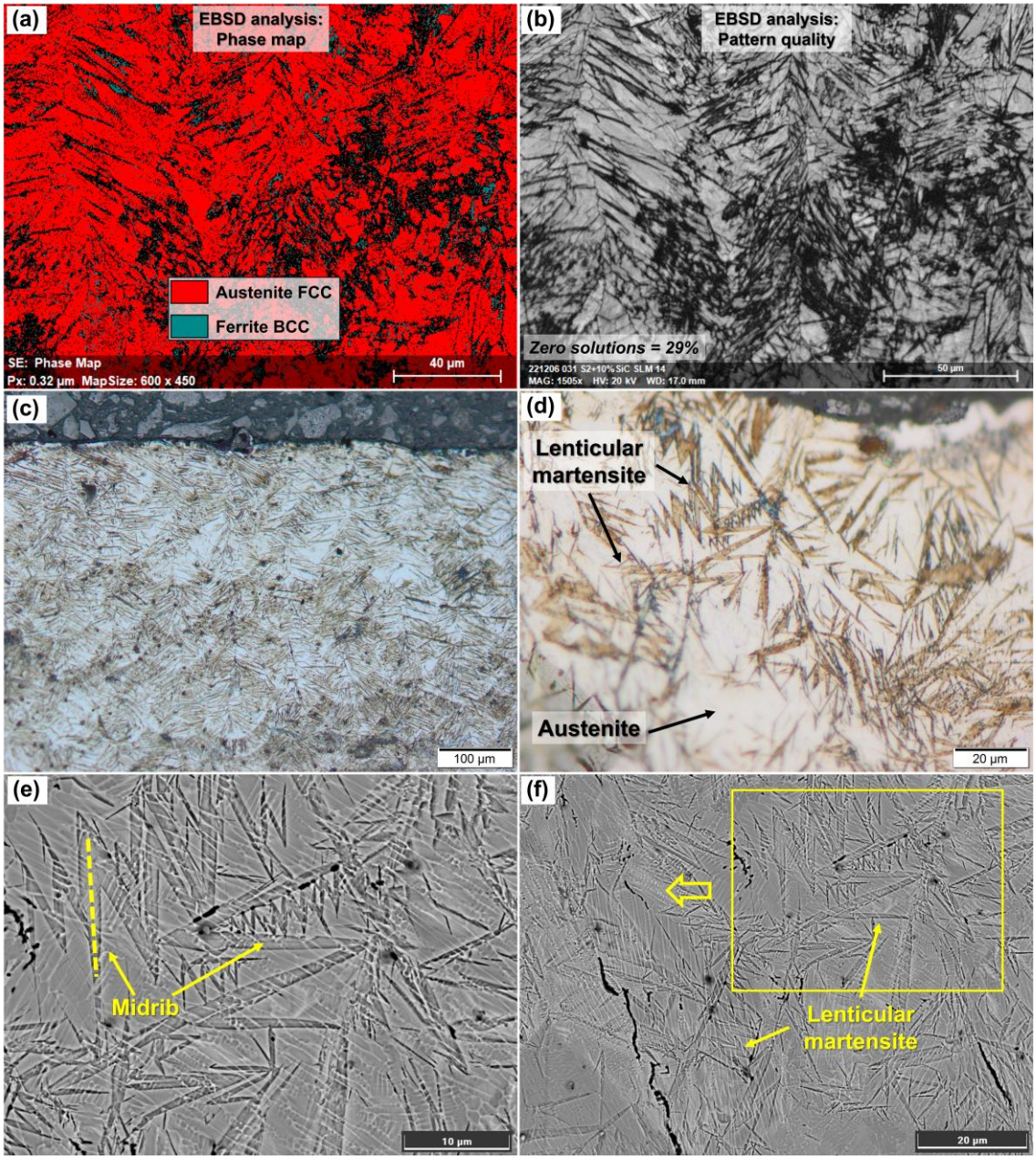


Fig. 5.11: S2 + 10% SiC without preheating: (a) Phase map and (b) pattern quality of the EBSD analysis, (c) cross section overview after Nital etching. (d) OM and (f) SEM micrographs of the same area, (d, f) highlighting the lenticular morphology of the martensite and (e) the central midrib.

As shown in section 4.3, optimal sample produced from S2 powder is fully dense and defect-free whereas all samples with S2 + 10% SiC exhibit big vertical cracks which grow vertically starting from the substrate. It is assumed that cracking phenomena occurred almost at the end of the printing, thus referred as cold cracking. Indeed, few samples exhibited protrusions coming out of the powder bed, due to the cracking favouring delamination of the sample from the substrate. Cracks appearance is the result of high stresses due to the martensitic transformation that strain the printed part. S2 samples do not exhibit cracks despite the fully

martensitic microstructure. In contrast, extensive cracks appear within S2 + 10% SiC despite the high content of residual austenite and the incomplete martensitic transformation. Usually, residual austenite is desired within the final microstructure as it can dampen residual stresses. Recent works showed new approaches to achieve defect-free high carbon tool steels by LPBF. Such approaches are based on the design of alloys. The aim is to reduce the volume fraction of martensite by increasing certain alloying elements. The effect is to reduce austenite grains and cells size, thus lowering the M_s temperature resulting in lower formation of martensite. Another way is to reduce the carbon content within the martensite, so it is less distorted (*Kosiba, 2023*; *Saewe, 2021*). However, there are contrasting opinions about the effectiveness of such approaches. In this work, it has been shown that the presence of residual austenite does not avoid cracks appearance but in contrast, it promotes it. Thus, for the microstructures considered in this work, cracks appearance can rather be correlated to the types of martensite generated, with the lenticular type favouring cracking. In contrast, lath martensite allows to avoid cracks. The reason might be associate to the higher tempering effect of the lath martensite. Indeed, tempering is promoted during in-situ thermal cycles, as explained in section 5.2.2.1. Tempering effect is to enhance the precipitation of carbides within the martensitic laths, with a consequent decrease in distortion of the BCT lattice structure and the release of stresses layer-by-layer. Such tempering effect was not detected within the microstructure of sample S2 + 10% SiC.

The achievement of defect-free high alloyed tool steels without the use of preheating is a current hot topic and several works showed the possibility to achieve it, based on the design of the chemical composition. In this work, however, the chemical composition was designed with another specific purpose, which is to achieve graphitization. Thus, no other modifications of the chemical composition are wanted. Furthermore, with the aim of achieving a wear resistant alloy, martensite should be avoided in view of its brittle nature which can be deleterious for wear resistance. Therefore, the subsequent step for the realization of a defect-free sample from S2 + 10% SiC powder was to apply preheating during the LPBF process, in order to avoid martensitic transformation, decrease residual stresses and more generally, change the solidification sequence of the alloy.

5.2.2.3 Microstructural changes induced by preheating

5.2.2.3.1 Identification of phases within the top layer

Substrate preheating during LPBF was beneficial to achieve cracks-free samples from S2 + 10% SiC powders (section 4.3.2). The reasons for crack avoidance lie on the type of microstructure formed. Indeed, applying the preheating decreased the G/R value, as explained earlier (section 5.2.1.2). Thus, martensitic transformation was avoided. A new type of microstructure less prone to cracking was achieved. An overview of the microstructure is visible in *Fig. 5.12*a, obtained by chemical etching with ASP. Detailed chemical composition of a printed sample was obtained by ICP-OES technique (*Table 5.2*). The measured composition is in line with the theoretical composition of the powder mixtures reported in section 3.3. Only carbon was measured 16% lower than the theoretical value. Macro-hardness measurements revealed an average hardness of 564 ± 11 HV5. No hardness differences were detected between the top layer and the rest of the cross section, in contrast to what occurred with S2 and S2 + 10% SiC without preheating.

The solidification mode for this alloy is dendritic (section 5.2.1.2). In contrast to what happened with S2 and S2 + 10% SiC without preheating, no martensitic transformation occurred at the solid-state. Therefore, the features of the macrostructure (dendrites and interdendritic segregations) are well distinguishable even at room temperature. Furthermore, the etching allowed to highlight another feature of the macrostructure, i.e. the prior grain boundaries (yellow in *Fig. 5.12*a,b). All these macrostructural features are characterized by complex microstructural phases, which will be discussed in what follows focusing on the top layer. Subsequently, the microstructure of the HAZ will be considered in section 5.2.2.3.2.

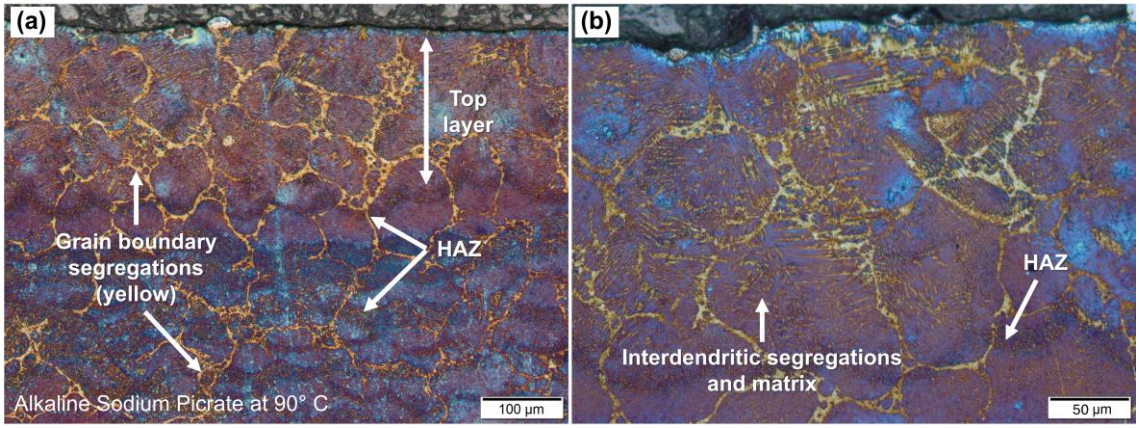


Fig. 5.12: S2 + 10% SiC with preheating 500 °C: Sample after etching with ASP, (a) overview and (b) zoom on top layer.

wt. %

Fe	C	Si	Mo	Mn
Bal.	1.48 ± 0.07	4.27 ± 0.2	0.488 ± 0.003	0.451 ± 0.01

Table 5.2: S2 + 10% SiC with preheating 500 °C: chemical composition of as-printed sample obtained by ICP-OES technique.

The prior grain boundaries form a network across the cross section, highlighted in yellow after ASP etching (*Fig. 5.12*a, *Fig. 5.13*a). Under SEM, these prior austenite grain boundaries reveal a complex structure, difficult to differentiate from the rest of the microstructure (*Fig. 5.13*b). The core appears bright, having a morphology of an irregular carbide with dimensions less than 1 µm (*Fig. 5.13*c,d). The shell is composed by a granular sub-structure, as highlighted by distinct boundaries (*Fig. 5.13*c,d). The dimensions of such sub-grains are of about 1 µm. EDS analysis reveals higher molybdenum and carbon concentration within the carbide compared to the neighbouring sub-grains (*Table 5.3*).

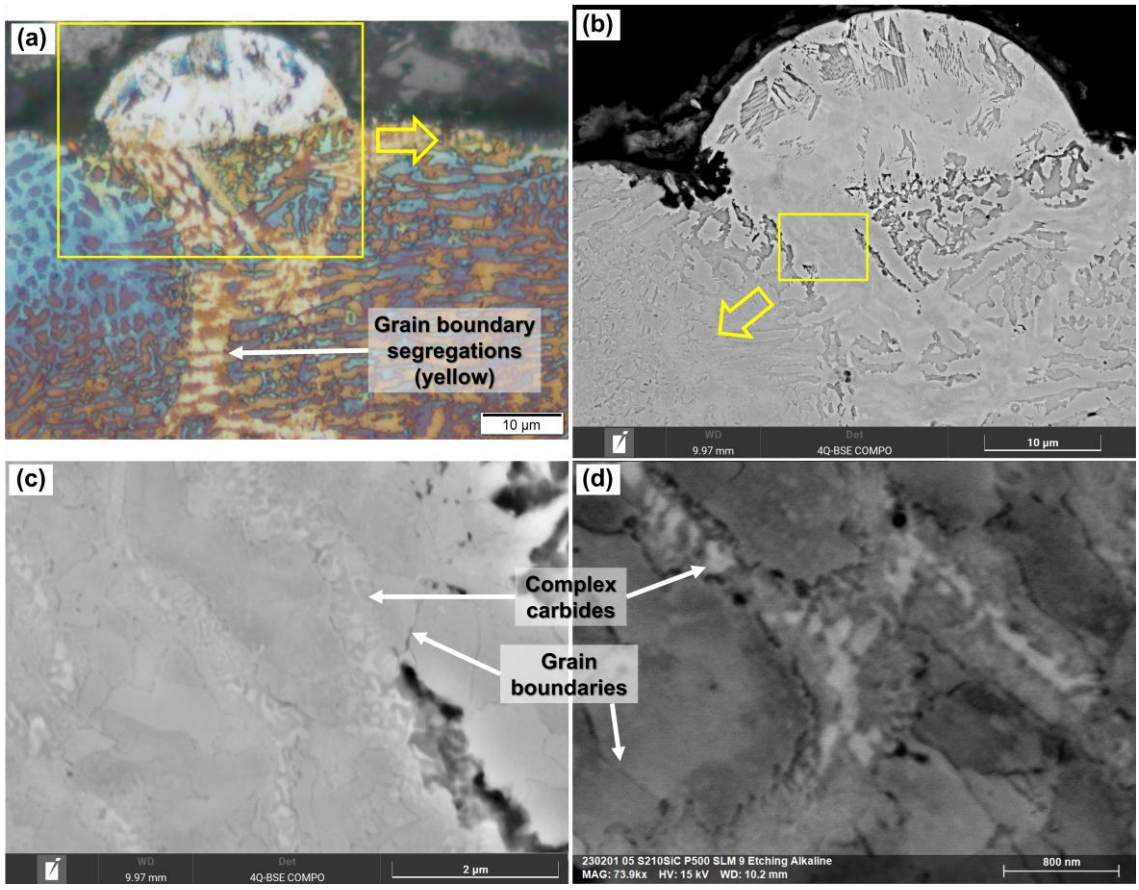


Fig. 5.13: S2 + 10% SiC with preheating 500 °C: (a, b) OM micrographs after etching with ASP to highlight the main phases, (c, d) SEM observations on grain boundary segregations, which are composed by sub-grains and complex carbides.

Atomic %

Phase	Fe	O	C	Si	Mn	Mo
Sub-grains	bal.	2.03±0.50	4.63±0.53	7.81±0.23	0.29±0.06	0.11±0.02
Complex carbides	bal.	4.17±0.48	9.4±1.00	6.98±0.61	0.35±0.08	0.43±0.19

Table 5.3: S2 + 10% SiC with preheating 500°C: EDS analysis of the phases within grain boundary segregations.

After etching with ASP, the dendritic matrix appears brown/orange, whereas interdendritic regions appear from white to light blue (*Fig. 5.14*a), which result as purple in the general overview (*Fig. 5.12*). Such colourations are typical of iron-carbon-silicon alloys such as High Carbon High Silicon (HCHS) steels and cast irons after etching with picrate-based solutions (*Basso, 2020*; *Hernando, 2019*), in view of the sensitivity of this etching to silicon content (*Rivera, 1995*; *Tenaglia, 2017*). Under SEM, matrix appears superimposed to interdendritic regions, contrary to what is seen after Nital etching (*Fig. 5.14*c,d,e,f). Etching with Nital allowed to highlight the existence of clear sub-grain boundaries within the dendritic matrix (*Fig. 5.14*f). EDS analyses on samples after the two different etchings reveal similar results in terms of chemical composition. For ease of description, only results obtained with ASP are reported here (*Table 5.4*). Despite the presence of elements from etching (e.g. Na and O), EDS analysis reveals higher content of carbon and molybdenum within interdendritic segregations compared to the dendritic matrix. Meanwhile, silicon and manganese content are similar in both constituents.

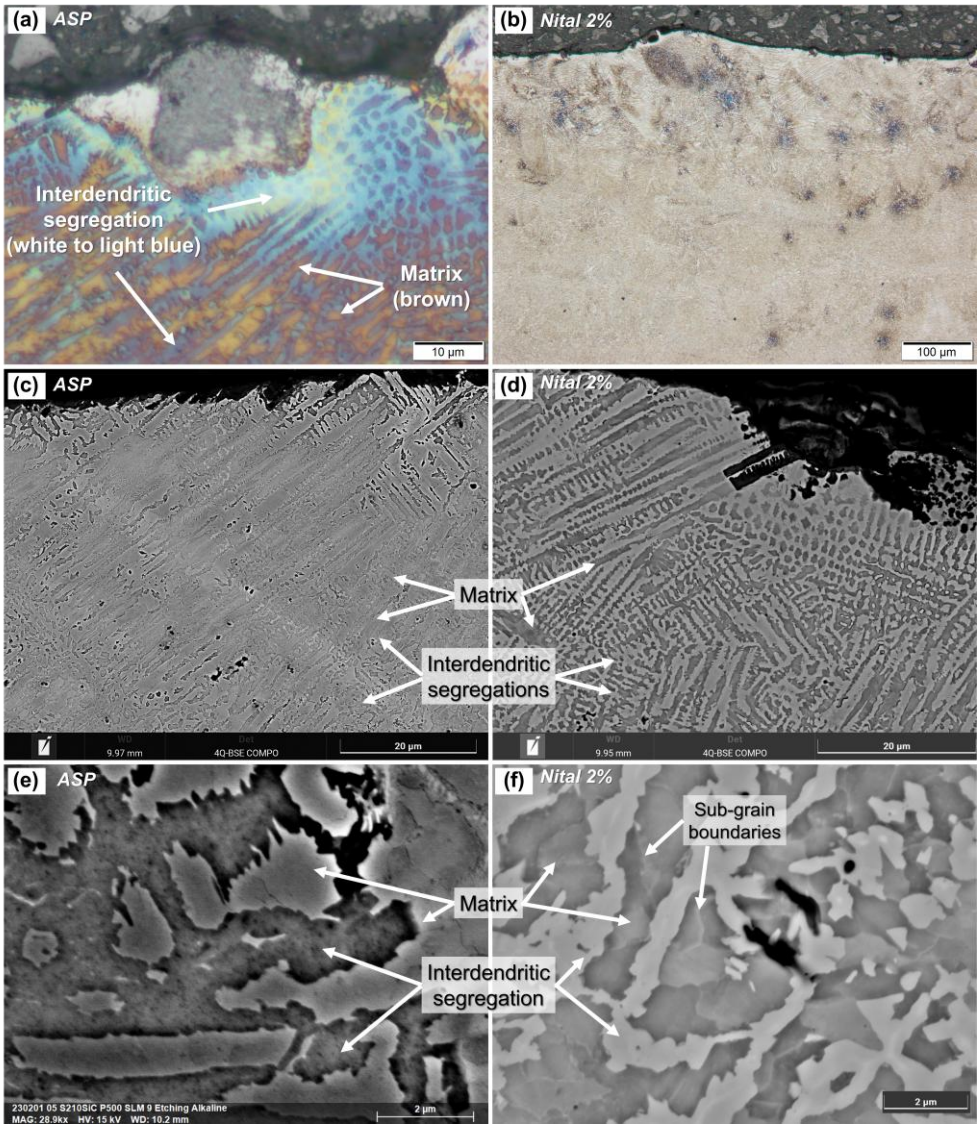


Fig. 5.14: S2 + 10% SiC with preheating 500 °C: (a) OM magnification within the top layer after etching with (a) ASP and (b) Nital. SEM micrographs revealing (c, e) the dendritic matrix superimposed to the interdendritic segregations after ASP etching and (d, f) vice versa after Nital etching. The matrix reveals sub-grains boundaries after Nital etching.

Atomic %

Phase	Fe	O	C	Si	Mn	Mo	Na
Dendritic matrix	bal.	3.17±1.2	3.88±0.25	8.07±0.27	0.32±0.04	0.09±0.03	0.86±0.29
Interdendritic segregations	bal.	5.61±0.78	8.13±0.49	8.36±0.75	0.37±0.09	0.30±0.11	1.75±0.31

Table 5.4: S2 + 10% SiC with preheating 500°C: EDS analysis of the main phases on samples after etching with Nital and ASP.

EBSD analyses were carried out for phase identification. The interdendritic segregations are identified as cementite (Fe_3C) (*Fig. 5.15*a,b). However, both phase map and pattern quality

reveal a poor indexation of this phase (*Fig. 5.15*c,d). Note that in *Fig. 5.15*b only cementite is displayed for better identification, whereas black areas correspond to the dendritic matrix. The dendritic matrix is identified as a phase with BCC lattice structure, well indexed according to the pattern quality. Associating this lattice structure to the classical iron products α Ferrite can oversimplify the true nature of this phase. Indeed, a BCC lattice can be associated to ferrite, bainite or martensite. The differentiation of such phases has always been a debated topic. However, a previous SEM micrograph (*Fig. 5.14*f) and the grain distribution obtained with EBSD analysis (setting a maximum misorientation angle of 1°) (*Fig. 5.15*e,f) reveal the existence of sub-grains with a size of about 1 µm. These characteristics exclude the possibility of it being martensite, whereas they establish that this phase could be granular ferrite or granular bainitic ferrite without secondary phases, according to (*Krauss, 1995*; *Zhu, 2013*).

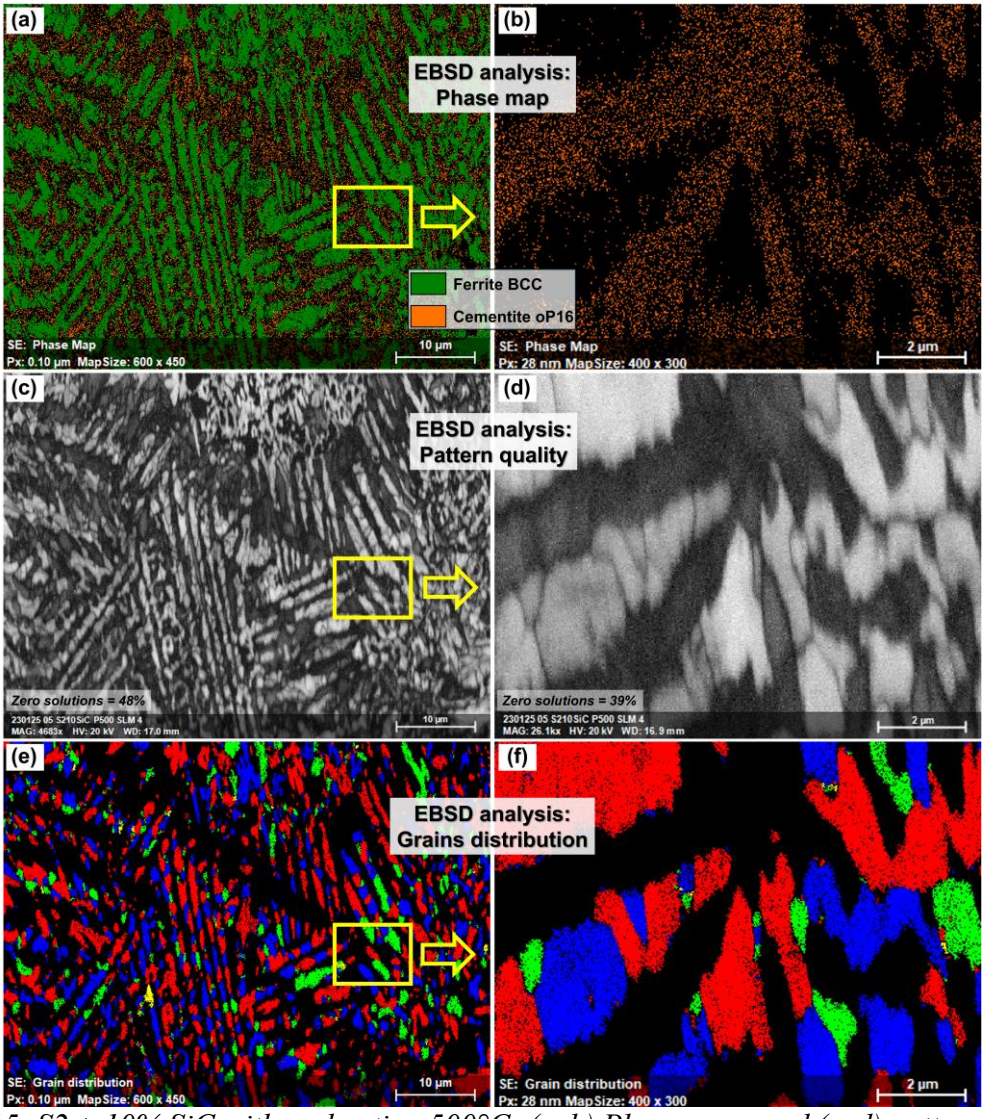


Fig. 5.15: S2 + 10% SiC with preheating 500°C: (a, b) Phase maps and (c, d) pattern quality obtained with EBSD analysis. (e, f) Sub-grains within the dendritic matrix with a maximum misorientation angle of 1°.

Nano-hardness indentations were performed on the bottom of a melt pool within the top layer, on a sample in the as-polished conditions (*Fig. 5.16*a). The map reveals an overall homogeneous nano-hardness, with local differences only associated to the different microstructural phases (*Fig. 5.16*b). The areas with high nano-hardness (up to 15 GPa) corresponds to the interdendritic regions. In contrast, lower nano-hardness values are associated to the dendritic matrix (about 6 GPa).

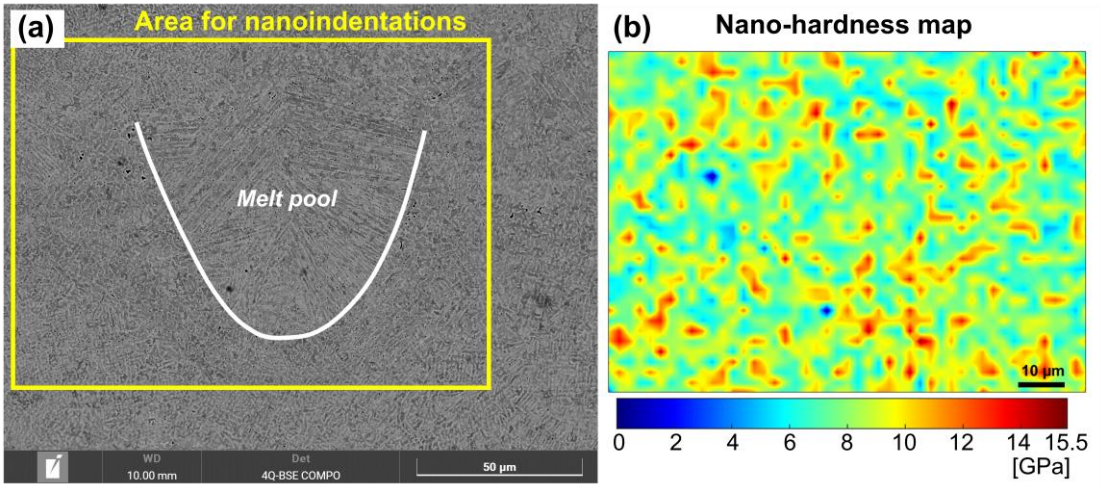


Fig. 5.16: S2 + 10% SiC with preheating 500 °C: (a) Area for nano-hardness indentations and (b) map obtained.

Whether it is bainitic or ferritic, the nature of the dendritic matrix is linked with the presence of the high silicon content within the general composition of the alloy (4.27 wt. %, *Table 5.2*) and as measured with EDS analysis (~ 8 at. %, *Table 5.4*). Silicon is well known for its capability to create a solid solution with a BCC Fe-based lattice structure, leading to a strengthening effect (*Maurizi Enrici, 2022*). As a consequence, the nano-hardness is enhanced, as in the current case where a relatively high value was measured (6 GPa, *Fig. 5.16*).

The nature of the dendritic matrix was further investigated, in particular to establish whether it is supersaturated in carbon or not. For this purpose, the heating stage of a DTA analysis on an as-built sample was considered (*Fig. 5.17*). Note that for the aim of this discussion, the curve is displayed only in the temperature range 25 – 800 °C. Full curve up to 1550°C is available in Appendix B. For a better understanding, the sample S2 + 10% SiC processed without preheating was also used as a comparison. This alloy exhibited a microstructure composed of lenticular martensite and of an austenitic matrix with an FCC lattice structure (see EBSD analysis in *Fig. 5.11*a, section 5.2.2.2). It was established that both phases are supersaturated in carbon.

The understanding of the transformations described below was achieved by carrying out specific thermal treatments through DTA on the two different samples. Those investigations are needed later on for the study of the graphitization mechanisms. Further details are available in Appendix C and section 5.3. The designation of each transformation given in *Table 5.5* only focus on the phenomena relevant for this discussion.

Three main exothermic peaks are visible within the DTA heating curve of the sample without preheating. Those exothermic peaks are not present within the curve of the sample processed with preheating. Exothermic peaks are more commonly observed during the solidification from liquid state, thus when considering the DTA cooling stage, as they refer to crystallization phenomena resulting in heat release. Meanwhile, exothermic peaks within a DTA heating curve are associated to precipitation of phases in the solid state, related to the main phases present within the microstructure. Considering that the main phases of the sample obtained without preheating are carbon supersaturated austenite and martensite (section 5.2.2.2), it is assumed that peaks 1 and 2 are associated to the precipitation of carbides within the parent martensite and austenite respectively. Thus, peaks 1 and 2 refers to a desaturation in carbon of the martensite and of the austenitic matrix. Finally, the third exothermic peak is associated to the complete decomposition of the martensite, where the previously desaturated martensite transforms into ferrite and eventually carbides and/or graphite. This transformation occurs before the subsequent endothermic peak (4), which refers to the transformation of ferrite into austenite. A similar peak (b) is present also within the curve of the sample obtained with preheating. In this case, it corresponds to the transformation of the BCC ferritic matrix into austenite. In contrast to the previous case, no exothermic peak precedes it. Therefore, DTA allowed to reveal that the BCC lattice structure in the pre-heated sample is not in supersaturated conditions.

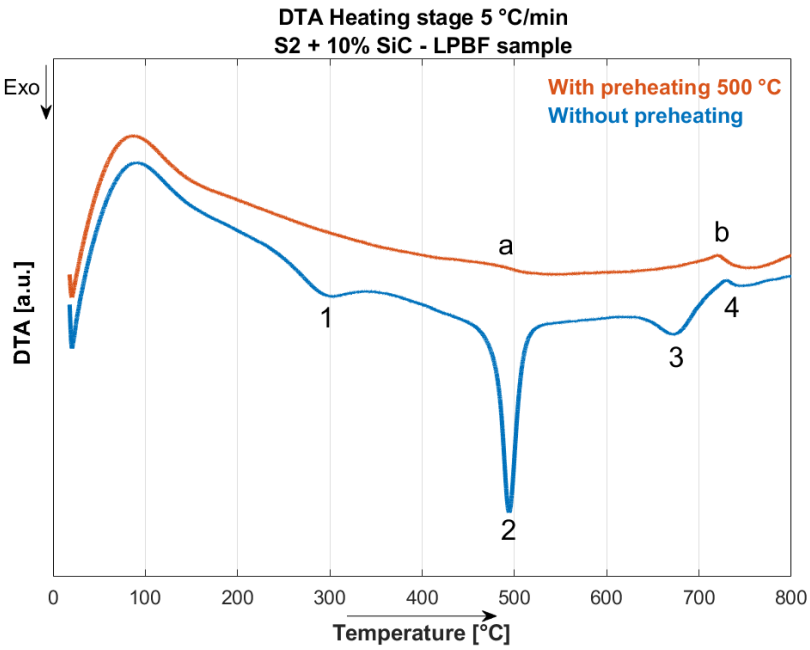


Fig. 5.17: S2 + 10% SiC with and without preheating: DTA heating stage of as-built samples until 800 °C. Full curve is available in Appendix B. The identification and designation of each peak transformation was possible after specific thermal treatment, which details are available in Appendix C.

Preheating	Peak	Temperature [°C]	Phase transformation designations
No	1	300	Desaturation of martensite
	2	495	Desaturation of austenite
	3	680	Decomposition of martensite into ferrite
	4	720	Reverse eutectoid
Yes	a	460	Dissolution of carbides
	b	730	Reverse eutectoid

Table 5.5: S2 + 10% SiC with preheating 500 °C: relevant peaks temperature and transformation detected within DTA heating curve of as-built sample.

All the results showed above allowed to partially restore the solidification sequence and to understand the phases found at room temperature in the pre-heated sample. In what follows, features of both macro- and micro-structure will be considered. Firstly, the solidification of the microstructure of dendrites and interdendritic regions will be explained, followed by the explanations regarding grain boundaries.

The SiC granules start to dissolve within the Fe-rich melt pool, acting as nuclei for the heterogeneous nucleation of grains (section 5.2.1.2). Within a grain, primary austenitic

dendrites start to grow, which reject carbon and molybdenum at the solidification front in view of the lower solubility of those alloying elements in the solid (*Saewe, 2021*). Those elements segregate within interdendritic regions, subsequently precipitating as carbides. Thus, in view of the lower concentration of the rejected elements, the dendritic matrix is the first solid to form, whereas the interdendritic carbides are formed subsequently (*Basso, 2020*). When the cooling goes on and the solidus point is attained, solid-state transformations occurred within the austenitic dendrites. In particular, a phase with a BCC crystal lattice is formed. This transformation is confirmed by the presence of distinct boundaries between each sub-grain, typical of the austenite to ferrite allotropic transformation. However, it remains unclear whether it is bainitic or purely ferritic. Its nature is deeply affected by the high content of silicon, present in solid solution, thus enhancing the nano-hardness (*Fig. 5.16*). Therefore, the dendritic matrix can be associated to a high silicon alloyed ferrite or a carbide-free bainitic ferrite. Moreover, in contrast to what happened without preheating where the austenitic matrix was retained at room temperature, in this case the BCC matrix was not supersaturated in carbon, as highlighted by the DTA analysis (*Fig. 5.17*). Indeed, most of the carbon segregate within the interdendritic regions at the beginning of the solidification.

At room temperature, carbides are found within the interdendritic regions, revealing a relatively high nano-hardness (15 GPa, *Fig. 5.16*) and a higher content of carbon and molybdenum compared to the dendritic matrix (*Table 5.4*). Silicon is also present in a considerable amount, comparable to that of the dendritic matrix. The presence of those elements is responsible for the lattice distortion and the consequent poor indexation of the cementite phase identified from EBSD analysis (*Fig. 5.14*c,d). Thus, the interdendritic regions (segregations) will be named as Fe -Si rich interdendritic carbides. In view of its complex nature, such phase can be considered as metastable. The metastability condition is typical of microstructures obtained in out-of-equilibrium conditions (section 2.2.3.1). Similar outcomes were obtained in the work of (*Lin, 2013*), where a metastable Fe_8Si_2C phase was formed (section 2.2.3.2).

Most of the carbon and silicon originated from the dissolution of SiC is consumed within each grain at the beginning of the solidification. Thus, within the inter grains areas, a liquid depleted in carbon and silicon was present, which experienced a different solidification sequence. At room temperature, a complex carbide surrounded by sub-grains was found (*Fig. 5.13*c,d). Such grains might consist of ferrite, which was formed subsequently during solid-state transformations, in particular the allotropic transformation of austenite into ferrite. Therefore, austenite was formed at high temperature in the inter grains regions, which probably had a

different composition than that present within the grains. The nature of the complex carbide remains unclear, especially if it was formed as the result of a eutectic reaction from the remaining liquid or at the solid state because of a peritectoid reaction. The identification of the complex ferrite and carbide microstructure was challenging in view of the small size of those phases and the consequent lack of identification through nano-indentation and EBSD techniques. Nevertheless, their presence at room temperature allowed to understand the CET that occurred when considering the macrostructure characterization (section 5.2.1.2).

The phenomena explained above highlight the effect of preheating in the change of solidification mechanisms when considering the same alloy processed without preheating. Especially, segregation phenomena are enhanced, in view of lower G/R.

5.2.2.3.2 Heat Affected Zone

The HAZ is visible in the overview of the cross section after etching with ASP, where darker areas with a thickness of about 20 µm are present (*Fig. 5.12*a,b). SEM observations on Nital etched sample allows to clearly differentiate the HAZ and melt pool (*Fig. 5.18*a,b). The matrix within the HAZ still remains similar to that within the top layer, with the presence of defined sub-grains boundaries (*Fig. 5.18*d). Etching with ASP proved useful to highlight the presence of nano-lamellar structures within the heat affected interdendritic carbides (*Fig. 5.18*c,e). Such structures are embedded within a second phase, whose nature remains unclear. The identification of both phases was challenging in view of their size. Indeed, EBSD analysis (*Fig. 5.15*) and nano-indentations (*Fig. 5.16*) were not able to differentiate them from the rest of the microstructure. EDS analysis revealed a higher content of carbon and molybdenum within the nano-lamellae compared to the dendritic matrix (*Table 5.6*).

The mechanism for the formation of such complex microstructure is related to the metastable condition of the Fe-Si rich carbides. Indeed, during the passage of the laser, the metastable Fe-Si rich carbides undergo an in-situ thermal treatment. This phenomenon leads to the migration of some atoms that escape from the parent Fe- Si rich phase and rearrange in more stable positions, forming the nano-lamellae and the second phase (*Maurizi Enrici, 2020*; *Tchuindjang, 2011*).

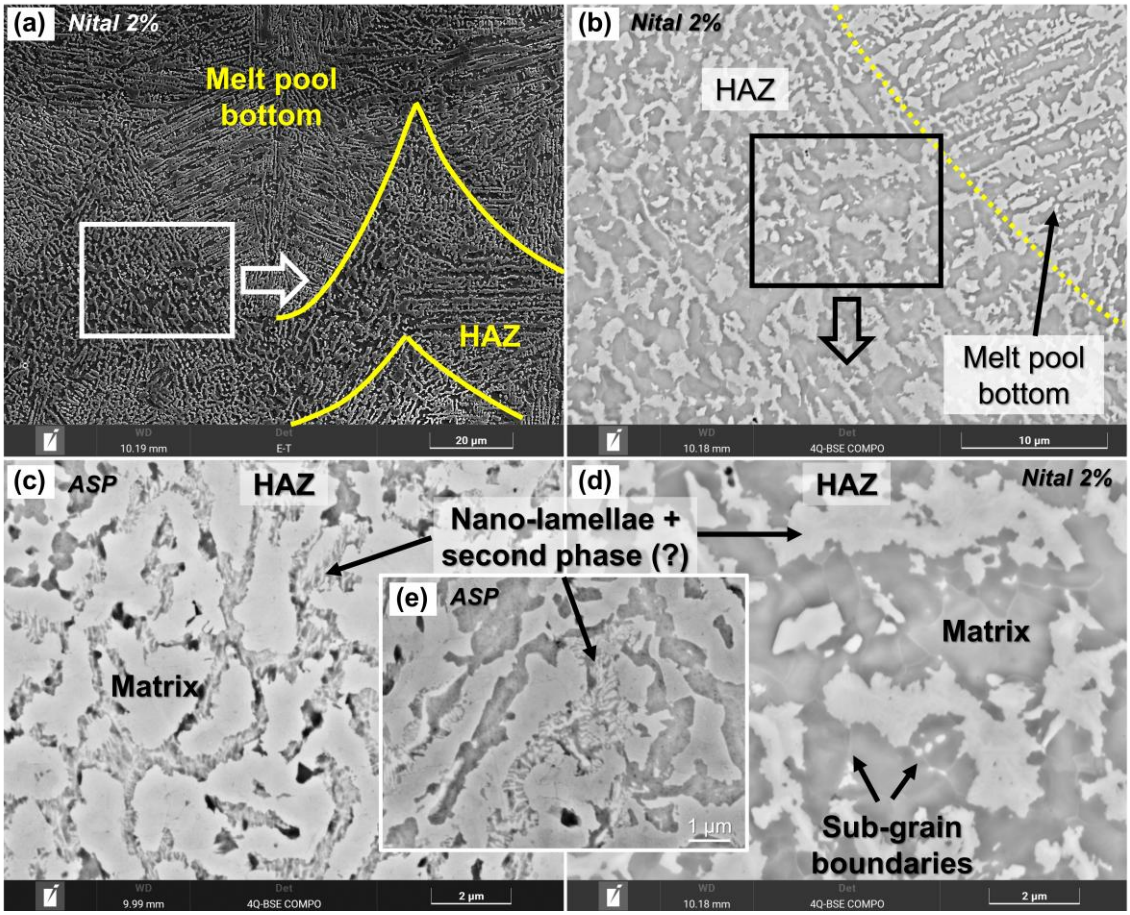


Fig. 5.18: S2 + 10% SiC with preheating 500 °C: (a, b) HAZ beneath the melt pool bottom where (c, d, e) nano-lamellae are detected within interdendritic segregations.

Atomic %

Phase	Fe	O	C	Si	Mn	Mo
Nano-lamellae	bal.	4.37±0.52	10.82±1.7	6.5±0.96	0.38±0.06	0.51±0.15
Dendritic matrix	bal.	3.86±0.20	4.47±0.14	7.12±0.01	0.31±0.02	0.10±0.04

Table 5.6: S2 + 10% SiC with preheating 500 °C: EDS analysis of the main phases on samples after etching with ASP.

5.3 Graphitization mechanism during thermal treatment

One of the main goals of this work is to achieve graphite within the microstructure of a defect-free sample. Primary graphitization from liquid state was achieved within the microstructure of samples obtained during the preliminary study with DTA (section 3.3.2). In contrast, primary graphitization was not achieved in-situ during the LPBF process. However, two main types of secondary graphitization were obtained, the first one through a post-production thermal treatment on sample processed with S2 + 10% SiC with and without preheating and the second one reached in-situ during the processing of S2 + 15% SiC. However, samples of S2 + 10% SiC processed without preheating exhibited cracks, while samples of S2 + 15% SiC revealed difficult processability with LPBF, as explained in section 4.3.3. Thus, in what follows, explanation will only regard the secondary graphitization mechanism that occurred during the thermal treatment of sample S2 + 10% SiC processed with preheating. The other graphitization mechanisms are described in Appendix C and D.

Important to mention is that the thermal treatment was specifically designed to achieve graphitization and is not intended to deal with internal residual stresses, as those have already been avoided thanks to the preheating during laser processing. Different temperatures and holding times of the thermal treatment were investigated. Preliminary experimental campaign was conducted on a DTA device under argon, in order to prevent oxidation and decarbonization phenomena. The heating rate was set at 5 °C/min, followed by the isothermal segment at the fixed temperature and subsequently cooling down to room temperature at 20 °C/min. A second campaign was repeated with the same temperature and holding time in a commercial oven under normal atmosphere. Samples were then air-cooled. Similar results in terms of microstructure and mechanical properties were obtained with both campaigns. Temperatures were chosen according to the DTA heating stage of the as-built sample (section 5.2.2.3.1, *Fig. 5.17*). The temperature of 680°C was chosen as the temperature just below austenization and above all the possible solid-state reactions. At this temperature, different times were tested (30, 60, 90 minutes). In addition, a temperature above austenization was chosen with only one holding time (800°C for 90 minutes), to see how graphitization phenomenon can be influenced.

In what follows, the discussion will first regard the effect of the temperature and secondly the effect of the holding time, focusing on the temperature of 680 °C. *Fig. 5.19* shows an overview of the samples obtained at 680 and 800 °C with 90 minutes of holding time. Graphitization was achieved in both cases, revealing homogeneous distribution covering a similar area fraction.

Graphite morphology is classified as type II based on ASTM A247 and as type V based on EN ISO 945. The difference between these microstructures lies on the matrix and carbides formed. Indeed, at 680 °C a microstructure similar to the original one is still present, with the dendritic matrix and the interdendritic carbides (*Fig. 5.19*a,b). In contrast, after the thermal treatment at 800 °C the microstructure reveals big ferritic grains of the matrix with dimensions up to 50 µm and big graphite particles (*Fig. 5.19*c,d). Furthermore, bright spots corresponding to precipitates within grains are visible under SEM (*Fig. 5.21*d). The overall macro-hardness decreased with the increase in temperature, passing from being 350 to 240 HV5 at 680 and 800 °C respectively. The reason for such decrease in hardness after the thermal treatment at 800 °C is due to recrystallization phenomena that altered the original microstructure, due to the reheating up to austenization and the formation of a new microstructure during the subsequent cooling.

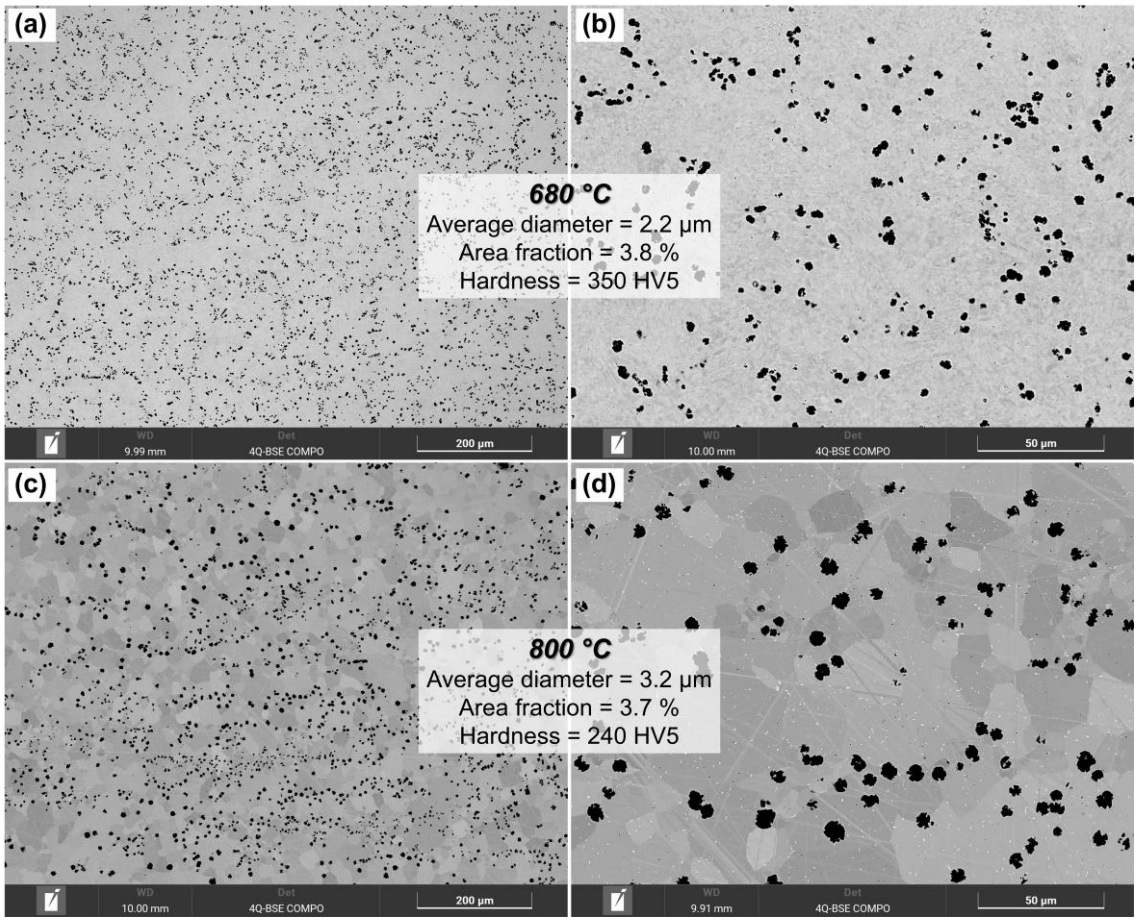


Fig. 5.19: S2 + 10% SiC with preheating 500 °C: SEM observations of the microstructure after graphitization thermal treatment at (a, b) 680 °C and (c, d) 800 °C for 90 minutes.

The effect of the holding time was investigated considering the temperature of 680 °C. In all cases graphite is present (*Fig. 5.20*), classified as type II based on ASTM A247 and as type V based on EN ISO 945, as in the previous case. Graphite particles show an increase in size with the increasing of holding time, passing from an average diameter of 2.5 µm to 4.5 µm. Furthermore, the distribution of particles becomes more homogeneous while increasing the holding time. The shorter holding time (30 min) helps to identify the regions where graphitization begins. Those regions correspond to the HAZ. With increasing time, graphitization will also occur inside melt pools zones. While higher graphitization is achieved increasing the holding time, the macro-hardness decreases, passing from 546 HV5 in the as-built microstructure to 280 HV5 after 180 minutes of thermal treatment. Intermediate values are reached for lower holding times (*Fig. 5.20*).

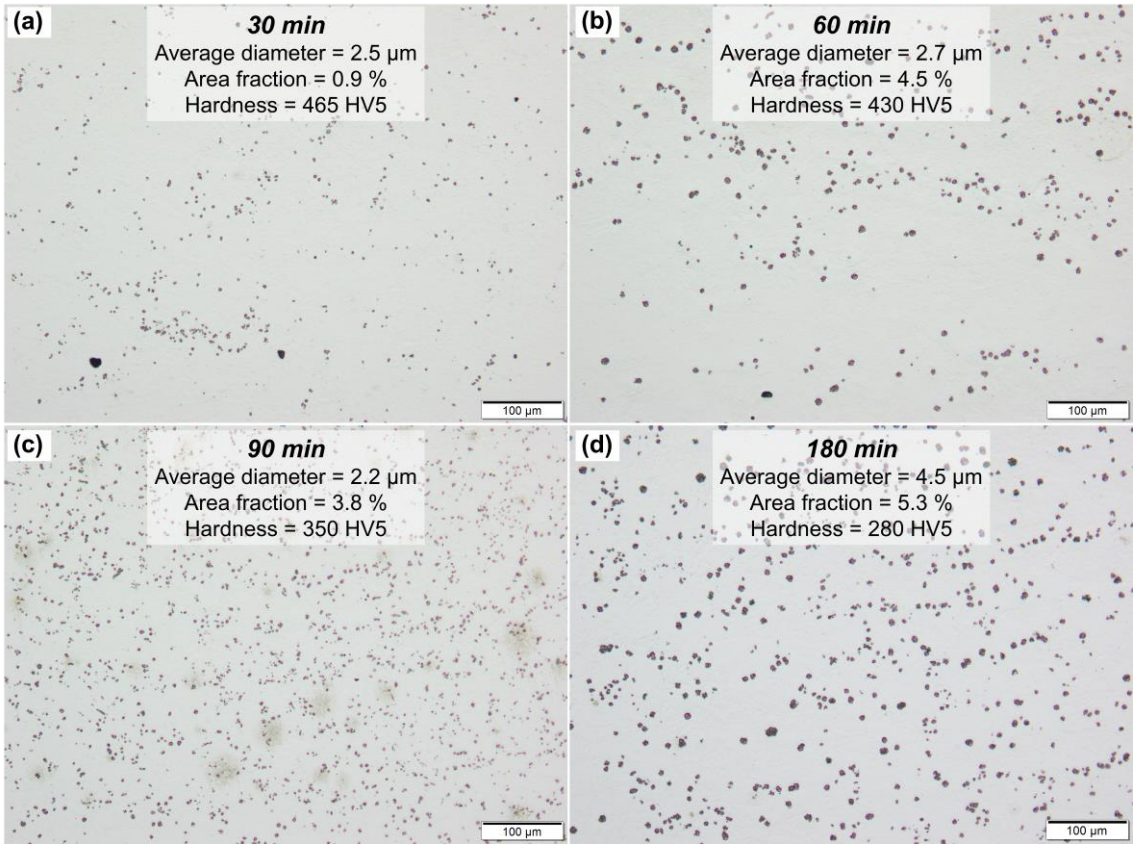


Fig. 5.20: S2 + 10% SiC with preheating 500 °C: overview of the microstructure under OM after graphitization thermal treatment at 680 °C after (a) 30, (b) 60, (c) 90 and (d) 180 minutes.

A detailed microstructural characterization was carried out after thermal treatment at 680 °C for 30 minutes. In this case, graphite particles appear mostly within the HAZ, below the bottom of the melt pool (*Fig. 5.21*a,b). Elemental mapping analysis (*Fig. 5.21*c) reveal a high

concentration of carbon corresponding to the areas of graphite particles in *Fig. 5.21*d. Meanwhile, the other elements are homogenously distributed around the particles. EBSD analysis reveals well indexed BCC crystal lattice corresponding to ferritic grains (*Fig. 5.21*e,f). The dimensions of such grains are up to 3 µm in the vicinity of graphite particles, whereas they are less than 1 µm within the melt pool bottom (*Fig. 5.21*b,d). The original interdendritic carbides are still well visible within the melt pool bottom, whereas they almost completely disappear within the HAZ (*Fig. 5.21*b,d). Thus, the size of the parent ferritic grains is affected by possible recrystallization phenomena promoted by the diffusion of iron and silicon from the decomposition of the interdendritic Fe- Si rich carbides.

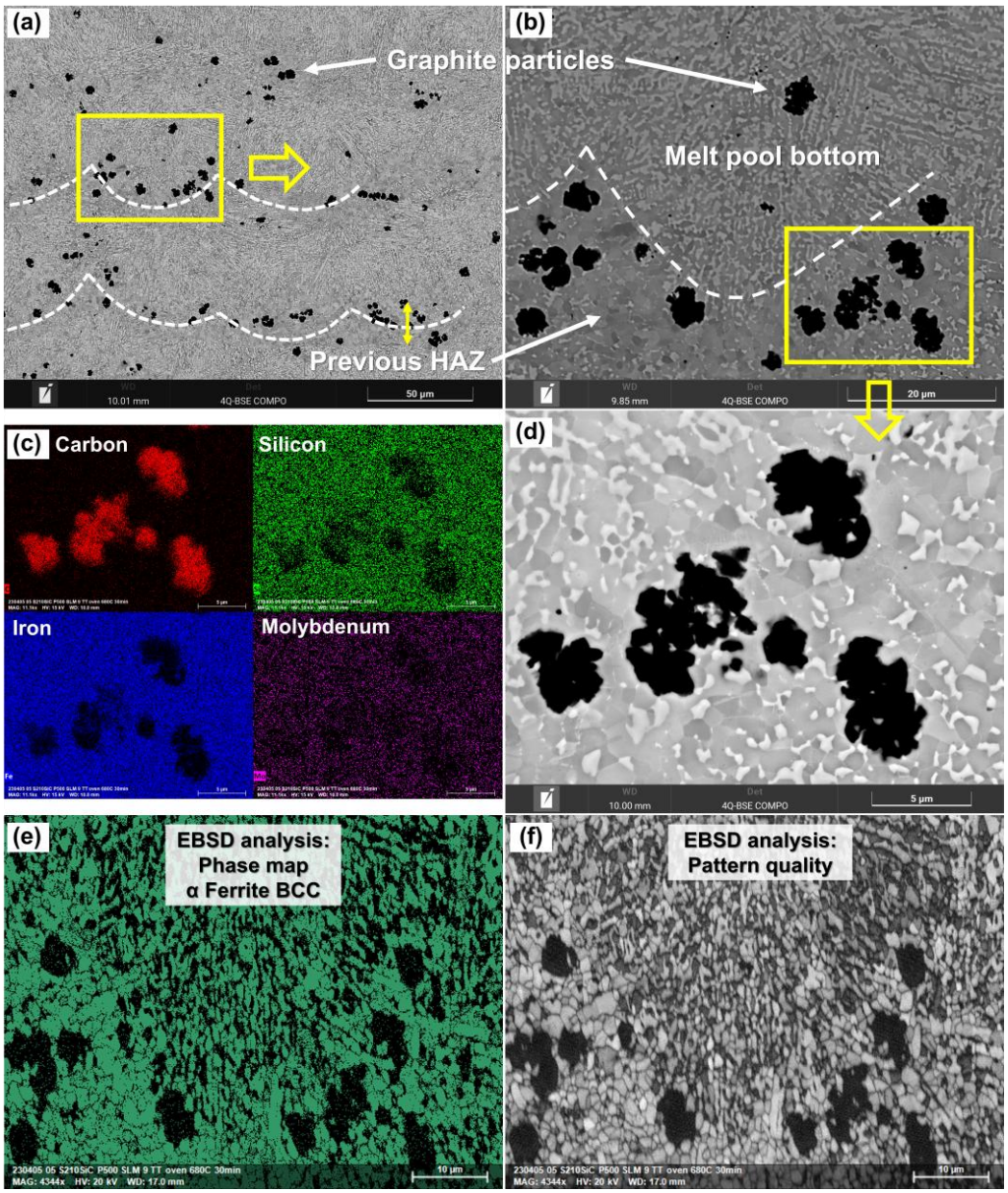


Fig. 5.21: S2 + 10% SiC with preheating 500 °C: microstructural characteristics after graphitization thermal treatment at 680 °C for 30 minutes. (a, b, d) SEM observations, (c) elemental mapping of area in fig. d and (e, f) EBSD analysis performed on area of fig. b.

The effects of preferential graphitization within the HAZ were also detected through nano-hardness measurements. Indeed, areas with values up to 15 GPa are confined only at the melt pool bottom (*Fig. 5.22*b,c). In contrast, such areas with high nano-hardness were found throughout the whole as-built microstructure (section 5.2.2.3.1, *Fig. 5.16*b), whereas low values of about 5 GPa were measured within the HAZ where graphitization occurred, corresponding to the ferritic grains formed during graphitization (*Fig. 5.22*b,c). Dark blue areas (close to 0 GPa) correspond exactly to the graphite particle in (*Fig. 5.22*b), Therefore, graphitization phenomena lead to a decrease in the local nano-hardness within HAZ.

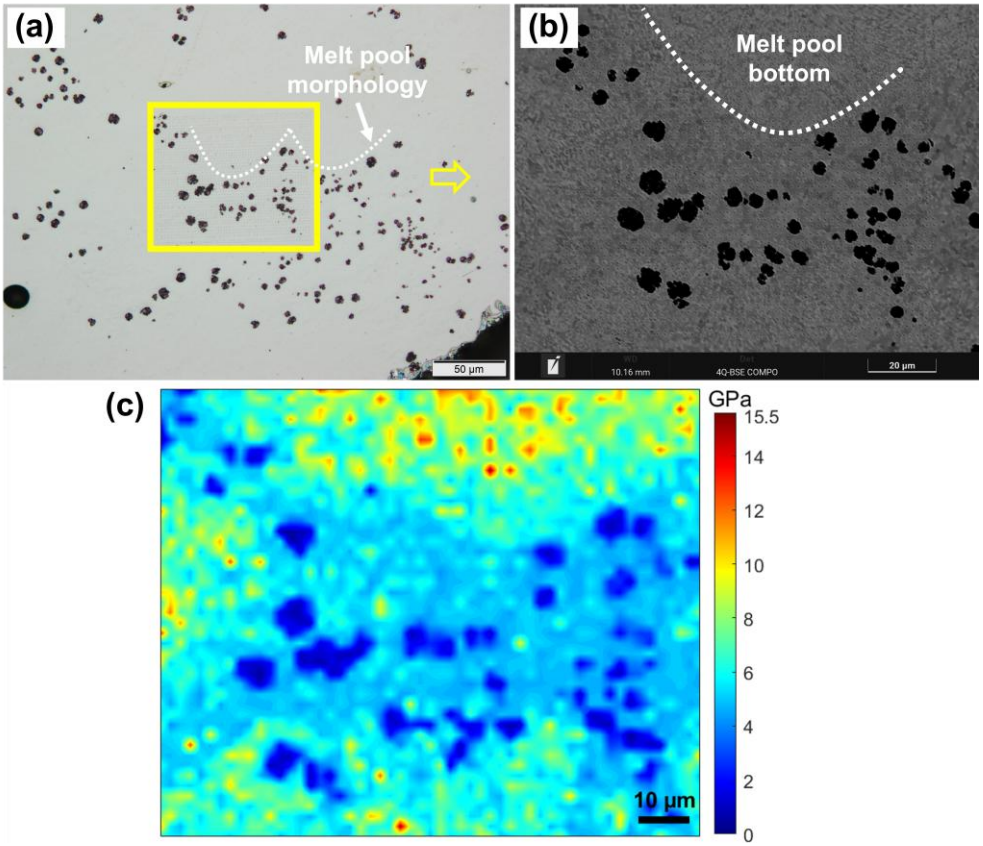


Fig. 5.22: S2 + 10% SiC with preheating 500 °C: nano-hardness analysis on the microstructure after graphitization thermal treatment at 680 °C for 60 minutes. (a) OM and (b) SEM micrographs of the area where (c) nano-hardness map was performed.

Usually, solid-state graphitization involves the transformation of iron carbides (e.g. cementite) into graphite, typical of the thermal treatment of white cast iron to achieve malleable cast iron (section 2.2). In particular, cementite evolves from lamellae into spherical particles, a process known as spheroidization, before further decomposition that allows carbon atoms to diffuse and aggregate forming graphite particles (*Gao, 2016*; *Kim, 2021*). In this case, Fe-Si rich interdendritic carbides were identified within the microstructure in the as-built conditions. Such

phase was considered in a metastable condition, especially within the melt pool (section 5.2.2.3.1). In contrast, within the HAZ, the Fe-Si rich carbides underwent a decomposition, promoted by the heat generated by the melt pool which result in the formation of nano-lamellar structures embedded in a second phase. In this case, atoms diffused in more stable positions. In particular, carbon and molybdenum redistribute to form the nano-lamellae, whereas silicon remained in higher concentration within the neighbouring second phase. This condition explains why the graphitization starts preferentially within the HAZ during the subsequent thermal treatment at 680 °C. In particular, carbon escape and diffuse out of the nano-lamellar structures, and then precipitate in form of graphite because no other carbides forming elements are present. In contrast, the appearance of graphite particles in other zones (e.g. in the centre of the melt pool) requires more time since the Fe- Si rich interdendritic carbides that were not heat affected are still in a supersaturated condition, and carbon first need to diffuse in more stable positions. Therefore, the longer the time of the thermal treatment, the longer the time for carbon mobility, favouring the nucleation and growth of graphite particles all over the microstructure. This mechanism was promoted by the supersaturation of the microstructural phases, enabled by the out-of-equilibrium conditions of LPBF. Later on, the post thermal treatment promotes a return to equilibrium conditions, where atoms diffuse in their most stable positions and equilibrium phases are formed. *Fig. 5.23* shows a sketch of the graphitization phenomena during the post-production annealing thermal treatment.

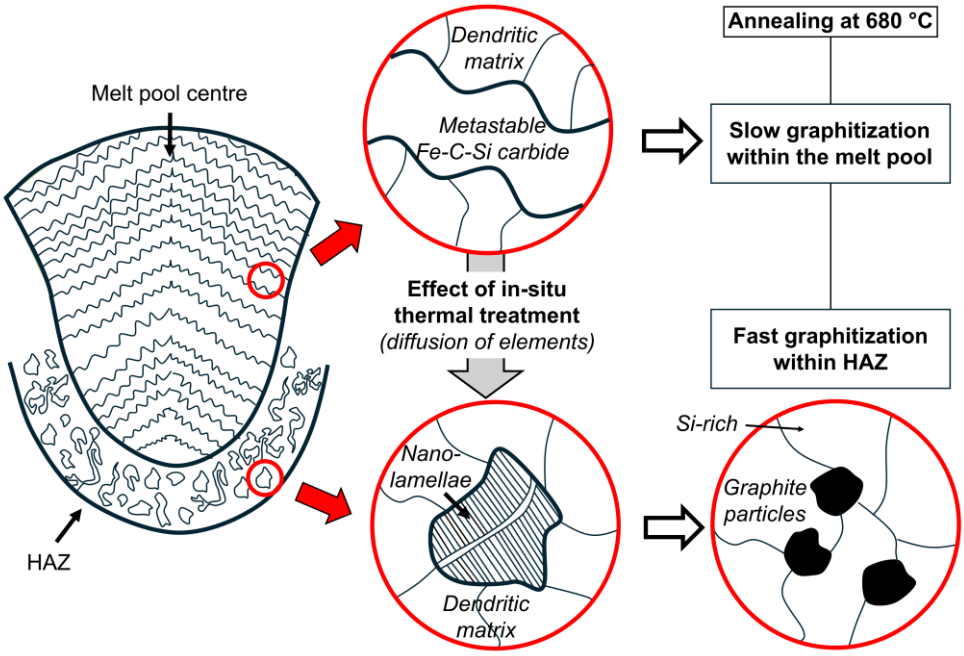


Fig. 5.23: S2 + 10% SiC processed with preheating 500 °C: Sketch of the graphitization phenomena during the post-production annealing thermal treatment, depending on the condition of the starting phases.

When considering the thermal treatment at 800 °C, complete transformation into austenite was achieved during reheating, where both desaturation and higher diffusion phenomena were enhanced. Therefore, a more stable microstructure was formed during the subsequent cooling, with graphite particles and ferritic grains. In this case, due to the complete dissolution of the hard interdendritic carbides, there is a loss in macro-hardness, which can be disadvantageous for the wear resistance.

Apart from carbon, the other element that play a crucial role and that accelerate the graphitization is silicon, well known for its properties of cementite destabiliser and graphite promoter (section 2.2.2). In view of its overall high concentration (4.27 wt. %, *Table 5.2*), the graphitization rate is accelerated. Furthermore, the advantage of having formed secondary graphite particles is the well-known lubrication effect enhanced by these particles during wear phenomena, that is the objective of this work. Thus, the advantages of the alloy developed in this work are the possibility to achieve defect-free samples with a microstructure that can be easily graphitized. Such achievements are of great importance, and they set a milestone for the research on new metal alloys for AM. To the best of the author knowledge, no similar results have been released so far.

With the current alloy, other thermal treatments may have been tested, in order to design a microstructure with specific mechanical properties. In such cases, the as-built microstructure would be deeply altered. However, another aim of this work is to avoid long and energy consuming post-treatment, providing an as-built microstructure which is close to the desired final application conditions. For these reasons, the microstructures obtained after thermal treatment at 680 °C provide homogenously distributed graphite and relative high hardness required for tool steels applications. Wear properties will be further addressed in chapter 6.

5.4 Conclusions

Macrostructural characterization:

- The reference material AISI S2 revealed a cellular solidification mode and an epitaxial grain growth. Side branching of intercellular segregations occur within a grain between two adjacent melt pool.
- A change in solidification mode is observed, passing from cellular mode on S2, to cellular dendritic and columnar dendritic when adding 10% SiC without and with preheating respectively, in views of the shifting towards lower G/R. In addition, SiC hinder the epitaxial grain growth, while preheating promote CET.

Microstructural characterization:

- *Reference AISI S2:* untempered martensitic laths are present within the top layer. The in-situ thermal cycles are responsible for the formation of a complex HAZ.
- *S2 + 10 % SiC without preheating:* adding SiC change the solid-state transformation, with lenticular martensite and residual austenite found within the final microstructure. This led to cold cracking phenomena during printing, whereas the in-situ tempering of the lath martensite within S2 allowed to avoid cracks nucleation.
- *S2 + 10% SiC with preheating:* a dendritic matrix (high silicon alloyed ferrite or carbide-free bainite), hard interdendritic carbides (metastable and Fe- Si rich) and prior grain boundaries (complex carbides + ferrite) were identified within the top layer (or melt pool centre).
    - The original interdendritic Fe- Si carbides underwent a decomposition within the HAZ. Nano-lamellar structures embedded within a second phase (unknown) were formed in view of diffusion of elements during the in-situ heat treatment.

Graphitization mechanism within S2 + 10% SiC with preheating:

- The presence of nano-lamellar structures is responsible for the fast secondary graphitization achieved within the HAZ after a post-production annealing thermal treatment at 680 °C. Higher graphitization is achieved increasing the temperature and holding time, at the expenses of losing hardness.

5.5 References

Andrews, K. W. (1965). “Empirical Formulae for the Calculation of Some Transformation Temperatures.” Journal of the Iron and Steel Institute, 203, 721–727. Retrieved from https://cir.nii.ac.jp/crid/1573105975589242368.bib?lang=en

Bartels, D., Novotny, T., Mohr, A., van Soest, F., Hentschel, O., Merklein, C., & Schmidt, M. (2022). “PBF-LB/M of Low-Alloyed Steels: Bainite-like Microstructures despite High Cooling Rates.” Materials, 15(17). https://doi.org/10.3390/ma15176171

Basso, A., Toda-Caraballo, I., San-Martín, D., & Caballero, F. G. (2020). “Influence of cast part size on macro- And microsegregation patterns in a high carbon high silicon steel.” Journal of Materials Research and Technology, 9(3), 3013–3025. https://doi.org/10.1016/j.jmrt.2020.01.052

Cayron, C. (2007). “ARPGE: A computer program to automatically reconstruct the parent grains from electron backscatter diffraction data.” Journal of Applied Crystallography, 40(6), 1183–1188. https://doi.org/10.1107/S0021889807048777

Cayron, C. (2014). “EBSD imaging of orientation relationships and variant groupings in different martensitic alloys and Widmanstätten iron meteorites.” Materials Characterization, 94, 93–110. https://doi.org/10.1016/j.matchar.2014.05.015

Cayron, C., Artaud, B., & Briottet, L. (2006). “Reconstruction of parent grains from EBSD data.” Materials Characterization, 57(4–5), 386–401. https://doi.org/10.1016/j.matchar.2006.03.008

Cayron, C., Baur, A., & Logé, R. (2018). “Intricate morphologies of laths and blocks in low-carbon martensitic steels.” Materials and Design, 154, 81–95. https://doi.org/10.1016/j.matdes.2018.05.033

Dilip, J. J. S., Ram, G. D. J., Starr, T. L., & Stucker, B. (2017). “Selective laser melting of HY100 steel: Process parameters, microstructure and mechanical properties.” Additive Manufacturing, 13, 49–60. https://doi.org/10.1016/j.addma.2016.11.003

Fang, Y., Kim, M. K., Zhang, Y., Kim, T., No, J., & Suhr, J. (2023). “A new grain refinement route for duplex stainless steels: Micro-duplex stainless steel matrix composites processed by laser powder bed fusion.” Materials Science and Engineering: A, 881(June), 145351. https://doi.org/10.1016/j.msea.2023.145351

Galbusera, F., Demir, A. G., Platl, J., Turk, C., Schnitzer, R., & Previtali, B. (2022). “Processability and cracking behaviour of novel high-alloyed tool steels processed by Laser Powder Bed Fusion.” Journal of Materials Processing Technology, 302(August 2021). https://doi.org/10.1016/j.jmatprotec.2021.117435

Gao, J. X., Wei, B. Q., Li, D. D., & He, K. (2016). “Nucleation and growth characteristics of graphite spheroids in bainite during graphitization annealing of a medium carbon steel.” Materials Characterization, 118, 1–8. https://doi.org/10.1016/j.matchar.2016.05.003

Hearn, W., Lindgren, K., Persson, J., & Hryha, E. (2022). “In situ tempering of martensite during laser powder bed fusion of Fe-0.45C steel.” Materialia, 23(February), 101459. https://doi.org/10.1016/j.mtla.2022.101459

Hernando, J. C., Elfsberg, J., Dahle, A. K., & Diószegi, A. (2019). “Evolution of primary austenite during coarsening and impact on eutectic microstructure in Fe–C–Si alloys.” Materialia, 7(April), 100391. https://doi.org/10.1016/j.mtla.2019.100391

Hooper, P. A. (2018). “Melt pool temperature and cooling rates in laser powder bed fusion.” Additive Manufacturing, 22(May), 548–559. https://doi.org/10.1016/j.addma.2018.05.032

Inam, A., Brydson, R., & Edmonds, D. V. (2015). "Effect of starting microstructure upon the nucleation sites and distribution of graphite particles during a graphitising anneal of an experimental medium-carbon machining steel." Materials Characterization, 106, 86–92. https://doi.org/10.1016/j.matchar.2015.05.014

Kim, Y. J., & Park, S. H. (2021). "Effect of initial microstructure on graphitization behavior of Fe–0.55C–2.3Si steel." Journal of Materials Research and Technology, 15, 4529–4540. https://doi.org/10.1016/j.jmrt.2021.10.071

Kitahara, H., Ueji, R., Tsuji, N., & Minamino, Y. (2006). "Crystallographic features of lath martensite in low-carbon steel." Acta Materialia, 54(5), 1279–1288. https://doi.org/10.1016/j.actamat.2005.11.001

Kosiba, K., Wolf, D., Bönisch, M., Neufeld, K., Hühne, R., Gustmann, T., … Hufenbach, J. K. (2023). "Achieving exceptional wear resistance in a crack-free high-carbon tool steel fabricated by laser powder bed fusion without pre-heating." Journal of Materials Science and Technology, 156, 1–19. https://doi.org/10.1016/j.jmst.2023.02.012

Krauss, G., & Marder, A. R. (1971). "The morphology of martensite in iron alloys." Metallurgical Transactions, 2(9), 2343–2357. https://doi.org/10.1007/BF02814873

Krauss, G., & Thompson, S. W. (1995). "Ferritic Microstructures in Continuously Cooled Low- and Ultralow-carbon Steels." ISIJ International, 35(8), 937–945. https://doi.org/10.2355/isijinternational.35.937

Lee, Y., Nordin, M., Babu, S. S., & Farson, D. F. (2014). "Effect of fluid convection on dendrite arm spacing in laser deposition." Metallurgical and Materials Transactions B: Process Metallurgy and Materials Processing Science, 45(4), 1520–1529. https://doi.org/10.1007/s11663-014-0054-7

Li, Q., Li, X. R., Dong, B. X., Zhang, X. L., Shu, S. L., Qiu, F., … Zhang, Z. H. (2024). "Metallurgy and Solidification Microstructure Control of Fusion-Based Additive Manufacturing Fabricated Metallic Alloys: A Review." Acta Metallurgica Sinica (English Letters), 37(1), 29–53. https://doi.org/10.1007/s40195-023-01656-y

Lin, Y. C., Chen, H. M., & Chen, Y. C. (2013). "Analysis of microstructure and wear performance of SiC clad layer on SKD61 die steel after gas tungsten arc welding." Materials and Design, 47, 828–835. https://doi.org/10.1016/j.matdes.2013.01.007

Maki, T. (2012). Morphology and substructure of martensite in steels. Phase Transformations in Steels. Woodhead Publishing Limited. https://doi.org/10.1533/9780857096111.1.34

Maurizi Enrici, T. (2022). Development, metallurgical and tribological characterization of complex alloys and metal matrix composites obtained from manufacturing processes under non-equilibrium conditions. University of Liège.

Maurizi Enrici, T., Mertens, A., Sinnaeve, M., & Tchuindjang, J. T. (2020). "Elucidation of the solidification sequence of a complex graphitic HSS alloy under a combined approach of DTA and EBSD analyses." Journal of Thermal Analysis and Calorimetry, 141(3), 1075–1089. https://doi.org/10.1007/s10973-019-09093-9

Morito, S., Huang, X., Furuhara, T., Maki, T., & Hansen, N. (2006). "The morphology and crystallography of lath martensite in alloy steels." Acta Materialia, 54(19), 5323–5331. https://doi.org/10.1016/j.actamat.2006.07.009

Narayana Samy, V. P., Schäfle, M., Brasche, F., Krupp, U., & Haase, C. (2023). "Understanding the mechanism of columnar–to-equiaxed transition and grain refinement in additively manufactured steel during laser powder bed fusion." Additive Manufacturing, 73(June). https://doi.org/10.1016/j.addma.2023.103702

Pham, M. S., Dovgyy, B., Hooper, P. A., Gourlay, C. M., & Piglione, A. (2020). "The role of side-branching in microstructure development in laser powder-bed fusion." Nature Communications, 11(1), 1–12. https://doi.org/10.1038/s41467-020-14453-3

Rivera, G. L., Boeri, R. E., & Sikora, J. A. (1995). "Revealing the solidification structure of nodular iron." Cast Metals, 8(1), 1–5. https://doi.org/10.1080/09534962.1995.11819186

Ryder, M. A., Montgomery, C. J., Brand, M. J., Carpenter, J. S., Jones, P. E., Spangenberger, A. G., & Lados, D. A. (2021). "Melt Pool and Heat Treatment Optimization for the Fabrication of High-Strength and High-Toughness Additively Manufactured 4340 Steel." Journal of Materials Engineering and Performance, 30(7), 5426–5440. https://doi.org/10.1007/s11665-021-05836-8

Saewe, J., Carstensen, N., Kürnsteiner, P., Jägle, E. A., & Schleifenbaum, J. H. (2021). "Influence of increased carbon content on the processability of high-speed steel HS6-5-3-8 by laser powder bed fusion." Additive Manufacturing, 46(May). https://doi.org/10.1016/j.addma.2021.102125

Shinohara, Y., Akabane, S., & Inamura, T. (2021). "Analysis of variant-pairing tendencies in lenticular martensite microstructures based on rank-1 connection." Scientific Reports, 11(1), 1–14. https://doi.org/10.1038/s41598-021-93514-z

Stjohn, D. H., Qian, M., Easton, M. A., & Cao, P. (2011). "The Interdependence Theory: The relationship between grain formation and nucleant selection." Acta Materialia, 59(12), 4907–4921. https://doi.org/10.1016/j.actamat.2011.04.035

Suikkanen, P. P., Cayron, C., DeArdo, A. J., & Karjalainen, L. P. (2013). "Crystallographic Analysis of Isothermally Transformed Bainite in 0.2C-2.0Mn-1.5Si-0.6Cr Steel Using EBSD." Journal of Materials Science and Technology, 29(4), 359–366. https://doi.org/10.1016/j.jmst.2013.01.015

Tchuindjang, J. T., Sinnaeve, M., & Lecomte-Beckers, J. (2011). "Influence of High Temperature Heat Treatment on in situ Transformation of Mo-rich Eutectic Carbides in HSS and Semi-HSS Grades." Abrasion 2011, (August 2011), 61–75.

Tenaglia, N. E., Boeri, R. E., Basso, A. D., & Massone, J. M. (2017). "Macro and microstructural characterisation of high Si cast steels–Study of microsegregation patterns." International Journal of Cast Metals Research, 30(2), 103–111. https://doi.org/10.1080/13640461.2016.1258515

Zhai, W., Zhou, W., & Nai, S. M. L. (2022). "Grain refinement and strengthening of 316L stainless steel through addition of TiC nanoparticles and selective laser melting." Materials Science and Engineering: A, 832(August 2021), 142460. https://doi.org/10.1016/j.msea.2021.142460

Zhu, K., Barbier, D., & Iung, T. (2013). "Characterization and quantification methods of complex BCC matrix microstructures in advanced high strength steels." Journal of Materials Science, 48(1), 413–423. https://doi.org/10.1007/s10853-012-6756-9

Chapter 6

Assessment of wear properties

Contents

6.1 Introduction 164
6.2 Approach for wear characterization 165
6.3 Wear sequence of reference material AISI S2 167
6.4 Wear properties of graphitic tool steels 174
6.4.1 Influence of hardness on the Coefficient of Friction 175
6.4.2 Effect of solidification carbides and graphite on wear resistance 181
6.5 Conclusions 185
6.6 References 186

6.1 Introduction

One of the aims of this work is to achieve self-lubricating properties during wear applications of the new material. Therefore, the wear behaviour of the new alloys is the last main information to provide. The assessment of wear properties is a topic on which the author focused at the beginning of the PhD project, using other materials previously developed at the MMS laboratory[10,11]. The approach used in that preliminary work will be explained in the next section and will be used for the wear characterization of the new alloys. The explanations will first regard the elucidation of the wear sequence at room temperature of the reference material AISI S2. Afterwards, general assessments of the wear properties of the new alloy (S2 + 10% SiC processed with preheating) will be given, comparing the sliding wear behaviour of as-built and thermal-treated samples. Furthermore, the elaboration route used to develop the new tool steel revealed a phenomenon of secondary graphitization, which led to a patent[12], given that its wear resistance was superior to that of conventional spheroidal graphite cast iron.

[10] Maurizi Enrici, T., et al. (2023). "Unveiling the complex wear sequence of a directed energy deposited 316L+WC hierarchical composite against alumina." Journal of Materials Research and Technology, 26(August), 621–638. https://doi.org/10.1016/j.jmrt.2023.07.172

[11] Saggionetto, E., et al. (2025). "On the role of the hierarchical structures in the friction- induced phenomena of directed energy deposited 316L+WC sliding against different counter-bodies." Tribology International, Volume 212, July 2025, https://doi.org/10.1016/j.triboint.2025.110973

[12] Saggionetto, E., Tchuindjang, J. T., Mertens, A. "GRAPHITE-BASED STEEL ALLOY AND METHOD FOR PRODUCING IT USING LASER POWDER BED FUSION". Europe: application ref. n° EP24167458 (28/03/24); International: application ref. n° PCT/EP2025/058128 (25/03/25), published under WO/2025/202196

6.2 Approach for wear characterization

As explained in section 2.4, wear behaviour of materials is a complex and debated topic, especially with the raise of new manufacturing technologies and the consequent development of new alloys. When evaluating the wear properties of a new alloy, it is always necessary to correlate the wear behaviour with the specific tribosystem under which the wear properties are being tested, without generalizing them. Indeed, wear phenomena are strongly dependent on the conditions of the testing/application. Usually, before arriving to the real application of the material, sliding wear properties can be evaluated under a common pin-on-disc device. However, changing one parameter of this testing method can affect the overall worn volume and the related wear phenomena, thus leading to incorrect and limited interpretation of the wear behaviour of the material. This aspect is even more intricated when considering complex material such as Metal Matrix Composites (MMCs), where the microstructure is reinforced by ex-situ addition of particles. Such materials can exhibit complex wear behaviour, as explained in a previous work of the MMS team, where a Direct Energy Deposited (DEDed) 316L + WC was tested against alumina (Al_2O_3) as counter-body (*Maurizi Enrici, 2023*). From that study, the author of this work further investigated the wear properties of the DEDed 316L + WC by using different counter-bodies (*Saggionetto, 2025*). The result showed that under different tribosystem conditions the same material can exhibit opposite wear regimes. The complexity of wear phenomena occurring with MMCs stands with the fact that cyclical wear regimes with different wear stages can occur. In contrast, more conventional metals exhibit a steady-state regime, which can make easier the identification and interpretation of the wear phenomena. To understand each wear stage and the overall wear regime, the approach of interrupted wear test was developed by (*Maurizi Enrici, 2023*). Although the new materials developed in the current work exhibit a steady-state wear regime, the wear properties will be evaluated using the interrupted wear test approach and considering the tribosystem at all levels, as in (*Saggionetto, 2025*). Evolution of Coefficient of Friction (CoF), quantification of worn volumes, microscope observations on worn track and friction induced subsurface and debris characterization will be combined to understand the wear phenomena of the reference material AISI S2 sliding against alumina. In-depth explanations about the wear phenomena and terminology, which will be used in the next sections (e.g. run-in period, tribolayer, friction-induced layers etc.), can be found in the two papers mentioned above.

The experimental methodologies used for wear characterization are based on the standard ASTM G99-17. Several blocks of 35 x 35 x 10 mm^3 were produced by LPBF with the

parameters explained in chapter 4, which were subsequently cut by electro-discharge machining to obtain samples of 5 mm of heights. Thus four faces in total were available for each block, which corresponds to two samples per block with two faces par sample, while considering both the top and the bottom surfaces. The top layer of the block was discarded to avoid microstructural differences. Each face of the sample was assumed to have similar characteristics, as the microstructure was found homogeneous from bottom to top during the previous metallurgical characterization (chapter 5). The surface was rectified to achieve a roughness of less than 0.8 µm on both faces of a given sample. The device used to test the sliding wear properties was a CSM high-temperature pin-on-disc tribometer. The wear specimen slid against an alumina counter-body pin with a spherical shape of 6 mm diameter. Tests were performed at room temperature in dry conditions. The sliding speed was 10 cm/s and the applied load was 10 N. During the pin-on-disc test, the CoF was measured by the tangential deviation of the pin-on-disc arm sensor. A reference test was performed first over a sufficiently long distance. Then, interrupted tests were performed to better understand specific variations of the CoF. Following the wear tests, the worn volume of both specimen and counter-body was estimated by using an Alicona Infinite Focus G5 optical profilometer with the ring-light option. The wear rates were estimated by dividing the worn volume [mm^3] by the sliding distance [m]. Transversal section parallel to the sliding direction was obtained by electro-discharge machining to observe the microstructure of the subsurface beneath the worn track. The subsurface sample was hot mounted using a conductive resin, then ground and polished down to 1 µm. The worn track, subsurface and debris were observed through Optical and Scanning Electron Microscopy. Similar methodological techniques were used to assess the wear properties at room temperature of the alloy S2 + 10% SiC processed with preheating.

6.3 Wear sequence of reference material AISI S2

According to the approach for wear characterization mentioned in the previous section, the wear sequence of the reference material AISI S2 will be elucidated. A first reference pin-on-disc test was performed until a total sliding distance of 1500 m with 11 mm of sliding radius. The CoF evolution reveals an initial rise from a value of about 0.1 up to 0.8, followed by a drop until 0.6 (*Fig. 6.1*a,b). Subsequently, the CoF rises again until 0.65 and then it decreases smoothly stabilizing at an average value 0.57 (*Fig. 6.1*a,b). A steady-state regime occurs, meaning that no cyclical regime is detected. To better understand the changes in CoF, specific interrupted wear tests were performed by selecting the appropriate sliding distance from the reference wear test. Test 1 was interrupted after the drop, around 18 m, while Test 2 was interrupted after the second rise, at 65 m. Profilometer measurements of the worn tracks after each test reveals an increase in worn volumes with the increase in the sliding distance (*Fig. 6.1*c). Such increase in worn volume is due to the increase in dimensions (width and depth) of the worn track (*Table 6.1*). At the end of the reference test, the track reveals an average depth of about 7.6 μm, which is almost the double of the average depth found after test interrupted at 65 m. Further explanations will be present later in this section. The worn counter-body exhibits a circular worn surface after the reference test, with a total worn depth of 10 μm (*Table 6.1*). In contrast, the counter-body after the interrupted wear tests has a negligible worn surface.

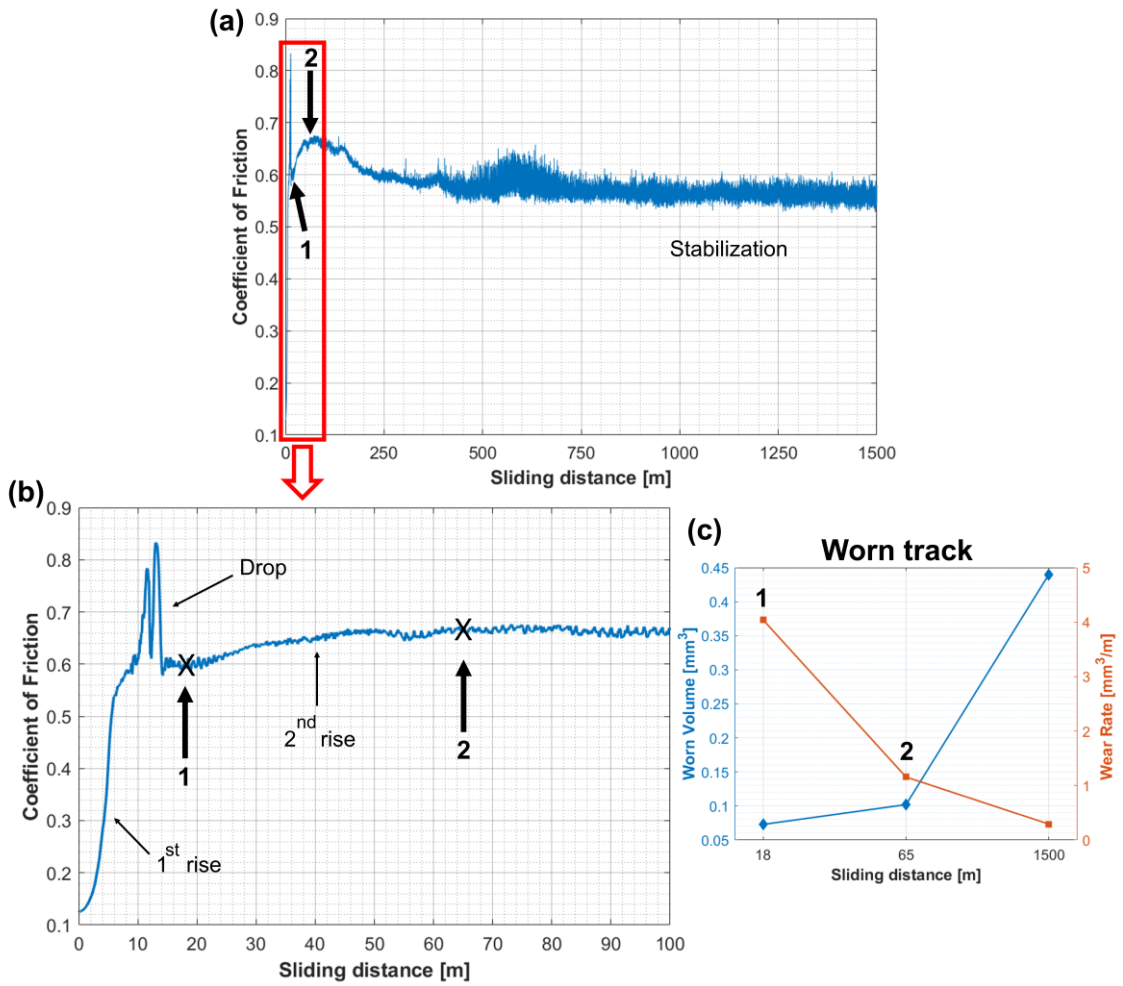


Fig. 6.1: (a) Evolution of Coefficient of Friction (CoF) during the reference test (1500 m), (b) magnification on the reference CoF curve in the range 0 - 100 m and (c) worn volume and wear rate of the worn track after each test.

Test	**Distance [m]**	*Worn track*		*Worn counter-body*
		Width [µm]	**Depth [µm]**	**Depth [µm]**
1	18	146	1	-
2	65	257	4.3	-
Reference	1500	500	8.0	10

Table 6.1: Profilometer measurements on the worn track and counter-body after each test.

Post-mortem SEM observations of the worn surface after the test interrupted at 18 m reveals high amount of debris accumulated within both the track and external areas (*Fig. 6.2*a). The accumulation within the track is found preferentially on delaminated areas (*Fig. 6.2*b). EDS analysis on debris revealed a certain degree of oxidation, as oxygen is about 47 at. %

(*Fig. 6.2*a). Signs of plastic flow of the material and grooves are visible in *Fig. 6.2*c. Big platelets with dimensions up to 30 µm are found on the side of the worn track (*Fig. 6.2*d). Powder-like debris are present on the external part of the worn track, revealing a coloration that gradually change from black to dark orange/brown (*Fig. 6.2*e,f).

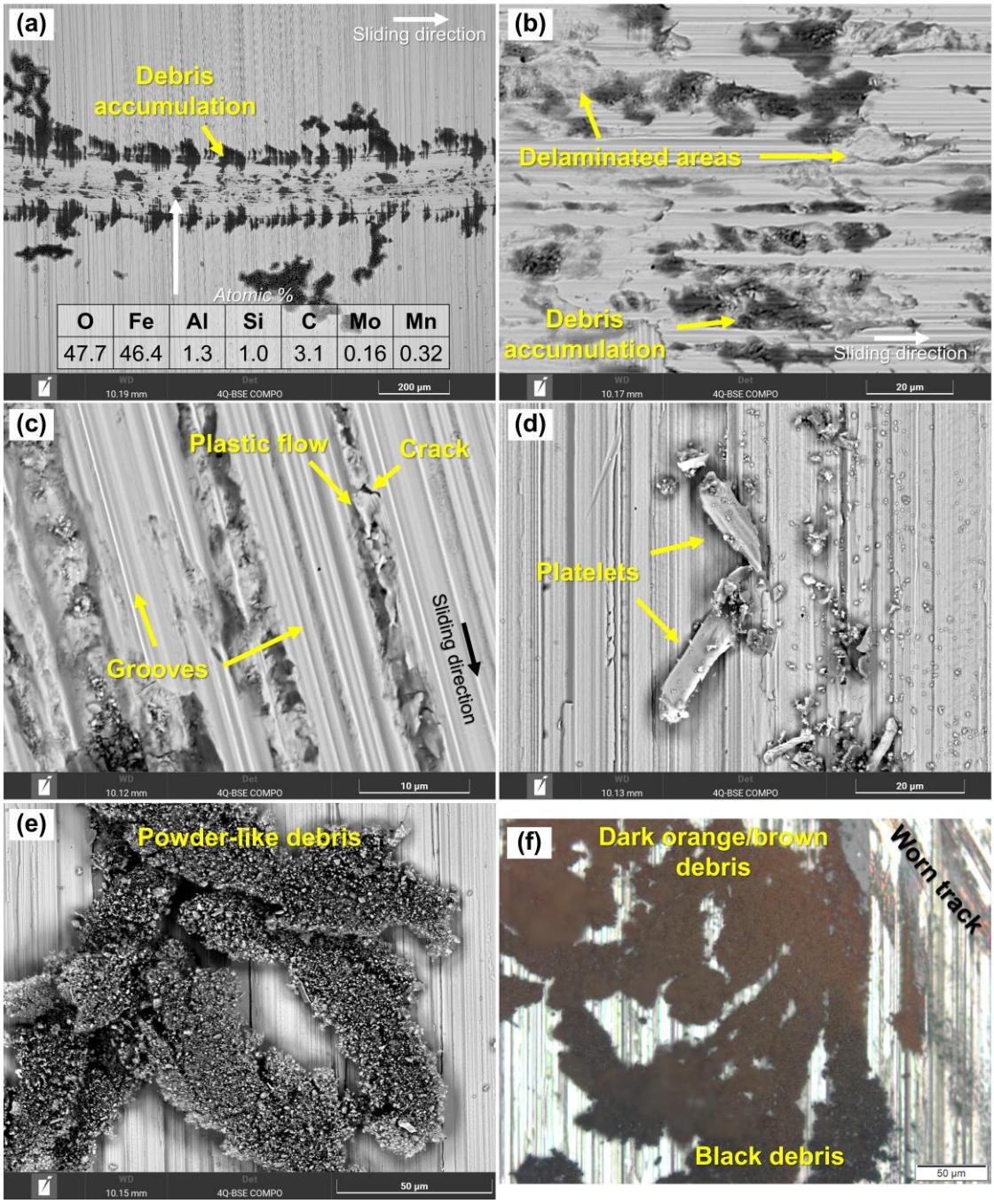


Fig. 6.2: (a) Overview of the worn surface after the interrupted test at 18 m, where (b) debris accumulate preferentially within delaminated areas. (c) Grooves and plastic flow are visible at high magnification. (d) Big platelets are found on the side of the worn track. (e,f) Powder-like debris away from the worn track, with a coloration that gradually change from black to dark orange/brown.

After Test 2 that was interrupted at 65 m, the central part of the worn track exhibits less debris compared to that of Test 1, which stop at 18 m (*Fig. 6.3*a). Areas of previously accumulated debris start to be compact, with sign of spalling and cracks (*Fig. 6.3*b). Meanwhile, the worn track is almost debris-free after the reference test (stopped at 1500 m), with an overall smooth appearance (*Fig. 6.3*c). Only thin grooves are present (*Fig. 6.3*d). In addition, it can be observed that debris are powder-like with a completely dark orange/brown coloration after the reference test (*Fig. 6.3*e,f).

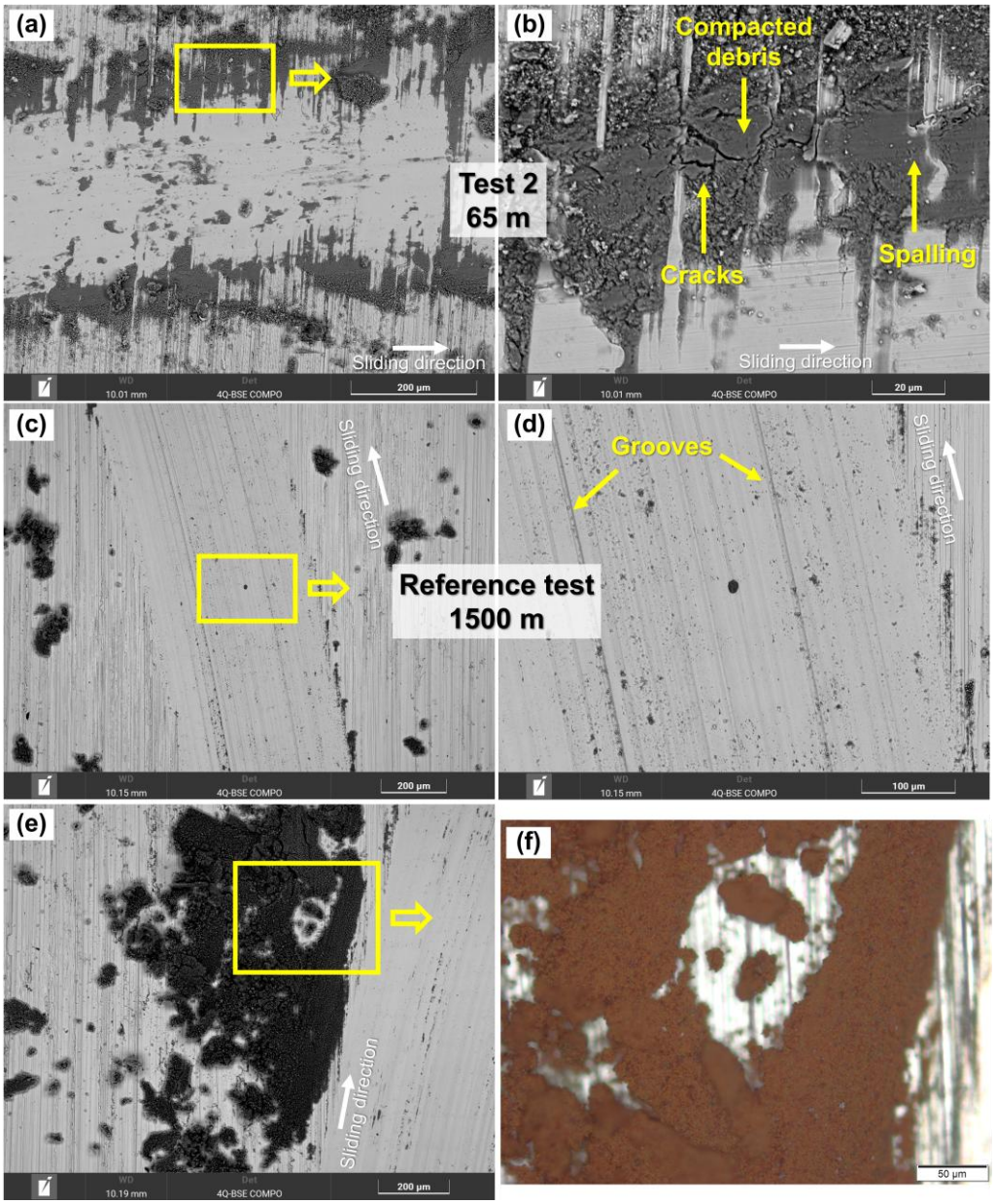


Fig. 6.3: (a) Overview of the worn track after Test 2 interrupted at 65 m, where (b) signs of spalling and cracks are found within the compacted debris. (c) Overview of the track after the reference test , where (d) thin grooves are visible. (e,f) Powder-like debris with a dark orange/brown coloration collected after the reference test.

During the wear test, the microstructure beneath the surface is affected by friction-induced phenomena, as an upper Mechanically Mixed Layer (MML) and a lower Plastic Deformed Layer (PDL) are formed (*Fig. 6.4*). Both layers have a thickness about 2-3 µm, and they are found homogeneously within the subsurface. The formation of both MML and PDL lies on modification occurring in the martensitic laths and intercellular carbides. The high stresses generated by the contact between counter-body and specimen leads to the fracture of both the martensitic laths and intercellular carbides, whose particles are mixed together forming the outer MML. Meanwhile, the microstructural phases are only deformed without cracking within the inner PDL.

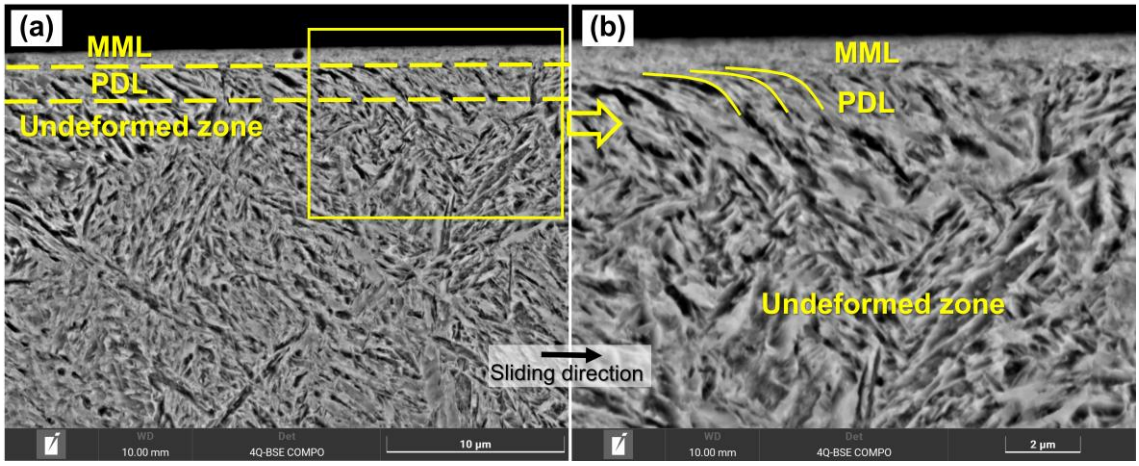


Fig. 6.4: Friction-induced layers within the subsurface underneath the worn track of the reference test.

In what follows, the elucidation of the wear sequence at room temperature is present while combining all the results showed above. The first rise and drop for CoF is ascribed to the so-called 'run-in period' (*Fig. 6.1*a,b). This initial wear stage is well known in tribology and was extensively studied (*Maurizi Enrici, 2023; Saggionetto, 2025*). During this period, the rough metal surface experience plastic flow, which leads to cracking followed by delamination of material (*Fig. 6.2*b). Big platelets are generated consequently (*Fig. 6.2*d), which are spread through the track causing grooves (*Fig. 6.2*c). Therefore, abrasive wear should be the main mechanism occurring at this initial stage. Although the worn volume is low in view of the small dimensions of the track, the wear rate is even higher within the run-period than the average achieved after the longer reference test (*Fig. 6.1*c). This fact highlights the severe nature of the abrasive wear that occur during the run-in period.

The platelets are crushed into smaller pieces with the continuation of the test. Such debris becomes oxidized, as revealed by EDS analysis (*Fig. 6.2*a), and it accumulates preferentially in the delaminated areas previously formed (*Fig. 6.2*a,b).

When a certain number of oxides cover the track, the direct contact between specimen and counter-body is mitigated. Thus, the CoF decreases (drop in *Fig. 6.1*b), setting the end of the run-in period. This stage corresponds to the protective effect acted by the so-called 'tribolayer' of oxides, which prevent both counter-body and specimen from further wear (*Maurizi Enrici, 2023; Saggionetto, 2025*). The end of the run-in period is also associated with a change in the appearance of the debris. Indeed, its coloration changes from black to dark orange/brown (*Fig. 6.2*f). The sharp drop in CoF only lasts for a few laps. Indeed, the tribolayer is not stable enough to resist for long and it starts to compact. Thus, the CoF increases again (second rise in *Fig. 6.1*b). Spalling phenomena occur within the compact tribolayer (*Fig. 6.3*b), leading to its delamination and to the generation of debris. The tribolayer gradually disappears during the subsequent smooth stabilization of the CoF. After 1500 m of sliding distance, SEM observations revealed an overall 'clean' track, only with thin grooves formed by the delaminated pieces of the compacted tribolayer (*Fig. 6.3*c,d). At the end of the reference test, debris is completely dark orange/brown (*Fig. 6.3*f), in view of oxidative wear phenomena.

The low stability of the tribolayer can also be detected within the subsurface underneath the worn track. Indeed, SEM observations on the transversal section parallel to the sliding direction reveal a thin MML (*Fig. 6.4*). Usually, when a stable tribolayer is formed during a sliding wear test, it can participate to the formation of a thick MML, as the oxides can penetrate and get mixed with the underneath metal. In contrast, in this case, the unstable nature of the tribolayer does not promote the thickening of the MML. Underneath the MML, a thin PDL is formed with a thickness of few microns. In another material that was developed and tested in a previous work, and which corresponds to the DEDed 316L + WC, a thicker PDL of around 10 µm was observed. Therefore, it can be assumed for the current case that the reduced thickness of the PDL reflects the higher resistance of the LPBF AISI S2 tool steel to plastic deformation. The reason might be associated either to the finer microstructures achieved with LPBF or to the nature of the matrix when compared to DED. Indeed, cells size is about 10 times lower within the AISI S2 LPBF microstructure compared to those observed in DEDed 316L + WC. Furthermore, the type of matrix also affected the resistance of the material to plastic deformation. Indeed, in the LPBF AISI S2 steel, the lath martensite ensures more resistance to

plastic deformation than the austenitic matrix of the DEDed 316L + WC, the latter may also undergo a friction-induced martensitic transformation.

To summarize, the AISI S2 tool steel processed by LPBF and tested under pin-on-disc exhibits a relatively short run-in period followed by a steady-state wear regime. A low wear rate and a smooth worn surface were found at the end of the reference test. Such results were obtained at room temperature. A change in the wear behaviour of the material may exists when tests are performed at higher temperatures. Preliminary investigations of high temperature wear properties were performed (Appendix E). There is a significant increase in wear for all temperatures tested (200, 300, 400 °C). Further testing and more in-depth analysis must be carried out.

6.4 Wear properties of graphitic tool steels

The wear behaviour of S2 tool steel changes when SiC is added. Indeed, the presence of such additive changes the type of phases within microstructure of the alloy, as described in chapter 5. Among all phases, graphite is present. Such phase is well known for its ability of acting as a solid lubricant capable of enhancing wear resistance.

This section focuses on how the newly developed alloy exhibits improved tribological properties. The study of the wear sequence as in the previous section (6.3) is no longer proposed. Instead, standard wear features such as CoF and wear rate will be determined and compared across different preparation conditions for the new alloy, to highlight the contribution of the optimized heat treatment. A comparison with a spheroidal graphite cast iron, which is considered the reference material for solid lubricants, is also proposed.

The as-built and thermal treated S2 + 10% SiC samples that were tested under pin-on-disc are listed in *Table 6.2*, that also provides a brief reminder of the main properties explained in chapter 5 (hardness, phases, size and area fraction of graphite particles). The parameters used are those explained in section 6.2. A preliminary reference wear test was performed with a material that has intrinsic and well-known self-lubricating properties acted by graphite particles. In particular, EN-GJS-400-15 Nodular Cast Iron (NCI) was selected as reference material. *Fig. 6.6*a shows an overview of its original microstructure, consisting of primary graphite nodules (up to 50 µm) within a ferritic microstructure. The average hardness is 180 HV5.

Material	**Thermal treatment**	**Hardness [HV5]**	**Phases**	**Graphite particles**	
				Size [µm]	**Area fraction %**
Cast Iron	-	180	Ferrite + Graphite	50	-
S2 + 10% SiC with preheating	as-built	564	Iron carbides + Ferrite/Bainite	-	
	680 °C – 30 min	465	Iron carbides + Ferrite/Bainite + Graphite	2.5	0.9
	680 °C – 60 min	430		2.7	4.5
	680 °C – 90 min	350		2.2	3.8
	800 °C – 90 min	240	Ferrite + Graphite	3.2	3.7

Table 6.2: List of samples and their main properties used for the wear characterization of the new alloys.

6.4.1 Influence of hardness on the Coefficient of Friction

*Fig. 6.5*a shows the CoF evolution during the pin-on-disc tests. In general, all samples exhibit a steady-state wear regime, as the CoF remains quite stable after an initial short run-in period. The reference cast iron material exhibits the lowest average CoF (0.3). In contrast, the as-built S2 + 10% SiC exhibits the highest average CoF (0.87). Intermediate average CoF are achieved with the thermal treated samples. At 680 °C the average CoF decreases with the increase in holding time, with values of 0.75, 0.70 and 0.65 for 30, 60 and 90 minutes of thermal treatment, respectively. Meanwhile, the sample tested after thermal treatment at 800 °C for 90 minutes exhibits an average value of 0.62. Considering all specimens, the average CoF decreases with the decrease in hardness of the sample (*Fig. 6.5*b).

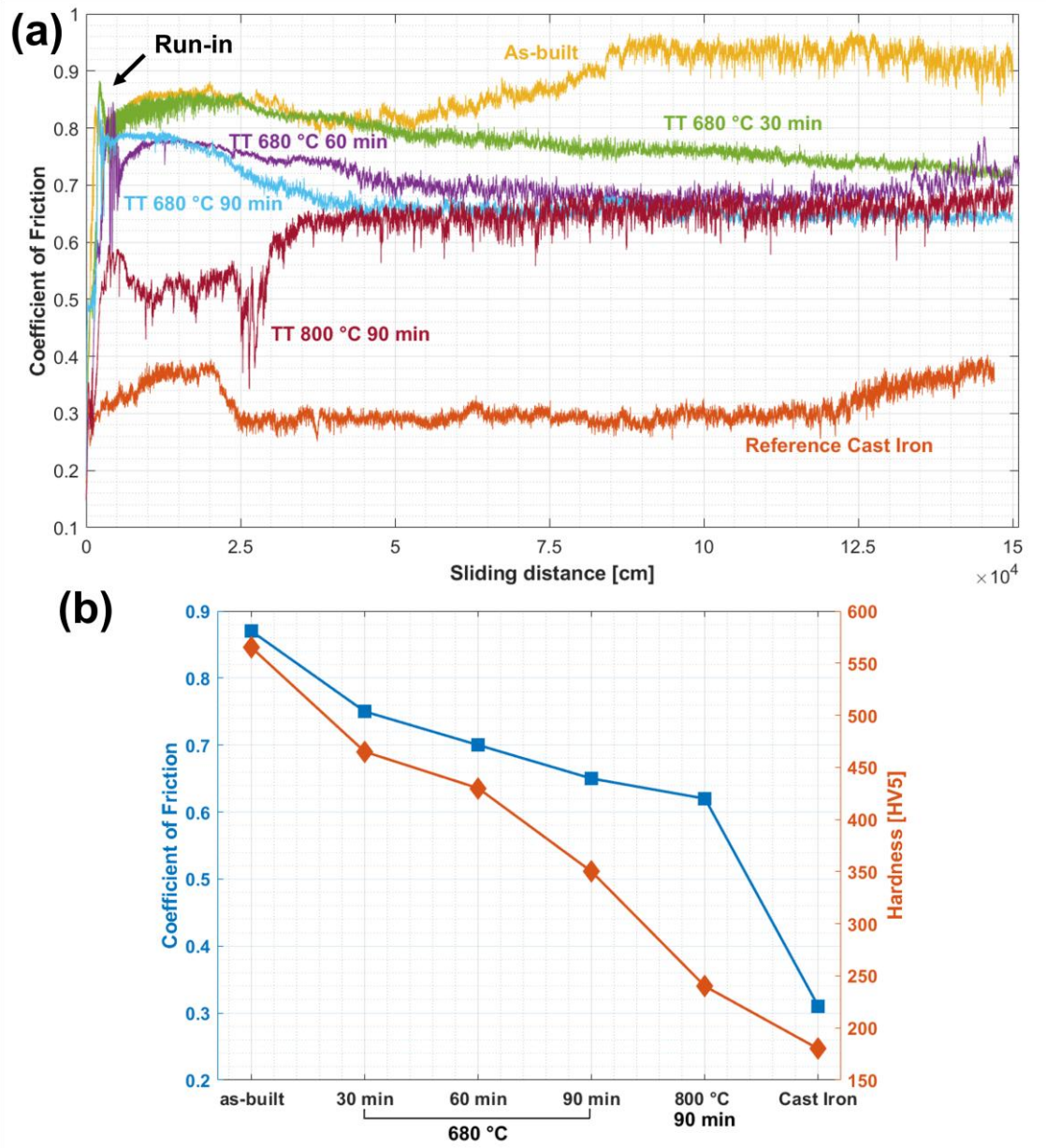


Fig. 6.5: (a) CoF evolution and (b) relation with hardness of each tested sample.

As explained in section 2.4.2, self-lubricating properties in metals induced by graphite particles can enhance the wear resistance of the material. Indeed, graphite particles can be deformed and eventually be pulled out from the material, thus participating in the formation of a film of graphite on the surface. Such film can act as a tribolayer, preventing from further wear both specimen and counter-body and decreasing CoF, even at values lower than 0.1 (*Campos, 2015*). Indeed, graphite is known as a solid lubricant with the role of reducing friction between the materials pair. The CoF can be affected by the type of matrix and the hardness of the metal (*Liu, Du, Wang, Zheng, 2023*; *Zhang, 2019*). Despite the properties of graphite, the presence of hard phases such as martensite, bainite and carbides can increase the CoF. Recently, cast irons

with martensite, bainite and/or ferrite as matrix phases are being developed to achieve superior wear resistance (*Du, 2021*). The work of (*Liu, Du, Wang, Hu, 2023*) reported that there is an increase in CoF with the increase in martensite fraction within the matrix of a dual phase cast iron, due to the high hardness of martensite. Thus, CoF is directly dependent on the hardness of the material, even with the presence of graphite nodules. Although the CoF is not lowered, the total wear resistance is enhanced thanks to the combination of a hard matrix and the presence of graphite particles. With lower content of martensite, the soft ferrite undergoes plastic deformation favouring a consequent pull out of the graphite spheroids, forming a self-lubricating film on the worn surface that reduce CoF. However, the overall wear resistance decreases.

The new tool steel developed in this work has a relatively soft ferritic matrix with hard iron carbides formed during solidification (Fe-C-Si rich interdendritic phase, section 5.2.2.3) and, if thermal treated, graphite particles. Size and fraction of graphite particles change depending on the thermal treatment, as well as the nature of carbides and matrix (*Table 6.2*). At 680 °C, the increase of the holding time leads to increase the size of the graphite particles, together with a decrease in the fraction of hard carbides and an increase in the number of the ferritic grains. At 800 °C the microstructure is similar to that of the reference NCI, with graphite spheroids surrounded by a ferritic matrix (section 5.3). The nature of the phases obtained in the new graphitic alloy is different compared to those present in conventional NCIs and graphitic steels, in view of different solidification conditions. However, comparisons between the new alloys and existing conventional materials can help to better understand the wear properties.

Fig. 6.6 shows microstructural and post-mortem SEM observation of the worn surface of the reference NCI. The low CoF achieved when testing the reference NCI is due to the presence of big graphite spheroids and a soft ferritic matrix (*Fig. 6.6*a). Similarly to the mechanism explained earlier, the soft ferritic matrix easily undergoes plastic deformation and delamination that gradually expose the graphite nodules embedded within the material (*Fig. 6.6*c,d), followed by their eventual pull out and the formation of a tribolayer enriched in graphite. The final worn surface has rough macro-features, with big grooves filled with oxides (*Fig. 6.6*b).

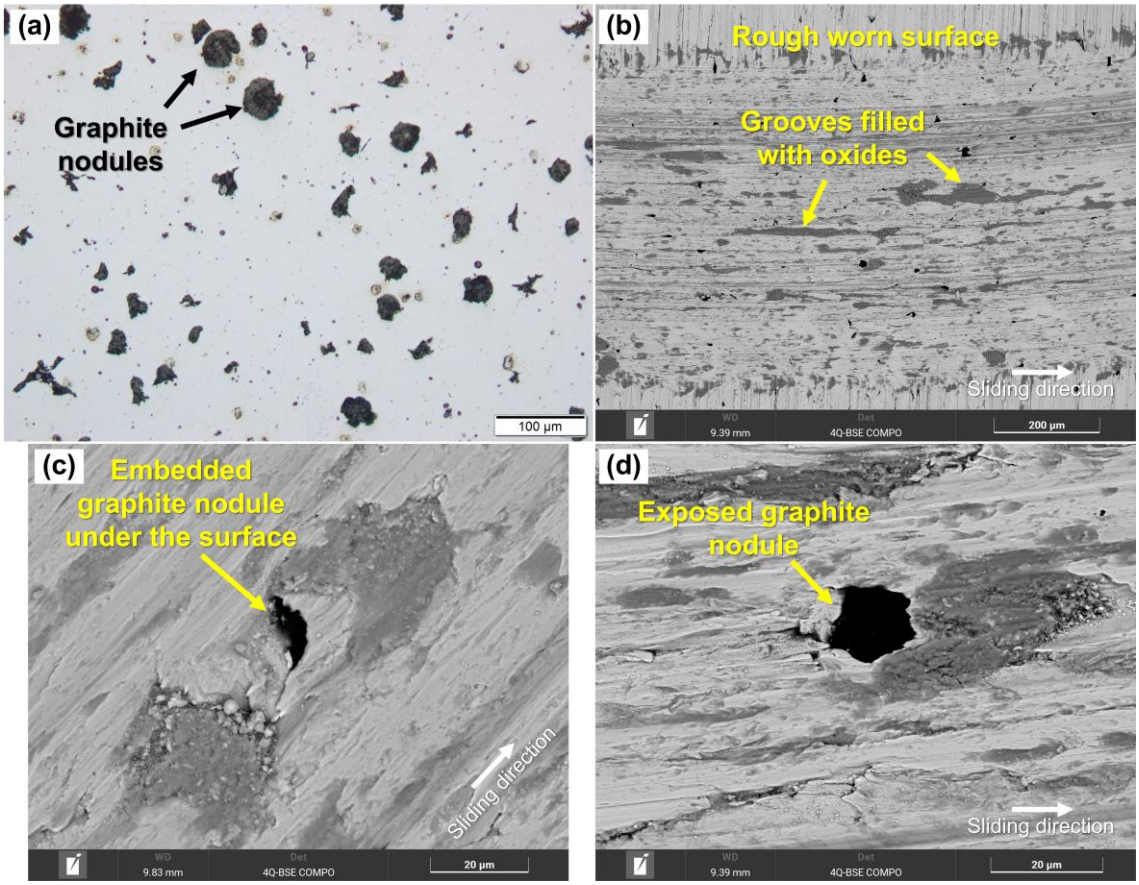


Fig. 6.6: (a) Microstructure of reference Cast Iron. (b) Post-mortem SEM observations of the rough worn surface, where graphite particles are (c) underneath the metal surface or (d) exposed.

A similar discussion can be done with the thermal treated sample at 800 °C for 90 minutes. Indeed, also in this case, a rough worn surface is visible (*Fig. 6.7*a,b), which reveals delaminated areas with partially exposed graphite particles (*Fig. 6.7*c,d). Such particles can be pulled out during the test. Despite the similar worn surfaces and wear phenomena, higher CoF is achieved during this test compared to that of the reference NCI (*Fig. 6.5*a). One reason is ascribed to the dimensions of the graphite particles, with the ones of the NCI being more than ten times bigger, thus covering a higher area fraction of the worn surface favouring the achievement of lower CoF (*Küçük, 2023*). The second reason can be associated with the dimensions of the ferritic grains of the matrix. Indeed, the low macro-hardness of the reference NCI (180 HV5) and the close-to-equilibrium conditions of the casting process suggest the presence of bigger grains compared to those obtained after thermal treatment at 800 °C of the LPBF alloy. Smaller grains can have a higher wear resistance compared to bigger grains, thus making it more difficult for the graphite spheroids to be pulled out and participate in the formation of the tribolayer (*Bregliozzi, 2003*; *Nafar Dehsorkhi, 2014*).

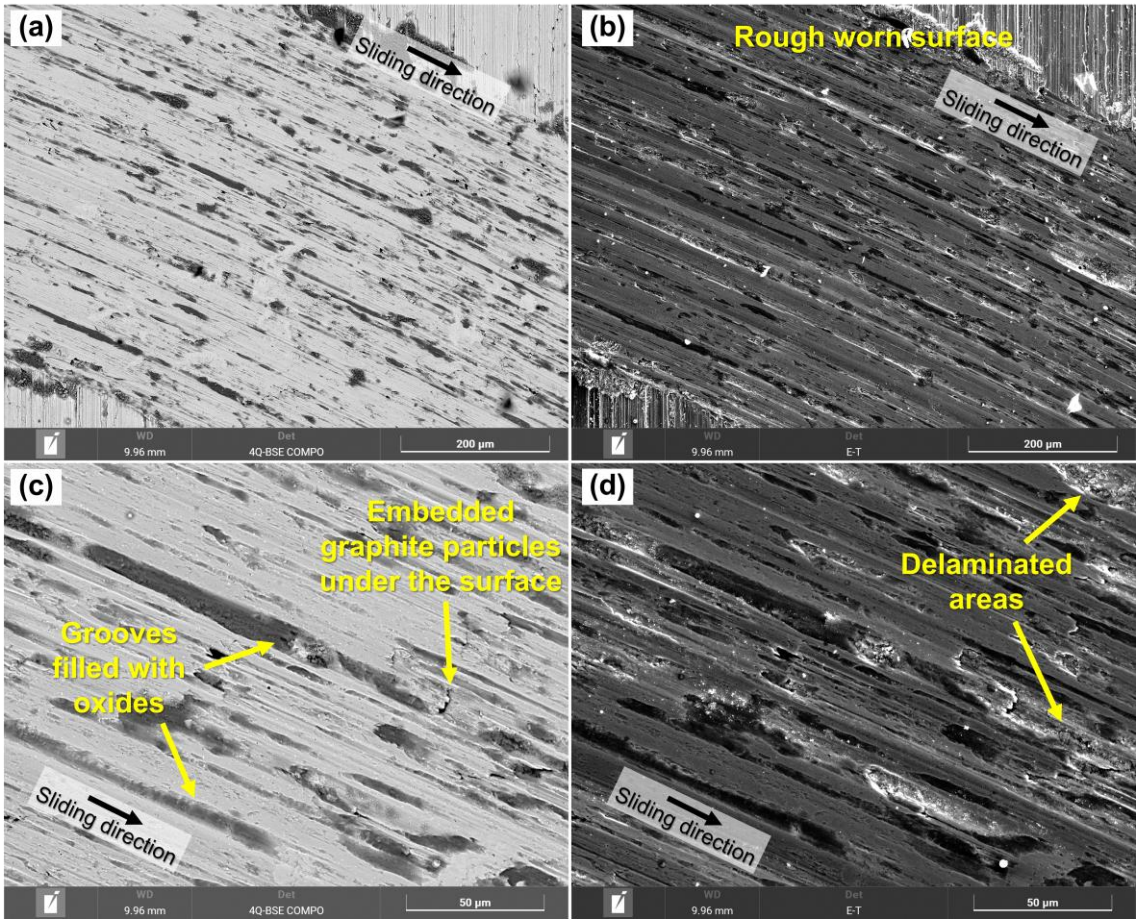


Fig. 6.7: Post-mortem SEM observations of the worn track of thermal treated S2 + 10% SiC at 800 °C for 90 minutes: overview of the rough worn surface with (a) BSE and (b) SE detector. Higher magnification under (c) BSE and (d) SE reveals delaminated areas, oxides and partially exposed graphite particles.

The highest CoF is achieved when testing the as-built S2 + 10% SiC sample, which does not have graphite particles and exhibits the highest hardness (*Fig. 6.5*a). In this case, a different wear mechanism occurs during the test, due to the presence of the hard solidification carbides (section 5.2.2.3.1). Further details will be given in the next section. The final worn surface is smooth, with sign of local spalling that leads to micro-voids subsequently filled with oxides (*Fig. 6.8*). Similar observations were done on the worn surface of samples after thermal treatment at 680 °C. In those cases, the decrease in hardness accompanied by the appearance of graphite leads to decrease the CoF when increasing the holding time, as visible in *Fig. 6.5*b. As explained in section 5.3, the decrease in hardness when increasing the holding time is due to the gradual disappearance of the hard iron carbides, the appearance of bigger graphite particles and more ferritic grains.

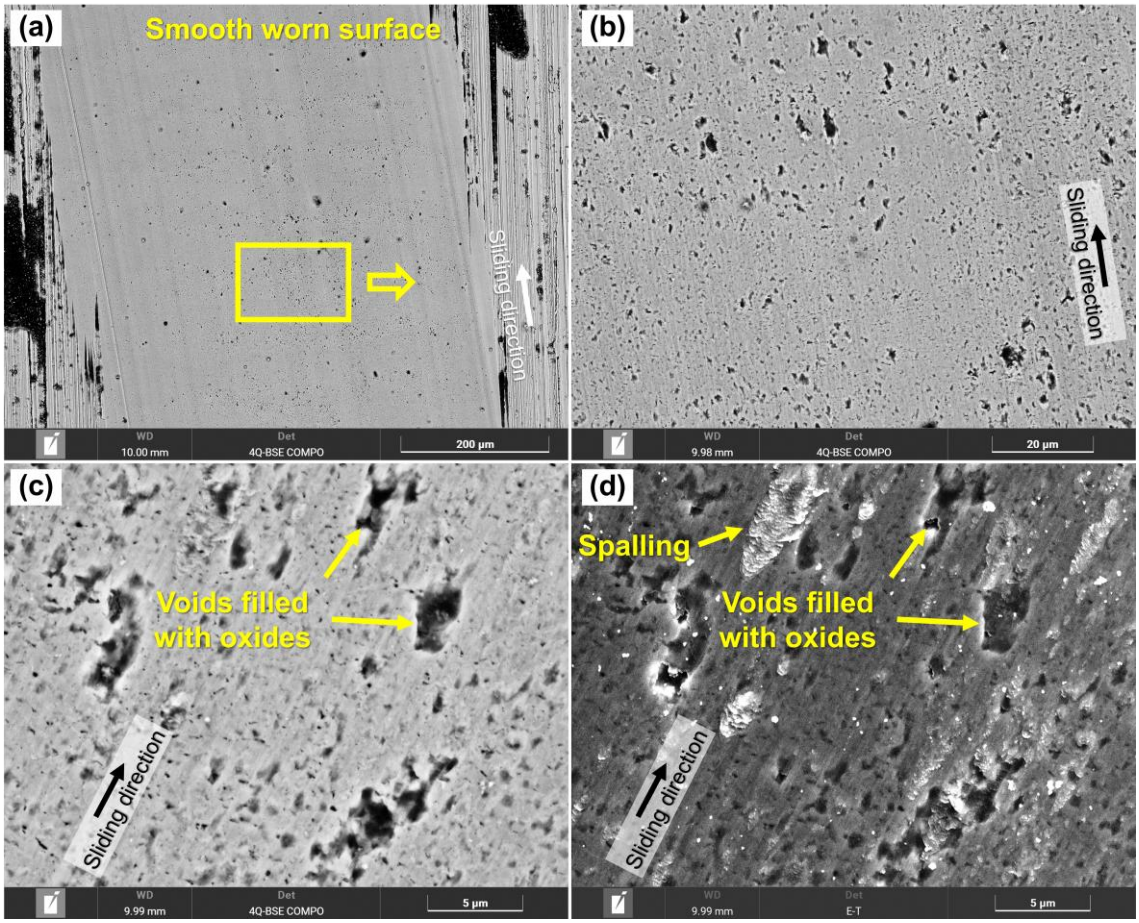


Fig. 6.8: Post-mortem SEM observations of the (a,b) smooth worn track of the as-built S2 + 10% SiC sample. Higher magnifications under (c) BSE and (d) SE imaging reveals sign of spalling on the metal surface and micro-voids filled with oxides.

Considering *Fig. 6.5*b. and the above explanations, the gradual change towards softer microstructures combined with the absence or decreased amount of solidification carbides, and with the increase in the amount of ferrite and graphite allow to decrease the CoF. Low CoF are usually desired during machining operations, and this is achieved by adding lubricants either externally or in-situ within the microstructure, as in the current case. The desired effect is to decrease the friction between the materials pair, thus avoiding energy dissipation and extending the tool life. Although the above results show that the presence of graphite allows the CoF to decrease, the latter remains high. However, a low CoF does not necessarily implies higher wear resistance, as the latter depends on other factors such as the type of matrix and the presence of carbides. Therefore, complementary to the evaluation of the CoF, it is important to estimate the overall wear resistance.

6.4.2 Effect of solidification carbides and graphite on wear resistance

Profilometer analysis on the track of as-built sample S2 + 10% SiC revealed the highest worn volume (orange bars in *Fig. 6.9*). The worn volume decreases almost linearly with the increase in holding time of the thermal treatment at 680 °C. In general, all thermal treated samples exhibit a lower worn volume than the one of the reference NCI, with the latter exhibiting a worn volume similar to that of the as-built sample. The worn volume depends on the dimensions of the width and depth of the track. The width is regular, varying between around 500 and 600 µm. In contrast, the depths change significantly, with that of thermal treated samples at 680 °C for 60 and 90 minutes being the lowest, even half that of NCI.

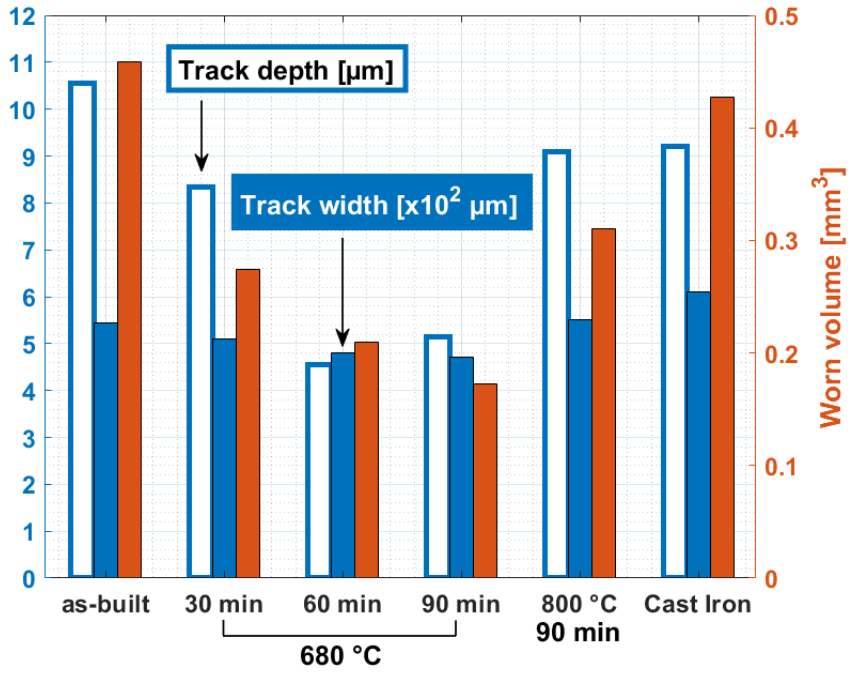


Fig. 6.9: Tracks dimensions and worn volumes obtained with profilometer after pin-on-disc tests on as-built and thermal treated S2 + 10% SiC and reference NCI samples.

All tests were performed under the same conditions. Therefore, the worn volume will be considered as the indicator of the wear resistance of the material. As mentioned in the previous section, low CoF does not necessarily imply higher wear resistance. Indeed, the reference NCI exhibited the lowest CoF, but it has a high worn volume, comparable to that of the graphite-free as-built S2 + 10% SiC. Thus, graphite is not the only phase that can guarantee a high wear resistance. Other phases participate in the achievement of low worn volumes, such as the type of matrix and the eventual presence of carbides. Indeed, the microstructure affects the wear

mechanism occurring during the test, with a consequent impact on the overall wear resistance. As mentioned in the previous section, delamination and abrasive wear are the main wear phenomena that occur with NCI. In contrast, a less severe wear occurs with the as-built S2 + 10% SiC sample, where only local spalling phenomena lead to micro-voids on an overall smooth worn surface. Similar observations were done on the worn tracks of the thermal treated samples at 680 °C with 30 and 60 minutes of isothermal holding. In these cases, compared to the as-built sample, the only difference is the presence of graphite particles which became exposed during the test (*Fig. 6.10*a,c). With the advancement of the test, graphite particles are deformed (*Fig. 6.10*b). In contrast, in NCI, they are pulled out due to delamination phenomena (*Fig. 6.6*).

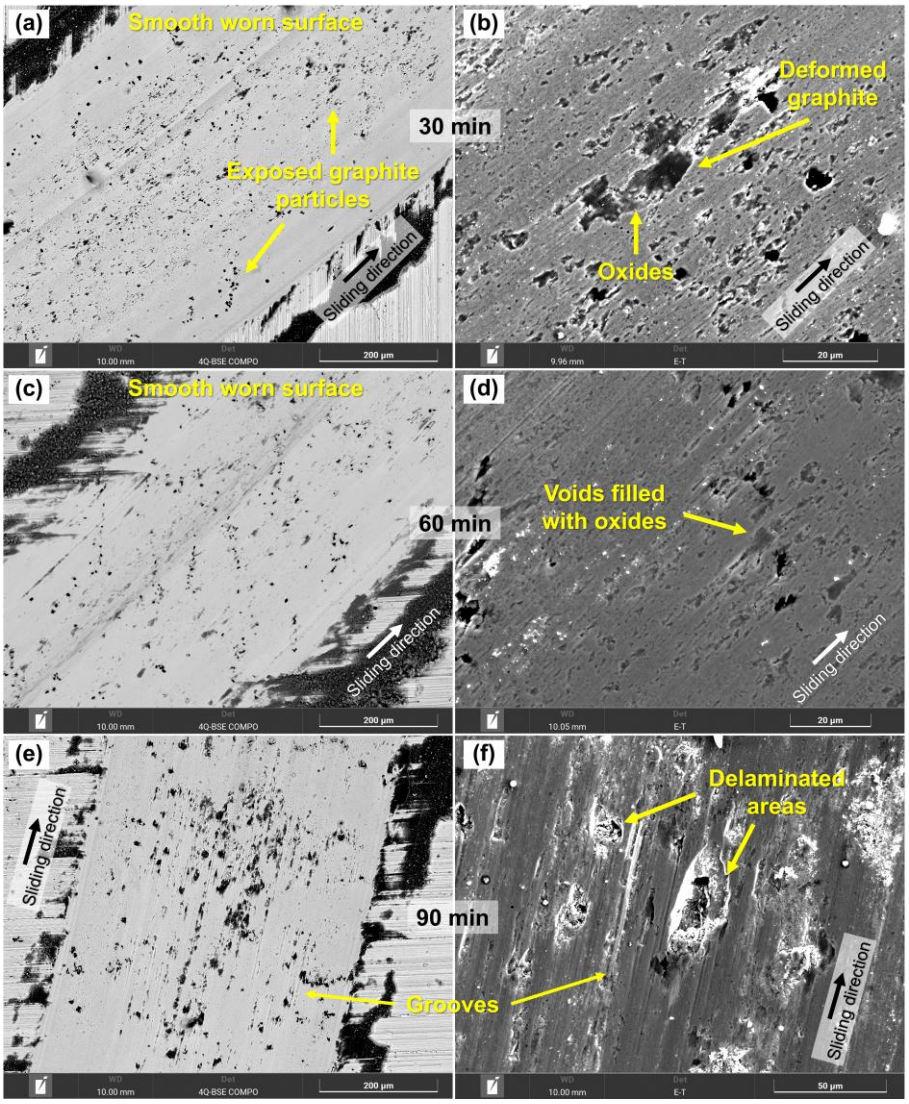


Fig. 6.10: Post-mortem SEM observations of worn tracks of sample S2 + 10% SiC thermal treated at 680 °C with different holding times. (a,c) Smooth worn surface with exposed graphite particles and (b,d) micro-voids appear on samples thermal treated up to 60 minutes. (e) Grooves and (f) delaminated areas appear with 90 minutes of thermal treatment.

The different phenomena occurring on samples thermal treated at 680 °C up to 60 minutes are due to the different microstructure compared to that of NCI. As mentioned in the previous section, the soft ferritic matrix of the NCI is subjected to plastic deformation during the wear test, which facilitates the pull out of graphite particles, but increases the worn volume. In contrast, with S2 + 10% SiC as-built and thermal treated, except for graphite particles, the microstructure consists of a bainitic/ferritic matrix with hard interdendritic carbides formed during solidification (section 5.2.2.3). These phases have a higher resistance to plastic deformation compared to the ferrite of NCI, thus disadvantaging the pull out of graphite particles. Furthermore, the hard interdendritic carbides are tightly embedded in the matrix phase. Therefore, they can contribute to improve the wear resistance, as they act as a network to strengthen the shear resistance of the alloy (*Scandian, 2009*). Usually, carbides are known to promote wear resistance but, if they are cracked and removed from the material during the wear test, they can act as hard debris promoting abrasive wear. In contrast, in these cases, no significant grooves are visible on the worn surfaces, thus confirming their good bonding with the matrix. Further investigations must be carried out, as analysis on the subsurface underneath the worn track can confirm these assumptions.

Although its microstructural characteristics and highest hardness are more prone to favour wear resistance, the as-built sample S2 + 10% SiC has a higher worn volume than that of the reference NCI. It has the highest depth of the track among all the samples (*Fig. 6.9*). By just graphitizing the microstructure with only 30 minutes of thermal treatment at 680 °C, the effect of graphite is significant, as almost half of the worn volume of the as-built sample is achieved (*Fig. 6.9*). The worn volume further decreases with 60 minutes of thermal treatments, reaching the minimum depth of the track among all the tests. The deformation of the graphite particles and the mixing with oxides within the micro-voids (*Fig. 6.10*b,d) allow the achievement of self-lubricating properties, which protect the material from wear. Since a homogeneous tribolayer is not present on the surface, these wear mechanisms only occur locally in the vicinity of graphite particles (*Fig. 6.10*b,d), but they contribute to promote the overall wear-resistant properties.

The lowest worn volume is achieved with the holding time of 90 minutes (*Fig. 6.9*). However, a slight increase in the depth of the worn track can be associated to more delaminated areas within the worn track (*Fig. 6.10*e,f). Although bigger graphite particles are formed (*Table 6.2*), the content of hard iron carbides decreases with this thermal treatment (section 5.3). Therefore, the improvement of wear resistance acted by the interdendritic carbides is diminished. Not

having at all the hard carbides, as in the microstructure of sample thermal treated at 800 °C, led to achieve higher worn volumes and depth of the track (*Fig. 6.9*).

Therefore, the right combination of hard carbides and graphite allows to achieve an alloy with enhanced wear-resistant properties. The novelty of this alloy is highlighted by the combination of self-lubricating properties of cast irons acted by graphite particles and the wear resistance of tool steels promoted by carbides. The application of this alloy as a self-lubricant tool allows to avoid the use of external lubricants during the service, as they can be harmful for both human and environment. Considering its microstructure and chemical composition, application conditions could only be at room temperature in a dry environment, as high temperatures can accelerate its wear rate, and corrosion can be promoted by contact with fluids. Further testing of its thermal behaviour and corrosion properties must be conducted.

6.5 Conclusions

Wear behaviour of as-built AISI S2:

- The assessment of wear properties was based on the approach previously developed at the MMS laboratory, which consider the tribosystem at all scales and involve the use of interrupted wear tests.
- The wear sequence at room temperature of AISI S2 consists of an initial run-in period, during which severe abrasive wear is the main mechanism. Subsequently, a change in a mild oxidative wear allow to achieve an overall smooth final worn surface.
- Preliminary investigations on the wear behaviour at high temperature (up to 400 °C) showed an increase in wear rate, thus suggesting the room temperature as possible service temperature of this alloy.

Wear behaviour of as-built and thermal treated S2 + 10% SiC processed with preheating:

- Sample hardness plays a direct role on the average CoF. Harder the material, higher the CoF, despite the presence of graphite particles.
- High hardness or low CoF do not imply higher wear resistance. The samples that exhibited the highest wear resistance (lower worn volume) were the samples thermal treated at 680 °C for 60-90 minutes.
- The high wear resistance is achieved thanks to the combination of hard solidification carbides and local self-lubricating properties acted by graphite particles.

6.6 References

Bregliozzi, G., Di Schino, A., Kenny, J. M., & Haefke, H. (2003). "The influence of atmospheric humidity and grain size on the friction and wear of AISI 304 austenitic stainless steel." Materials Letters, 57(29), 4505–4508. https://doi.org/10.1016/S0167-577X(03)00351-3

Campos, K. R., Kapsa, P., Binder, C., Klein, A. N., & de Mello, J. D. B. (2015). "Tribological evaluation of self-lubricating sintered steels." Wear, 332–333, 932–940. https://doi.org/10.1016/j.wear.2015.01.056

Du, Y., Wang, X., Zhang, D., Wang, X., Ju, C., & Jiang, B. (2021). "A superior strength and sliding-wear resistance combination of ductile iron with nanobainitic matrix." Journal of Materials Research and Technology, 11, 1175–1183. https://doi.org/10.1016/j.jmrt.2021.01.104

Gowd, G. H., Vali, S. S., Ajay, V., & Mahesh, G. G. (2014). "Experimental Investigations & Effects of Cutting Variables on MRR and Tool Wear for AISI S2 Tool Steel." Procedia Materials Science, 5, 1398–1407. https://doi.org/10.1016/j.mspro.2014.07.458

Küçük, Y., Altaş, E., & Topcu, M. E. (2023). "A comparative analysis of the effect of laser surface treatment on the dry sliding wear behavior of ductile cast irons with different microstructures." Optik, 274(January). https://doi.org/10.1016/j.ijleo.2023.170540

Liu, C., Du, Y., Wang, X., Hu, Z., Li, P., Wang, K., … Jiang, B. (2023). "Mechanical and tribological behavior of dual-phase ductile iron with different martensite amounts." Journal of Materials Research and Technology, 24, 2978–2987. https://doi.org/10.1016/j.jmrt.2023.03.210

Liu, C., Du, Y., Wang, X., Zheng, Q., Zhu, X., Zhang, D., … Jiang, B. (2023). "Comparison of the tribological behavior of quench-tempered ductile iron and austempered ductile iron with similar hardness." Wear, 520–521(February), 204668. https://doi.org/10.1016/j.wear.2023.204668

Maurizi Enrici, T., Mario, D., Dedry, O., Castagne, S., Mertens, A., & Tchuindjang, J. T. (2023). "Unveiling the complex wear sequence of a directed energy deposited 316L+WC hierarchical composite against alumina." Journal of Materials Research and Technology, 26(August), 621–638. https://doi.org/10.1016/j.jmrt.2023.07.172

Nafar Dehsorkhi, R., Sabooni, S., Karimzadeh, F., Rezaeian, A., & Enayati, M. H. (2014). "The effect of grain size and martensitic transformation on the wear behavior of AISI 304L stainless steel." Materials and Design, 64, 56–62. https://doi.org/10.1016/j.matdes.2014.07.022

Saggionetto, E., Maurizi Enrici, T., Dedry, O., Boschini, F., Tchuindjang, J. T., & Mertens, A. (2025). "On the role of the hierarchical structures in the friction- induced phenomena of directed energy deposited 316L+WC sliding against different counter-bodies.", Tribology International, Volume 212, 2025. https://doi.org/10.1016/j.triboint.2025.110973

Scandian, C., Boher, C., de Mello, J. D. B., & Rézaï-Aria, F. (2009). "Effect of molybdenum and chromium contents in sliding wear of high-chromium white cast iron: The relationship between microstructure and wear." Wear, 267(1–4), 401–408. https://doi.org/10.1016/j.wear.2008.12.095

Zhang, H., Wu, Y. xin, Li, Q. ju, & Hong, X. (2019). "Effect of matrix structure on mechanical properties and dry rolling–sliding wear performance of alloyed ductile iron." Journal of Iron and Steel Research International, 26(8), 888–897. https://doi.org/10.1007/s42243-019-00302-1

Chapter 7
General conclusions and perspectives

7.1 General conclusions

Additive Manufacturing technology is being adopted for mass production by several industries across the world. The need for alloys specifically designed for AM will keep increasing in the coming years, as international players in metal production understand the potential and capabilities of AM. This project wanted to centre on this goal by introducing a new iron-based alloy specifically designed for AM. The steps used in this work for alloy development can be easily extended to other classes of metals, such as aluminium-, nickel-, and titanium-based alloys, thus lying the basis for future development of further alloys.

The desired final microstructure was designed through basic metallurgical concepts: carbide-forming elements were avoided, whereas silicon and carbon were given high importance. Under these conditions, graphite is supposed to form. While alloys with this type of composition already exist and are produced through conventional metallurgical methods, nothing exists in the form of powder for AM. Therefore, the first challenge of this project was the selection of the feedstock powder material with strict requirements for LPBF. Excluding the possibility of having one single type of powder with the desired chemical composition, given the high cost and delivery time of gas-atomized powders, it was decided to have two different powders, namely the main steel alloy and the SiC additive. For the same reasons mentioned above, not many steel alloys with few carbide-forming elements and in powder form exist commercially. Only AISI S2 Tool Steel was found. SiC was selected because of the presence of graphite-promoting elements. These two powders have good chemical affinity, and the DTA approach proved useful for demonstrating it. Having two different powders instead of a single one also provided the possibility of varying the concentration of the additive to understand its effect on the final alloy in terms of microstructure and properties. Achieving a proper mixture suitable for LPBF was the next challenge, in view of the poor flowability of the selected SiC. However, after several trials, a good mixing procedure was established using commercial tools such as ball milling and test sieves. The results demonstrated that, despite the addition of the secondary powder, an appropriate powder preparation and mixing procedure starting from commercially available powders could provide a feedstock suitable for LPBF.

The processability by LPBF was approached through methods also used by industrial players. Starting from the deposition of single tracks and moving to cubes, using a so-called dynamic refinement of parameters allowed the establishment of the process map for the reference material AISI S2 initially, and later for the different mixtures with SiC addition. The use of preheating was extremely important for the processability of the alloy, as it allowed crack-free samples to be achieved. As a general statement, having the possibility of using a high preheating temperature (500°C or more) for the substrate is an effective tool for the development of new alloys. So far, this is still a limitation, as many commercial LPBF machines are not equipped with such an option, or its installation is still expensive. During the establishment of the process map, particular attention was given to the type of melt pool generated, as its morphology is directly responsible for process-induced defects. These results demonstrate that the proposed alloy composition, despite its intentionally modified chemistry and heterogeneous feedstock, can be successfully processed by LPBF.

The metallurgical characterization of the reference alloy AISI S2 was needed as a basis for understanding the microstructure of the new alloy with SiC addition, whose characterization proved challenging. The complex thermal history due to the rapid heating and cooling of the metal led to the solidification of complex supersaturated phases. This phenomenon is an intrinsic capability of LPBF, or more generally of fusion-based AM technologies. Although its occurrence can sometimes lead to unprocessable alloys, it must be seen as an advantage and used as a concrete tool for the development of new alloys. Therefore, somehow, the development of new alloys for AM must consider this metallurgical phenomenon and combine material design with solidification models that promote it while maintaining material processability. Indeed, supersaturation can promote the formation of exotic phases, such as those found in the alloy of the present work. Through post-thermal treatments, such phases can be transformed into other desired ‘conventional’ phases. In this case, the post-thermal treatment was needed for the precipitation of graphite. Although it is secondary graphite, the presence of this ‘equilibrium’ phase within an ‘out-of-equilibrium’ AM microstructure is something of an exceptional nature and somehow fascinating. So far, this type of microstructure obtained by LPBF has not been reported elsewhere. Therefore, these results demonstrate the feasibility of achieving an innovative microstructure with LPBF process.

The presence of graphite and the high hardness of the new alloy allowed better wear resistance compared to the reference AISI S2 and Cast Iron. A low CoF, such as that of Cast Iron, was not achieved, probably because of the larger graphite nodules in Cast Iron. In general, the

developed alloy has good wear properties, but further characterization and comparison with other existing materials are needed to better classify its capabilities.

In conclusion, the results presented in this manuscript demonstrate that LPBF can be used not only as a manufacturing technology for producing complex geometries, but also as a powerful metallurgical processing route for the development of novel materials. By deliberately combining tailored powder chemistry with the unique solidification conditions of the process, new microstructures and associated combinations of properties can be achieved. The work therefore contributes to the broader objective of moving from materials BY Additive Manufacturing to materials FOR Additive Manufacturing.

7.2 Perspectives

General perspectives valid for AISI S2, as-built and graphitized S2 + 10% SiC alloys:

- Investigate the thermal stability to understand the range of temperatures for applications of interest. From the results, optimize the microstructure to enhance the thermal behaviour. The optimization of the microstructure can be done by designing a post-process thermal treatment.
- Macro-, nano-hardness and wear properties need to be complete with further testing of the mechanical properties (e.g. tensile, compression and fatigue behaviour). All the mechanical properties need to be investigated at room and high temperature, complementary to thermal stability investigation.
- With the purpose of using the new alloy as tool steels for wear applications, the investigations of the corrosion properties can provide important insights to understand the behaviour of the materials under corrosive environments. Indeed, if used as cutting tool or punch tool, the material would enter in contact with external fluids (e.g. cooling liquids), thus being in a potential corrosive environment.
- Solidification phenomena and microstructures can be better understood by developing models and simulations. Such investigation can be carried out together with the use of Thermo-Calc and data collected from in-situ monitoring of the LPBF process with radiative (e.g. cameras, X-ray imaging, pyrometer etc.) and non-radiative (e.g. acoustic, thermocouples, etc.) sensors. In addition, post-processing of EBSD data (ARPGE software), TEM and XRD analysis on printed samples can help for such purposes.

Change of SiC raw material:

The SiC powders used in this work consist of granules (of about 50 μm) composed of agglomerated primary particles (of about 1 μm). The granules worsened the rheological properties, negatively affecting the handling and preparation of the mixture. During the initial search and purchase of the powder, the idea was to have only free particles of about 1 μm, but this proved much more expensive. This option can still be explored, as it would be beneficial:

- To improve rheological properties of the final mixture, as SiC would be mainly decorating the S2 surface instead of being present as big granules.
- To make the mixture S2+15%SiC better processable. Although deeper metallurgical investigations of these samples are needed, it is believed that the big porosities found after

printing the mixture S2+15%SiC can somehow be related to the SiC granules. Indeed, their presence can lead to a local change of the chemical composition of the melt pool due to higher content of dissolved Si and C, thus affecting the solidification phenomenon. As a consequence, high level of porosity can be formed, as observed. Therefore, having free micron-size SiC particles instead of granules can be beneficial as the dissolution would be more homogeneous.

In-situ graphitization during LPBF process:

As mentioned above, it may be possible to optimize the mixture S2 + 15%SiC in order to obtain defect-free samples. This achievement would be of great importance as this mixture prove to lead to in-situ graphitization during the LPBF process. Having graphite formed directly during the process allows to avoid post thermal treatment, thus limiting the time and cost needed for further operation after the LPBF process.

Despite the fact that obtaining graphitization with a post thermal treatment can already be considered a great achievement, the in-situ graphitization would be seen as a higher step, as it has not been mentioned elsewhere.

Develop this alloy for Direct Energy Deposition (DED):

DED process might be of interest for the development of the same powder mixture (with tailored PSD). Indeed, it is believed that in-situ graphitization would be more easily achieved in DED compared to LPBF. If graphitization occurred under the more 'extreme' out-of equilibrium conditions of LPBF, the lower cooling rates of DED can even better promote it. Indeed, bigger melt pools and lower thermal gradients would promote higher elemental segregation, which in combination with an environment rich in Silicon and free of carbide forming elements would push the carbon to form graphite.

A particular branch of DED is Laser Cladding (LC). In view of the wear resistant properties and the presence of graphite within the microstructure, this alloy can be also intended as a coating to protect an underneath material from wear. Therefore, its study as a LC coating can be pursued.

Atomize and print one single powder:

It is believed that the graphitization-ability of this alloy is given by the final chemical composition of the mixture. While developing a powder mixture can give advantages in terms

of cost of raw materials, its preparation takes long time, and it can bring challenges during handling and subsequent processing with LPBF. Thus, having one single powder can be advantageous for the LPBF process. Obtaining one single powder can be done through atomization. This step can be pursued by atomizing the alloy with targeted chemical composition based on the results obtained with the powder mixtures.

Appendix

Contents

A. Effect of laser defocus on processability of S2 + 15% SiC 194
B. Full DTA Heating stage of S2 + 10% SiC w/ and w/o preheating 197
C. Thermal treatments of S2 + 10% SiC w/o preheating 198
D. In-situ graphitization of S2 + 15% SiC 200
E. Worn volumes and track dimensions after high temperature pin-on-disc tests of LPBF as-built AISI S2 202

A. Effect of laser defocus on processability of S2 + 15% SiC

After having showed the difficult processability of S2 + 15% SiC (section 4.3.3), the subsequent attempts to optimize the process was changing the laser beam diameter. The diameter of the laser beam is obtained by shifting the focal plane, thus using a defocused laser. A positive or negative defocus is obtained when the focal plane is above or below the substrate respectively. Usually, the laser beam diameter was set at 80 µm, corresponding to a positive defocus of 1.6 mm. Based on the Aconity3D system, the approximation of the beam radius w(z) depends on the defocus value z. The following parameters values are based on a mathematical fitting approach for a laser power of 200 W:

$$w(z) = w_0 * (1 + \left({}^{z}/_{z_r}\right)^2)^{0.5} \quad \text{(A.1)}$$

where w_0 is the Waist radius (10.0 µm) and z_r is the Rayleigh length (0.417 mm).

From equation A.1, the laser beam diameter D is calculated as follows:

$$D = 2 * w(z) \quad \text{(A.2)}$$

With the purpose of exploring the effect of the laser beam diameter on the type of melt pool generated, it is necessary to include the value of the laser beam diameter on $E_{d,v}$. Therefore, the following equation was used to compute the new $E_{d,v}$ DEF:

$$E_{d,v}\ DEF = \frac{4*P}{\pi*D*v_s} \quad \text{(A.3)}$$

Table A.1 shows the processing parameters used for S2 + 15% SiC with the approach of the laser defocus.

Fig. A.1 shows the cross-section overviews of each sample. In all of them, key-hole porosities are present.

Sample	P [W]	v_s [mm/s]	D [mm]	z [mm]	$E_{d,v}$ [J/mm^3]	$E_{d,v}$ DEF [J/mm^3]
1	200	200	0.10	2.043	417	127
2	200	200	0.12	2.467	417	88
3	200	200	0.14	2.889	417	65
4	200	200	0.16	3.309	417	50
5	200	300	0.10	2.043	278	85
6	200	300	0.12	2.467	278	59
7	200	300	0.14	2.889	278	43
8	200	400	0.06	1.179	208	177
9	200	400	0.10	2.043	208	64
10	200	400	0.12	2.467	208	44
11	200	400	0.14	2.889	208	33
12	200	500	0.04	0.722	167	318
13	200	500	0.06	1.179	167	142
14	200	500	0.10	2.043	167	51
15	200	500	0.12	2.467	167	35
16	200	500	0.14	2.889	167	26
17	200	600	0.04	0.722	139	265
18	200	600	0.06	1.179	139	118
19	200	600	0.10	2.043	139	42
20	200	600	0.12	2.467	139	29

Table A.1: Processing parameters of S2 + 15% SiC with laser defocus.

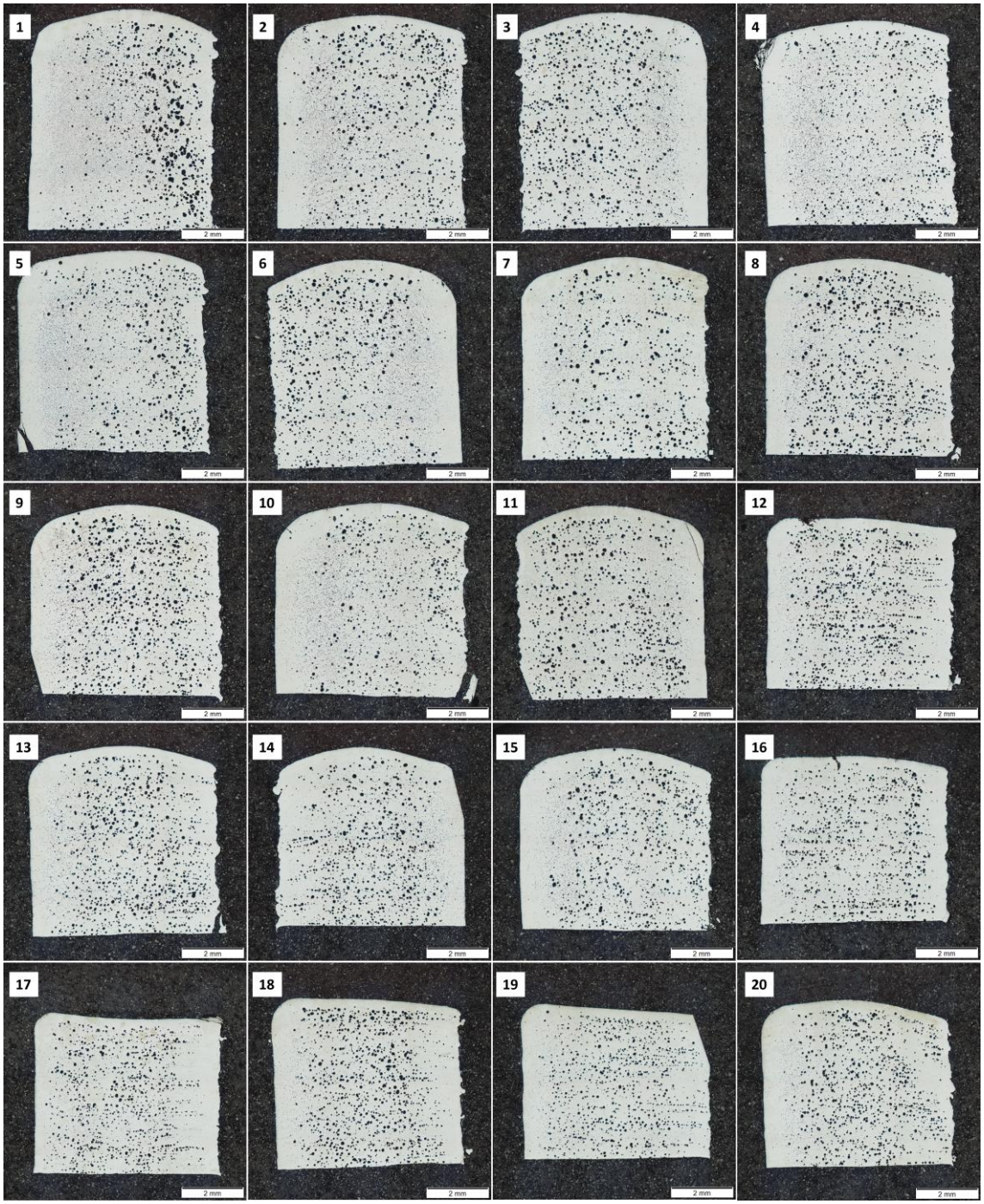


Fig. A.1: S2 + 15% SiC with preheating and different laser defocuses: Cross section overviews, where key-hole defects are present within all samples.

B. Full DTA Heating stage of S2 + 10% SiC w/ and w/o preheating

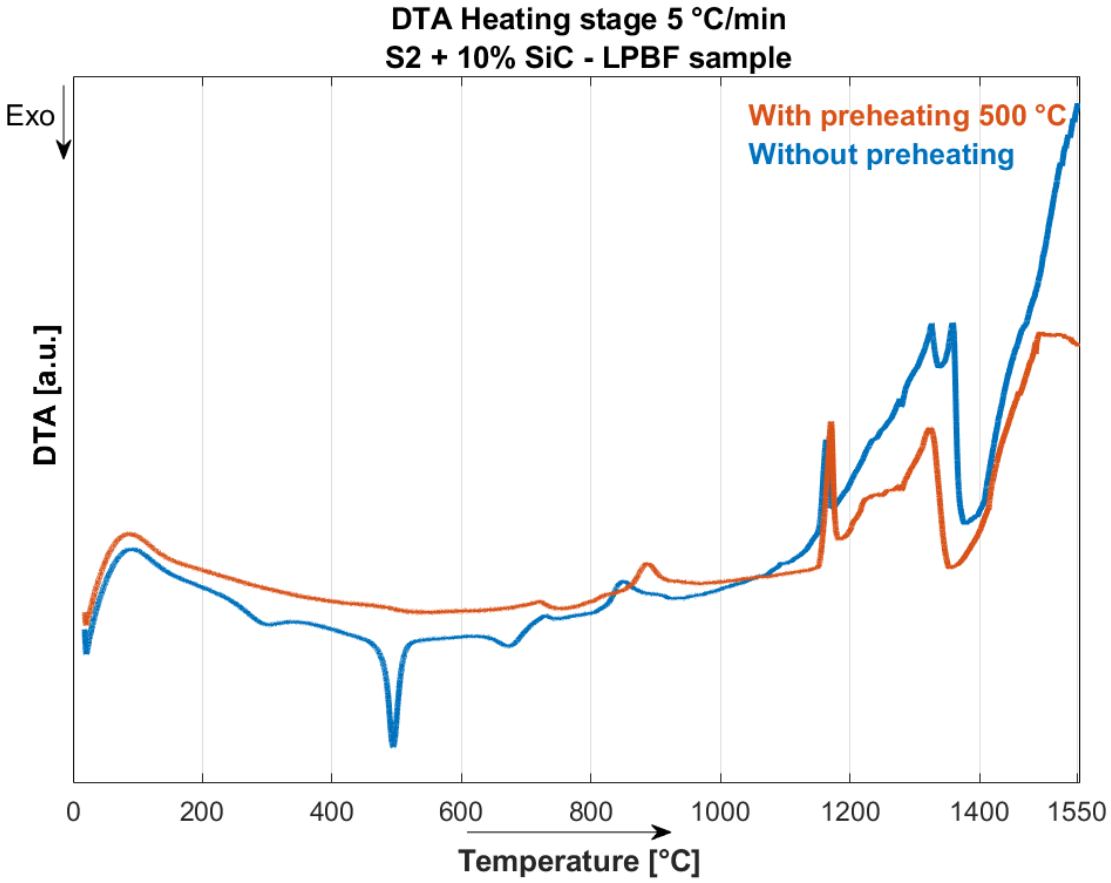


Fig. B.1: S2 + 10% SiC with and without preheating: DTA heating stage of as-built samples.

C. Thermal treatments of S2 + 10% SiC w/o preheating

Specific thermal treatments were performed on as-built sample S2 + 10% SiC processed without preheating. This investigation was needed for the understanding of the graphitization mechanism. It provided important information regarding the nature of the phases in the as-built condition, useful for the discussion in section 5.2.2.3.1. The thermal treatments were carried out with a DTA device, under argon protection. Four temperatures were selected according to the DTA heating stage (Appendix B, *Fig. B.1*). After heating up to the selected temperature at 5 °C/min, an isothermal holding was performed for 60 minutes, followed by the cooling until room temperature at 20 °C/min.

After thermal treatment at 250 °C and 390 °C, martensite is still present (*Fig. C.1*-a,b,c,d). In contrast, thermal treating at 550 °C leads to decompose the martensite (*Fig. C.1*-e,f). Thermal treatment at 680 °C allowed to form graphite particles (black spots in *Fig. C.1*-g,h).

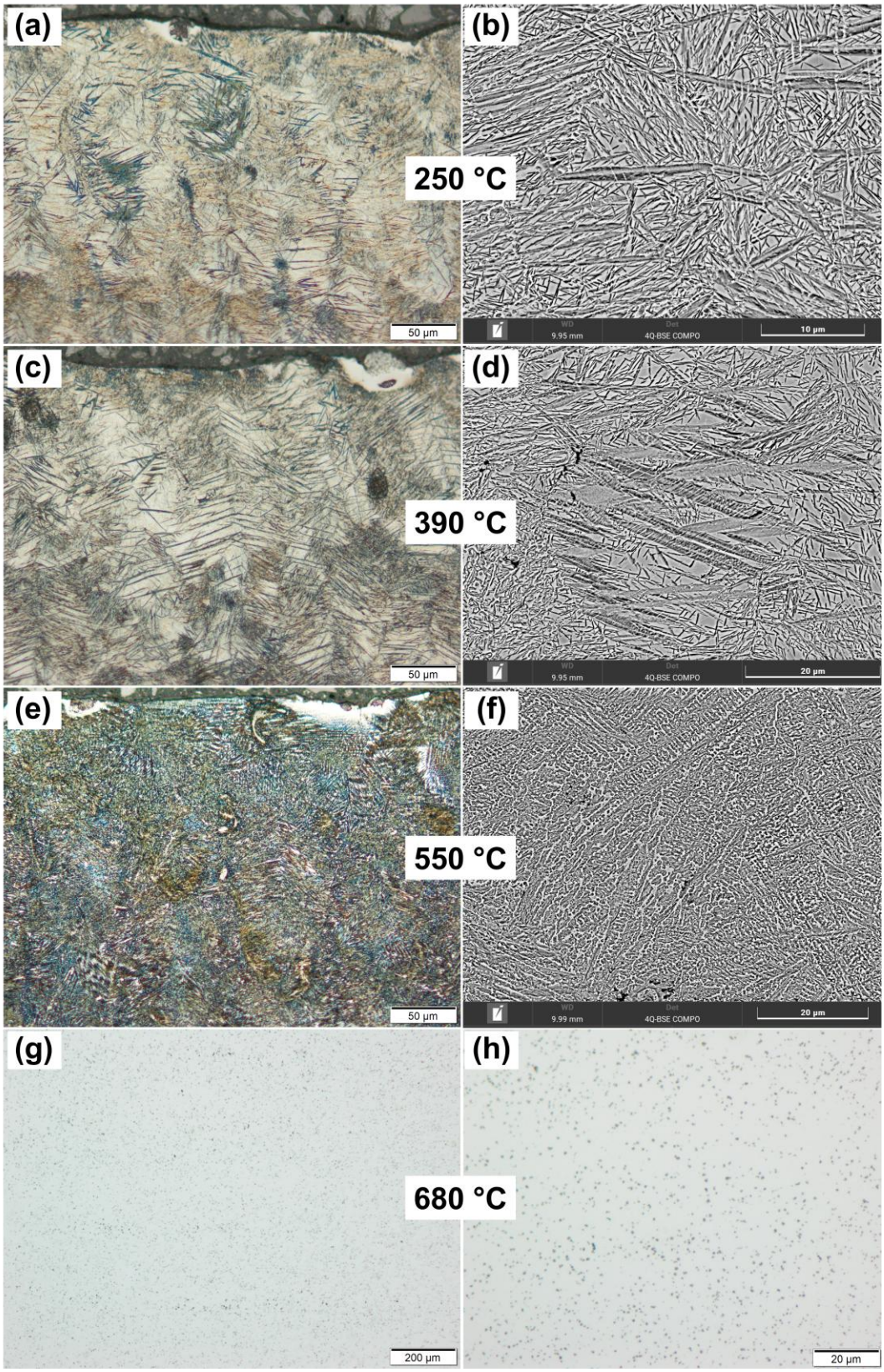


Fig. C.1: S2 + 10% SiC without preheating: OM and SEM micrographs of isothermally treated samples at (a, b) 250 °C, (c, d) 390 °C, (e, f) 550 °C and (g, h) 680 °C for 60 minutes. (g, h) are in as-polished to highlight graphite particles, whereas the others are obtained after etching with Nital 2%.

D. In-situ graphitization of S2 + 15% SiC

In-situ graphitization was obtained during the LPBF process within the microstructure of samples obtained from S2 + 15% SiC powders. SEM observations of the as-built microstructure reveal the presence of a high number of key-hole porosities (*Fig. D.1*-a), as explained in section 4.3.3. The microstructure is fully dendritic, with secondary arms more developed than in S2 + 10% SiC (*Fig. D.1*-b). Indeed, the increase in the amount of SiC further shifted the solidification towards lower G/R (section 5.2.1). Lower G/R values are also assumed in view of visual observations during printing. Indeed, the typical red coloration of metal at high temperature was always visible following the scan direction of the laser. This colouration smoothly disappears in few seconds due to cooling, but its appearing time is enough to detect it in each sample. This phenomenon is visible in *Fig. D.1*-c, where red-hot metal is still present in the last scanned area of sample 15.5 when, in the meantime, the laser has already moved on to the next sample (15.6). Usually, such phenomenon was not visible at naked eyes during the printing of the other powder mixtures (S2, S2 + 5, 10% SiC).

The microstructure consists of lamellar structures within the interdendritic regions and a dendritic matrix (*Fig. D.1*-d). Agglomerations of graphite particles are randomly located within the microstructure, and they are surrounded by distinct sub-grains (*Fig. D.1*-e). Such particles exhibit a better spherical morphology compared to those obtained with the post-thermal treatment (section 5.3), with dimensions ranging between 1.5 – 5.5 µm. EBSD analysis revealed the BCC crystal lattice of the ferritic grains around graphite particles (*Fig. D.1*-g). Meanwhile, the interdendritic segregations are identified as iron carbides (*Fig. D.1*-f), with higher indexation in areas that correspond to the lamellar structures in (*Fig. D.1*-d). For the EBSD analysis, different Fe – C phases were used, being iron carbides with different stoichiometry. None of them can be clearly indexed among the interdendritic segregations, whereas all together give the result shown in (*Fig. D.1*-f).

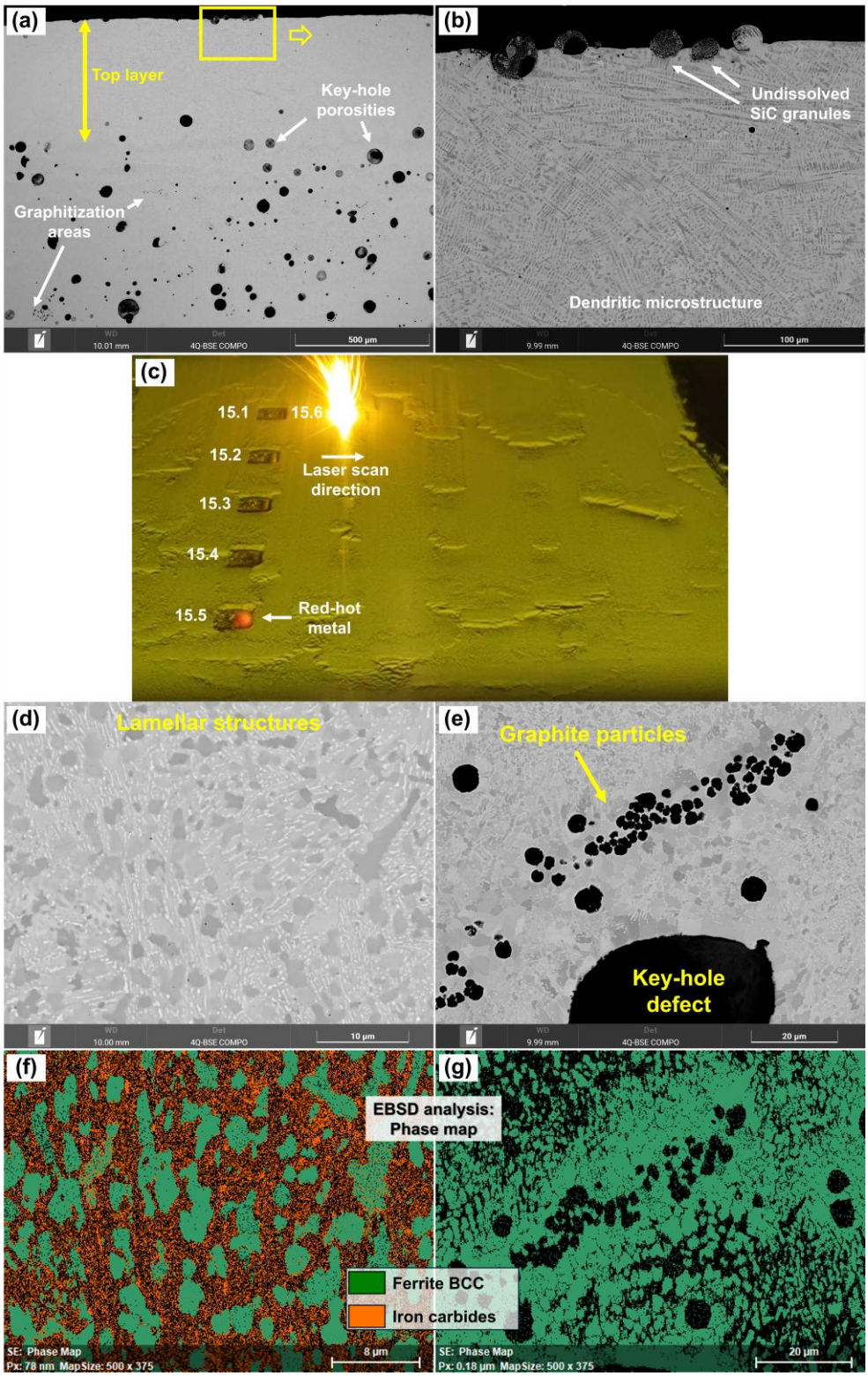


Fig. D.1: S2 + 15% SiC with preheating 500 °C: (a) cross section overview, (b) magnification within top layer, (c) LPBF chamber overview during printing. Microstructural features: (d) lamellar structures (f, g) partially identified as iron carbides within the interdendritic segregations and BCC matrix. (e) Agglomeration of graphite particles randomly located within the microstructure, close to a key-hole defect. (f, g) EBSD analyses were carried out in the same areas of (d, e).

E. Worn volumes and track dimensions after high temperature pin-on-disc tests of LPBF as-built AISI S2

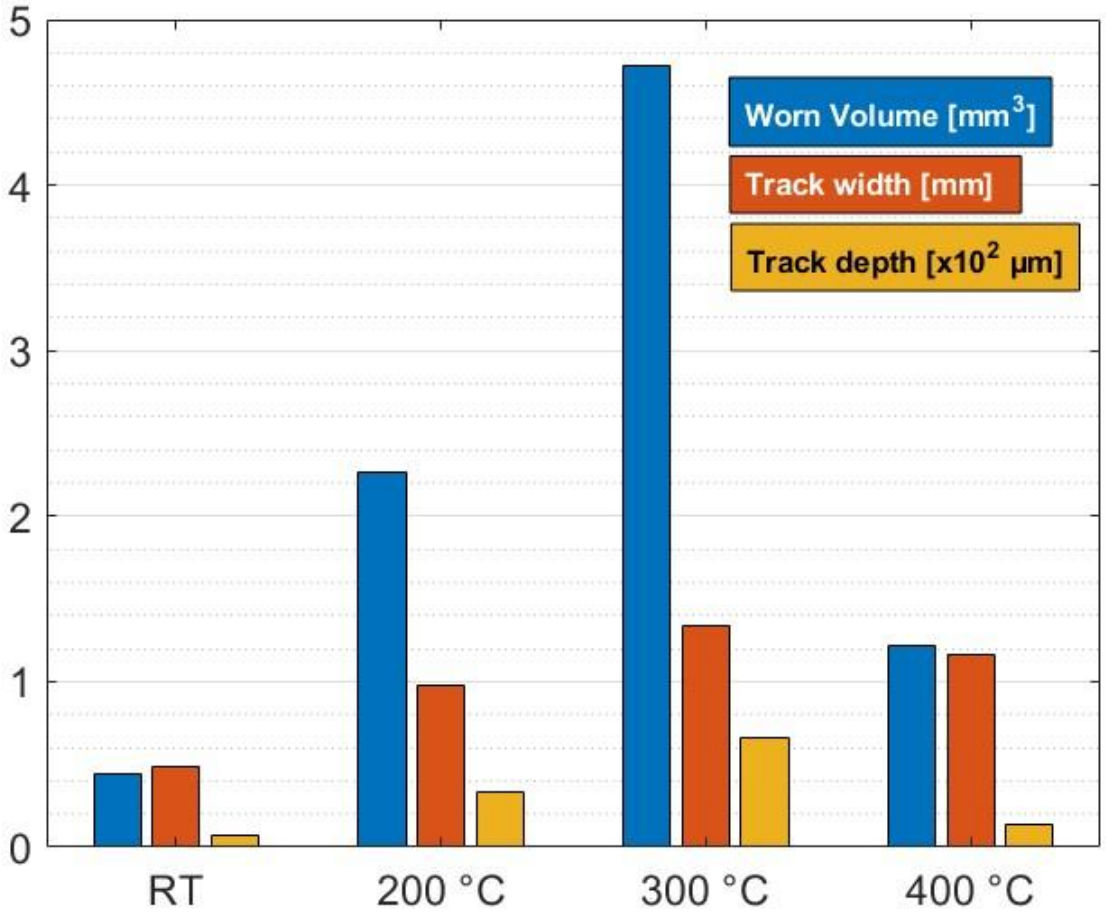


Fig. E.1: Worn volumes and worn tracks dimensions measured by profilometer after pin-on-disc tests at Room Temperature (RT) and High Temperatures (200, 300, 400 °C).

List of publications

Publications in peer-reviewed journals

Saggionetto, E., Bio Seidou, A., H., Caubergh, S., Boschini, F., Dedry, O., Tchuindjang, J. T., & Mertens, A. (n.d.) "*Preparation of powder feedstock and processability of a low alloy tool steel modified by SiC for Laser Powder Bed Fusion*" (in preparation)

Maurizi Enrici, T., **Saggionetto, E.**, Dedry, O., Ertugrul, O., Boschini, F., Tchuindjang, J. T. & Mertens, A. (n.d.). "*On the microstructures and strengthening mechanisms of new high-silicon austenitic stainless steels obtained by Laser Cladding*" (in preparation)

Segatto, A., **Saggionetto, E.**, Dedry, O., Tchuindjang, J. T., & Mertens, A (2026). "*A Comparative Analysis of LPBF Process Maps for S2 and S6 Grades Tool Steel*", Key Engineering Materials, 1047, p. 21-29, https://doi.org/10.4028/p-94l5jS

Tuninetti, V., Castro, J., Valle, R., Bustos, F., **Saggionetto, E.**, Garrido, C., Oñate, A., Salas, A., Lanziotti, C., Pincheira, G., & Mertens, A., (2026) "*Ultrahigh Damping Efficiency in Laser Powder Bed Fusion Kelvin Metamaterials for Hysteretic Applications*", Adv. Eng. Mater., 2026, 28, e202502470. https://doi.org/10.1002/adem.202502470

Castro, J., Valle, R., Leiva, J., Oñate, A., **Saggionetto, E.**, Mertens, A., & Tuninetti, V., (2025). "*Density-Based Topology-Optimized 3D-Printed Fixtures for Cyclic Mechanical Testing of Lattice Structures*". Polymers 2025, 17, 2468. https://doi.org/10.3390/polym17182468

Saggionetto, E., Maurizi Enrici, T., Dedry, O., Boschini, F., Tchuindjang, J. T., & Mertens, A. (2025). "*On the role of the hierarchical structures in the friction- induced phenomena of directed energy deposited 316L+WC sliding against different counter-bodies*", Tribology International, Volume 212, 2025. https://doi.org/10.1016/j.triboint.2025.110973

Franceschi, M., **Saggionetto E.**, Yazdanpanah, A., Pezzato, L., Mertens, A. & Dabalà, M. (2025). "*On the L-PBF Fabrication of a Novel Medium Carbon, High Silicon Nanostructured Bainitic Steel with and Without Substrate Pre-heating: Density and Microstructural Investigation*", JOM : the journal of the Minerals, Metals and Materials Society, Volume 77, pages 9330–9350 (2025), https://doi.org/10.1007/s11837-025-07633-3

Saggionetto, E., Roger Vila, G., Dedry, O., Tchuindjang, J. T., & Mertens, A. (2024). "*Effect of SiC addition on processability of AISI S2 tool steel for laser powder bed fusion*", Materials Research Proceedings, Vol 41, p. 216-223, https://doi.org/10.21741/9781644903131-24

Ríos I., Martínez A., **Saggionetto, E.**, Mertens, A., Duchêne L., Habraken A. M., & Tuninetti V. (2024). "*Numerical modeling of the compressive behavior of 316L body-centered cubic lattice structures*" Materials Research Proceedings 41 (2024) 224-233 https://doi.org/10.21741/9781644903131-25

Saggionetto, E., Filippi, E., Dedry O., Tchuindjang, J. T., & Mertens, A. (2023). "*Development and processability of AISI S2 tool steel by Laser Powder Bed Fusion*", Material Forming – ESAFORM 2023, Vol. 28, pp 41-48, 2023, https://doi.org/10.21741/9781644902479-5

Ertugrul, O., Maurizi Enrici, T., Paydas, H., **Saggionetto, E.**, Boschini, F., & Mertens, A. (2020). *"Laser cladding of TiC reinforced 316L stainless steel composites: Feedstock powder preparation and microstructural evaluation*" Powder Technology, 375, 384–396. https://doi.org/10.1016/j.powtec.2020.07.100

Oral and poster presentations at international conferences

Bio Seidou, A. H., Maurizi Enrici, T., **Saggionetto, E.**, Dedry, O., Tchuindjang, J. T., & Mertens, A. "*Microstructure and corrosion behaviour of a modified Si-rich austenitic stainless steel obtained by directed energy deposition*", MPA Seminar 2024 : Materials - Properties – Applications, Stuttgart, October 8th, 2024, oral presentation (presented by Mertens A.)

Saggionetto, E., Segatto, A., Dedry, O., Tchuindjang, J. T., & Mertens, A (2024). "*Wear behavior of AISI S2 tool steel processed by Laser Powder Bed Fusion*", 19th European Mechanics of Materials Conference (EMMC19), Madrid, May 29th-31st, 2024, oral presentation

Saggionetto, E., Bio Seidou, A. H., Roger Vila, G., Dedry, O., Tchuindjang, J. T., & Mertens, A "*Development of SiC-enriched tool steel by Laser Powder Bed Fusion*", High Strength Steel - International Workshop, Bergamo, October 26th-27th, 2023, oral presentation

Franceschi, M., **Saggionetto E.**, Yazdanpanah, A., Pezzato, L., Mertens, A. & Dabalà, M., "*L-PBF fabrication of a novel high silicon carbide-free bainitic high strength steel*", High Strength Steel - International Workshop, Bergamo, October 26th-27th, 2023, oral presentation (presented by Franceschi M.)

Saggionetto, E., Bio Seidou, A. H., Filippi, E., Roger Vila, G., A., Dedry, O., Tchuindjang, J. T., & Mertens, A "*On the Laser Powder Bed Fusion of a Modified AISI S2 Tool Steel Enriched with SiC*", Thermec 2023 - International Conference on Processing & Manufacturing of Advanced Materials, Vienna, July 2nd-7th, 2023, oral presentation (presented by Mertens A.)

Saggionetto, E., Bio Seidou, A. H., Roger Vila, G., Boschini, F., O., Tchuindjang, J. T., & Mertens, A "*Preparation of powders mixture of AISI S2 Tool Steel and Silicon Carbide for use in Laser Powder Bed Fusion*", Thermec 2023 - International Conference on Processing & Manufacturing of Advanced Materials, Vienna, July 2nd-7th, 2023, poster presentation

Saggionetto, E., Filippi, E., Dedry O., Tchuindjang, J. T., & Mertens, A. "*Development and processability of AISI S2 tool steel by Laser Powder Bed Fusion*", Material Forming – ESAFORM 2023, Krakow, April 19th-21st, 2023, oral presentation

Saggionetto, E., Bio Seidou, A. H., Roger Vila, G., Boschini, F., O., Tchuindjang, J. T., & Mertens, A "*Optimization of powder feedstock for use in Laser Powder Bed Fusion*", EDT-MAIN PhD Scientific Day / NanoWal annual meeting, Namur, January 31st, 2023, poster presentation

Bio Seidou, A. H., **Saggionetto, E.**, Dedry, O., Tchuindjang, J. T., & Mertens, A "*Preliminary investigation on the solidification AISI S2 Tool Steel modified by Silicon Carbide additions*", EDT-MAIN PhD Scientific Day / NanoWal annual meeting, Namur, January 31st, 2023, poster presentation (presented by Bio Seidou, A. H.)

Maurizi Enrici, T., **Saggionetto, E.**, Dedry, O., Boschini, F., Tchuindjang, J. T. & Mertens, A., "*High-silicon austenitic stainless steels obtained by laser cladding: elaboration, microstructure and local properties*", Alloys for Additive Manufacturing Symposium 2022, Munich, September 11th-14th, 2022, oral presentation (presented by Mertens A.)

Saggionetto, E., Maurizi Enrici, T., Dedry, O., Tchuindjang, J. T., & Mertens, A., "*On the influence of the Counter-body Material on the Wear Rate of 316L+WC Composite Coatings processed by Laser Cladding*", EDT-MAIN PhD Scientific Day / NanoWal Annual Meeting, Bruxelles, October 29th, 2021, oral presentation

Saggionetto, E., Maurizi Enrici, T., Dedry, O., Mario, D., Serrano Martin, I., Tchuindjang, J. T., & Mertens, A., "*The role of the Counterbody Material on Tribological Properties of 316L+WC Composite Coatings processed by Laser Cladding*", 23rd International Conference on Wear of Materials (WOM 2021), Online, April 26th-29th, 2021, poster presentation

Patent

Saggionetto, E., Tchuindjang, J. T., & Mertens, A. (2025). "*Graphite-based Steel Alloy and Method for Producing it using Laser Powder Bed Fusion*", Europe: application ref. n° EP24167458 (28/03/24); International: application ref. n° PCT/EP2025/058128 (25/03/25), published under WO/2025/202196).

Curriculum vitae



Enrico Saggionetto

Materials Engineer
PhD in Additive Manufacturing Metallurgical Engineering

Differdange, Luxembourg | enrico.saggionetto@gmail.com
+393475560552 | https://www.linkedin.com/in/enrico-saggionetto-7b3b39184/

PROFESSIONAL SUMMARY

Detail- and process-oriented mind. Passionate about materials science and manufacturing processes.

EXPERIENCE

- *Metal Powder Atomization Engineer*
  AM 4 AM, Luxembourg
  February 2026 – present

Main skills acquired on:
- Alloy development
- Powder Atomization
- Metallurgical characterization
- Assessment of mechanical properties
- Post-production thermal treatments
- Rheology and preparation of powder mixtures
- Process maps of new metal alloys for Additive Manufacturing
- 3DPrinting of complex shape parts

- *Technical Service Engineer*
  Circuit Foil, Luxembourg
  November 2024 – February 2026

Main skills acquired on:
- Technical support to customers: investigation and analyses, follow-up of customer's new project evaluation and new product qualification.
- Samples analysis, communication of technical solutions with technical report.
- Use of Quality Tools (8D – Fishbone – 5 Why – Pareto charts – Cpk).
- Close collaboration with R&D-, Production-, Quality-, Sales- and Customer Care- dpts.

EDUCATION

- *Doctorate in Additive Manufacturing Metallurgical Engineering*
  Université de Liège, Belgium
  August 2020 – July 2024

- *Master Degree in Materials Engineering*
  Università degli Studi di Padova, Italy
  October 2017 - December 2019

- *Bachelor Degree in Chemical and Materials Engineering*
  Università degli Studi di Padova, Italy
  October 2013 - March 2017

KEY SKILLS

- Materials Science
- Additive Manufacturing
- Product Qualification
- Technical Support
- Quality Tools

SOFT SKILLS

- Problem solving
- Patience
- Autonomy
- Critical thinking
- Project Management

ACHIEVEMENTS

- Inventor of a European patent: GRAPHITE-BASED STEEL ALLOY AND METHOD FOR PRODUCING IT USING LASER POWDER BED FUSION - Publication Number WO/2025/202196.
- Author of Scientifical Articles:
  - On the role of the hierarchical structures in the friction-induced phenomena of directed energy deposited 316L+WC sliding against different counter-bodies, Saggionetto E. et al., 2025, Tribology International, DOI: 10.1016/j.triboint.2025.110973
  - Effect of SiC addition on processability of AISI S2 tool steel for laser powder bed fusion, Saggionetto E. et al., 2024, Material Forming, Conference paper, DOI: 10.21741/9781644903131-24
  - Development and processability of AISI S2 tool steel by Laser Powder Bed Fusion, Saggionetto E. et al.,2023, Material Forming, Conference paper, DOI: 10.21741/9781644902479-5
- Peter Blau Best Poster Award – 2nd place achieved in occasion of the 23rd Wear of Materials International Conference, April 2021. Poster title: *The role of the counterbody material on tribological properties of 316L+WC composite coatings processed by laser cladding.*

LANGUAGE AND TOOLS

- Italian: Native | English: Full professional proficiency C1 | French: Professional working proficiency B2
- Software: Microsoft Office | SAP | Adobe Tools | Matlab | Origin | Minitab | Fusion360 | SolidEdge | Netfabb | Ultimaker Cura

HOBBIES

Football, Running, Hiking, Cooking, Reading

